# Tracing life through light: towards detecting life on exoplanets with spectroscopy and spectropolarimetry

Mulder, W.

# TRACING LIFE THROUGH LIGHT

## TOWARDS DETECTING LIFE ON EXOPLANETS WITH SPECTROSCOPY AND SPECTROPOLARIMETRY

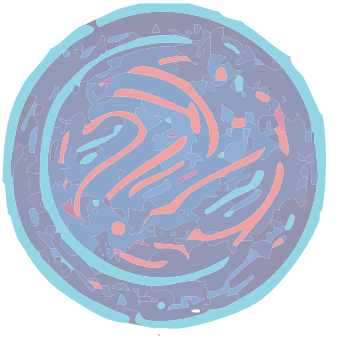

WILLEKE MULDER

# Tracing life through light

Towards detecting life on exoplanets with spectroscopy and spectropolarimetry

Proefschrift

ter verkrijging van
de graad van doctor aan de Universiteit Leiden,
op gezag van rector magnificus prof. dr. S. de Rijcke,
volgens besluit van het college voor promoties
te verdedigen op donderdag 2 april 2026
klokke 10:00 uur

door

Willeke Mulder

geboren te Hengelo, Nederland
in 1993

| | | |
|---|---|---|
| Promotores: | Prof. dr. I. A. G. Snellen | |
| | Prof. dr. C. U. Keller | |
| Co-promotor: | Dr. ir. F. Snik | |
| Promotiecommissie: | Prof. dr. M.P. van Exter | |
| | Prof. dr. A. Vidotto | |
| | dr. N. van der Marel | |
| | Prof. dr. W. Sparks | University of Maryland |
| | Prof. dr. B.-O. Demory | University of Bern |

Printed by: Gildeprint

ISBN: 978-94-6496-510-0

An electronic copy of this thesis can be found at https://openaccess.leidenuniv.nl.

**Cover design:**
The cover reflects the title of and my journey during my PhD - tracing life through light, both in science and in spirit. Just as we search for signs of life beyond our planet, we also learn to keep following the light through moments of darkness, stumbling yet moving forward toward understanding. This cover was designed by the author using Adobe Illustrator, aided by AI.

*Those who claim to be entirely unbiased often conceal their prejudices the deepest;*
*acknowledging bias is the first step toward equity.*

# Contents

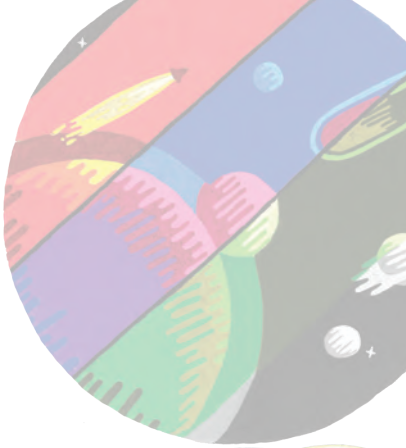

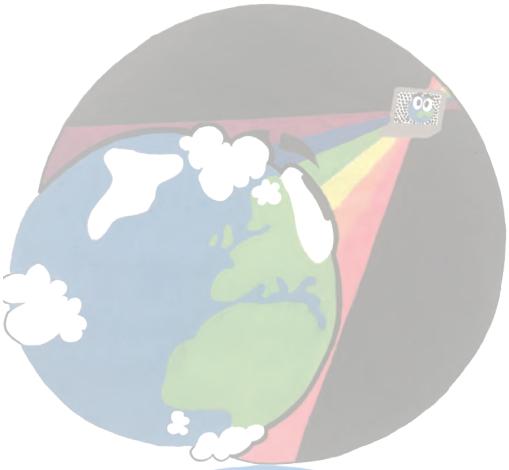

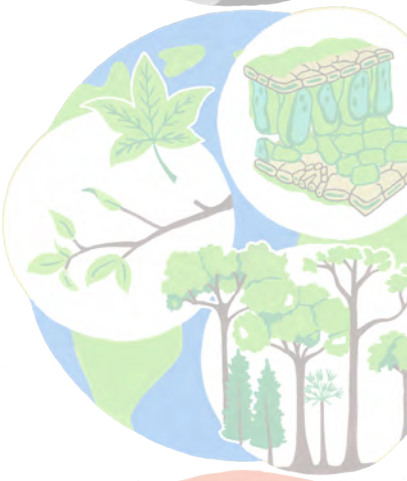


ANGRY PHOTONS


THE BEETLES

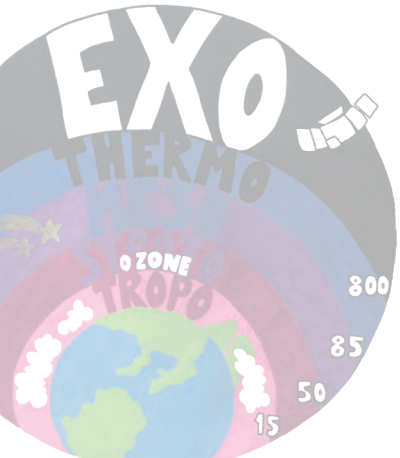
EXO
THERMO
OZONE
TROPO
800
85
50
15



# 1 | Introduction



*With planetary exploration, there has been one general theme, and that is diversity. Everything is more diverse when we look at it than was predicted.*

– Jack Lissauer, 2022

## The revolutionary hunt for exoplanets and characterising atmospheres

How did we come into existence? Are we alone? These questions have driven humans for centuries. Despite long-standing speculations about extrasolar planets and extraterrestrial life, it was only three decades ago that astronomers discovered the first worlds beyond our solar system. In 1992, (Wolszczan & Frail, 1992) discovered planetary-mass objects orbiting the pulsar PSR B1257+12, believed to be second-generation products (Patruno & Kama, 2017) of stellar evolution. The first exoplanet around a main-sequence star was found by (Mayor & Queloz, 1995), marking the start of an exoplanet revolution and earning a Nobel Prize in 2019. This gaseous planet, 51 Pegasi b, orbits very close to its star, leading to the discovery of many "Hot Jupiters".

## 1.1 Exoplanet detection methods

Today, more than five thousand confirmed exoplanets have been discovered through methods like radial velocity, transit observations, and direct imaging. Figure 1.1 shows the wide diversity of the discovered exoplanets in terms of their mass and orbital period. It reveals classes that have no counterparts in the solar system, such as super-Earths and Hot Jupiters. Each of the before-mentioned detection methods are prone to detection biases and thus detection of specific types of exoplanets, as briefly explained below.

### 1.1.1 Radial-velocity method

A star with an orbiting planet experiences a gravitational pull from the planet, causing the star to wobble in a small orbit around the common centre of mass. The radial-velocity method, also known as Doppler spectroscopy, detects these wobbles as the Doppler shift of stellar spectral lines due to the periodic changes of the stellar velocity along the line of sight. The radial-velocity method provides only constraints on planetary masses, since the amplitude of the variation depends on the planet's mass, orbital distance and inclination. It is most sensitive to massive planets on close-in orbits, e.g. the first exoplanet discovery 51 Pegasi b, see Fig. 1.1, because signals with large amplitudes are easier to detect.

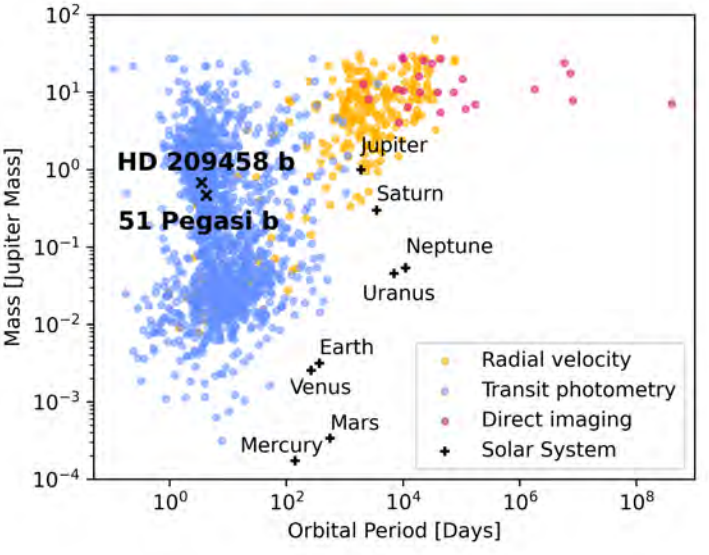


Figure 1.1: Mass of exoplanets plotted against their orbital period. The overview reveals the diverse population of all confirmed exoplanets to date (November, 24, 2025). The Solar System planets are marked using black crosses. The data, used in this figure, is coming from the NASA Exoplanet Archive.

However, stellar activity (e.g. rotation, spots and plages [1]) also induces apparent radial velocity variations, and these activity-driven signals can mimic or obscure the Doppler wobble of a planet. This makes the identification of low-amplitude planetary signals particularly challenging when the planet's orbital period is similar to the characteristic timescales of stellar activity. Over the years, the precision of radial velocity measurements has improved significantly as highly sensitive spectrographs are able to detect rocky planets around low-mass stars, and the stellar velocity signal becomes smaller as the planets are more distant, e.g. Proxima Centauri b and d (e.g. Anglada-Escudé et al., 2016; Faria et al., 2022) and planets with even longer orbital periods (e.g. Dubber et al., 2019).

### 1.1.2 Transit photometry

After the discovery of the first five planets around solar-type stars, photometric searches had been carried out to try to detect planet transits, however without success (e.g. Henry et al., 1997; Baliunas et al., 1997; Henry et al., 2000). These early surveys lacked the continuous, high-precision photometry required to detect the shallow and infrequent dips caused by most planets. It was not until 1999, when Charbonneau et al. (1999) was the first to use the transit method to find the hot Jupiter orbiting the G0 dwarf HD 209458, the first exoplanet for

[1] Plages are bright, elongated regions on a star's surface, often associated with star spots and strong magnetic fields, that are a key part of stellar activity. star spots, however, appear as dark spots.

which a transit was observed after its initial radial-velocity discovery. The planet received the designation HD 209458 b, see Fig. 1.1.

The exoplanet discoveries with the space missions CoRoT (Baglin et al., 2009), Kepler (Howell et al., 2014) and TESS (Ricker et al., 2015) completely changed the field of exoplanets, as these missions enabled continuous, ultra-precise photometric monitoring of large stellar samples and revealed thousands of small planets. Ever since the data release of Kepler in 2014, transit photometry has been the most widely used technique for detecting and studying exoplanets. The mission carried out accurate photometry of many stars and searched for dips in their light curves caused by orbiting exoplanets that block parts of the starlight. This already implies that the orbits need to be aligned near edge-on from our viewpoint, and that only a small geometric fraction of planetary systems can be detected in transit.

The depth of the dips in the transit light curves are used to determine the radii of the planets, whereas observing multiple transits allows for the determination of the orbital period. Therefore, just as for the radial-velocity method, transit photometry is most effective for detecting larger exoplanets with shorter orbital periods, because these produce deeper and more frequent transit signals and are easier to distinguish from noise.

Combining the latter methods breaks the degeneracy of the planet mass and orbital inclination and therefore provides a method to determine the bulk density given the planet mass and radius, yielding a direct constraint on the planet's internal structure and composition.

### 1.1.3 Direct imaging

The direct depiction of an exoplanet on an image requires a method to angularly resolve the dim planet from its host star. To do so, an imaging system needs to overcome the huge contrast between the star and the planet at small angular separations. This requires so-called High Contrast Imaging (HCI). For example, in the optical wavelength regime, the detection of light reflected off an Earth-like planet orbiting a Sun-like star, requires a contrast of $\sim 10^{-10}$ and for a Jupiter-analogue a contrast of $\sim 10^{-8} - 10^{-9}$ relative to their host star. In the near-infrared regime, young giant planets generally have contrasts in the range $10^{-4} - 10^{-6}$. The majority of the heat from their formation is emitted as near-infrared radiation. It remains the region of most favourable contrast even as planets age, improving the $\sim 10^{-8} - 10^{-9}$ contrast ratio to $\sim 10^{-5}$ for the same Jupiter-analogue. Current ground-based high-contrast imaging instruments can directly image bright self-luminous brown dwarf companions in NIR total intensity at contrasts of $10^{-2} - 10^{-6}$ (e.g. Nielsen et al., 2019; Langlois et al., 2021).

Achieving high contrasts at small angular separation requires adaptive optics (compensating atmospheric disturbances of the incoming light using wavefront sensing and a deformable mirror and allowing diffraction-limited imaging), coronagraphy (blocking on-axis starlight and with that boosting the contrast of the off-axis companions, (e.g. Lyot, 1939; Ferrari et al., 2007), and advanced data processing techniques for optimal suppression of the remaining starlight like e.g. Spectral Differential Imaging (SDI; Racine et al., 1999), Polarimetric Differential Imaging (PDI; Kuhn et al., 2001), Imaging Spectroscopy (IS; Sparks & Ford, 2002) or Angular Differential Imaging (ADI; Marois et al., 2006).

In 2004, Chauvin et al. (2004) was the first to directly image an exoplanet using the Very Large Telescope (VLT). It concerned the planetary mass object 2M1207 b orbiting a brown

dwarf. This so-called 'Super Jupiter' has a mass of a bit more than five Jupiter masses. To date, 82 planets have been directly imaged, including about 50 other Super Jupiters. These gas giants function as a laboratory for understanding the atmospheric physics of substellar objects and their possible link to planet formation.

**Investigating the diversity of exoplanets with direct imaging**

There are two main planet formation theories that could explain the resulting diverse planetary systems: the core-accretion (Pollack et al., 1996) and the disk gravitational instability (Boss, 1997) models. In the core-accretion model, dust grains in a protoplanetary disk gradually collide and grow into massive solid cores (a few Earth masses), which then trigger rapid gas accretion to form giant planets over millions of years. In contrast, the disk gravitational instability model envisions that in a massive, cool disk, parts of the gas rapidly collapse under their own gravity - on dynamical timescales of thousands of years - forming self-gravitating clumps that can contract into gas giants, especially in the disk's outer regions. The former explains the observed metallicity correlation and prevalence of gas giants at moderate orbital distances, while the latter provides a fast route to giant planet formation in massive or at larger orbital distances. Circumstellar disks are used to investigate these formation processes as they shape the planet-forming environments (e.g. Mizuno, 1980; Harsono et al., 2018; Keppler et al., 2018). Focusing on polarimetric observations, in the last few decades PDI has been used to image bipolar and cometary nebulae (Gledhill, 1991) and protoplanetary nebulae (Gledhill et al., 2001). Recently van Holstein et al. (2021) reported the polarimetric detections of the substellar companions DH Tau B and GSC 6214-210 B, likely originating from the circumsubstellar accretion disk. PDI records two orthogonal linear polarisation states simultaneously on the detector (Andreou & Kalayjian, 2002; Dohlen et al., 2008; de Boer et al., 2020). The emission from an unresolved host star is predominantly unpolarised (Kemp et al., 1987) and results in two nearly identical beams, whereas the stellar light that has been reflected on dust grains becomes polarised through scattering. As a result, the starlight will be largely removed during the post-processing and the reflected polarised light will reveal itself. These scattered-light observations do not only reveal the presence of dust particles, but also provide information regarding the properties of dust grains, as encoded in the intensity and degree of polarisation as a function of phase angles and wavelength (Ginski et al., 2023). This provides us with valuable insights into the birth environment of planets.

## 1.2 From detecting to characterizing exoplanets

An initial understanding of the bulk density of the discovered exoplanets can be achieved by combining the transit and radial velocity techniques. Nevertheless, significant ambiguities complicate the in-depth analysis of exoplanet compositions when relying solely on mass and radius measurements (Seager et al., 2007). Additional spectroscopic observations of exoplanet atmospheres yield details concerning their thermal structures, dynamic behaviours and atmospheric composition with possible leftover molecules from their birthplaces (e.g. Madhusudhan et al., 2014; Thiabaud et al., 2014), clarifying their formation history.

### 1.2.1 Transmission spectroscopy

In the case of a planet transiting its host star, some starlight is blocked by the planet while some shines through the upper layers of the planet's atmosphere. The light is absorbed and scattered by aerosols and molecules, leading to a wavelength-dependent absorption in the stellar spectrum. Consequently, measuring the transit depth as a function of wavelength allows for the identification of chemical species in the exoplanet's atmosphere (Seager & Sasselov, 2000).

The first detection of a chemical species in an exoplanetary atmosphere was the identification of the sodium doublet in HD 209458 b. Charbonneau et al. (2002) found a slight enhancement of the transit depth of the planet at the sodium-line wavelengths. Thereafter, other species like water (e.g. Deming et al., 2013; Evans et al., 2016) and more recently molecules including $CO_2$ (e.g. Ahrer et al., 2022; Madhusudhan et al., 2023; Rustamkulov et al., 2023), $SO_2$ (Tsai et al., 2023), $CH_4$ (Bell et al., 2023; Madhusudhan et al., 2023) and $H_2S$ (Fu et al., 2024) using JWST.

### 1.2.2 Emission spectroscopy

During a secondary eclipse, the thermal radiation and reflected light from a planet will disappear and reappear. The (near-)infrared radiation emitted by the exoplanet is observed by comparing the flux of the planetary system before, after, and during its secondary eclipse (e.g. Richardson et al., 2003; Charbonneau et al., 2005). This observational method, referred to as emission spectroscopy, enables the characterization of the planetary atmosphere properties such as the pressure-temperature profile (P-T profile), molecular composition, and cloud properties (Madhusudhan, 2019). Additionally, it can probe the temperature structure on the daysides of these planets (e.g. Cubillos et al., 2011; Yan, F. et al., 2022), and infer the presence of potential thermal inversions (e.g. Burrows et al., 2007; Knutson et al., 2008).

### 1.2.3 High-resolution Doppler spectroscopy

High-resolution Doppler spectroscopy plays a crucial role in our understanding of exoplanet atmospheres, offering insights into the chemical composition, dynamics, and physical conditions of exoplanets. Similar to the radial-velocity method, Doppler spectroscopy relies on the Doppler shift of spectral lines. In addition, it takes advantage of the relative large radial velocity of the companion compared to its host star.

The high spectral resolution disperses into a larger number of spectral channels, which significantly decreases the signal-to-noise per channel. One way to compensate for this loss is using the cross-correlation technique. It measures the similarity of a spectrum reflecting one or more species or even a full atmospheric model shifted with various radial velocities and the observational data. In addition, the high resolution ensures that the spectral features of different species can be resolved into unique ensembles of individual lines, allowing the unambiguous identification of even minor species and isotopologues (Mollière & Snellen, 2019; de Regt et al., 2024; González Picos et al., 2024; Gandhi et al., 2025).

Snellen et al. (2010) was the first to successfully apply high-resolution spectroscopy on the transiting hot Jupiter HD 209458 b using the CRyogenic high-resolution InfraRed Echelle

Spectrograph (CRIRES; Kaeufl et al., 2004) instrument on the VLT. CRIRES was designed for high-resolution spectroscopy in the infrared. This is particularly useful for detecting molecules in the atmospheres of cooler exoplanets, which emit more strongly in the infrared part of the spectrum. The instrument was recently upgraded to CRIRES+ (Dorn et al., 2023) with cross-dispersing elements and larger, more sensitive detectors. The simultaneous wavelength range increased by a factor of $\sim 10$, while preserving the total operational wavelength range.

### 1.2.4 Atmospheric models & retrievals

High-resolution spectroscopy allows us to quantify the species and isotopologues in the atmospheres of extrasolar objects. To do so, we apply an atmospheric retrieval technique that couples an atmospheric model of the object's atmosphere with a nested sampling tool to obtain the posterior distributions of the given parameters of the object. Our models make use of a 'free chemistry' temperature profile. It allows the chemical abundances to vary freely within fixed boundaries, while being vertically constant throughout the atmosphere. This 'free' retrieval offers a high degree of flexibility. The parameter space is initiated by a set of priors and boundary constraints for a set of parameters describing the atmospheric chemistry, cloud structure, surface gravity, and molecular or atomic opacities. This technique has been applied to various exoplanets (e.g. Crossfield et al., 2019; Welbanks et al., 2019; Mollière et al., 2020; Zhang et al., 2022; Grasser et al., 2024; Landman et al., 2024; Xuan et al., 2024), and other self-luminous objects, like brown dwarfs (e.g. González Picos et al., 2024; de Regt et al., 2024; Gandhi et al., 2025; Mulder et al., 2025).

The atmospheric retrieval framework used in this chapter is based on the radiative transfer code `petitRadTrans` (`pRT`; Mollière et al., 2019). It is a powerful Python interface to calculate planetary transmission and/or emission spectra (including multiple scattering). `pRT`'s built-in retrieval package provides the option to run retrievals that combine data sets of varying resolution, wavelength coverage and atmospheric contexts. `pRT`'s extensive opacity database includes gas and cloud opacities. `pRT` was integrated with the nested sampling tool `PyMultiNest` (Buchner et al., 2014), a Python interface for the `MultiNest` algorithm.

A significant and time expensive number of `pRT` model spectra are needed to statistically support the retrievals. To speed up the process, the spectral computations were sped up by undersampling the high-resolution spectra, i.e. by a factor of 3). All computations were executed in parallel on the Dutch National Supercomputer Snellius.

## 1.3 Current and future research in exoplanetary science

### 1.3.1 Observational probes of planet formation history

Isotopes in exoplanet atmospheres have the potential to provide important insights into the origin and evolution of planetary systems. In the Solar System, the deuterium-to-hydrogen (D/H) ratio traces the origin and evolution of water within our own celestial neighbourhood. Therefore, it can function as a key diagnostic to determine where objects were formed. Also outside the Solar System, the D/H ratio may vary for different exoplanets. This variation

may be linked to the varying isotope ratios in the protoplanetary disks that are caused by deuterium fractionation due to temperature differences (Aikawa & Herbst, 1999; Ceccarelli et al., 2014). Deuterium fractionation arises because the heavier deuterium-bearing molecules have slightly lower zero-point energies than their protium ($^1$H) counterparts, making ion–molecule exchange reactions (e.g., $H_3^+ + HD \rightarrow H_3D^+ + H_2$) strongly favoured at low temperatures. As a result, cold regions of protoplanetary disks become enriched in deuterium relative to hydrogen, while warmer areas support less fractionation and can even reverse it through exchange with HD and $H_2O$, producing the spatial D/H variations observed in exoplanet-forming material. The D/H ratio may change over time after a planet is formed, as atmospheric loss processes can still alter the D/H ratio.

Carbon and oxygen are two of the most abundant elements in the universe and play key roles in the chemistry of protoplanetary disks and planetary atmospheres. A disk midplane, the region where planets form, a radial gradient in the gas–ice C/O ratio is expected due to temperature-dependent freeze-out of major volatiles (Öberg et al., 2011). As molecules such as $H_2O$, $CO_2$ and CO condense at progressively larger orbital distances, this creates chemically distinct zones in which either carbon- or oxygen-rich material dominates the gas or solid phase. Planets assembling in these regions may therefore inherit characteristic atmospheric C/O ratios.

However, recent studies suggest that this simple static picture is likely incomplete. The radial transport of solids - particularly the inward drift of icy pebbles - can redistribute volatile ices across large distances, altering both the local gas-phase and solid-phase C/O ratios (e.g. Schneider & Bitsch, 2021; Eistrup & Henning, 2022). The sublimation of drifting pebbles inside their respective ice lines can locally enrich the gas with oxygen- or carbon-bearing species, smoothing or even reversing the expected radial gradients. As a result, the C/O ratio imprinted on forming planets may be influenced not only by the nominal ice-line locations, but also by the efficiency of pebble drift, the disk's dust-to-gas ratio, and the evolutionary stage of the disk.

Some isotope ratios are (roughly) constant on Solar System scales. (Woods & Willacy, 2009) measured a carbon $^{12}C/^{13}C$ isotope ratio of ~89. On larger, galactic scales, the ratio varies. $^{13}C$ is produced within stars that enrich the interstellar medium over time. The current, local ISM has an average $^{12}C/^{13}C$ ratio of ~68 (Langer & Penzias, 1993; Milam et al., 2005), which is significantly lower than that of the Solar System. Similar to deuterium fractionation, fractionation processes could create isotope-ratio variations on protoplanetary disk scales (Woods & Willacy, 2009), which could be passed on to exoplanet atmospheres (Zhang et al., 2021; Mollière et al., 2019; Line et al., 2021; Bergin et al., 2024).

High-resolution spectroscopy has proven to be able to constrain isotopic compositions of BDs, as Zhang et al. (2021) illustrated using the NIRSPEC instrument on the Keck telescope and de Regt et al. (2024) using CRIRES+ on the VLT. This opens up the possibility of investigating the carbon $^{12}C/^{13}C$ isotope ratio as a formation tracer. Additional isotope ratios might be within the reach of current high-resolution spectrographs, such as CRIRES+, and space-based facilities, such as JWST (Gandhi et al., 2023). Looking further ahead, the ex-

tremely large telescope will include a high-resolution spectrograph operating in the infrared regime (METIS; Brandl et al., 2021) and the Giant Magellan Telescope (GMT) one operating in the optical regime (GCLEF; Szentgyorgyi et al., 2016). These new instruments will make substantial advances with high-resolution spectroscopy by detecting minor chemical species in both BDs and exoplanet atmospheres, e.g. possibly identifying biomarkers in rocky planet atmospheres.

### 1.3.2 Working towards the search for extraterrestrial life

The search for life in the universe is a driving force for (exo)planetary research. On average, every star hosts at least one planet (Cassan et al., 2012), and one in two Solar-like stars could host a rocky planet in their habitable zone (Hsu et al., 2019; Bryson et al., 2021).

The observation of a transit requires a planetary system with a specific edge-on geometry. As a result, many of the potential close-by Earth-like planets will be missed. In addition, in the case of an optimal orientation, there will be only one transit every year when considering Earth-like planets around Sun-like stars. Even if we would observe a transit, many observations would be required to obtain a high enough signal-to-noise ratio to detect biosignatures (Serindag & Snellen, 2019; Hardegree-Ullman et al., 2023).

In the end, direct imaging may offer the best means to detect possible life on other planets. There is still much work to be done before instruments can reach the required contrasts to detect Earth-like planets using reflected starlight. In the coming years, there will be a large focus on the development of (new) technology (e.g. adaptive optics focal-plane wavefront sensing techniques (Haffert et al., 2023), predictive control (e.g. Males & Guyon, 2018; Landman et al., 2021; Haffert et al., 2021), development of very high-order deformable mirrors), improving post-processing algorithms (e.g. SDI, PDI, IS and ADI), and the construction of large ground- and space-based observatories. The Nancy Grace Roman Space Telescope will be testing the first dedicated high-contrast imaging instrument in space (Kasdin et al., 2020). The main science goal of NASA's Habitable World Observatory will be to directly image Earth-like planets in the habitable zone of Sun-like stars, and identify biosignatures in their atmosphere. European Southern Observatory's Extremely Large Telescope will have instruments such as METIS (Brandl et al., 2021) that will push the capabilities of ground-based high-resolution spectroscopy to smaller planets and more detailed characterization of their atmospheres. Proxima Centauri b would be a prominent target, which may be detectable when combining high-contrast imaging with high-dispersion spectroscopy on the Extremely Large Telescope (Snellen et al., 2015). Adaptive optics will be the most crucial technology for ground-based high-contrast imaging, bringing detection of potential biomarker gases within reach within the next decade.

1

*Who are we? We find that we live on an insignificant planet of a humdrum star lost in a galaxy tucked away in some forgotten corner of a universe in which there are far more galaxies than people.*

– Carl Sagan, 1980s

## *Observing the Earth as an Exoplanet using spectropolarimetry*

To detect extraterrestrial life, we need dedicated instruments, data-analysis algorithms and observation strategies; what are we looking for? New opportunities will emerge once the technology is ready to resolve Earth-like planets from their host stars. Direct-imaging spectroscopy and polarimetry will open up another source of information by studying the properties of planets via spectral flux and polarisation measurements. Light emitted by a solar type star is in general unpolarised when integrated over the stellar disk (Kemp et al., 1987). Light observed from a planet will usually be polarised, since starlight is scattered by particles and aerosols in its atmosphere, or reflected by a surface (in the case of a rocky planet). In theory, the atmosphere of an exoplanet could be characterized, without even optically resolving the planet since the polarisation depends on the physical circumstances of the scatterers, e.g. their shapes, sizes and chemical composition. Polarised radiative transfer simulations have shown that light reflected by an Earth-like exoplanet is indeed polarised by either surface reflection or atmospheric scattering (e.g. Hansen & Travis, 1974; Stam, 2008; Karalidi et al., 2012; Trees & Stam, 2019). The degree and the direction of polarisation also depend on the viewing geometries and wavelength (e.g. Groot et al., 2020; Gordon et al., 2023, and references therein). This allows us to use polarimetry to detect traces of bio-signatures and possibly extraterrestrial life.

Despite the strong astronomical science cases that polarimetry has to offer, polarimetry has not been featuring in any space telescope as a first science goal, yet. However, space missions have delivered valuable polarimetric insights by carrying instruments or filters capable of measuring polarisation. For example, the NICMOS instrument on the Hubble Space Telescope underwent a dedicated nine-orbit calibration during Cycle 15, enabling high-accuracy near-infrared imaging polarimetry (~1% precision) of circumstellar structures. In addition polarimetric observations of comet ISON at a distance of 3.8 astronomical unit, made with Hubble's ACS-WFC instrument, provided the first sub-arcsecond visible-light polarisation maps of an Oort-cloud comet, revealing distinct dust-jet signatures.

The Nancy Grace Roman Space Telescope will be the first space-based observatory demonstrating high-contrast polarimetry using the Roman Coronagraph (Doelman et al., 2023). Its implementation presents trade-offs for both imaging and spectroscopy. All components in an instrument may change or add to the incoming polarisation of the incident light, complicating the calibration and observation strategies. Furthermore, polarisation optics reducing the intensity of incoming light (even up to a half) are unfavourable in the field of exoplanetary science, where photons are scarce. Moreover, polarimetry, being a differential technique, usually comes with all kinds of systematic errors, like spurious polarisation signals created by varying atmospheric properties, imperfect (knowledge of the) optics or

even detector properties. To this end, the implementation of polarimetry in an astronomical instrument requires a careful instrument design.

## 1.4 Definitions for polarimetry

The study of polarisation requires precise definitions, as the interpretation of polarimetric measurements depends critically on the underlying concepts. Polarisation is a property of transverse waves which specifies the geometrical orientation of the electric field vector of light. The definition of polarisation is widely explained and discussed in literature (e.g. Collett, 2005; Goldstein, 2011; Hecht, 2017; Pedrotti et al., 2019).

Follow the definition according to Hecht (2017), we describe polarisation using the Jones and the Stokes formalism. The Jones formalism is limited to treating fully polarised electromagnetic beams and their phase information. The formulation is applicable to perfectly coherent beams, which does allow a description of interference phenomena, however, it can neither describe randomly (better known as unpolarised) or partially polarised light nor the depolarisation of light. In the intensity domain, a beam can be described with the Stokes formalism. This formalism can describe full, partially and unpolarised light. Phenomena like interference cannot be represented with the Stokes formalism, as it does not contain phase information.

### 1.4.1 Jones formalism

The Jones formalism is able to handle coherent waves, meaning that the phase information is preserved. Each electro-magnetic beam can be represented in terms of the electric field vector components. Therefore, in column form, the $2 \times 1$ (complex) Jones vector is:

$$\mathbf{E} = \begin{bmatrix} E_x \\ E_y \end{bmatrix} = \begin{bmatrix} E_{0x} e^{i\varphi_x} \\ E_{0y} e^{i\varphi_y} \end{bmatrix}, \tag{1.1}$$

where $E_{0x}$ and $E_{0y}$ are the amplitudes and $\varphi_x$ and $\varphi_y$ are the phases. Linear, circular, and elliptical polarisation correspond to special cases of the relative amplitudes and phase difference between $E_x$ and $E_y$. Linear polarisation arises when the phase difference is zero or $\pi$, circular when the amplitudes are equal and the phase difference is $\pm\pi/2$, and elliptical in the general case. Two orthogonal linear polarisation states are represented by substituting either $E_{0y} = 0$ for fully horizontal, see Eq. 1.3, and $E_{0x} = 0$ for vertical polarisation:

$$\mathbf{E}_{\text{hor}} = \begin{bmatrix} E_{0x} e^{i\varphi_x} \\ 0 \end{bmatrix} \qquad \mathbf{E}_{\text{ver}} = \begin{bmatrix} 0 \\ E_{0y} e^{i\varphi_y} \end{bmatrix} \tag{1.2}$$

The sum of two coherent beams is simply the sum of their corresponding components. For simplicity, the irradiance can be normalized to unity when the exact amplitude and phase are not of importance, resulting in the vectors:

$$\vec{\mathbf{E}}_{\text{hor}} = \begin{bmatrix} 1 \\ 0 \end{bmatrix} \qquad \vec{\mathbf{E}}_{\text{ver}} = \begin{bmatrix} 0 \\ 1 \end{bmatrix} \tag{1.3}$$

After a polarised incident beam $\mathbf{E}_{\text{in}}$ passes through a series of $n$ optical elements, $\mathbf{J}_1, \mathbf{J}_2, \cdots \mathbf{J}_n$, the outgoing modified Jones vector equals $\mathbf{E}_{\text{out}} = \mathbf{J}_n \cdots \mathbf{J}_2 \mathbf{J}_1 \mathbf{E}_{\text{in}}$. Each matrix $\mathbf{J}_i$ is a $2 \times 2$ Jones matrix, that represents the interaction with a single optical element;

$$\mathbf{J} = \begin{pmatrix} j_{xx} & j_{xy} \\ j_{yx} & j_{yy} \end{pmatrix}. \tag{1.4}$$

For an ideal linear polariser the off-diagonal elements $j_{yx} = j_{xy}$ are 0 and the diagonal elements have a value between 0 and 1, see Eq. 1.5. As a result, this element only changes the amplitude of the incoming Jones vector, while its phase remains the same.

$$\mathbf{J}_{\text{hor,pol}} = \begin{pmatrix} 1 & 0 \\ 0 & 0 \end{pmatrix}, \qquad \mathbf{J}_{\text{ret}} = e^{i\delta/2} \begin{pmatrix} 1 & 0 \\ 0 & -i \end{pmatrix}. \tag{1.5}$$

As the name reveals, a wave plate changes the phase $\varphi_x$ and $\varphi_y$ of the incoming wave with a given retardance $\delta$. As a result, for a wave plate the off-diagonal elements are again zero, however, we add a phase shift of $\varphi_x = \delta/2$ along the x-axis, $j_{xx} = e^{i(\delta/2)}$ and $\varphi_y = -\delta/2$ along the y-axis, $j_{yy} = e^{-i(\delta/2)}$). The retardance equals $\delta = \pi$ for a half-wave plate and $\delta = \pi/2$ for a quarter-wave plate.

### 1.4.2 Stokes and Mueller formalism

Light is generally neither completely polarised nor completely unpolarised; more often, it is partially polarised, with the electric-field vector varying in a statistically incoherent manner, typically described in terms of photon fluxes. A useful way to characterise such light is as a superposition of specific proportions of unpolarised and polarised components. Stokes (1852) introduced four observables to describe any such superposition: the Stokes polarisation parameters `I`, `Q`, `U`, and `V`, which together form the so-called Stokes vector, $\mathbf{S}$ (Stokes, 1852; Chandrasekhar, 1946):

$$\mathbf{S} = \begin{pmatrix} S_0 \\ S_1 \\ S_2 \\ S_3 \end{pmatrix} = \begin{pmatrix} \langle E_x^* E_x + E_y^* E_y \rangle \\ \langle E_x^* E_x - E_y^* E_y \rangle \\ \langle E_x^* E_y + E_y^* E_x \rangle \\ \langle i\left(E_y^* E_x - E_x^* E_y\right) \rangle \end{pmatrix} = \begin{pmatrix} I_{0^\circ} + I_{90^\circ} \\ I_{0^\circ} - I_{90^\circ} \\ I_{45^\circ} - I_{-45^\circ} \\ I_{\circlearrowright} - I_{\circlearrowleft} \end{pmatrix} = \begin{pmatrix} \texttt{I} \\ \texttt{Q} \\ \texttt{U} \\ \texttt{V} \end{pmatrix} \tag{1.6}$$

The second definition in Eq. 1.6 shows the calculation of the Stokes vector as ensemble of the averages and covariances of the electric field vector components. The third definition provides a description on how to measure the Stokes parameters using flux measurements through linear polarisers at certain angles and either left- or right-handed circular polarisers.

In the literature, the Stokes parameters are represented as $S_0$, $S_1$, $S_2$, $S_3$, as well as `I`, `Q`, `U` and `V`. To prevent confusion, we will only use the latter. The first Stokes parameter, `I`, represents the total intensity of the optical beam; the second and third, `Q` and `U`, describe the linear polarisation state and are defined as differential intensity measurements between orthogonal linear bases. The fourth parameter, `V`, quantifies the circularly polarised component as the difference between right- and left-handed circular polarisation intensities. In this dissertation, we refer to the horizontal, vertical, 45° and 135° linear polarisation states

as Q+, Q−, U+, U−, whereas V+ and V− represent right- and left-handed circular polarisation. Throughout the text, when fractional polarisation is discussed, the absolute values of Q, U and V are normalized with respect to the intensity I.

Measurements of incoming polarisation from inclined or moving platforms - such as airborne remote sensing - are susceptible to small errors in the reference orientation used to define viewing angles. This poses a particular challenge for interpreting the linear Stokes parameters, Q and U, which depend explicitly on the choice of reference frame. In such cases, it is often more practical to derive orientation-independent quantities such as the degree of polarisation, $P$, which describes the fraction of the wave that is polarised, as well as the degree and angle of linear polarisation, $P_{\mathrm{L}}$ and $\chi_{\mathrm{L}}$ respectively.

$$P = \frac{\sqrt{\mathtt{Q}^2 + \mathtt{U}^2 + \mathtt{V}^2}}{\mathtt{I}}; \qquad P_{\mathrm{L}} = \frac{\sqrt{\mathtt{Q}^2 + \mathtt{U}^2}}{l}; \qquad \chi_{\mathrm{L}} = \frac{1}{2}\arctan\frac{\mathtt{U}}{\mathtt{Q}}. \tag{1.7}$$

These quantities remain well-defined regardless of the exact reference orientation, making them more robust for field applications.

### Mueller calculus

Stokes vectors can be manipulated using the Mueller calculus. A single or a stack of multiple optical elements can be represented by a $4 \times 4$ Mueller Matrix, $\mathbf{M}$. If an incoming beam of light with a given polarisation state, $\mathbf{S}_{\mathrm{in}}$, propagates through an element $\mathbf{M}$, the observed outgoing beam $\mathbf{S}_{\mathrm{obs}}$ is linearly related to $\mathbf{S}_{\mathrm{in}}$, through $\mathbf{S}_{\mathrm{obs}} = \mathbf{M}\mathbf{S}_{\mathrm{in}}$. This can be expressed in terms of Mueller matrix elements $m_{\mathrm{i,j}}$ as:

$$\begin{pmatrix} \mathtt{I}_{\mathrm{obs}} \\ \mathtt{Q}_{\mathrm{obs}} \\ \mathtt{U}_{\mathrm{obs}} \\ \mathtt{V}_{\mathrm{obs}} \end{pmatrix} = \begin{pmatrix} m_{11} & m_{12} & m_{13} & m_{14} \\ m_{21} & m_{22} & m_{23} & m_{24} \\ m_{31} & m_{32} & m_{33} & m_{34} \\ m_{41} & m_{42} & m_{43} & m_{44} \end{pmatrix} \begin{pmatrix} \mathtt{I}_{\mathrm{in}} \\ \mathtt{Q}_{\mathrm{in}} \\ \mathtt{U}_{\mathrm{in}} \\ \mathtt{V}_{\mathrm{in}} \end{pmatrix} \tag{1.8}$$

Mueller matrices can describe optics that (de)polarise and/or change the phase of the light. For example, the Mueller matrix for a perfect, horizontal polariser and a retarder with retardance $\delta$ with the fast axis orientation in the +Q direction are given by

$$\mathbf{M}_{\mathrm{hor,pol}} = \frac{1}{2}\begin{pmatrix} 1 & 1 & 0 & 0 \\ 1 & 1 & 0 & 0 \\ 0 & 0 & 0 & 0 \\ 0 & 0 & 0 & 0 \end{pmatrix}, \qquad \mathbf{M}_{\mathrm{ret}} = \begin{pmatrix} 1 & 1 & 0 & 0 \\ 1 & 1 & 0 & 0 \\ 0 & 0 & \cos\delta & \sin\delta \\ 0 & 0 & -\sin\delta & \cos\delta \end{pmatrix}. \tag{1.9}$$

If an optical component is rotated with an angle $\theta$, its Mueller matrix is multiplied with a rotation matrix, $\mathbf{M}(\theta) = \mathbf{M}_{\mathrm{rot}}(-\theta) \cdot \mathbf{M} \cdot \mathbf{M}_{\mathrm{rot}}(\theta)$, where the rotation matrix is given by

$$\mathbf{M}_{\mathrm{rot}}(\theta) = \begin{pmatrix} 1 & 0 & 0 & 0 \\ 0 & \cos 2\theta & \sin 2\theta & 0 \\ 0 & -\sin 2\theta & \cos 2\theta & 0 \\ 0 & 0 & 0 & 1 \end{pmatrix} \tag{1.10}$$

### 1.4.3 Scattering and phase matrix

The Jones and Stokes formalisms generally assume that the propagation direction of a beam of light remains unchanged. In applications where the direction is constant - such as through uniform optical elements - they provide powerful tools for analysing polarisation changes without the need for complex directional scattering considerations. For scenarios involving reflection or refraction, such as the Fresnel effect, the associated Mueller matrix implicitly accounts for changes in direction and amplitude due to the interface. *Scattering and phase matrices* do include the change in propagation direction after a scattering event. Scattering matrices account for changes in the propagation direction that occur when light interacts with particles (e.g., in a planetary atmosphere or with biotic molecules on a planetary surface). The phase matrix captures both the angular distribution of scattered light and changes to the polarisation state due to scattering. It describes how an incident wave transforms into a scattered wave in terms of both its direction and polarisation.

Chandrasekhar (1950) and Hovenier (1971) advanced the theory of radiative transfer, allowing for a quantitative description of scattered light in terms of Stokes parameters. By linking these parameters to phase and scattering matrices, researchers can rigorously describe how intensity and polarisation evolve through complex media, providing insights into the optical properties of particles and surfaces in various environments.

#### Scattering geometries

The direction of scattering after a scattering event is given by the scattering angle, $0 \leq \Theta \leq \pi$, and the azimuth angle, $0 \leq \varphi \leq 2\pi$, see Fig. 1.2. $\Theta$ is the cosine of the angle between the direction of the incident $(\vartheta, \varphi)$ and scattered $(\vartheta\prime, \varphi\prime)$ beam. $\phi$ the azimuth angle measured in the clockwise direction.

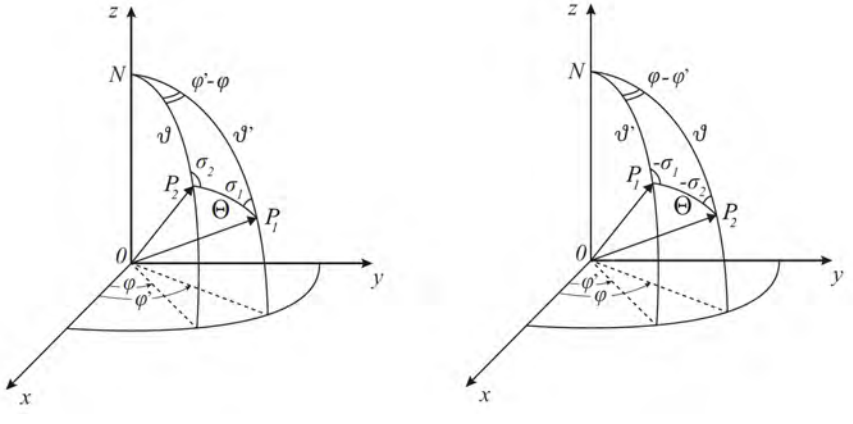


Figure 1.2: The geometry of scattering event at $O$, where $OP_1$ and $OP_2$ are the directions of the incident and scattered light. The azimuth difference is $0 < \phi' - \phi < \pi$ and $0 < \phi - \phi' < \pi$ for the **left** and **right panel**, respectively. Image credits Hovenier & van der Mee (1983).

### Scattering matrix

The *scattering matrix*, $\mathbf{F}(\Theta)$, transforms the Stokes vector of the incident beam into the Stokes vector of the scattered beam, with the scattering plane defined as the plane of the reference of the Stokes parameters. For spherical symmetry, the scattering matrix will be of the relative simple form (Hulst, 1981; Hovenier & van der Mee, 1983, 1988):

$$\mathbf{F}(\Theta) = \begin{bmatrix} a_1(\Theta) & b_1(\Theta) & 0 & 0 \\ b_1(\Theta) & a_2(\Theta) & 0 & 0 \\ 0 & 0 & a_3(\Theta) & b_2(\Theta) \\ 0 & 0 & -b_2(\Theta) & a_4(\Theta), \end{bmatrix} \tag{1.11}$$

where the matrix contains six real functions that depend on the scattering angle. Note that this form of the scattering matrix is valid in the case of (i) Rayleigh scattering with(out) depolarisation effects, (ii) scattering on randomly oriented particles, of which each has a plane of symmetry, and (iii) scattering on an equal number of particles and their mirror particles, both having a random orientation. The first element, $a_1(\Theta)$, is known as the scattering function or *phase function*. $a_1(\Theta)$ is the only element required to calculate scattering when polarisation is ignored, thus may be considered as the probability of scattering of unpolarised light in any given direction. This probability depends on the particle size and shape distribution of the particles, the complex refractive index, and the wavelength of the incident light. $\mathbf{F}(\Theta)$ is often normalized such that, $a_1(\Theta)$, averaged over all scattering directions $(\Theta, \varphi)$ equals 1 (Hansen & Travis, 1974).

### Phase matrix

To describe multiple scattering of polarised light in a medium, one needs a function that can describe the direction of the incident and scattered with respect to various scattering planes. The scattering matrix $\mathbf{F}(\Theta)$ for randomly oriented particles is defined with respect to one specific scattering plane, $OP_1P_2$ see Fig. 1.2. To transform the planes of reference for the incident and scattered light to another scattering plane, $\mathbf{F}(\Theta)$ is multiplied by the rotation matrix (similar to Eq. 1.10). This results in the so-called phase matrix.

While Sobolev (1963) laid important groundwork for understanding scattering and polarisation in radiative transfer, it was Hansen & Travis (1974) who formally introduced the phase matrix as it is widely used in modern radiative transfer and scattering physics. They systematically formulated the phase matrix specifically for scattering processes across arbitrary scattering planes, in a manner that became the standard in atmospheric and planetary sciences. Thereafter, Hovenier & van der Mee (1983) established fundamental relationships relevant to multiple scattering theories and general transfer of polarised light in a plane-parallel atmosphere.

The phase matrix $\mathbf{P}(\Theta)$ for isotropic Rayleigh scattering[2] is given by:

[2]Isotropic Rayleigh scattering yields symmetric, spherical particles that are much smaller than the wavelength of the incident light, e.g. gas molecules. Most real molecules exhibit some level of anisotropy. We refer to Hansen & Travis (1974) for the phase matrix for anisotropic Rayleigh particles in random orientation.

$$\mathbf{P}(\Theta) = \frac{3}{4}\begin{pmatrix} 1+\cos^2\Theta & -\sin^2\Theta & 0 & 0 \\ -\sin^2\Theta & 1+\cos^2\Theta & 0 & 0 \\ 0 & 0 & 2\cos\Theta & 0 \\ 0 & 0 & 0 & 2\cos\Theta \end{pmatrix}, \tag{1.12}$$

The first element, $P_{11} = \frac{3}{4}(1+\cos^2\Theta)$ describes the angular distribution of the scattered intensity, indicating that most light is scattered in directions close to the forward or backward direction, $P_{12} = P_{21} = -\frac{3}{4}\sin^2\Theta$ describes the polarisation change upon scattering, showing that the scattered light can become partially polarised, and $P_{33} = P_{44} = \frac{3}{2}\cos\Theta$ relates to the circular and linear polarisation components and shows how these change as function of scattering angle.

As discussed in this section, the scattering matrix and the phase matrix are fundamentally linked. The phase matrix typically represents a normalized version of the scattering matrix that accounts for various orientations of scattering planes. This enables the phase matrix to describe the angular distribution of scattered light, making it especially valuable in applications such as radiative transfer modelling in planetary atmospheres (e.g. Hansen, 1971; Stam et al., 1999; Karalidi et al., 2013), biomedical optics (Rogers et al., 2014; Kienle et al., 2001), and remote sensing (Myneni et al., 1995; Verhoef, 1998).

## 1.5 Sources of polarisation

Broad–band polarised light can be created by reflection, refraction, scattering and differential absorption. Light becomes polarised when transmitted through or reflected off surfaces. In the case of optical elements, polarisation optics rely on anisotropic effects, meaning that anisotropy influences the transmission, absorption, or phase delay experienced by different components of the electric field. The way in which light is affected depends on the orientation of its electric field vector relative to the optical axis of the anisotropic medium. A polariser selectively absorbs one of two orthogonal components of the electric field, effectively transmitting only the component aligned with its transmission axis. A wave plate (or retarder) alters the relative phase between two orthogonal electric field components, thereby modifying the overall polarisation. A birefringent crystal spatially separates an incident beam into two beams with orthogonal polarisations and different propagation directions (ordinary and extraordinary rays). Unfortunately, there are also general non-polarimetric optics that unwillingly change the polarisation state of the light.

Polarisation obviously does not only exist in an optical lab environment. There are some sources of polarisation in nature as well. Here we give a short summary of how reflection, refraction, scattering and differential absorption mechanisms produce polarised light in nature.

### 1.5.1 Surface reflection

Light reflected off dielectric surfaces such as wet surfaces, leaves, or other non-shiny objects will generally become polarised. To which extent depends on the angle of incidence

and the material of the surface. Reflection between two types of media with different refractive indices (e.g. air and glass) can be described using the Fresnel equations (Fresnel, 1819). Surfaces tend to reflect light anisotropically. A bidirectional reflectance distribution function (BRDF; Nicodemus, 1965) defines how light with an incident direction $(\theta_0, \phi_0)$ is reflected off an opaque surface into an outgoing direction $(\theta, \phi)$, where $\theta$ is the zenith and $\phi$ the azimuth angle. The BRDF provides a complete description of the angular distribution of reflected light, which is important for accurately modelling both the intensity and polarisation of radiation when performing radiative transfer simulations.

A Lambertian reflector is a simplified version of the BRDF in which the surface reflects the light in the same way in all directions. This simplification is often adopted in radiative transfer models to reduce the size of look-up tables and speed up calculations, because it avoids storing the full angle-resolved BRDF for every surface and illumination geometry. Although it ignores directional and polarisation-dependent effects, it allows the radiative transfer solver, which already accounts for multiple scattering through the phase matrix, to run efficiently for planetary-scale simulations. The disadvantage of using a Lambertian surface is that it is fully depolarising the incident light and causes systematic angle-dependent biases in derived surface reflectance reducing the anisotropy of reflectance, which might lead to minor errors in reflectance calculations (e.g. Qin et al., 2001; Lyapustin et al., 2010; O'Dell et al., 2012). However, research has shown that for modelling a partially cloudy, Earth-like planet covered in vegetation, the Lambertian surface appears to be a reasonable assumption (Wolstencroft & Breon, 2005; Wolstencroft et al., 2005; Stam, 2008).

There are BRDF models that include polarisation information. Empirical BRDF models for Earth surfaces (e.g. Nadal & Breon, 1999; Maignan et al., 2009) have been created using space-based polarisation measurements[3]. These models can be directly incorporated into radiative transfer calculations, where the phase matrix describes scattering in the atmosphere and the surface reflection contributes an additional polarisation signal at the bottom boundary, improving the accuracy of simulated polarimetric observations.

For every transparent dielectric surface, there is a specific angle of incidence at which light with an electric field polarised parallel to the plane of incidence is perfectly transmitted through with no reflection. This angle is better known as the Brewster angle (Brewster, 1815) . Electric fields orthogonal to the parallel polarisation are reflected, creating a beam of light that is polarised perpendicular to the plane of incidence. This is why this angle is often referred to as the *polarising angle*.

One striking example of a polarised surface reflection is an ocean glint (e.g. McCullough, 2006; Lynch et al., 2011; Shaw & Vollmer, 2017; Trees & Stam, 2022). Oceans are typically dark at most wavelengths due to the absorption of sunlight. However, under certain angles, reflection produces a glint which yields a clear polarimetric signature of liquid water. Solid surfaces, such as ice, sand or any type of vegetation, reflect and scatter light differently. Surfaces that are covered in ice scatter light in a way that produces a weaker polarisation signal compared to liquid water. This difference can be used to distinguish planetary or satellite surfaces that are covered in water from planets covered in ice.

[3]The POLDER, (Deschamps et al., 1994) and PARASOL (Tanré et al., 2011) instrument were the first to provide spectral, directional and polarisation measurements of radiation reflected from the Earth's surface and its atmosphere.

### 1.5.2 Atmospheric refraction and scattering

Sunlight becomes polarised through scattering by molecules and aerosols in the atmosphere. How a particle scatters the light depends mainly on its size. In the general case of a spherically symmetric particle, its size is expressed through a dimensionless size parameter $x$, defined by $x = 2\pi r/\lambda$. Here, $r$ is the particle's radius and $\lambda$ the wavelength of the scattered light. Rayleigh scattering is the elastic scattering of light by tiny particles ($x \ll 1$, e.g. molecules) much smaller than the wavelength of the light. Particles with sizes in the order of the wavelength ($x \approx 1$, e.g. cloud droplets) scatter according to Mie scattering. Geometrical scattering applies to even larger particles ($x \gg 1$, e.g. ice crystals, hail, graupel, rain droplets). These are treated as geometric shapes when determining their scattering properties.

Atmospheric refraction effects are wavelength dependent. A rainbow is a classic example of an atmospheric polarisation phenomenon resulting from white light undergoing two refractions and one internal reflection within water droplets. Due to dispersion, blue light emerges at a smaller angle relative to the incident white light than red light; consequently, blue appears on the inner edge of the rainbow arc and red on the outer edge. This bright arc is known as the primary rainbow. A less commonly observed feature, the secondary rainbow, arises from light that is internally reflected twice within the water droplet. This second reflection not only reduces the intensity but also reverses the colour order. In both primary and secondary rainbows, the internal reflection occurs at angles close to Brewster's angle (approximately 53° for air-to-water and 37° for water-to-air interfaces) enhancing the degree of polarisation in the reflected light. Brewster (1812) showed that the reflected rainbow light was almost fully polarised. A primary rainbow can reach a degree of linear polarisation of 96% and the secondary rainbow one of 90% (Adam, 2002). In atmospheres of distant planets, the occurrence of a rainbow in reflected light is an indicator of spherically shaped atmospheric particles (e.g. Hansen & Travis, 1974; Liou & Takano, 2002; Bailey, 2007; Karalidi et al., 2013).

Polarisation signatures can reveal details about the optical depth, phase, and composition of clouds, (e.g. Karalidi et al., 2012). These atmospheric phenomena provide critical clues to the composition and structure of distant planetary atmospheres, which are essential for assessing their habitability.

### 1.5.3 Differential absorption

Different polarisation states of light can be absorbed to different degrees by various crystals lattices and chiral molecules. This cam be described by the Mueller matrix in Eq. 1.8. Linear dichroism, $m_{12}$ and $m_{13}$, occurs when the absorption of light polarised parallel to an orientation axis is larger or smaller than light polarised perpendicular to the axis. Circular dichroism, $m_{14}$, is the differential absorbance of left- and right-handed circularly polarised light.

Special polymers, like Polaroid, absorb a specific polarisation state while transmitting the rest. As of this property, the polymer can be used as dichroic polarisers. There are also chiral molecules that selectively absorb polarisation states of light. In this work, we focus on a specific group of chiral molecules that occur in only single-handed forms in nature, also known as homochirality (e.g. Guijarro & Yus, 2008; Carroll, 2009; Caglioti et al., 2010). All the basic building blocks of life, like chlorophyll (e.g. Jacobs et al., 1957; Patty et al.,

2017), proteins (Bulheller et al., 2007), amino acids (Amdursky & Stevens, 2015), and sugars (Johnson, 1987), almost exclusively occur in only one enantiomeric form. The exact origin of homochirality remains unknown, (Fuß, 2008; Weller, 2024). Nevertheless, homochirality is an exclusive feature of life on Earth and homochiral molecules induce non-zero fractional circular polarisation. This makes homochirality a powerful tool to search for remote extraterrestrial life by means of polarisation (e.g. Patty et al., 2018a, 2019; Glavin et al., 2019; Gleiser, 2022).

Polarisation provides a wealth of information about planetary atmospheres and surfaces that cannot be obtained from intensity measurements alone. By breaking the cylindrical symmetry of light through reflection, scattering, or interaction with biological molecules, polarisation allows us to probe the physical and chemical properties of distant worlds in unprecedented detail. From detecting oceans and clouds to identifying potential biosignatures, polarisation serves as a powerful tool in the search for habitable planets and extraterrestrial life.

## 1.6 The measurement of polarisation

Polarimeters are optical instruments used to determine the polarisation properties of light beams and samples. In practice, they perform different intensity measurements after spatial or temporal modulation of the polarisation, which will be explained in more details in Section 1.6.3.

The quality of polarisation measurements relies on accurate and precise control and quantification of the polarisation state of light, as described by the Stokes formalism. This includes not only the orientation of the electric field vector but also the degree and type of polarisation. Various optical elements can be used to manipulate or analyse the polarisation state; those listed below were employed in the research presented in this work.

- A linear polariser polarises incident light by transmitting only the component of the electric field that is aligned with its transmission axis and suppressing the component perpendicular to it. The polarisation axis defines the direction of the electric-field oscillations that are allowed to pass.

- Wave plates are optical devices that introduce a phase shift (a retardance) between two orthogonal components of the electric field vector, typically aligned with the fast and slow axes of a birefringent material. This phase difference enables transformation between different polarisation states, e.g. converting linearly polarised light into circular or elliptical polarisation and vice versa. A quarter-wave plate introduces a $\lambda/4$ phase delay, and a half-wave plate introduces a $\lambda/2$ delay, but only at their design wavelength, $\lambda$. Since birefringence depends on wavelength, all single-plate retarders are inherently chromatic, meaning their exact retardance deviates from the nominal value as the wavelength shifts. To minimise this variation, achromatic wave plates are constructed by combining multiple birefringent crystals with their optical axes oriented at specific angles. This configuration compensates for the wavelength dependence of

birefringence across a broader spectral range. Nonetheless, even achromatic designs exhibit residual wavelength-dependent deviations from ideal retardance.

- Fresnel rhombs is a prism that act like a broadband wave plate. They provide a quarter- or half-wave retardance, through respectively two or four internal reflections, over a wider range of wavelengths than a birefringent wave plate.
- Circular polarisers are a combination of a quarter-wave plate with a fast axis orientation of 45° with a linear polariser. The retarder transforms incident circular to linear and vice versa, after which the polariser filters the linear, thus originally circular, polarisation state accordingly.
- Polarising beam splitters separate two orthogonal linear polarisation states, enabling simultaneous measurements of multiple components.
- Polarisation gratings separate left-handed from right-handed circular polarisation while simultaneously dispersing the light (Nikolova & Todorov, 1984; Lajunen et al., 2005; Oh & Escuti, 2007).

### 1.6.1 Classical polarimeter

A classic example of a polarimeter consist of a rotating wave plate and a (fixed) linear polariser (or e.g. a polarising beam splitter). This configuration allows the polarisation state of the incident light to be modulated and analysed through intensity variations measured by a detector. Depending on the type of wave plate, different components of the Stokes vector are modulated at characteristic frequencies:

- A half-wave plate rotates the plane of linear polarisation, therefore modulating $\mathtt{Q}$ and $\mathtt{U}$. The resulting intensity varies at four times the rotation frequency of the half-wave plate.
- A quarter-wave plate modulates all Stokes parameters. The linear and circular components are modulated at distinct frequencies, allowing the recovery of the full-Stokes vector.

The general expression for the detected intensity as a function of the retarder angle $\phi$, its retardance $\delta$, and the polariser angle $\theta$ is:

$$\begin{aligned} I_{\text{obs}}(\theta,\phi,\delta) =& \frac{1}{2}(\mathtt{I} + (\mathtt{Q}\cos 2\phi + \mathtt{U}\sin 2\phi)\cos 2(\theta-\phi) \\ &+ [(\mathtt{U}\cos 2\phi - \mathtt{Q}\sin 2\phi)\cos\delta + \mathtt{V}\sin\delta]\sin 2(\theta-\phi)) \\ I_{\text{obs}}(\theta=0^\circ,\phi,\delta) =& \frac{1}{2}(\mathtt{I} + \frac{\mathtt{Q}}{2}[(1+\cos\delta) + (1-\cos\delta)\cos 4\phi] \\ &+ \frac{\mathtt{U}}{2}(1-\cos\delta)\sin 4\phi - \mathtt{V}\sin\delta\sin 2\phi), \end{aligned} \tag{1.13}$$

Fixing the linear polarisation angle to 0° simplifies the expression simplifies: it reveals how the resulting intensity is a combination of the Stokes parameters being modulated with different modulation frequencies. We refer to Snik & Keller (2013) for an elaborate description.

This modulation-based method improves signal-to-noise ratios and enables sensitive polarisation measurements. In dual-beam implementations, the fixed polariser is replaced by a polarising beam splitter, and the two orthogonal polarisation channels are measured simultaneously, further reducing systematic effects due to atmospheric or instrumental variability.

### 1.6.2 Instrumental polarisation & cross-talk

In astronomical polarimetry, measurements are typically taken after the incoming light has passed through the telescope optics, including multiple reflections on mirrors and lenses. These optical elements can alter the polarisation state of the light, introducing what is referred to as instrumental polarisation: the net polarisation effect introduced by the telescope and/or polarimetric instrument.

The performance of a polarimeter is limited by its systematic effects and noise. We characterise the performance by three key concepts as presented by Snik & Keller (2013), accuracy, efficiency, and sensitivity:

- Polarimetric accuracy refers to how closely the measured Stokes parameters represent the true polarisation state of the source. It is primarily limited by systematic effects and the quality of calibration. For many astronomical polarimeters, typical calibration accuracy reaches the level of $10^{-3}$ in fractional polarisation (Ichimoto et al., 2008).
- Polarimetric efficiency describes how well each Stokes parameter is transmitted through the system, taking into account the propagation of noise f rom the input to the output. It is defined through the Stokes efficiencies, which are derived from the modulation matrix of the polarimeter.
- Polarimetric sensitivity defines the smallest polarisation signal that can be distinguished above the noise floor. It can be improved through optimized modulation schemes and signal processing techniques, such as lock-in detection.

In addition to these, instrumental cross-talk must be accounted for. Cross-talk refers to the mixing of Stokes parameters introduced by the instrument, e.g., a portion of `Q` appearing in the measurements as `U`. We talk about pure cross-talk if $P$ remains constant while the Stokes parameters are misrepresented (Snik & Keller, 2013). In the case of depolarisation, $P$ is reduced and part of the polarised intensity is lost to `I`, the unpolarised Stokes component. A clear understanding of these effects is crucial for accurate polarimetric measurements.

### 1.6.3 Polarisation modulation

At the core of any polarimeter is a linear polariser or polarising beam-splitter, commonly referred to as the *analyser*. It selects a specific polarisation state and converts it into a measurable intensity signal at the detector. To control which polarisation state is being analysed, a polarimeter typically includes a *polarisation modulator*. This modulator alters the polarisation state of the incoming light in a controlled way, enabling the analyser to extract different components of the polarisation. To improve polarimetric sensitivity, most polarimeters rely on modulation techniques. These are strategies that transform the incoming polarisation state into measurable intensity variations. These modulation schemes fall into two main categories:

**Spatial modulation** splits the beam into multiple components that are analysed simultaneously. A common implementation is the dual-beam technique, in which a polarising beam splitter separates orthogonal polarisation states into two beams directed to different regions of the detector. This method enables simultaneous measurement of complementary polarisation states, reducing the effects of seeing or time-varying noise. Differential measurements between the two beams yield the desired polarisation signals with improved precision. See Tinbergen, J. (1996) and Bagnulo et al. (2009) for foundational work on dual-beam polarimetry.

**Temporal modulation** involves modulating the polarisation state over time using rotating elements, such as linear polarisers or wave plates. By synchronizing these modulations with the detector readout, one can sequentially measure intensities corresponding to different polarisation projections. This approach benefits from the ability to use lock-in detection techniques, which boost signal-to-noise by isolating the modulated polarisation signal from background noise or system drifts. High-frequency modulators, such as photo-elastic modulators (PEMs) or ferroelectric liquid crystals (FLCs), dynamically vary their retardance at kHz rates, thereby modulating the incoming polarisation state over time. For example, PEMs achieve this by applying a periodic stress to an optical element, while FLCs electrically switch between discrete retardance states. This enables real-time modulation of polarisation, making them well-suited for high-sensitivity polarimetry. Kemp et al. (1987) demonstrated a sensitivity of $3 \cdot 10^{-7}$ in measuring the linear polarisation of broad-band sunlight using a PEM-based aperture polarimeter modulating above 30 kHz. Similar high-sensitivity techniques have been applied to stellar polarimetry (Hough et al., 2006) and solar spectropolarimetry (Povel et al., 1994), the latter requiring fast detectors capable of kHz-rate demodulation, reaching sensitivity levels of $10^{-5} - 10^{-6}$. Polarimetric sensitivity at the $10^{-5}$ level can also be reached using slow modulation, but only when combined with spatial modulation in a dual-beam configuration. This technique is especially advantageous in astronomical applications where there is a shortage of photons since it allows for long exposures and avoids the light loss inherent to single-beam systems.

In all cases, the Stokes parameters are reconstructed via demodulation, a process involving linear combinations of intensity measurements taken at different modulation states. This makes polarimetry a fundamentally differential technique and thus susceptible to any effects that break the assumption of identical measurement conditions like time variations in the source, atmospheric fluctuations, or instrument instability.

While modulation increases sensitivity, it does not inherently correct for systematic errors. Therefore, optimization of both modulation strategies (for sensitivity) and calibration routines (for accuracy) is essential. When combined, these can push polarimetric sensitivity, enabling the detection of very weak polarisation signals in challenging observational environments.

### Fresnel–Arago laws

Polarisation describes the orientation of the electric field vector in electromagnetic waves. One distinct but related wave phenomena is interference. Interference describes the interac-

tion of waves, where their amplitudes combine to produce regions of enhanced or reduced amplitude. The interference pattern observed for polarised light depends on the relative polarisation states of the interfering waves.

The Fresnel-Arago laws describe the behaviour of polarised light upon interference. In brief:

- Two waves, that are linearly polarised in the same plane, can interfere.
- Two waves, that are linearly polarised in orthogonal planes, cannot interfere.
- Two waves, that are linearly polarised in orthogonal planes, derived from the same natural light source and brought together into the same plane of polarisation, cannot interfere.
- Two waves, that are linearly polarised in orthogonal planes, derived from the same linear polarised wave source and brought together into the same plane of polarisation, can interfere.

These laws are particularly relevant when analysing the propagation of light through polarisation modulation devices. In spatial modulation schemes, such as those employing liquid crystal polarisation modulators, the local polarisation state of the light varies across the beam. As a result, interference effects may arise due to spatially dependent polarisation transformations, especially in near-field (Fresnel) diffraction patterns observed behind the modulator. Understanding which polarisation components can interfere is essential for interpreting the resulting intensity distributions and optimizing polarimetric system performance.

## 1.7 Spectropolarimeters

Three spectropolarimeters were used during the research presented in this dissertation. This section will provide a brief overview of their optical set-ups, science goals, and relevant literature.

### 1.7.1 TreePol & FlyPol

TreePol (Patty et al., 2017, 2018a, 2019) is a circular spectropolarimeter developed by the Astronomical Instrumentation group at the Leiden Observatory. It measures the fractional circular polarisation of transmitted or reflected sunlight as a function of wavelength (400-900 nm) after interaction with a sample or surface.

The polarisation states of the incident light are modulated by a ferro-electric liquid crystal, FLC. This is a fast-switching liquid crystal device capable of actively flipping its fast axis orientation between two discrete angles. This contrasts with the solidified (polymerized) liquid-crystal elements used in spatially patterned modulators, as will be discussed in subsection 1.7.2. The FLC in TreePol functions as a half-wave retarder (at $\lambda = 590$ nm) and can switch orientation at rates up to several kHz. It is followed by a polarising beam splitter that separates the light into two beams with orthogonal linear polarisation states. These beams are directed to a dual-beam spectrograph, each feeding an one-dimensional detector.

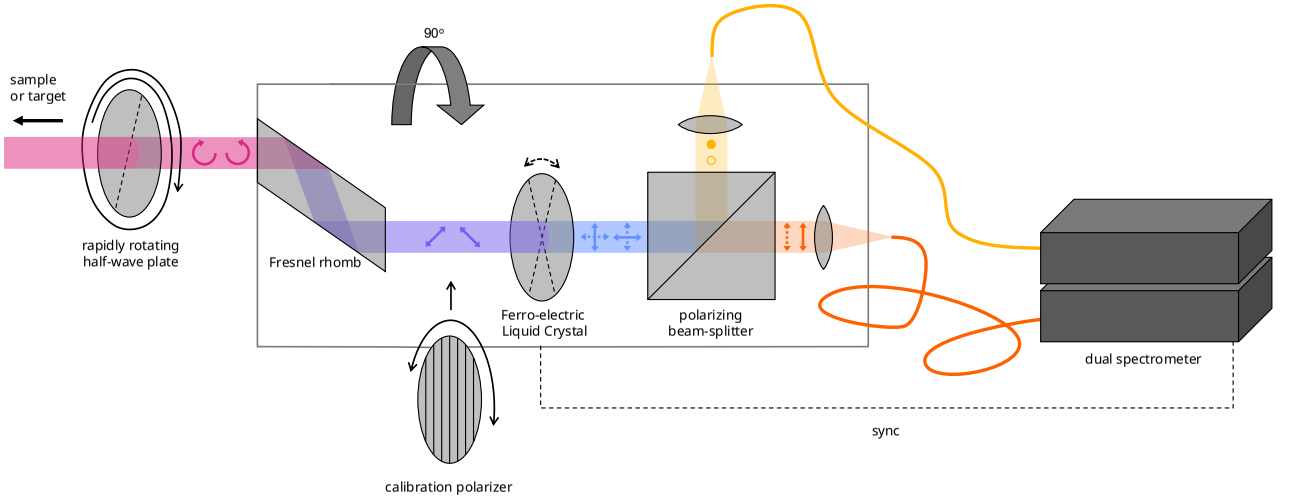


Figure 1.3: Schematic representation of TreePol (after Patty et al. (2017)). A Fresnel rhomb converts circular to linear polarisation (with a rotating half-wave plate before it to reduce instrumental crosstalk). A fast-switching FLC (half-wave at 590 nm) toggles the polarisation between two states, a polarising beam-splitter sends orthogonal states to a dual-beam spectrograph and detectors, and a double-difference demodulation recovers the circular-polarisation spectrum $V(\lambda)$. Treepol's sensitivity is of order $10^{-5}$; a calibration polariser can be inserted for calibrations.

TreePol achieves a polarimetric sensitivity of approximately $10^{-5}$, which is sufficient to detect the weak circular polarisation signals associated with biological matter. The fast switching of the FLC is synchronized with the high frame rate ($\sim$ 952 fps) of the detectors. However, the sensitivity is ultimately limited by temperature-induced spectral polarisation fringes, which also limit the polarimetric accuracy by masking the true circular polarisation signal.

Figure 1.3 shows the optical set-up of TreePol. After interaction with the sample, a Fresnel rhomb converts the incident circular polarisation into linear polarisation. The FLC continuously toggles its half-wave fast axis orientation between ±22.5°, swapping the polarisation content of the two beams. The polarising beam splitter then separates the beams into horizontal and vertical polarisation states, which are converted into intensity spectra that scale with $[\mathtt{I} \pm \mathtt{V}](\lambda)$, $[\mathtt{I} \mp \mathtt{V}](\lambda)$ respectively. By applying a double-difference scheme (e.g. Clarke & Barocas, 1965; Snik & Keller, 2013; Martí-Vidal et al., 2016), the circular polarisation spectrum $\mathtt{V}\lambda$) is extracted from these redundant intensity spectra. The half-wave plate in front of the Fresnel Rhomb is rapidly and continuously spinning. Doing so, it can mitigate possible linear polarization crosstalk within the instrument.

Using TreePol, Patty et al. (2017) demonstrated in the lab that the antisymmetric circular polarisation signal in the chlorophyll absorption band typical for a leaf in transmission disappears as a leaf dies. This is attributed to the breakdown of the chiral macrostructures formed by chlorophyll molecules as they degrade. Later, Patty et al. (2019) showed the potential of the remote biosignature detection: while healthy vegetation produced clear circular polarisation signals, artificial turf did not.

FlyPol (Patty et al., 2021; Mulder et al., 2022) is an adaptation of the TreePol instrument, constructed in Bern, Switzerland. Its optical configuration is nearly identical, but the Fresnel Rhomb is replaced by an achromatic quarter-wave plate to maintain a straight optical path. The spectrographs were also upgraded for faster, more stable readouts, and active temperature control was added to improve temporal stability. Patty et al. (2021) used FlyPol for the first remote circular polarisation measurements from a helicopter, which was later extended to measurement from a hot-air balloon (Mulder et al., 2022).

### 1.7.2 Life Signature Detection Polarimeter

The Life Signature Detection Polarimeter (LSDPol; Snik et al., 2019; Keller et al., 2020; Mulder et al., 2021) is a compact, solid-state, snapshot, non-imaging full-Stokes spectropolarimeter designed to remotely detect biosignatures on Earth. Its goal is to conduct circular spectropolarimetric surveys from aerial or orbital platforms, ultimately enabling a mission from a low earth obit, such as using the International Space Station, to globally map the polarisation signature of life on Earth.

The optical design of LSDPol is based on a patterned liquid-crystal polymer with an achromatic quarter-wave retardance and a spatially varying fast-axis orientation. This static polarisation modulator encodes the polarisation state of incoming light into a spatially modulated intensity pattern. The approach of using a spatially varying polymer is derived from the concept of classical polarimetry without moving parts as proposed by Sparks et al. (2019). Their patterned polarisation modulator acts as a quarter-wave plate whose fast-axis angle

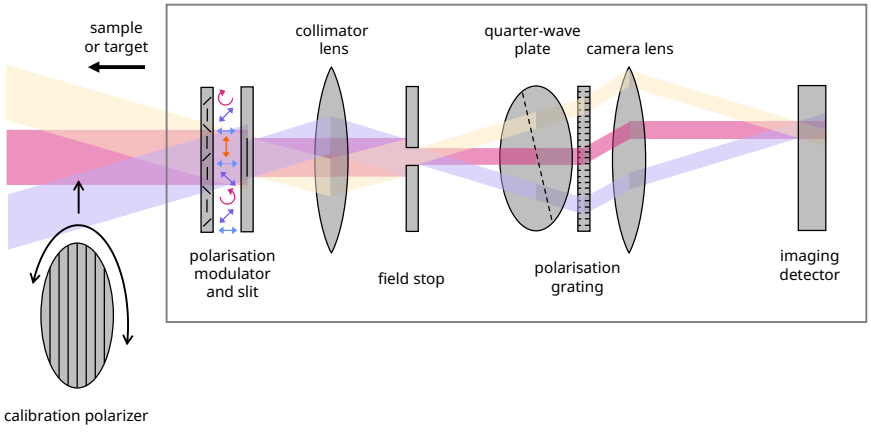


Figure 1.4: Schematic representation of LSDpol. A patterned liquid-crystal quarter-wave plate with a spatially varying fast-axis encodes the incoming Stokes vector as spatial intensity modulations along the slit, so `V`, `Q`, and `U` appear at distinct spatial frequencies. A fixed quarter-wave plate followed by a polarization grating then disperses the light spectrally while separating left- and right-handed circular polarisation into different diffraction orders, allowing full-Stokes retrieval from the modulation at each wavelength.

varies along one spatial direction. This converts circular and linear polarisation into distinct spatial modulation frequencies in the intensity distribution along the slit. Specifically, circular polarisation, `V`, and linear polarisation, `Q` and `U`, manifest as sinusoidal modulations at different spatial frequencies (differing by a factor of two). This spatially modulated light is fed into a long-slit spectrograph, where each wavelength yields a unique intensity modulation profile. Assuming that the polarisation state and illumination are approximately constant along the slit direction, a fit of the theoretical modulation function allows the extraction of full-Stokes parameters. In their concept, Sparks et al. (2019) used a fixed linear polariser as the polarisation analyser. In the LSDpol implementation, the analyser is a fixed quarter-wave plate directly followed by a polarisation grating. The grating acts as both a spectrograph and a circular-polarisation-sensitive beam splitter, separating left- and right-handed circular polarisation into different diffraction orders, while simultaneously dispersing the light spectrally. In theory, this would result in an exceptional snapshot full-Stokes spectropolarimeter.

Despite the sophisticated design, the prototype instrument as described by Keller et al. (2020) suffered from cross-talk between linear and circular polarisation, as well as spurious modulation artifacts in the zeroth diffraction order. The dissertation builds upon this foundation to mitigate these limitations and further develop the technology.

## 1.8 This dissertation

The overarching aim of this dissertation, **Tracing life through light: Towards detecting life on exoplanets with spectroscopy and spectropolarimetry**, is to explore how light - its spectrum, its polarisation, and the physical processes that transform it - can be used to uncover the nature of distant worlds. The work spans both observational astronomy and instrumental development, reflecting the dual challenge of interpreting atmospheric signatures while designing the tools capable of detecting them[4]. To address this broad goal, the dissertation is structured into two interconnected parts: the first focuses on extracting atmospheric properties from spectroscopic observations of substellar objects, and the second investigates the use of polarisation - both as a biosignature and as a powerful tool in next-generation space-based instrumentation.

**Part I: Characterising atmospheres through spectroscopy**

### Chapter 2: Atmospheric characterization of brown dwarf atmospheres

This part begins by exploring substellar atmospheres as natural laboratories for understanding planetary formation pathways. Brown dwarfs are believed to form through the collapse of molecular clouds (Bate et al., 2002; Whitworth et al., 2007), while giant planets such as super-Jupiters may follow distinct formation pathways involving solid and gas accretion Pollack et al. (1996); Helled et al. (2014). However, atmospheric characteristics of brown dwarfs do resemble those of super-Jupiters in atmospheric characteristics. Despite these different origins, their atmospheric characteristics often show strong similarities, making brown dwarfs particularly valuable for spectroscopic studies as they are significantly more accessible observationally.

We analyse three L-type brown dwarfs, selected from the European Southern Observatory SupJup survey (Program ID: 1110.C-4264, PI: Snellen) (de Regt et al., 2024). Measurements of chemical abundance ratios (C/O) and isotopic ratios ($^{12}$C/$^{13}$C) in representative samples of brown dwarfs and super-Jupiters can offer important constraints on formation processes. For the three targets, we retrieved C/O ratios between 0.65 and 0.71, consistent with the solar elemental ratio. The $^{12}$C/$^{13}$C retrievals show strong $^{13}$CO signals in two brown dwarfs, and a tentative detection in the third. These ratios appear slightly higher than typical interstellar medium values, suggesting that brown dwarfs may exhibit modestly elevated carbon isotope ratios compared to super-Jupiters.

[4] At least half of the project time was dedicated to simulating and modelling a realistic spectropolarimetric signal of the Earth as it would appear if observed as an exoplanet. These simulations served as an independent validation of the results presented in Gordon et al. (2023), but the associated work is not discussed in this dissertation.

**Part II: Observing the Earth as an exoplanet using polarimetry**

## Chapter 3: Spectropolarimetric measurements of life from a hot-air balloon

Building on the theme of using light as a tracer of life, the second part of this dissertation focuses on the observation of fractional circular polarisation in sunlight reflected from biotic surfaces, such as vegetation. Homochirality is the single handedness of many biomolecules like amino acids, sugars, and photosynthetic pigment–protein complexes, which makes it a fundamental and distinguishing feature of life on Earth. Homochirality is often argued to be widespread among living systems, although its universality beyond Earth remains a hypothesis rather than a certainty. Because homochiral molecules imprint characteristic circular polarisation signatures on reflected light via circular dichroism and supramolecular chiral ordering, measuring this fractional circular polarisation offers a promising remote biosignature (Patty et al., 2019). This makes circular spectropolarimetry a complementary technique to traditional reflectance spectroscopy rather hence a powerful tool to detect life.

To explore how homochiral signals appear under realistic conditions, we used the highly sensitive FlyPol instrument (Patty et al., 2021). This spectropolarimeter measures the fractional circular polarisation, $\mathtt{V/I}$, of incident light within the wavelength range of 400-900 nm, with a sensitivity better $> 10^{-4}$. Observations were carried out from a hot-air balloon, providing an airborne vantage point for measuring vegetation and other Earth surfaces. This platform offers an intermediate step between laboratory measurements and future space-based observations, allowing us to assess how circular polarisation biosignatures evolve with increasing distance and changing illumination geometry while introducing realistic atmospheric and bidirectional reflectance effects.

Observations of diverse scenes - farmland, forests, lakes, and urban areas - allowed us to explore the feasibility of distinguishing biotic from abiotic features. Optimal solar angles and integration times were established that resulted in accurate circular polarisation spectra. We report circular polarisation spectra of grass observed from various heights, measuring $\mathtt{V/I} = 2 \cdot 10^{-3}$ from $\sim$ 20 m and $\mathtt{V/I} = -5 \cdot 10^{-4}$ from $\sim$ 650 m elevation. We did not observe circular polarisation signals from surface water, which is consistent with low concentrations of photosynthetic biomass (e.g. phytoplankton) during early spring and the dominance of reflection suppressing chiral signatures. For subsequent observations of farmland that featured various types of grass, we report a fractional circular polarisation that varies between $\mathtt{V/I} = -9.0 \cdot 10^{-2}$ to $0.25 \times 10^{-2}$. The successful detection of circular polarisation from terrestrial vegetation demonstrates that biological activity can imprint measurable polarimetric signatures on reflected light.

## Chapter 4: Diffraction effects from spatial polarisation modulators

Building on the demonstration that circular polarisation can be used to remotely probe biological activity on Earth, we now turn to the instrumental requirements for detecting similar signals on exoplanets. Such observations demand sensitivity not only to circular polarisation but to all components of the Stokes vector. This motivates the design of a snapshot full-Stokes spectropolarimeter for space-based observations, LSDpol, whose configuration, challenges,

and diffraction-induced artefacts are examined.

The design of LSDpol incorporates a spatial polarisation modulator in the instruments' entrance slit. This element is implemented as a liquid-crystal quarter-wave retarder with a fast axis that rotates continuously as a function of position along the slit. This spatial modulation allows for simultaneous encoding of polarisation states in a snapshot measurement. Positioned downstream, a second quarter-wave plate together with a polarisation grating serves as both the spectral disperser and the circular-polarisation beam splitter. However, early tests of this configuration revealed significant linear-to-circular cross-talk, complicating the accurate demodulation of the full Stokes parameters.

To identify the origin of this spurious modulation, we carried out numerical simulations exploring several potential sources, including circular-to-linear cross-talk and diffraction effects induced by the structured phase profile of the spatial modulator. Particular attention was given to near-field (Fresnel) diffraction occurring immediately after the modulator, as the rotating fast-axis pattern introduces spatially varying phase delays.

These simulations showed that Fresnel diffraction effects downstream of the spatial polarisation modulator were the dominant contributor to the observed artefacts. Laboratory measurements using fully linearly and circularly polarised input light confirmed these predictions. The findings establish the theoretical and numerical basis for understanding diffraction-induced polarisation artefacts, which is expanded upon in Chapter 5.

## Chapter 5: Polarisation-dependent Talbot diffraction in spatial phase modulators

This chapter presents an experimental investigation of diffraction-induced artefacts in full-Stokes spectropolarimetry using Spatial Polarisation Modulators (SPMs). These modulators enable snapshot measurements without moving parts but inherently contain structured phase patterns that can generate polarisation-dependent diffraction effects, most notably the Talbot effect. Such effects introduce unintended intensity modulations that are especially problematic during calibration. Even slight defocusing enhances these modulations, producing patterns that can mimic linear-to-circular polarisation cross-talk and thereby obscure the true polarisation state.

The results highlight the importance of precise optical alignment and rigorous calibration procedures to mitigate these artefacts. A detailed analysis is provided of the polarisation-dependent Talbot effect, supported by visualisations of diffraction arising from phase variations within the modulator. To probe this behaviour further, a linear polarisation analyser was placed after the SPM, and both the input polarisation state and the modulator's retardance were systematically varied. These measurements confirm the strong sensitivity of the system to spatial phase structure and alignment, underscoring the critical role of careful calibration in snapshot full-Stokes spectropolarimetry.

# Part I

# Characterising atmospheres through spectroscopy

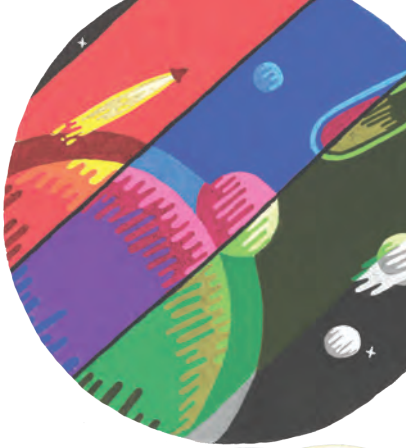

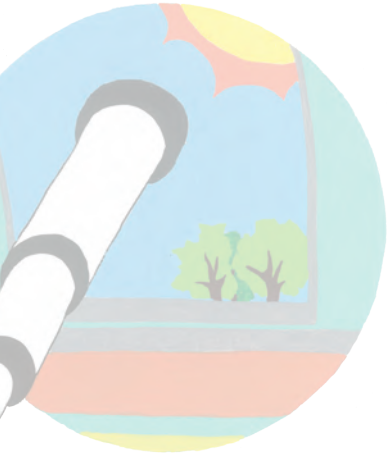

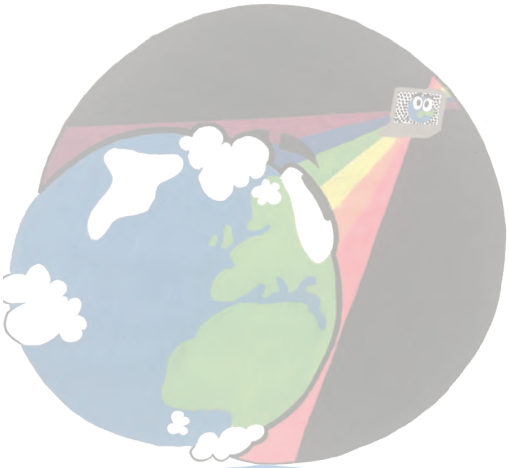

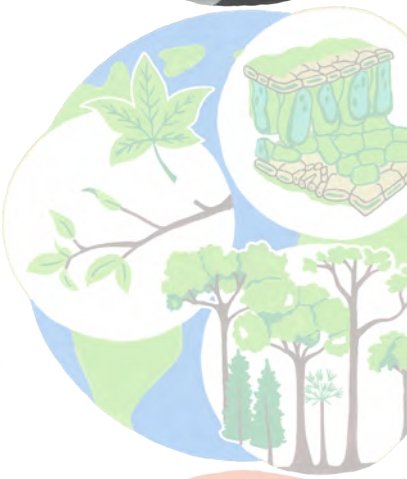


ANGRY
PHOTONS


THE
BEETLES

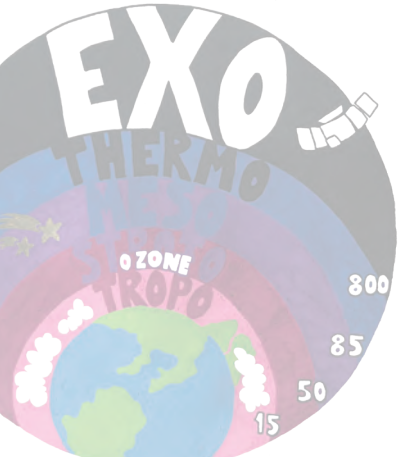
EXO
THERMO
OZONE
800
85
50
15



# 2 | Atmospheric characterisation of brown dwarf atmospheres



Published as

**The ESO SupJup Survey VI:**
**$^{12}C/^{13}C$ isotope ratio comparison of three L-type brown dwarfs**

W. Mulder, S. de Regt, R. Landman, D. González Picos, I. A. G. Snellen, Y. Zhang, S. Gandhi, C. Ginski, A. Y. Kesseli, P. Mollière, E. Nasedkin, and T. Stolker

*Astronomy & Astrophysics, 694, A164 (2025)*

Recent research suggests that the distinct formation processes of exoplanets and brown dwarfs may have an influence on the chemical and isotopic composition of their atmospheres. Variations in the carbon $^{12}C/^{13}C$ isotope ratio have been observed and tentatively linked to the top-down formation of brown dwarfs and the core accretion pathway of super-Jupiters. The European Southern Observatory SupJup Survey, conducted with CRIRES+ on the Very Large Telescope, aims to characterise the atmospheres of young brown dwarfs and super-Jupiters, specifically by investigating the $^{12}C/^{13}C$ ratio as a tracer of their formation pathways. We present the atmospheric characterisation of three isolated L-type brown dwarfs (2MASS J08354256-0819237, 2MASS J05012406-0010452, and 2MASS J05002100+0330501) included in the ESO SupJup Survey. We aim to constrain the C/O and $^{12}C/^{13}C$ ratios, and investigate whether the oxygen $^{16}O/^{18}O$ isotope ratio can be probed. We analysed the CRIRES+ K-band spectra of the three targets using our atmospheric retrieval framework. This framework couples the radiative transfer code `petitRADTRANS` with the sampling algorithm `MultiNest`. We report $^{12}C/^{13}C$ ratios of $89^{+11}_{-11}$ and $117^{+20}_{-17}$ for J0835 and J0500 with strong $^{13}CO$ significance ($> 6.8\sigma$) and a tentative ($3\sigma$) detection of $^{13}CO$ for J0501, resulting in a carbon isotope ratio of $155^{+56}_{-53}$. Only a weak detection of the $H_2^{18}O$ isotope was found in J0835. The C/O ratios are found to be in the range 0.65 to 0.71 for the three targets, and all exhibit strong detections of hydrogen fluoride. The $^{12}C/^{13}C$ ratios appear to be higher than that of the interstellar medium.

## 2.1 Introduction

Spectroscopic observations of exoplanetary atmospheres allow us to trace their chemical compositions and determine their thermal structure and possible cloud properties (Janson et al., 2010; Barman et al., 2011; Currie et al., 2011; Skemer et al., 2012; Oppenheimer et al., 2013). In addition to providing information about their atmospheric conditions, such a characterisation may help in constraining exoplanet formation and evolutionary processes. High-resolution spectroscopy plays an important role in unveiling the intricacies of exoplanet atmospheres, as it unequivocally determines the presence (Brogi et al., 2012; Hoeijmakers et al., 2020) and abundances (Brogi & Line, 2019; Line et al., 2021) of molecular and atomic species, as well as atmospheric dynamics (Brogi et al., 2016; Snellen et al., 2014; Schwarz et al., 2016).

The chemical composition of planetary atmospheres is believed to be linked to local formation conditions (Mollière et al., 2022). The chemical abundance ratios may deviate from that of the interstellar medium (ISM) and are governed by the material (gas or ice) they accrete from their environment during formation. As a result, various chemical abundance ratios have been suggested as tracers of planet formation. One planet formation tracer that is commonly studied is the carbon-to-oxygen (C/O) ratio (Öberg et al., 2011; Madhusudhan et al., 2010; Madhusudhan, 2012). The local C/O ratio in a protoplanetary disk is likely affected by various snow lines (Piso et al., 2015), namely of $H_2O$, CO, and $CO_2$, which determine whether these molecular species are generally present as ices or in the gas phase. This will subsequently influence the chemical buildup of the planets that form. Other chemical abundance ratios that have been suggested as formation and evolution tracers are, for example, the nitrogen-to-oxygen (N/O) or nitrogen-to-carbon ratio (N/C) for hot Jupiters (Cridland et al., 2016) and gas giants (Turrini et al., 2021), as well as the refractory-to-volatile ratio for ultra-hot Jupiters (Lothringer et al., 2021).

Isotope ratios have also been proposed as potential tracers of planetary formation history and evolution (Clayton & Nittler, 2004; Mollière et al., 2019; Zhang et al., 2021). The deuterium-to-hydrogen (D/H) ratio in our Solar System is of importance for our understanding of the origin and evolution of water within our celestial neighbourhood. In contrast to D/H ratios, the carbon isotope ratio is roughly constant (~89) in the Solar System (Woods & Willacy, 2009); however, it varies on galactic scales as $^{13}C$ is produced within stars that enrich the ISM over time. The current local ISM has an average isotopologue ratio of $68 \pm 15$ (Langer & Penzias, 1993; Milam et al., 2005), significantly lower than that of the Solar System. Interestingly, isotope fractionation processes create variations on protoplanetary disk scales (Woods & Willacy, 2009), which could be passed on to exoplanet atmospheres. (Zhang et al., 2021; Mollière et al., 2019; Line et al., 2021; Bergin et al., 2024).

Young brown dwarfs (BDs) closely resemble super-Jupiters (SJs) in terms of atmospheric characteristics, but are significantly more observationally accessible. This makes them highly valuable for spectroscopic studies. Formed with high temperatures and inflated radii, these self-luminous objects subsequently cool and undergo gravitational contraction, meaning that they are particularly amenable to detailed spectroscopic observations at a young age. Recent advancements in atmospheric retrieval techniques enable the quantitative characterisation of both young BDs and SJs, taking advantage of instruments such as the upgraded Cross-

dispersed hIgh-Resolution Infrared Spectrograph (CRIRES+; Dorn et al., 2023) and the Keck Planet Imager and Characterizer (KPIC; Delorme et al., 2021; Wang et al., 2021; Xuan et al., 2022), along with space-based facilities such as the James Webb Space Telescope (JWST; Gandhi et al., 2023).

(Isolated) BDs are believed to form similarly to stars, through the collapse of molecular clouds (Bate et al., 2002; Whitworth et al., 2007), while giant planets such as SJs can follow distinct formation pathways that involve solid and gas accretion (Pollack et al., 1996; Helled et al., 2014). Reliable measurements of chemical abundance (C/O) and isotopic ($^{12}C/^{13}C$) ratios in representative samples of BDs and SJs could provide crucial insights into these formation processes.



This chapter is organised as follows. In section 2.2 we summarise the main characteristics of our sample of BDs taken from literature. Section 2.3 addresses the CRIRES+ observations of the BD sample and the corresponding data reduction. Section 2.4 discusses our forward modelling and the atmospheric retrieval framework. In section 2.5 the main results of the retrievals are reported, and we discuss the implications of our findings in the context of young BDs and recent literature on C/O and isotope ratios. Finally, section 5.6 summarises our conclusions.

## 2.2 Sample selection

In this chapter we present high-resolution spectra of three isolated L-type BDs: 2MASS J08354256-0819237, 2MASS J05012406-0010452, and 2MASS J05002100+0330501. These objects were selected from the European Southern Observatory SupJup Survey (programme ID 1110.C-4264, PI: Snellen), which aims to compare the atmospheres of sub-stellar companions and isolated BDs (de Regt et al., 2024; González Picos et al., 2024). The complete sample consists of 49 targets, ranging from early M-type stars to cool T-dwarfs (see Fig. 2.1). Ultimately, we aim to run retrievals for all objects in the sample.

The three BDs selected for this study have similar spectral types (L4.0-5.0) and effective temperatures ($T_{\rm eff}$ =1700 − 1800K), which allows a comparison between atmospheres at comparable conditions. As a result, differences in the atmospheric chemistry between the BDs could possibly inform us of distinct formation scenarios. In addition, the presented constraints for these isolated BDs can serve for comparison with planetary-mass companions in a similar temperature regime (Zhang et al., 2021; Zhang et al., 2021). The probed effective temperatures are typical for sub-stellar L-type objects ($T_{\rm eff}$ = 1300 – 2200K, Filippazzo et al. 2015) and allow the formation of mineral and metal condensate clouds in their atmospheres (Tsuji et al., 1996; Visscher et al., 2010). We refer to Table 2.1 for more detailed properties of the studied BDs.

### 2.2.1 J0835

2MASS J08354256-0819237 (J0835 hereafter) is an isolated L-type BD. Its spectral type, based on photometry, is L5.0 Cruz et al. (2003); Burgasser et al. (2010); Andrei et al. (2011). Previous work used various methods to estimate the effective temperature of J0835, reporting 2200 K (Blake et al., 2010), 1800 ± 100 K (Gagné et al., 2015), 1754 ± 112 K (Filippazzo

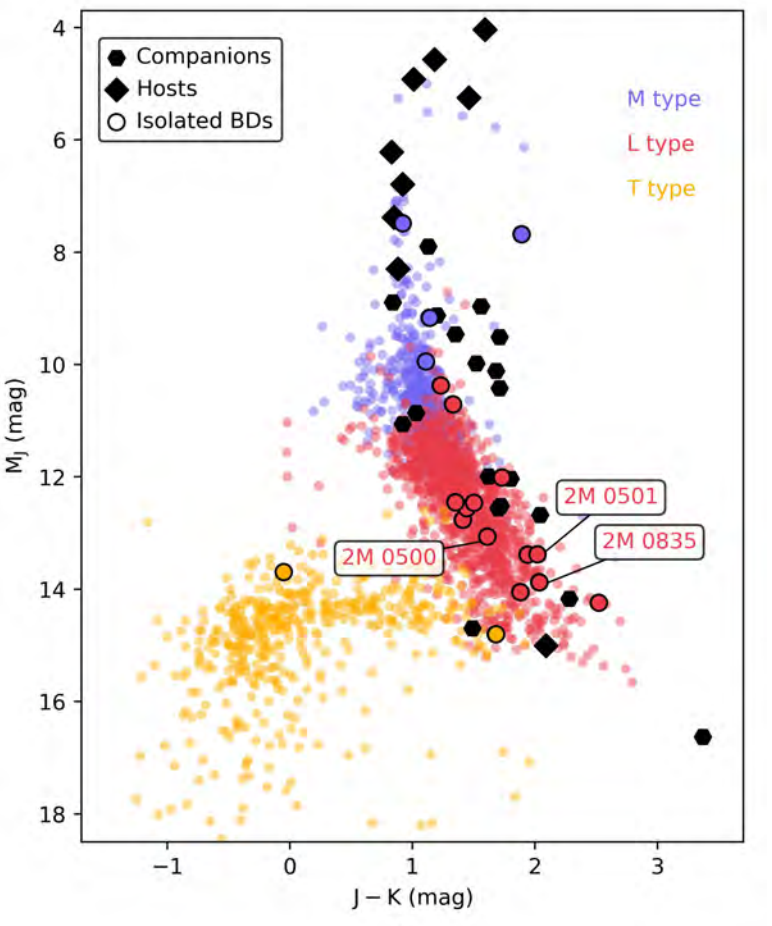


Figure 2.1: Colour-magnitude diagram of $M_J$ vs $J - K$ showing the observed low- and planetary-mass objects of the ESO SupJup Survey. The companions and their hosts are pictured as black hexagons and diamonds, respectively. All 19 observed isolated BDs are marked as black-outlined circles, and the colour denotes their spectral type. The same colour coding is used for the population of isolated cool dwarfs indicated in the background. These objects, originating from the `UltracoolSheet` (Best et al., 2024), are shown as a reference.

| System name | Distance (pc) | Spectral type | $T_{eff}$ (K) | Mass ($M_{Jup}$) | Radius ($R_{Jup}$) | $v \sin i$ (km $s^{-1}$) | i (°) |
|---|---|---|---|---|---|---|---|
| J0835 | $7.23 \pm 0.01^{(1)}$ | L5.0$^{(2)}$ | $1754 \pm 112^{(4)}$ | $62.47 \pm 15.86^{(6)}$ | $1.00 \pm 0.08^{(6)}$ | $9.65 \pm 0.36^{(7)}$ | $21^{(4)}$ |
| J0501 | $20.9 \pm 0.3^{(1)}$ | L4.0$\gamma^{(5)}$ | $1720 \pm 55^{(5)}$ | $21.45 \pm 13.71^{(6)}$ | $1.38 \pm 0.18^{(6)}$ | $9.57^{+0.67\,(7)}_{-0.58}$ | $60^{+20(4)}_{-9}$ |
| J0500 | $13.23 \pm 0.05^{(1)}$ | L4.0 pec C$^{(3)}$ | $1793 \pm 72^{(6)}$ | $63.68 \pm 14.44^{(6)}$ | $1.00 \pm 0.08^{(6)}$ | $9.57^{+0.67\,(8)}_{-0.58}$ | — |

Table 2.1: Properties of our L-type BD sample: (1) Gaia Collaboration (2020), (2) Cruz et al. (2003), (3) Gagné et al. (2015), (4) Schlawin et al. (2017), (5) Zapatero Osorio et al. (2014), (6) Filippazzo et al. (2015), (7) Vos et al. (2020), (8) Blake et al. (2010).

| System name | RA | Dec. | Obs. date (UT) | K (mag) | iTime (s) | S/N | Seeing(") | Std star |
|---|---|---|---|---|---|---|---|---|
| J0835 | 08 35 42.53 | -08 19 15.85 | 2023-01-02 | $11.14 \pm 0.02^{(5)}$ | 1200 | 70 | ~0.7 | pi.05 Ori |
| J0501 | 05 01 24.09 | -00 10 49.19 | 2023-02-02 | $12.96 \pm 0.04^{(5)}$ | 3600 | 20 | ~0.8 | HD 31331 |
| J0500 | 05 00 21.01 | 03 30 45.40 | 2023-02-28 | $12.06 \pm 0.02^{(5)}$ | 5400 | 40 | ~0.7 | 3 Hya |

Table 2.2: Observational parameters for the three L-type BDs: The parameters include observation date, apparent K-band magnitudes from the 2MASS catalogue (Cutri et al., 2003), total integration time, S/N at 2166nm, and standard star used for telluric corrections.

et al., 2015; Schlawin et al., 2017) and 1374 ± 52 K (Sanghi et al., 2023). Blake et al. (2010) based their $T_{\rm eff}$ on a best-fit synthetic template with $\log g = 5.0$, Gagné et al. (2015) fitted a model using WISE W1 and W2 photometry as well as near-infrared (NIR) spectra in the J-, H-, and K-bands, Filippazzo et al. (2015) used the bolometric luminosity, and Sanghi et al. (2023) combined their own observations and evolutionary model-derived radii to determine semi-empirical effective temperatures.

Gagné et al. (2015) reported no clear signatures of low surface gravity. They determined a surface gravity of $\log g = 5.0 \pm 0.5$ using optically anchored NIR spectral average templates. Subsequently, Filippazzo et al. (2015) noted a similar surface gravity of $\log g_{\rm J0835} = 5.19 \pm 0.21$. In general, low surface gravity BDs are thought to be younger objects with inflated radii, which has been confirmed in previous work (e.g. Kirkpatrick et al., 2008; Liu et al., 2016; Schlawin et al., 2017). Young BDs stand out because of their redder NIR and mid-infrared (MIR) colours and fainter absolute magnitude in the K-band when compared to their older spectral counterparts with higher field surface gravities (Gagné et al., 2015; Filippazzo et al., 2015). Liu et al. (2016) describes that J0835 appears to be redder than the bulk of low gravity BDs in the colour–magnitude diagram. They used the gravity-sensitive features (e.g. FeH, Na I, K I, and the H-band continuum shape) in its NIR SpeX prism spectrum (Burgasser et al., 2010) to classify J0835 as on the border between intermediate and field gravity. Their gravity classifications correspond to ages of, respectively, ~30–200 Myr and ~200 Myr. Sanghi et al. (2023) noted a lower surface gravity of $\log g = 4.32 \pm 0.24$, which may be related to their significantly different estimate of $T_{\rm eff}$.

The narrow CO features in the NIRSpec spectra of Blake et al. (2010) are indicative of it being a slow rotator ($< 20$ km s$^{-1}$). They forward-modelled the extracted spectra and found a rotational velocity of $v \sin i = 4.18 \pm 0.43$ km s$^{-1}$. With those values, Schlawin et al. (2017) provided an estimation of the inclination angle $i$ of 21° (close to pole-on) from photometric variability monitoring, assuming a radius of one Jupiter radius.

L dwarfs often exhibit low-level, rotationally modulated photometric variability generally associated with heterogeneous, cloud-covered atmospheres. High-precision ground-based NIR spectrophotometry revealed its spectral variability, likely to be induced by the rapid 3.1 h rotation Koen et al. (2004). In contrast, Schlawin et al. (2017) observed a variability of less than 0.5% per band, with no clear spectral dependence, which is less variability than reported in previous work (Koen et al., 2004; Wilson et al., 2014). They use it to provide an estimation of the inclination angle $i$ of 21° (close to pole-on), assuming a radius of 1 Jupiter radius.

### 2.2.2 J0501

2MASS J05012406-0010452, hereafter referred to as J0501, is a BD located in the constellation Orion (Reid et al., 2008). Cruz et al. (2009) classifies J0501 as a spectral type L4$\gamma$ in the optical regime, after which both Liu et al. (2016) and Faherty et al. (2016) classify it as a young field object. Cruz et al. (2009) noted its unusual spectral features, such as notably weak FeH molecular absorption and weak Na I and K I doublets. From this, they concluded the object should have a low surface gravity and is likely a young, low-mass BD. Zapatero Osorio et al. (2014) estimated its effective temperature to be 1720 ± 55 K. Gagné et al. (2015) categorised J0501 in the IR as spectral type L3$\gamma$, providing evidence that J0501 is a member

of the Columba or Carina moving group (coeval at 20-40 Myr). In this case, the mass is estimated to be, $10.2^{+0.8}_{-1.0}$ $M_{Jup}$ giving rise to a surface gravity of $\log g = 4.0 \pm 0.5$. Vos et al. (2020) measured a rotational velocity of $v \sin i = 9.57^{+0.67}_{-0.58}$ km s$^{-1}$, which in combination with a radius estimate (Filippazzo et al., 2015) results in a maximum rotation period of 15.7 ± 0.2 hr.



### 2.2.3 J0500

2MASS J05002100+0330501, from hereon referred to as J0500, is a BD at a distance of 13.23 ± 0.05 pc (Gaia Collaboration, 2020). Just like J0501, it is also located in the constellation Orion and part of the same moving group. Reid et al. (2008) characterised this BD as a spectral type L4. Filippazzo et al. (2015) estimated an effective temperature of 1793 ± 72 K and a surface gravity of $\log g = 5.2 \pm 0.19$ based on its bolometric luminosity. In addition, they derive a mass of $64 \pm 14$ $M_{Jup}$ and a radius of $1.00 \pm 0.08$ $R_{Jup}$. Burningham et al. (2017) also estimated its effective temperature and surface gravity. They applied a spectral inversion technique in the cloudy L dwarf regime to obtain a temperature estimate of $1796^{+23}_{-25}$ K, a surface gravity of, $\log g = 5.21^{+0.05}_{-0.08}$ together with $H_2O$, CO, TiO, VO, CaH, CrH, FeH, Na, and K abundances. In comparison to thermochemical equilibrium abundances, they found that the CO and alkali abundances are a factor of ∼ 10 higher and ∼ 2 lower, respectively.

## 2.3 Observations and data reduction

### 2.3.1 Observations

The observations of J0835, J0501 and J0500, on January 2, February 2 and 28, 2023, respectively, were conducted as part of the SupJup Survey utilising CRIRES+ at the Very Large Telescope. CRIRES+ (Kaeufl et al., 2004; Dorn et al., 2014, 2023) is an advanced slit spectrograph with adaptive optics capabilities (Paufique et al., 2004), providing high resolution and able to target a broad wavelength range from 0.95 to 5.3 microns with a resolving power of up to $R \sim 100,000$. Our observations employed the K2166 wavelength setting (1.90 − 2.48 µm), focusing on regions featuring prominent $^{12}$CO and $^{13}$CO absorption lines. By utilising the wide slit mode, 0.4", a spectral resolution of $R \sim 64,000$, $R \sim 56,000$, and $R \sim 58000$ was obtained for the J0835, J0501, and J0500 observations, respectively (values calculated as described in Appendix A of González Picos et al. 2024). We were not able to use the adaptive optics system as the target BDs are too faint in the R-band used for wavefront sensing. Our observation sequence followed an ABBA nodding pattern, of 18, 12, and 4 individual exposures of 300 seconds for J0835, J0501, and J0500, respectively (see Table 2.2 for a complete overview of the observation parameters).

### 2.3.2 Data reduction

The data processing was conducted using the open-source package `excalibuhr` (Zhang et al., 2024). This involved various corrections including dark-subtraction, flat-fielding, bad-pixel masking and removal of sky emission via AB (or BA) pair subtraction. A and B nodding

position frames were mean-combined to produce master frames. After slit curvature and tilt adjustments, the optimal extraction algorithm (Horne, 1986) was applied to convert calibrated images into one-dimensional spectra. Telluric standard stars (see Table 2.2), observed with the same slit- and wavelength settings as the target observations and at similar airmasses, underwent the same reduction procedure.

Atmospheric corrections were performed using `Molecfit` (Smette et al., 2015). The standard star observations were used to fit the telluric model, which were subsequently scaled to the airmass and precipitable water vapour of the target observation (see González Picos et al. 2024). Detector pixels with telluric transmission of $< 70\%$ were masked in the observed spectra since they cannot be adequately corrected. The bluest of the seven spectral orders is heavily contaminated with tellurics and therefore not included in our analysis. In addition, the `Molecfit` model provides a secondary wavelength correction. Finally, the telluric-corrected spectra were flux-calibrated using a simple scaling factor derived from integrated flux measurements in the 2MASS Ks filter-curve and photometry data (Table 2.2).

## 2.4 Atmospheric modelling

We adopted a similar atmospheric retrieval framework as used in de Regt et al. (2024). We refer to their work for an elaborate description of the algorithm, likelihood and correlated noise. In this section we summarise the main principles.

### 2.4.1 Retrieval framework

The atmospheric retrieval framework is based on the radiative transfer code `petitRADTRANS` (`pRT`; Mollière et al., 2019), which computes emission spectra using descriptions of the atmospheric chemistry, cloud structure, surface gravity, and molecular or atomic opacities. `pRT` was integrated with the nested sampling tool `PyMultiNest` (Buchner et al., 2014), a Python interface for the `MultiNest` (Feroz et al., 2019) algorithm. All computations were executed in parallel on the Dutch National Supercomputer Snellius.

The model atmosphere was subdivided into a series of 50 layers covering the atmospheric vertical extent using a pressure range of $P = 10^2 - 10^{-5}$ bar. Each layer was characterised by a temperature and mass fractions of relevant chemical species. The radiative transfer equation was solved for each layer to obtain the flux as a function of wavelength.

Our models accounted for collision-induced absorption (Borysow et al., 1988) from $H_2$-$H_2$ and $H_2$-He (Dalgarno & Williams, 1962; Chan & Dalgarno, 1965; Gray, 2008), as well as Rayleigh scattering of $H_2$ and He. $H_2O$ (or $H_2^{16}O$), $^{12}CO$, $^{13}CO$, hydrogen fluoride (HF), Ca and heavy-oxygen water ($H_2^{18}O$) were included as line opacities. We used ExoMol line lists for the opacities of heavy-oxygen water ($H_2^{18}O$; Polyansky et al. 2017) and $H_2^{16}O$ (Polyansky et al., 2018). The HITEMP (Rothman et al., 2010) line lists were employed for $^{12}CO$, $^{13}CO$ (Li et al., 2015). Moreover, opacity from HF (Li et al., 2013; Coxon & Hajigeorgiou, 2015; Somogyi et al., 2021) was included as a line species following the detection of HF in the atmosphere of two young BDs (González Picos et al., 2024) and in YSES 1b (Zhang et al., 2024). Atomic opacity was included for Ca (Castelli & Kurucz, 2003) and several other atoms

were evaluated, but not included in the final model. Furthermore, no clouds were included in the atmospheric models (see section 2.4.3, for more details).

The pRT model spectra were Doppler-shifted to probe the object's radial velocity ($v_{\rm rad}$) and subsequently convolved with a rotational broadening kernel using the `fastRotBroad` routine (Gray, 2008) of `PyAstronomy`[1] (Czesla et al., 2019). The routine applies the projected rotational velocity ($v \sin i$) while taking into account the effects of limb-darkening, fitted with a linear limb-darkening coefficient ($\epsilon_{\rm limb}$). We implemented instrumental broadening, introduced by the slit spectrograph, by convolving the rotationally broadened spectra with a Gaussian kernel. The width of this kernel corresponds to the $R \sim 50.000$ spectral resolution of the CRIRES+ instrument. Lastly, the spectra are resampled to the observed wavelength grid for direct comparison with the data.

Generating the significant number of pRT model spectra needed for a statistically supported retrieval is time expensive. The computations of the pRT spectra were sped up by under-sampling the high-resolution ($\lambda/\Delta\lambda = 10^6$) line-by-line opacities (implemented by setting `lbl_opacity_sampling= 3`, i.e. $R \sim 10^6/3$). The work, done by de Regt et al. (2024) and González Picos et al. (2024), demonstrates that this degree of undersampling is appropriate given the CRIRES+ spectral resolution.

The sampling tool `PyMultiNest` builds up posterior distributions by sampling the parameter-space of the 18 free parameters and evaluating the likelihood function between the observed and pRT spectra, while obtaining Bayesian evidence (Z) estimates simultaneously. This is an efficient method for exploring and sampling from complex, high-dimensional parameter spaces. A constant sampling efficiency of 5% was used in the importance nested sampling mode. Following Feroz et al. (2019), González Picos et al. (2024), and de Regt et al. (2024), we used 400 live points and an evidence tolerance of 0.5 to sample the posterior distributions. The priors of the retrieved parameters can be found in Table 2.3.

### 2.4.2 Likelihood and correlated noise

We adopted the same likelihood function as used in Landman et al. (2024), González Picos et al. (2024), and de Regt et al. (2024), which is based on the formalism defined by Ruffio et al. (2019). For 18 order-detector pairs (6 spectral orders covered by 3 detectors each), the log-likelihood ($\ln \mathcal{L}$) is calculated as

$$\ln \mathcal{L} = -\frac{1}{2}\left(N \ln(2\pi) + \ln\left(|\boldsymbol{\Sigma}_0|\right) + N \ln\left(s^2\right) + \frac{1}{s^2}\boldsymbol{R}^T \boldsymbol{\Sigma}_0^{-1} \boldsymbol{R}\right), \tag{2.1}$$

where $N$ is the number of unmasked pixels (2048 at most), $s$ is the uncertainty scaling factor for the total covariance matrix $\boldsymbol{\Sigma}_0$ and $\boldsymbol{R} = \boldsymbol{d} - \phi\boldsymbol{m}$ represents the residuals between the observed ($\boldsymbol{d}$) and model ($\boldsymbol{m}$) spectra for each order-detector pair. The optimal solution for the flux-scaling parameter $\tilde{\phi}$ and the optimally scaled residuals $\tilde{s}^2$, are found by calculating

$$\tilde{\phi} = (\boldsymbol{m}^T \Sigma_0^{-1} \boldsymbol{m})^{-1} \boldsymbol{m}^T \Sigma_0^{-1} \boldsymbol{d}, \qquad \text{and} \quad \tilde{s}^2 = \frac{1}{N} \boldsymbol{R}^T \boldsymbol{\Sigma}_0^{-1} \boldsymbol{R}\Big|_{\phi=\tilde{\phi}}. \tag{2.2}$$

[1] https://github.com/sczesla/PyAstronomy

de Regt et al. (2024) highlighted the importance of accounting for correlated noise in CRIRES+ spectra when retrieving model parameter solutions. Using Gaussian processes (GPs), we made sure to model the correlated noise (Kawahara et al., 2022), and address the problem of biases in the retrieved parameters and underestimation of their uncertainties. The covariance of pixels $i$ and $j$ are calculated by adding a diagonal, uncorrelated variance term and an off-diagonal correlated uncertainty term to achieve

$$\Sigma_{0,ij} = \delta_{ij}\sigma_i^2 + a^2\sigma_{\mathrm{eff},ij}^2 \exp\left(-\frac{r_{ij}^2}{2\ell^2}\right). \tag{2.3}$$

In Eq. 2.3, $\delta_{ij}$ is the Kronecker delta function, $\sigma_i$ the flux uncertainty of pixel $i$, $\sigma_{\mathrm{eff},ij}$ the effective uncertainty derived from the data arithmetic mean of the variances of pixels $i$ and $j$, $r_{ij}$ the wavelength separation between pixels, and $a$ and $\ell$ the GP amplitude and length scale, respectively. The GP amplitude and length scale are retrieved as free parameters.

### 2.4.3 Pressure–temperature profile

In general, BDs are self-luminous objects devoid of significant external irradiation. In the atmosphere, where convection dominates, the atmospheres are expected to have a pressure–temperature (P–T) profile in an adiabatic form (Baraffe et al., 2002; Ludwig et al., 2006; Freytag et al., 2010), which implies that both the atmospheric pressure and temperature increase with the atmospheric depth.

The atmospheres were modelled using a similar parametrisation as presented in Zhang et al. (2023). The temperature was parametrised as a function of pressure using values for the temperature gradient $\nabla T_i \equiv \frac{d\ln T_i}{d\ln P_i}$, where, $i$ corresponds to the number of pressure knots in log-space. In our retrievals, we used five pressure knots where the higher and lower knots are fixed ($P_1 = 10^2$ and $P_5 = 10^{-5}$). The three intermediate knots were allowed to shift their values. This approach prevented a biased location of the photosphere (see González Picos et al. (2024)).

The temperature gradients, $\nabla T_j$, of each atmospheric layer were calculated using linear interpolation of the temperatures associated with the pressure knots. Thereafter, the temperatures of each layer were determined using

$$T_j = T_{j-1}\left(\frac{P_j}{P_{j-1}}\right)^{\nabla T_j}. \tag{2.4}$$

The central knot ($i = 3$) was set to be an anchor point for the temperature. As a result, for each model, we retrieved five temperature gradients, three pressure points, and the temperature at the central knot.

We investigated the presence of clouds in the atmospheres of our targets. We made no assumptions regarding cloud composition, and we parametrised the clouds using a 'grey' continuum opacity applied at all wavelength. Clouds are likely to have an effect on the strength of the overall continuum and the shape of the temperature profile. No evidence of the presence of clouds was found and therefore clouds were excluded from the final retrieval analyses. This does not mean that these are cloudless objects. They may be present below the K-band

photosphere, or equally modelled with a more isothermal P-T profile with similar values for $T_{\rm eff}$, $\log g$ and chemical abundances (Mollière et al., 2020; Zhang et al., 2023). Various retrieval studies of high-resolution K-band spectra resulted in cloud-free solutions as well (e.g. Zhang et al., 2021; Landman et al., 2024), where Landman et al. (2024) compared models with various and without clouds revealing a consistent C/O abundance ratio. Combining the K-band observations with short-wavelength observations (e.g. Y- or J-band), combining extensive BD photometry measurements with a wider wavelength range, or using the silicate features around 8 – 10 μm (Miles et al., 2023), may further constrain the cloud properties (de Regt et al., 2024).

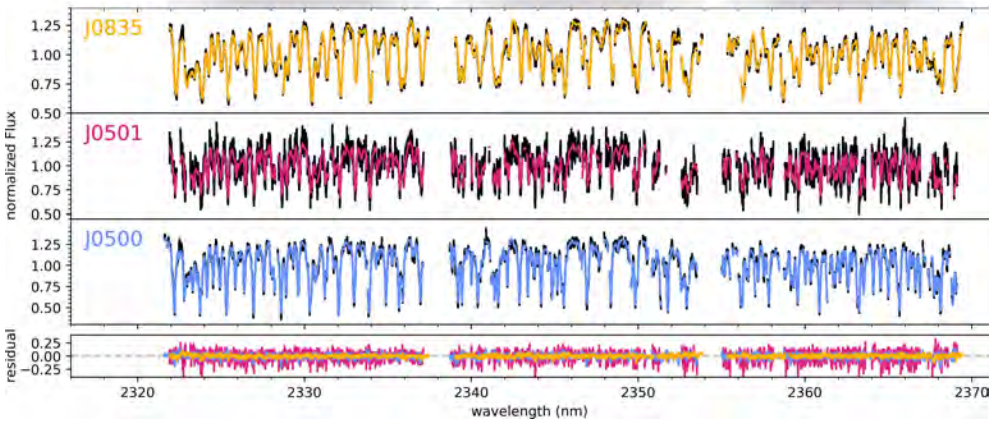


Figure 2.2: Best-fitting models retrieved for J0835, J0501 and J0500 (top to bottom). The upper three panels show the observational flux in black, and the best-fitting model spectra for the three BDs. The observed flux is normalised to the mean flux of each order–detector pair after telluric correction. The lower panel shows the residuals between the observed and model spectra. The data and the models are displayed in the rest frame of each object. The shaded region at the top of the image indicates the wavelength coverage of the three detectors for each spectral order (CRIRES+ and K2166 wavelength setting). They slightly differ in the rest-frame of the BDs as presented by the gradient. The sixth order (2321.6 – 2369.6 nm) is shown because it contains several $^{12}$CO and $^{13}$CO lines. The data and best-fitting models of the remaining orders can be found in Appendix 2.B.

### 2.4.4 Chemical Composition

A free-chemistry approach (de Regt et al., 2024) was adopted in which the mixing ratios of line species were treated as independent parameters. This method, also referred to as the free composition (FC) method, includes vertically constant abundances of relevant chemical species while not enforcing any constraints on the relative abundances. The He abundance is held constant at $n_{\rm He} = 0.15$ and the $H_2$ abundance is adjusted to obtain a total $n_{\rm tot}$ equal to unity. The constant-with-altitude mixing ratios are expected to be valid for most scenarios for our K-band spectra, as only a limited vertical extent of the BD atmospheres is probed.

The C/O ratios are determined using the chemical abundances of carbon $n_C$ and oxygen $n_O$ bearing species, according to

$$C/O = \frac{n_{^{12}CO} + n_{^{13}CO}}{n_{H_2O} + n_{^{12}CO} + n_{^{13}CO}}. \tag{2.5}$$

The C/O ratio is constant, due to the constant-with-altitude mixing ratios.

The carbon abundance relative to hydrogen is used as a measurement of metallicity:

$$[C/H] = \log_{10}\left(\frac{n_C}{n_H}\right) - \log_{10}\left(\frac{n_C}{n_H}\right)_\odot, \tag{2.6}$$

where the solar value is $\log_{10}\left(\frac{n_C}{n_H}\right)_\odot = -3.54 \pm 0.04$ (Asplund et al. (2021). In a similar manner, the fluorine abundance from HF is calculated through

$$[F/H] = \log_{10}\left(\frac{n_{HF}}{n_H}\right) - \log_{10}\left(\frac{n_{HF}}{n_H}\right)_\odot, \tag{2.7}$$

where the solar value is $\log_{10}\left(\frac{n_F}{n_H}\right)_\odot = -7.6 \pm 0.25$ (Asplund et al. (2021).

We independently retrieved the number fractions of $^{12}CO$, $^{13}CO$, $H_2^{16}O$, and $H_2^{18}O$ to determine the carbon and oxygen isotopologue ratios ($^{12}C/^{13}C$ and $^{16}O/^{18}O$, respectively) of our BD sample. We want to compare our values of the retrieved carbon and oxygen isotope ratios with those of González Picos et al. (2024). We calculated these ratios using

$$^{12}C/^{13}C = \frac{n_{^{12}CO}}{n_{^{13}CO}}; \qquad ^{16}O/^{18}O = \frac{n_{H_2^{16}O}}{n_{H_2^{18}O}}. \tag{2.8}$$

To ensure the reliability of detecting molecular species, we employ a cross-correlation analysis, as detailed in Zhang et al. (2021). The cross-correlation function (CCF) for each species, $X$, is computed as follows:

$$CCF_X(v) = \sum_{i=1}^{N_\lambda} \frac{\left(d_i - m_{i,\bar{X}}\right)\left(m_i - m_{i,\bar{X}}\right)}{\sigma_i^2}, \tag{2.9}$$

where $m_{i,\bar{X}}$ is the atmospheric model without the species $X$, and $m_i$ is the model with all species included in the retrieval.

## 2.5 Results & Discussion

This section summarises the main results regarding the chemical composition, thermal profile, surface gravity, and rotational velocity of the three BDs, and provides a comparison between free and equilibrium chemistry (EC) models.

All results were obtained by analysing the atmospheric retrievals run for J0835, J0501 and J0500. Our best-fitting spectral models resulting from the retrieval analysis are shown

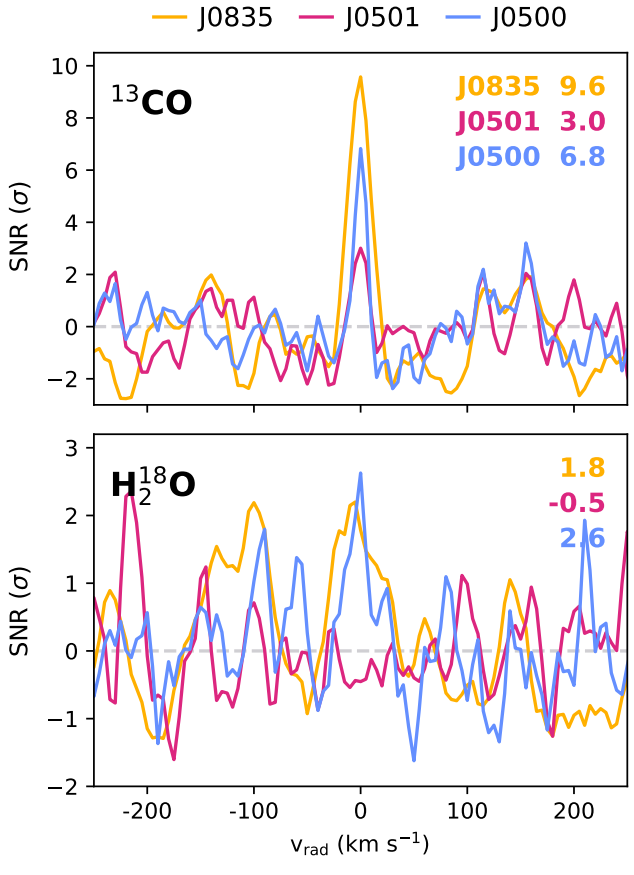


Figure 2.3: CCFs for $^{13}$CO and $H_2^{18}O$. The CCFs were calculated for each order–detector pair and summed over all orders and detectors, after which they were converted to S/N by dividing by the standard deviation of the CCFs away from the peak, excluding the values within $-100 < v_{rad} < 100$ km s$^{-1}$. The different colours represent the different targets, J0835, J0501 and J0500. The S/Ns of the peaks of the CCFs for each individual species are shown in the upper-right corner.

in the top three panels of Fig. 2.2. These models implement a free-chemistry atmosphere and account for pixel-to-pixel correlation using GPs (de Regt et al., 2024; González Picos et al., 2024). The detection significances ($X$) of four species ($^{13}$CO, $H_2^{18}O$, HF, and Ca) were determined from a Bayesian model comparison. This included running 15 retrievals, five retrievals for every BD, one model including all $X$ and the main species ($^{12}$CO, $H_2^{16}O$), and four models where one $X$ was excluded. We computed the logarithm of the Bayes factor $B_m$ according to

$$\ln B_m = \ln \mathcal{Z}_{\text{full model}} - \ln \mathcal{Z}_{\text{w/o } X}, \tag{2.10}$$

where $\ln \mathcal{Z}$ stands for the log-evidence calculated for every retrieval. Thereafter, this is translated to a detection significance, also referred to as the 'sigma' significance, in units of $\sigma$ (Benneke & Seager, 2013). For $^{13}$CO, we report moderate to strong detections of $9.6\sigma$, $3.0\sigma$, and $6.8\sigma$ for J0835, J0501, and J0500, respectively, see Figure 2.3. For $H_2^{18}O$ only one weak detection ($2.6\sigma$) for J0835 was found. All other BDs did not show any evidence of the presence of $H_2^{18}O$. This is the same case for Ca, with one weak detection ($2.1\sigma$) for J0500. All BDs show a strong detection significance for HF ($> 4.0\sigma$). An overview of all $B_m$ and sigma significance values is presented in Appendix A.

We calculated the CCF using Eq. 2.9 between the data and the best-fit model of each individual species for every order-detector pair in the object rest frame. These CCFs are then combined across all orders and detectors and converted to signal-to-noise ratios (S/Ns) [$\sigma$] by dividing by the standard deviation of the CCFs away from the peak, excluding the values within $-100 < v_{\text{rad}} < 100$ km s$^{-1}$. The resultant S/Ns distinctly show the presence of various species in the BD atmospheres (see Appendix 2.C).

The three objects generally show comparable chemical compositions and temperature distributions. However, variations are noted due to differences in their effective temperatures, surface gravities, rotational velocities, and the quality of the observational data. Table 2.3 provides an overview of the retrieved parameters for all three best-fitting spectral models, with their prior values. All uncertainties indicate $1\sigma$ intervals.

### 2.5.1 Chemical Composition

Our best-fitting spectral models yield the volume mixing ratios (VMRs) of detectable species (see Table 2.3) in the atmospheres of the three BDs. Constraints are obtained for both $H_2O$ and CO for all three targets, leading to a gaseous C and O inventory and subsequent C/O ratio, metallicity, and isotope ratios of the targets. In addition, we present the fluorine abundance for all three BDs.

#### C/O ratio

The C/O ratio posteriors are shown in Fig. 2.4, which presents the retrieved values:

$$\begin{aligned} \text{C/O}_{\text{J0835}} &= 0.65^{+0.02}_{-0.02} \\ \text{C/O}_{\text{J0501}} &= 0.68^{+0.04}_{-0.04} \\ \text{C/O}_{\text{J0500}} &= 0.71^{+0.01}_{-0.01}. \end{aligned}$$

| Parameter | Description | Prior Range | J0835 | J0501 | J0500 |
|---|---|---|---|---|---|
| log $^{12}$CO | log mixing ratio of $^{12}$CO | [-12.0, -2.0] | $-2.85^{+0.02}_{-0.02}$ | $-2.89^{+0.05}_{-0.05}$ | $-3.03^{+0.02}_{-0.02}$ |
| log $^{13}$CO | log mixing ratio of $^{13}$CO | [-12.0, -2.0] | $-4.80^{+0.05}_{-0.05}$ | $-5.06^{+0.14}_{-0.15}$ | $-5.10^{+0.06}_{-0.07}$ |
| log $H_2^{16}O$ | log mixing ratio of $H_2^{16}O$ | [-12.0, -2.0] | $-3.23^{+0.02}_{-0.02}$ | $-3.19^{+0.05}_{-0.05}$ | $-3.29^{+0.02}_{-0.02}$ |
| log $H_2^{18}O$ | log mixing ratio of $H_2^{18}O$ | [-12.0, -2.0] | $-5.73^{+0.12}_{-0.16}$ | $-8.92^{+1.96}_{-1.99}$ | $-5.69^{+0.13}_{-0.21}$ |
| log HF | log mixing ratio of HF | [-12.0, -2.0] | $-7.03^{+0.05}_{-0.05}$ | $-7.10^{+0.19}_{-0.19}$ | $-7.30^{+0.06}_{-0.06}$ |
| log Ca | log mixing ratio of Ca | [-12.0, -2.0] | $-6.03^{+0.22}_{-0.64}$ | $-5.86^{+0.40}_{-1.38}$ | $-5.95^{+0.14}_{-0.18}$ |
| C/O | carbon-to-oxygen ratio | — | $0.65^{+0.02}_{-0.02}$ | $0.68^{+0.04}_{-0.04}$ | $0.71^{+0.01}_{-0.01}$ |
| $^{12}$C/$^{13}$C | carbon isotope ratio | — | $89^{+11}_{-11}$ | $155^{+56}_{53}$ | $117^{+20}_{-17}$ |
| $^{16}$O/$^{18}$O | oxygen isotope ratio | — | $316^{+117}_{-89}$ | — | $251^{+122}_{-76}$ |
| [F/H] | fluorine abundance w.r.t. solar | — | $0.41^{+0.05}_{-0.05}$ | $0.26^{+0.19}_{-0.19}$ | $0.07^{+0.06}_{-0.06}$ |
| [C/H] | metallicity w.r.t. solar | — | $0.54^{+0.04}_{-0.04}$ | $0.44^{+0.06}_{-0.06}$ | $0.28^{+0.04}_{-0.04}$ |
| log $g$ | log surface gravity (cm s$^{-2}$) | [4.00, 6.00] | $5.40^{+0.03}_{-0.03}$ | $4.51^{+0.07}_{-0.07}$ | $5.55^{+0.03}_{-0.03}$ |
| $\epsilon_{\rm limb}$ | limb darkening coefficient | [0.00, 1.00] | $0.63^{+0.06}_{-0.07}$ | $0.37^{+0.28}_{-0.22}$ | $0.31^{+0.24}_{-0.20}$ |
| $v \sin i$ | projected rotational velocity (km s$^{-1}$) | [0.0, 40.0] | $15.42^{+0.14}_{-0.12}$ | $6.90^{+0.25}_{-0.24}$ | $5.05^{+0.21}_{-0.16}$ |
| $v_{\rm rad}$ | radial velocity (km s$^{-1}$) | [-50.0, 50.0] | $29.59^{+0.04}_{-0.04}$ | $23.15^{+0.05}_{-0.05}$ | $15.65^{+0.02}_{-0.02}$ |
| $\nabla_{T,0}$ | temperature gradient at $P_0 = 10^2$ bar | [0.12, 0.40] | $0.15^{+0.03}_{-0.02}$ | $0.15^{+0.09}_{-0.09}$ | $0.22^{+0.06}_{-0.06}$ |
| $\nabla_{T,1}$ | temperature gradient at $P_1$ | [0.13, 0.40] | $0.13^{+0.00}_{-0.00}$ | $0.14^{+0.06}_{-0.06}$ | $0.15^{+0.01}_{-0.01}$ |
| $\nabla_{T,2}$ | temperature gradient at $P_2$ | [0.03, 0.40] | $0.06^{+0.00}_{-0.00}$ | $0.10^{+0.02}_{-0.02}$ | $0.09^{+0.01}_{-0.01}$ |
| $\nabla_{T,3}$ | temperature gradient at $P_3$ | [0.00, 0.40] | $0.26^{+0.07}_{-0.06}$ | $0.05^{+0.01}_{-0.01}$ | $0.09^{+0.02}_{-0.01}$ |
| $\nabla_{T,4}$ | temperature gradient at $P_4 = 10^{-5}$ bar | [-0.20, 0.20] | $0.01^{+0.12}_{-0.13}$ | $0.07^{+0.02}_{-0.03}$ | $0.01^{+0.11}_{-0.12}$ |
| log $P_3$ | log pressure of central ($i = 3$) knot | [-3, 1] | $-0.30^{+0.08}_{-0.06}$ | $0.66^{+0.19}_{-0.22}$ | $0.12^{+0.18}_{-0.18}$ |
| $\Delta \log P_{23}$ | log pressure difference $P_2$ and $P_3$ | [0.5, 2.0] | $1.66^{+0.22}_{-0.30}$ | $1.40^{+0.08}_{-0.09}$ | $1.46^{+0.34}_{-0.40}$ |
| $\Delta \log P_{34}$ | log pressure difference $P_3$ and $P_4$ | [0.5, 1.0] | $0.93^{+0.05}_{-0.06}$ | $0.69^{+0.06}_{-0.06}$ | $0.81^{+0.11}_{-0.14}$ |
| $T_3$ | temperature at central ($i = 3$) knot (K) | [500, 2500] | $1566^{+16}_{-13}$ | $1977^{+85}_{-92}$ | $1570^{+69}_{-59}$ |
| log $a$ | GP amplitude | [-0.70, 0.30] | $-0.01^{+0.01}_{-0.01}$ | $0.07^{+0.01}_{-0.01}$ | $0.12^{+0.00}_{-0.00}$ |
| log $\ell$ | GP length scale nm) | [-3.00, -1.00] | $-1.32^{+0.02}_{-0.02}$ | $-2.06^{+0.01}_{-0.01}$ | $-1.58^{+0.01}_{-0.01}$ |

Table 2.3: Retrieved best-fit parameters and their $1\sigma$ uncertainty intervals: We imposed uniform priors. The table includes the VMRs of the chemical species, physical properties (surface gravity and projected rotational velocity), temperature gradients and GP parameters.

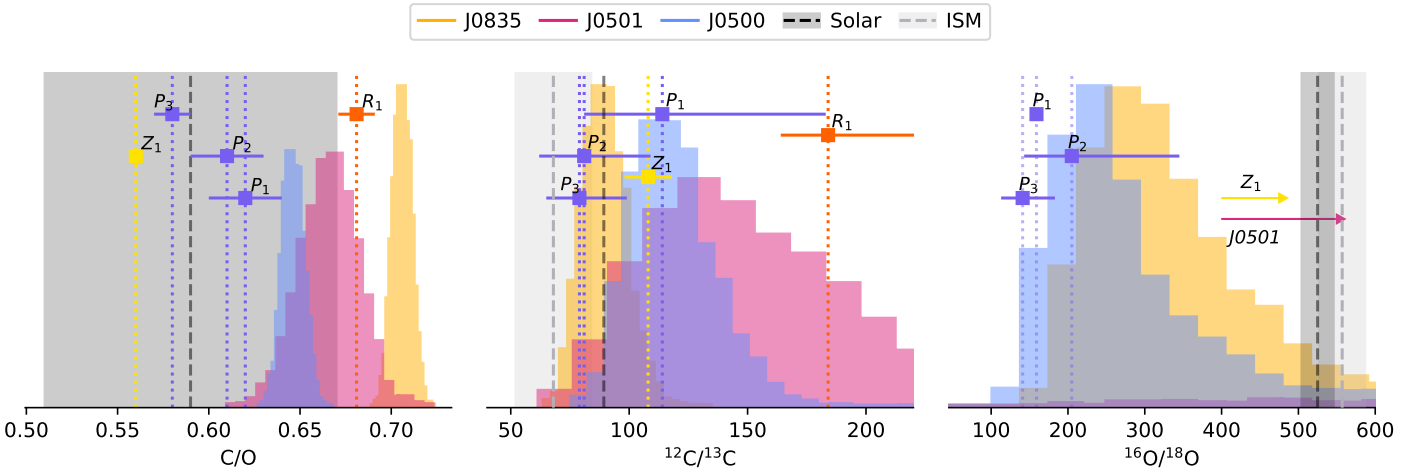


Figure 2.4: Posterior distributions of the C/O (left), carbon $^{12}C/^{13}C$ isotope (middle), and oxygen $^{16}O/^{18}O$ isotope ratio (right) for J0835, J0501 and J0500. The $^{12}C/^{13}C$ values for the Solar System (terrestrial value) and ISM are $89.3 \pm 0.2$ (Meija et al., 2016) and $68 \pm 16$ (Milam et al., 2005), respectively. The C/O value for our Sun is $0.59 \pm 0.08$ (Asplund et al., 2021). The $^{16}O/^{18}O$ values for the Solar System and ISM are $557 \pm 30$ (Wilson, 1999) and $525 \pm 21$ (Lyons et al., 2018). The purple error bars represent the young BDs observed and analysed by González Picos et al. (2024, $P_1$: J1200, $P_2$: TWA28 and $P_3$: J0856), the orange error bar DENIS J0255 ($R_1$) by de Regt et al. (2024), and the yellow 2M0355 ($Z_1$) by Zhang et al. (2022).

The C/O ratios are comparable among the three BDs, but slightly enhanced compared to the solar C/O ratio (0.59 ± 0.08, Asplund et al. (2021)). This enhancement may be explained by oxygen sequestration, (Line et al., 2021) leading to the condensation of oxygen into silicate-oxide clouds. This scenario was brought up by (de Regt et al., 2024) to explain the increased C/O ratio of ∼0.68 of BD DENIS J0255.

In Fig. 2.4, we compare the retrieved values for the three BDs to the values of other isolated BDs. The C/O ratios retrieved by González Picos et al. (2024) for three young late M-type BDs were within the margins of the solar ratio. In comparison, González Picos et al. (2024) studied M-type objects that have high enough atmospheric temperatures that silicate-oxide clouds do not form, thus explaining their agreement with the solar value. For 2M0355, Zhang et al. (2021) obtained a C/O ratio using an EC model that accounts for condensation. As such, their C/O ratio, which is in agreement with the solar ratio, represents the bulk elemental abundances.

Using the same EC set-up as de Regt et al. (2024), we find bulk C/O ratios of $0.58^{+0.01}_{-0.01}$, $0.60^{+0.02}_{-0.05}$, and $0.60^{+0.01}_{-0.01}$ for J0835, J0501, and J0500, respectively. They are in agreement with the solar C/O ratio.

### Metallicity

The [C/H] ratio is used as a proxy for metallicity. The derived posterior distributions of [C/H] are shown in the bottom graph of Fig. 2.5. The [C/H] values are significantly larger than the solar value and other work that used this same proxy (Zhang et al., 2022; González Picos et al., 2024; de Regt et al., 2024). It is unfortunately not straightforward to interpret these values, since metallicities cannot be constrained well with solely K-band high-resolution spectroscopy because of the strong correlation between surface gravity and metallicity in atmospheric retrieval analyses (e.g. González Picos et al., 2024).

### Isotope ratios

Constrained $^{12}$CO and $^{13}$CO abundances were retrieved for all three BDs. From those, the following $^{12}$C/$^{13}$C ratios for J0835, J0501, and J0500 were determined (see Fig. 2.4):

$$
\begin{aligned}
^{12}\mathrm{C}/^{13}\mathrm{C}_{\mathrm{J0835}} &= 89^{+11}_{-11} \\
^{12}\mathrm{C}/^{13}\mathrm{C}_{\mathrm{J0501}} &= 155^{+56}_{-53} \\
^{12}\mathrm{C}/^{13}\mathrm{C}_{\mathrm{J0500}} &= 117^{+20}_{-17}.
\end{aligned}
$$

The values are similar among the three objects within their $1\sigma$ uncertainties. The ratio for J0835 is in agreement with the solar value of 89.3 ± 0.2 (Meija et al., 2016), while the other two objects appear to have slightly larger ratios. All three of them have significantly higher ratios than the present day ISM value 68 ± 16 (Milam et al., 2005). Figure 2.4 gives an overview of our retrieved ratios in comparison to previous work as part of the SupJup Survey (González Picos et al., 2024; de Regt et al., 2024), and the work on BD 2M0355, the first BD for which the $^{12}$C/$^{13}$C was determined (Zhang et al., 2021; Zhang et al., 2022).

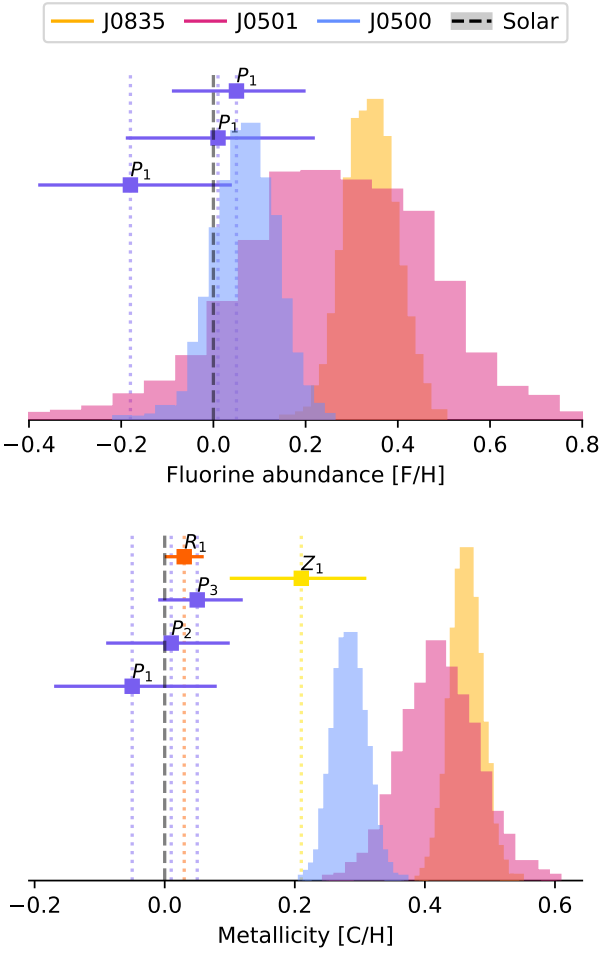


Figure 2.5: Posterior distributions of the fluorine abundance relative to hydrogen [F/H] (**top panel**) and carbon abundance relative to hydrogen [C/H], used as a measure of metallicity (**bottom panel**) for J0835, J0501 and J0500. J1200, TWA28, and J0856 are the young BDs observed and analysed by González Picos et al. (2024), DENIS by de Regt et al. (2024), and 2M0355 by Zhang et al. (2022). $\log_{10}[\mathrm{F/H}]_\odot = -7.6 \pm 0.25$ (Asplund et al. (2021)) and $\log_{10}[\mathrm{C/H}]_\odot = -3.54 \pm 0.04$ (Asplund et al. (2021)).

The $H_2^{18}O$ isotope was included in the retrievals because of the positive detection of $H_2^{18}O$ by González Picos et al. (2024) in TWA 28 ($^{16}O/^{18}O \sim 205^{+140}_{-62}$) and J0856 ($^{16}O/^{18}O \sim 141^{+42}_{-28}$). As mentioned before, only one weak detection was found for J0835. From these retrieved VMRs, we calculated the $^{16}O/^{18}O$ ratio for J0835:

$$^{16}O/^{18}O_{J0835} = 311^{+100}_{-86}.$$

Zhang et al. (2021) and Line et al. (2021) have highlighted the potential of the carbon isotope ratio to serve as an additional diagnostic of planet and BD formation histories. However, evolution on a galactic timescale is also expected to alter the average $^{12}C/^{13}C$ ratio, since $^{13}C$ is produced in asymptotic giant branch stars that subsequently enrich the ISM (Iben & Renzini, 1983). Therefore, young objects are generally expected to have lower ratios than old objects. Crossfield et al. (2019) found isotopologue ratio measurements for GJ 745 A and B of $^{12}C/^{13}C = 296 \pm 45$ and $224 \pm 26$, and $^{16}O/^{18}O = 1220 \pm 260$ and $1550 \pm 360$, respectively. Caramazza, M. et al. (2023) suggested, after observing the X-ray emission for GJ 745 A and B, that the extremely low X-ray activity of the binary, their ultra-low metallicity, non-detection of photometric star spot variability, and low chromospheric emission are in line with an older age object. As far as we know, these are the highest carbon and oxygen isotope ratios measured for mature low-mass stars.

**Hydrogen fluoride**

The abundances of fluorine (F) with respect to solar were computed from the retrieved VMRs of HF:

$$[\mathrm{F/H}]_{\mathrm{J0835}} = 0.41^{+0.05}_{-0.05}$$
$$[\mathrm{F/H}]_{\mathrm{J0501}} = 0.26^{+0.19}_{-0.19}$$
$$[\mathrm{F/H}]_{\mathrm{J0500}} = 0.07^{+0.06}_{-0.06}.$$

All BDs show a strong HF detection significance: $14.5\sigma$, $4.2\sigma$, and $9.2\sigma$ for J0835, J0501, and J0500, respectively.

The computed [F/H] ratio for J0500 is in a $1\sigma$ agreement with the solar abundance of $\log_{10}\left(\frac{n_{\mathrm{F}}}{n_{\mathrm{H}}}\right)_{\odot} = -7.6 \pm 0.25$ (Asplund et al., 2009), J0501 is in agreement within $2\sigma$, and J0835 shows a higher value for [F/H]. It should be noted that the [F/H] suffers from the same metallicity-surface gravity degeneracy as the [C/H] and thus the absolute fluorine abundance of J0835 is not necessarily super-solar.

For our K-band observations, we are sensitive to the HF $1-0$ vibrational transitions, as it has prominent absorption lines in the $2.3-2.5$ µm region (Wilzewski et al., 2016). Recent work in the SupJup Survey, operating in the K-band, has revealed the presence of HF in several sub-stellar objects (González Picos et al., 2024; Zhang et al., 2024; de Regt et al., 2025). Figure 2.5 gives an overview of all values obtained so far.

### 2.5.2 Free chemistry versus equilibrium chemistry

As elaborated in section 2.4.4, the FC method (e.g. de Regt et al., 2024; González Picos et al., 2024) was applied. This method assumes a constant-with-altitude mixing ratio for every species in the model atmospheres. Despite the FC method providing a good approximation for our spectra, it is insightful to compare our retrieved abundances against those predicted by EC. The EC method assumed element abundances as retrieved from the `pRT` models (see Fig. 2.6).

Using `FastChem` (Stock et al., 2018, 2022; Kitzmann et al., 2024) we compared our retrieved mixing ratios against EC predictions (see Fig. 2.6). The VMRs are normalised

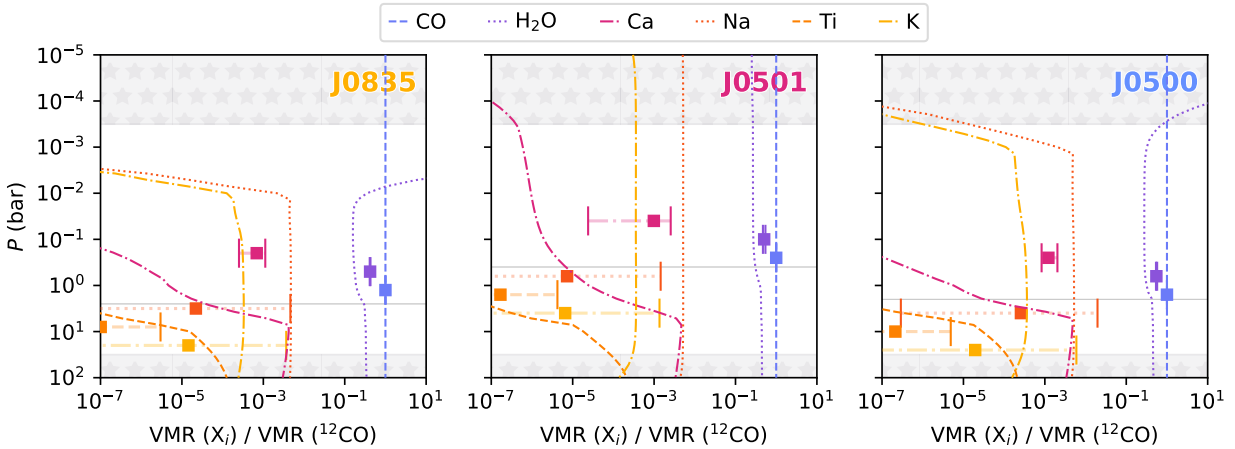


Figure 2.6: VMRs of line species ($^{12}$CO, $H_2O$, Ca, Na, Ti, and K) for the three BDs using the FC and EC method. The error bars represent the values retrieved with the FC method. The dashed lines show the `Fastchem` EC abundances corresponding to the best-fitting P-T profile, C/O ratio, and metallicity for each of the BDs. The EC abundances have a similar line style and colour as those of the associated FC VMR. The black lines indicate the location of the peak of the integrated contribution functions, and the shaded areas indicate the pressures where we expect large uncertainties as we are not sensitive to probe these atmospheric pressures.

relative to the VMR of $^{12}$CO, which corrects for any potential systematic offsets due to the metallicity-surface gravity degeneracy (González Picos et al., 2024; de Regt et al., 2024). The $H_2O$ abundance retrieved with the FC method deviates slightly from the EC predictions, which could indicate the presence of quenching and/or disequilibrium chemistry.

Besides the line species presented in Table 2.3 various `pRT` models including the atomic species Na, Ti and K were tested against the spectra. The Na and K, or alkali lines, have been found to be a very good probe for differences in surface gravity for late-type objects (Gorlova et al., 2003; Schlieder et al., 2012; Allers & Liu, 2013; Martin et al., 2017; Manjavacas et al., 2020). For young BDs, alkali lines have been observed to be weaker than for field BDs (Steele & Jameson, 1995; Gorlova et al., 2003; Allers et al., 2007; Allers & Liu, 2013; Bonnefoy et al., 2014).

The atomic opacities from Na, K (Allard et al., 2019), and Ti (Castelli & Kurucz, 2003) were included in our FC retrievals, but not detected. The retrieved abundances using the FC models are displayed by the error bars in Fig. 2.6. The dashed lines represent those for the EC models. Indeed, the derived VMR upper limits for Na, Ti, and K are in line with those expected from the EC models.

The $H_2O$, Na and K EC abundances of J0835 and J0500 are skewed for smaller pressures. For lower temperatures, $CH_4$ becomes the dominating carbon species, yielding a drop-off for the CO abundances. The increase in the relative $H_2O$ abundances is expected since the models are normalised towards CO. We retrieved a lower temperature in the upper atmosphere of J0835 than J0500, which explains the drop-off location for J0835 to be at a higher pressure. For J0501, the temperature does not get low enough to see this CO-$CH_4$ switch. Even though we retrieve these abundances, the presence of a similar shift is unlikely due to the vertical mixing in the atmospheres (Zahnle & Marley, 2014).

### 2.5.3 Thermal Profile

The best-fitting P-T profiles (the solid line and the shaded areas indicate the $1\sigma$, $2\sigma$, and $3\sigma$ uncertainties in Fig. 2.7) of the BDs J0835 and J0500 are similar, while the profile of J0501 is warmer by ~100 K at similar pressures. Since the retrieved surface gravity of J0501 is lower than that of the others by an order of magnitude, the photospheric region, as indicated by the integrated contribution function (shaded area on the left in Fig. 2.7), is found to be located at lower pressures (order of ~10). This is in line with the mass and radii estimates for the three targets by Filippazzo et al. (2015), where J0501 is found to be of significantly lower mass and larger radius. As expected, the confidence envelopes of the P-T profile show larger uncertainties outside the photosphere, at the higher and lower altitudes. These regions are not probed by the K-band spectrum.

The self-consistent Sonora elf owl models ($SE_1$ and $SE_2$ in Fig. 2.7) were calculated using $T_{eff}$ = 1800 K and $\log g = 5.5$, and $T_{eff}$ = 1700 K and $\log g = 4.5$, both assuming a solar metallicity and C/O ratio. Just as found for YSES 1b (Zhang et al., 2024), the retrieved P-T profiles are more isothermal than the self-consistent models. This may indicate the absence of continuum opacity, for example clouds, since a spectrum of a cloudless atmosphere combined with an isothermal temperature gradient is equivalent to a spectrum of a cloudy atmosphere.

To a first order, the retrieved thermal profiles for all three objects seem to agree well

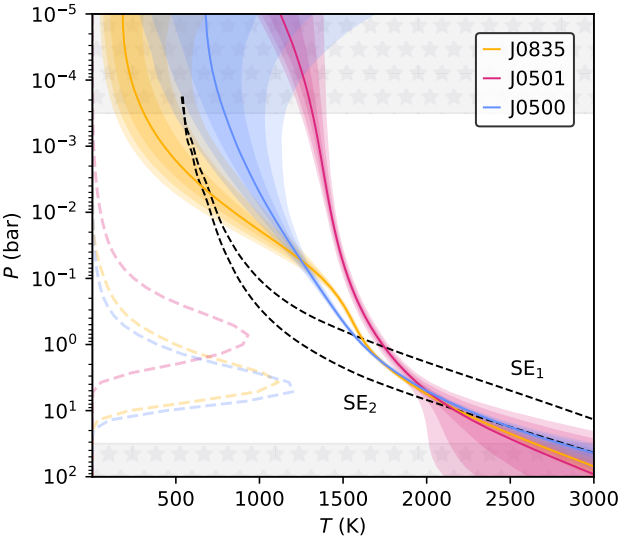


Figure 2.7: Best-fit P–T profiles (solid lines) for BDs J0835, J0501 and J0500. The associated shaded regions indicate the $1\sigma$, $2\sigma$, and $3\sigma$ regions. The integrated contribution functions are indicated on the left vertical axis. Two self-consistent Sonora elf owl P-T profiles, $SE_1$ ($T_{eff}$ = 1800 K, $\log g = 5.5$) and $SE_2$ ($T_{eff}$ = 1700 K, $\log g = 4.5$) are over-plotted with dashed black lines.

with the literature values for the effective temperature of each object (see Table 2.1). A direct comparison of our profiles to the literature values is unfavourable, due to the disparate methods used to derive the literature values.

### 2.5.4 Surface gravity

The retrieved values for the surface gravity, $\log g$, are in line with the expectations for young, low-surface gravity objects (Baraffe et al., 2002; Allers et al., 2007; Bonnefoy et al., 2014). While the surface gravity values for J0835 and J0500 are similar, J0501 shows a significantly lower value. This explains the shift of the emission contribution towards lower pressures. Unfortunately, the limited spectral range of the K-band makes these types of observations less sensitive to $\log g$. The surface gravity, metallicity, and effective temperature govern the atmospheric gaseous optical depth of an object. Since the atmospheric scale height is inversely proportional to the surface gravity, the latter influences the pressure range of the photosphere. Therefore, it plays a significant role in shaping the observed spectra as it affects line shapes, temperature profiles, and the overall continuum (Marley & Robinson, 2015; Mukherjee et al., 2024). González Picos et al. (2024) show that the posterior distributions of surface gravities

and metallicities exhibit a high degree of degeneracy in the K-band, as we also notice for our targets, hampering an accurate constraint.

### 2.5.5 Rotational velocity

J0835 has a rotational velocity of

$$v \sin i_{\mathrm{J0835}} = 15.42^{+0.14}_{-0.12} \text{ km s}^{-1}.$$

It is the fastest rotator of our small sample, as is also apparent from the broadened spectral features in Fig. 2.2. Blake et al. (2010) reported a similar value for the projected rotational velocity of $v \sin i_{\mathrm{J0835}} = 14.18 \pm 0.43$ km s$^{-1}$. For J0500 we retrieve a value of

$$v \sin i_{\mathrm{J0500}} = \ 5.05^{+0.21}_{-0.16} \text{ km s}^{-1},$$

while Blake et al. (2010) finds $v \sin i_{\mathrm{J0500}} = 9.65 \pm 0.36$ km s$^{-1}$. A possible explanation for this difference could be that their lower spectral resolution of $R \sim 35000$ hinders the measurement of low projected rotational velocities.

J0501 has a retrieved projected rotational velocity of

$$v \sin i_{\mathrm{J0501}} = 6.90^{+0.25}_{-0.24} \text{ km s}^{-1},$$

which is also lower than the velocity found by Vos et al. (2020), $9.57^{+0.67}_{-0.58}$ km s$^{-1}$, which was based on Gemini Near-InfraRed Spectrograph (GNIRS; Elias et al., 2006) high-resolution observations with $R \sim 18000$. Again, the higher resolution of our CRIRES+ observations likely aids in resolving such a low rotational velocity.

The projected rotational velocities are consistent with the expected slow rotation of young, bloated BDs. However, their intrinsic rotation velocities also depend on viewing angle. Similar to González Picos et al. (2024), there is a tentative relation between our GP parameters and the $v \sin i$. Slower rotators exhibit smaller GP length-scales, $\ell$, and larger amplitudes, $a$, compared to fast rotators. This is as expected from the fact that for fast rotators, differences between model and observations will be smeared out over more spectral pixels, resulting in lower GP amplitudes and larger length-scales.

## 2.6 Conclusions and future work

We analysed high-resolution CRIRES+ spectra for three young BDs, providing insights into their atmospheric composition. Their C/O ratios are somewhat higher than that of the Sun, which could be the result of oxygen sequestration. Their metallicities are also higher by a factor of a few compared to the Sun. However, uncertainties may be underestimated due to the known correlation with surface gravity, to which these K-band observations are not very sensitive.

Performing precise measurements of isotope ratios is a challenge. However, we were able to constrain the isotopic composition of the BDs. The $^{12}$C/$^{13}$C ratios for J0835, J0501, and J0500 are $93^{+10}_{-10}$ ($9.1\sigma$), $155^{+56}_{-53}$ ($3.0\sigma$), and $117^{+20}_{-17}$ ($6.8\sigma$), respectively. All values suggest a slightly depleted $^{13}$CO concentration compared to that of the local ISM.

The remaining observational data of the SupJup Survey are being analysed, including tens of other BDs and SJs, to constrain their C/O, $^{12}C/^{13}C$, and $^{16}O/^{18}O$ ratios.

## Acknowledgements

W.M. acknowledges funding from NWO grant from the second round of the Planetary and Exoplanetary Science Programme (PEPSci-II). S.d.R. and I.S. acknowledge funding from NWO grant OCENW.M.21.010. We thank the SURF Cooperative (www.surf.nl) for the support in using the National Supercomputer Snellius using grant no. EINF-4556 and EINF-9460. This research has made use of the following software: `Astropy` (Astropy Collaboration et al., 2022), `corner` (Foreman-Mackey, 2016), `Matplotlib` (Hunter, 2007), `MultiNest` (Feroz et al., 2019), `NumPy` (Harris et al., 2020), `petitRADTRANS` (Mollière et al., 2019), `picaso` (Mukherjee et al., 2023), `PyAstronomy` (Czesla et al., 2019), and `PyMultiNest` (Buchner et al., 2014).

## 2.A Posterior distributions of atmospheric retrievals

Supplementary graphs and tables are stored and can be found in the Zenodo repository: https://zenodo.org/records/14713641



### 2.A.1 Atmospheric retrieval of J0835

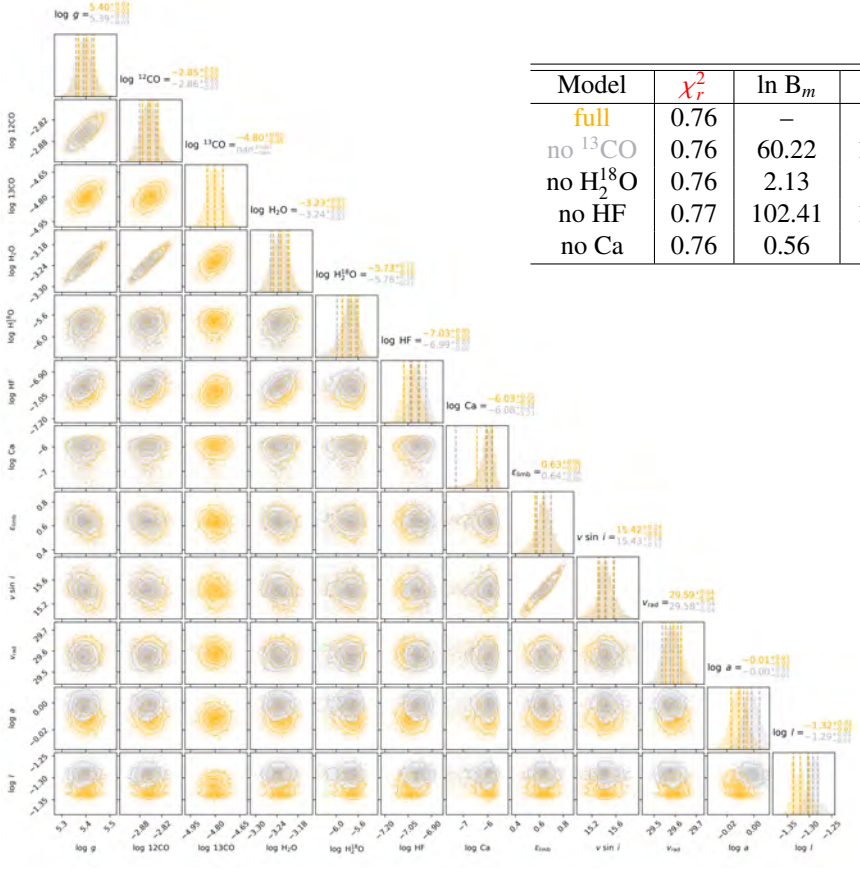


| Model | $\chi^2_r$ | ln $B_m$ | $\sigma$ |
|---|---|---|---|
| full | 0.76 | – | – |
| no $^{13}$CO | 0.76 | 60.22 | 11.20 |
| no $H_2^{18}O$ | 0.76 | 2.13 | 2.60 |
| no HF | 0.77 | 102.41 | 14.50 |
| no Ca | 0.76 | 0.56 | 1.72 |

Figure 2.8: Posterior distributions of the retrieved parameters for J0835. In yellow, we show the distributions for a model fitted for 21 free parameters including $^{12}$CO, $^{13}$CO, $H_2^{16}O$, $H_2^{18}O$, HF and Ca. The grey distributions represent a model where $^{13}$CO is excluded. The reduced chi-squared values for the models with and without $^{13}$CO, $H_2^{18}O$, HF and Ca are shown in the top right corner.

### 2.A.2 Atmospheric retrieval of J0501

| Model | $\chi^2_r$ | ln $B_m$ | $\sigma$ |
|---|---|---|---|
| full | 0.56 | – | – |
| no $^{13}$CO | 0.58 | 6.62 | 4.06 |
| no $H_2^{18}O$ | 0.56 | -0.35 | 1.00 |
| no HF | 0.57 | 7.17 | 4.20 |
| no Ca | 0.57 | 0.31 | 1.50 |

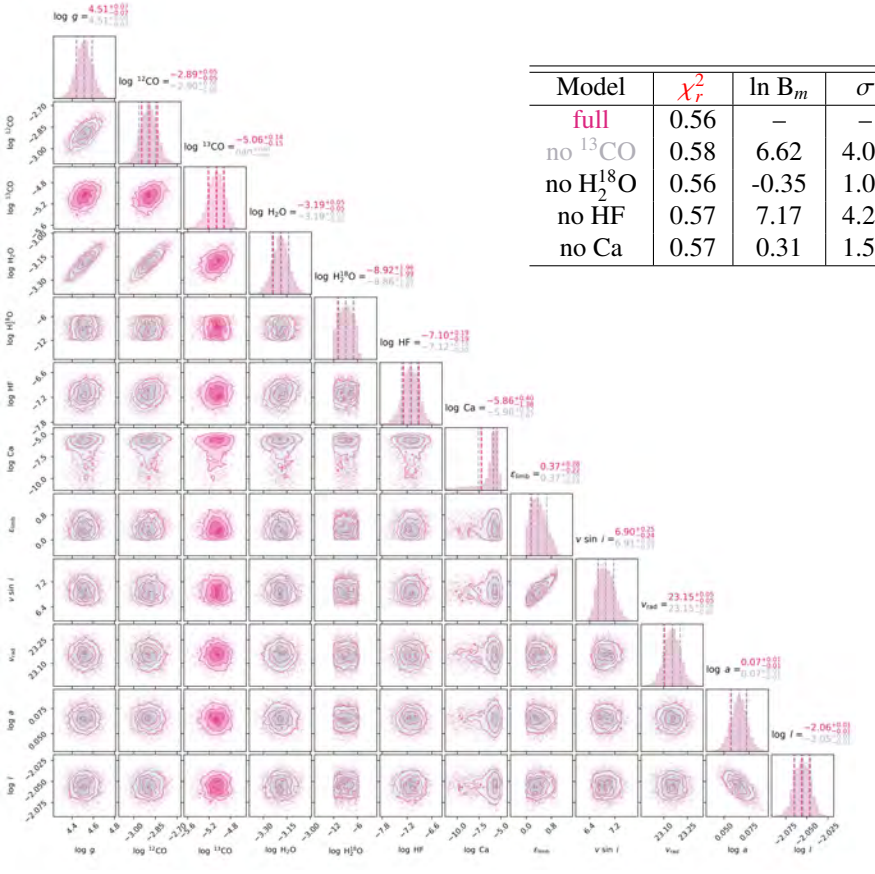


Figure 2.9: Posterior distributions of the retrieved parameters for J0501. In pink, we show the distributions for a model fitted for 21 free parameters including $^{12}$CO, $^{13}$CO, $H_2^{16}O$, $H_2^{18}O$, HF and Ca. The grey distributions represent a model where $^{13}$CO is excluded. The reduced chi-squared values for the models with and without $^{13}$CO, $H_2^{18}O$, HF and Ca are shown in the top right corner.

### 2.A.3 Atmospheric retrieval of J0500

| Model | $\chi^2_r$ | ln $B_m$ | $\sigma$ |
|---|---|---|---|
| full | 0.43 | – | – |
| no $^{13}$CO | 0.43 | 19.99 | 6.64 |
| no $H_2^{18}O$ | 0.43 | 0.00 | 0.00 |
| no HF | 0.43 | 39.64 | 9.16 |
| no Ca | 0.43 | 1.07 | 2.07 |

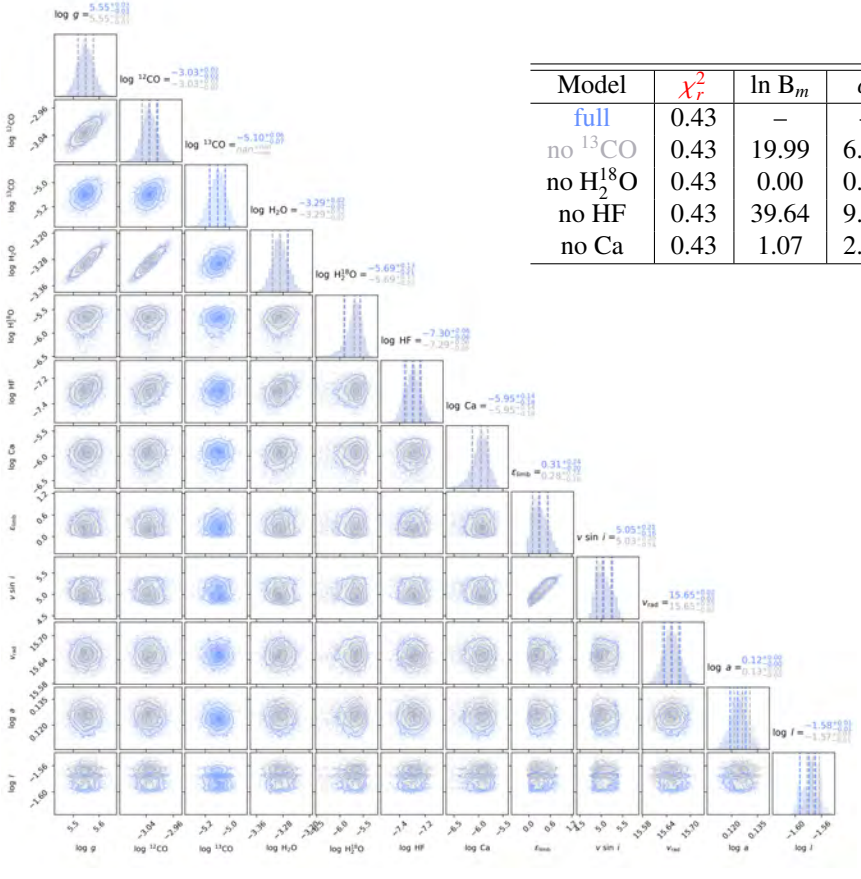


Figure 2.10: Posterior distributions of the retrieved parameters for J0500. In blue, we show the distributions for a model fitted for 21 free parameters including $^{12}$CO, $^{13}$CO, $H_2^{16}O$, $H_2^{18}O$, HF and Ca. The grey distributions represent a model where $^{13}$CO is excluded. The reduced chi-squared values for the models with and without $^{13}$CO, $H_2^{18}O$, HF and Ca are shown in the top right corner.

## 2.B Best Fitting Spectra

Supplementary graphs and tables are stored and can be found in the Zenodo repository: https://zenodo.org/records/14713641

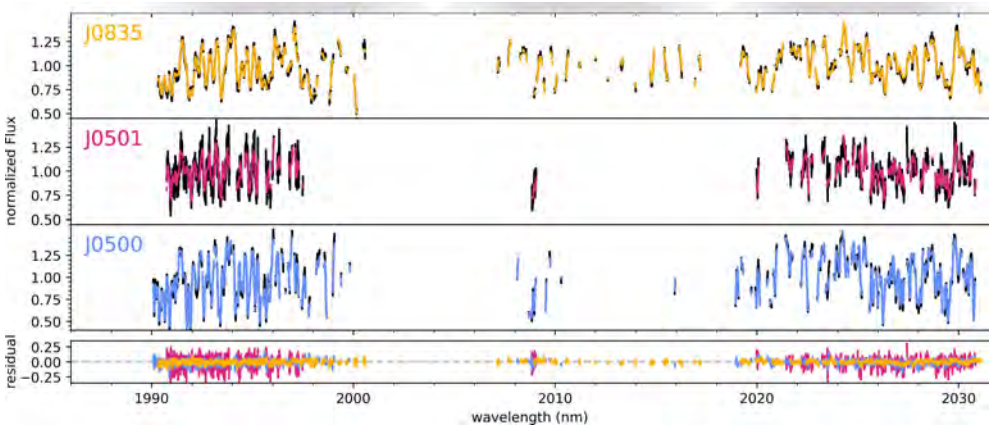


Figure 2.11: Best-fitting models of 2nd K2166 order (upper three panels) retrieved for J0835, J0501 and J0500 (top to bottom) plotted on top of the observational flux in black. This order contains many masked telluric lines, resulting in large gaps in the data.

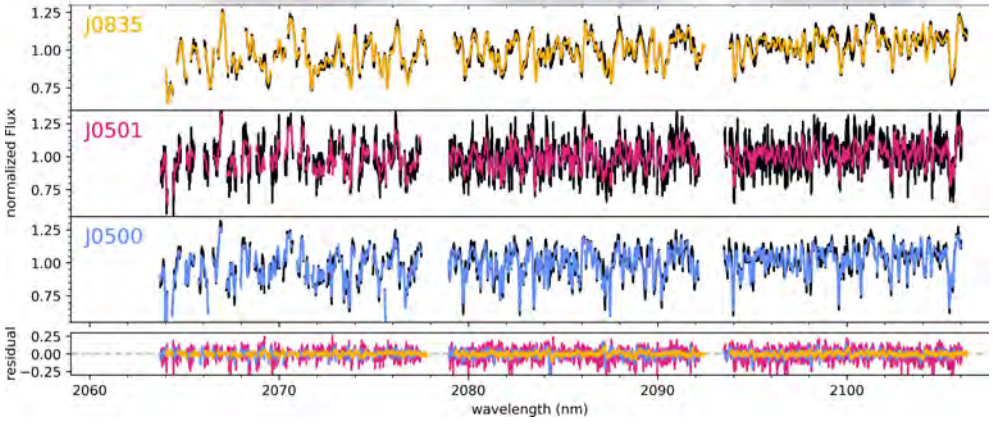


Figure 2.12: Best-fitting models of 3rd K2166 order (upper three panels) retrieved for J0835, J0501 and J0500 (top to bottom) plotted on top of the observational flux in black.

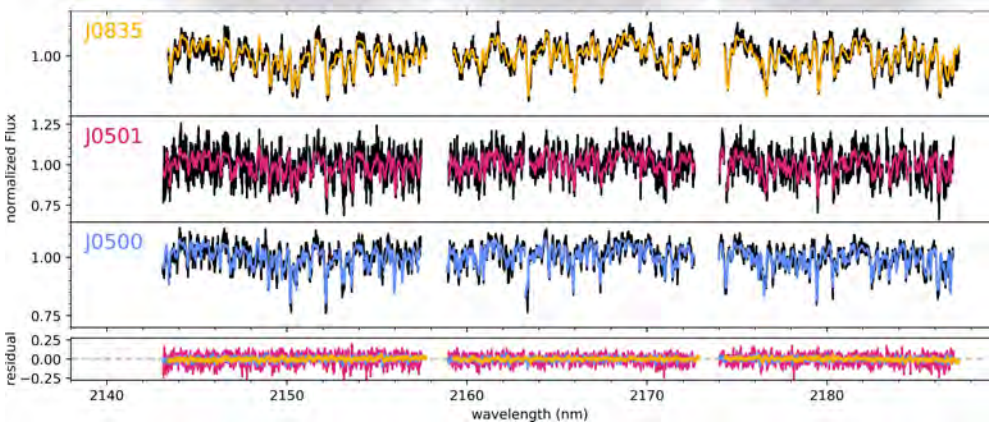


Figure 2.13: Best-fitting models of 4th K2166 order (upper three panels) retrieved for J0835, J0501 and J0500 (top to bottom) plotted on top of the observational flux in black.

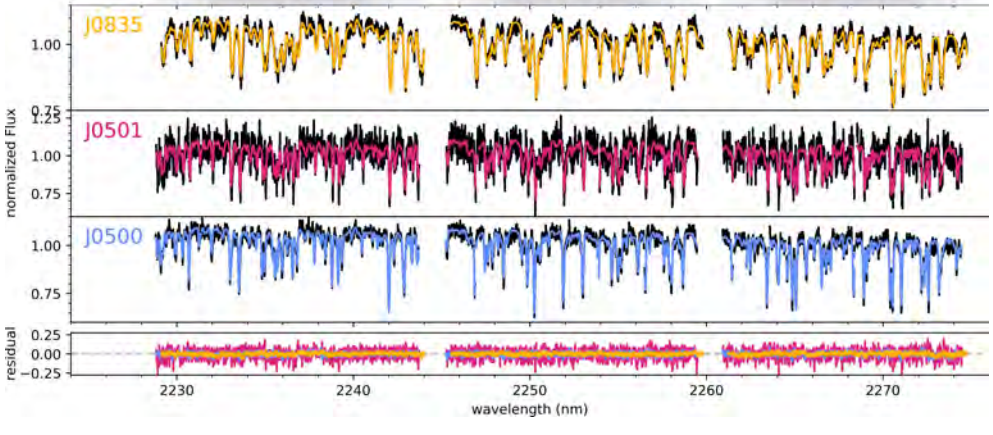


Figure 2.14: Best-fitting models of 5th K2166 order (upper three panels) retrieved for J0835, J0501 and J0500 (top to bottom) plotted on top of the observational flux in black.

## 2.C Cross-correlation analysis of $^{12}$CO, $^{13}$CO, $H_2^{16}O$, $H_2^{18}O$, HF, and Ca abundances

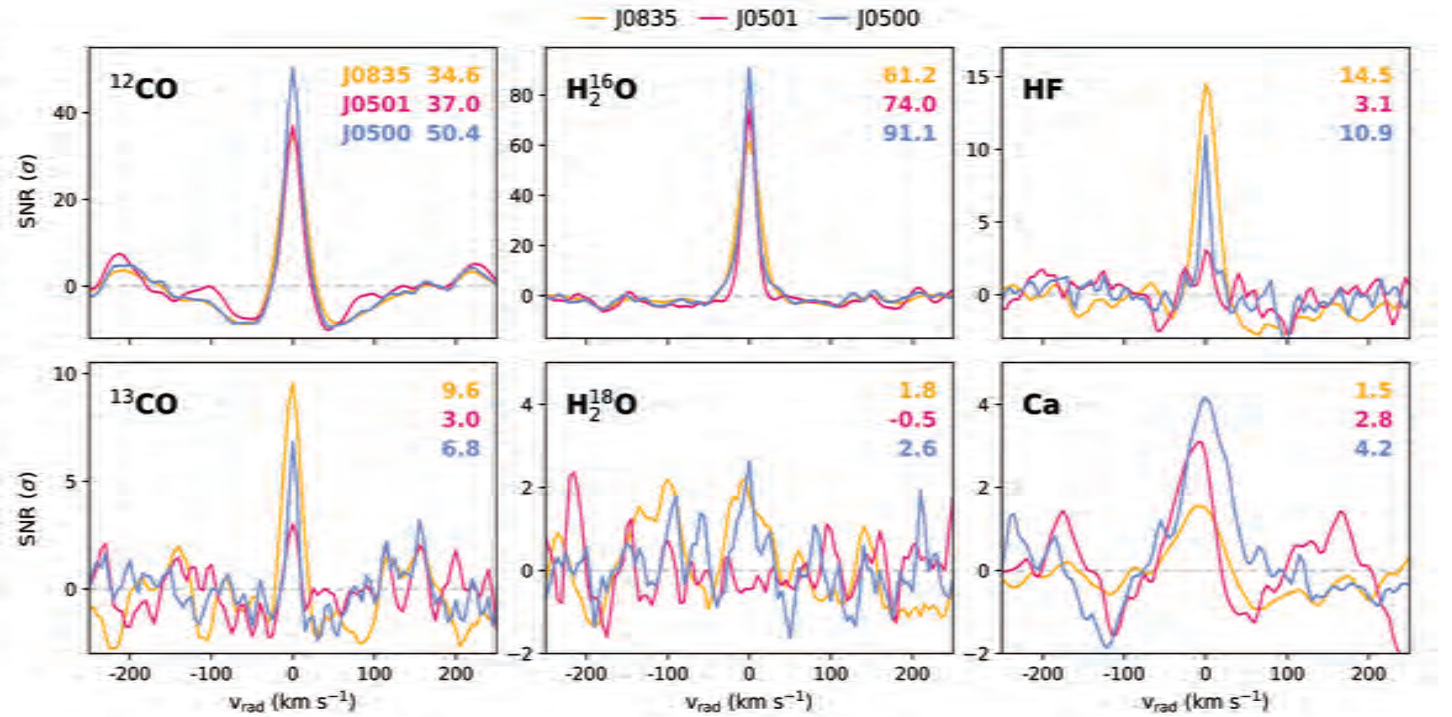


Figure 2.15: CCFs for $^{12}$CO, $^{13}$CO, $H_2^{16}O$, $H_2^{18}O$, HF, and Ca abundances. The CCFs were calculated for each order–detector pair and summed over all orders and detectors, after which they were converted to S/Ns by dividing by the standard deviation of the CCFs in the range $|v_{\rm rad}| > 100$ km s$^{-1}$. The different colours represent the different targets, J0835, J0501, and J0500. The peaks at $v_{\rm rad} = 0$ km s$^{-1}$ are a result of the cross-correlation being performed on the observed spectrum centred in its rest frame. We indicate the peak S/N values in units of $\sigma$ for each species and BD in the upper-right corner.

# Part II

# Observing the Earth as an exoplanet using spectropolarimetry

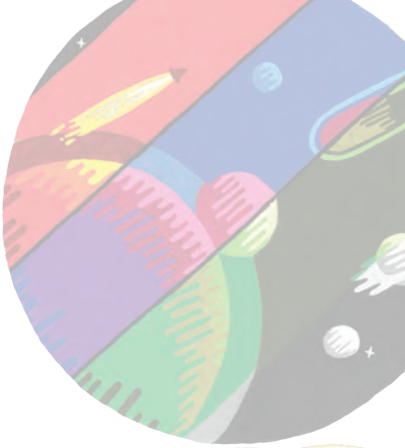

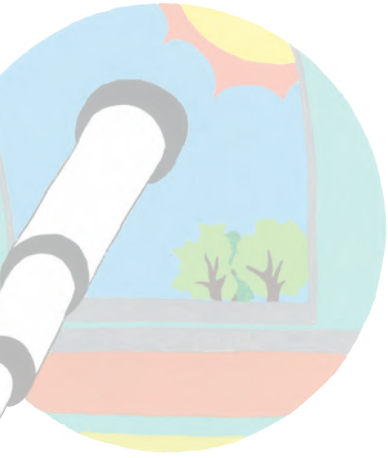

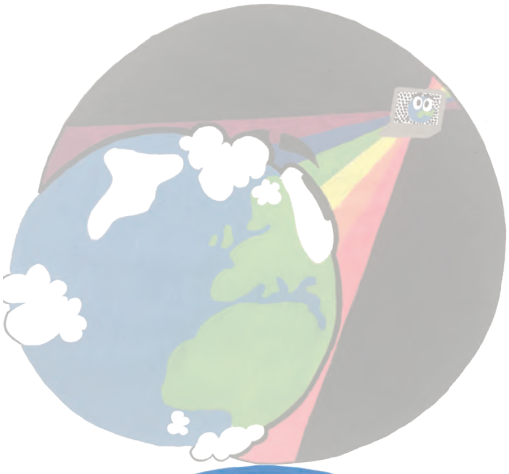

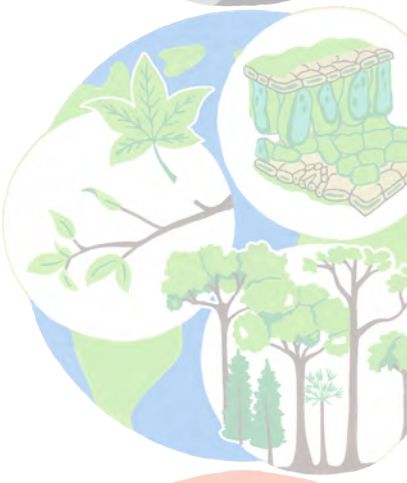


ANGRY
PHOTONS


THE
BEETLES

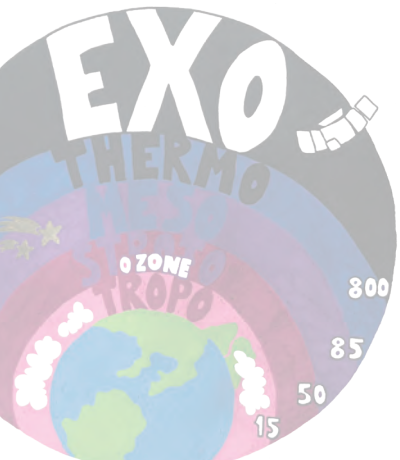
EXO
THERMO
OZONE
800
85
50
15



# 3 | Spectropolarimetric measurements of life from a hot-air balloon

Adapted from

**Spectropolarimetry of life:**
**Airborne measurements from a hot-air balloon**

W. Mulder, C. H. L. Patty, S. Spadaccia, A. Pommerol, B. O. Demory, C. U. Keller, J. G. Kühn, F. Snik, D. M. Stam

*Light in Nature IX,*
*Proceedings of the SPIE, 12214, 1221404 (2022)*



Does life exist outside our Solar System? A first step towards searching for life outside our Solar System is detecting life on Earth by using remote sensing applications. One powerful and unambiguous biosignature is the circular polarisation resulting from the homochirality of biotic molecules and systems. We aim to investigate the possibility of identifying and characterising life on Earth by using airborne spectropolarimetric observations from a hot-air balloon during our field campaign in Switzerland, May 30, 2022.

In this work we present the optical-setup and the data obtained from aerial circular spectropolarimetric measurements of farmland, forests, lakes and urban sites. We make use of the well-calibrated FlyPol instrument that measures the fractional circular polarisation (V/I) of light with a sensitivity of $< 10^{-4}$. The instrument operates in the visible spectrum, ranging from 400 to 900 nm. We demonstrate the possibility to distinguish biotic from abiotic features using circular polarisation spectra and additional broadband linear polarisation information. We review the performance of our optical-setup and discuss potential improvements. This sets the requirements on how to perform future airborne spectropolarimetric measurements of the Earth's surface features from several elevations.

## 3.1 Introduction

The remote-sensing of the Earth gives us indispensable information for our preparations to search for extraterrestrial life. Well-known examples of biosignatures that can be identified in the reflected sunlight are atmospheric constituents such as $O_2$ and spectral signatures of vegetation, such as the green bump and the red edge (see Seager et al., 2005, for a detailed description of the red edge). In addition, spectropolarimetry proves itself to be a robust remote-sensing tool. Complementary to the reflectance, it carries additional and unique information, such as surface roughness or particle size of the scatterers, which helps us to look for and characterise bio-signatures. Spectropolarimetry also provides unique biosignatures itself, such as the linear polarisation resulting from the O2-A band (Stam et al., 1999; Fauchez et al., 2017) and from vegetation (Vanderbilt et al., 1985, 1991), as well as circular polarisation resulting from the homochirality of biotic systems (Patty et al., 2019; Gimenez et al., 2019).

Homochirality is what we refer to as the single handedness of chiral molecules. Terrestrial chiral molecules that are utilised by life, e.g. amino acids, sugars and the biological polymers they construct, almost always exists in either left-handed or right-handed forms, and are therefore homochiral. This is in contrast to abiotic chemistry, which produces equal amounts of these mirror forms, resulting in a racemic mixture. Circular polarisation originates from the differential absorption by homochiral molecules and macromolecular structures. As biochemical homochirality is essential for life and thought to be a universal property of life, the circular polarisation life produces constitutes an unambiguous bio-signature (Patty et al., 2018a). Therefore, circular polarisation promises to be a powerful tool for the remote-sensing of biotic matter on Earth (Wolstencroft et al., 2004; Patty et al., 2017, 2019; Patty et al., 2021) and beyond (Sparks et al., 2005; Patty et al., 2018a).

In general, direct light emitted by a solar type star is virtually unpolarised when integrated across its stellar disk (Kemp et al., 1987). Since linear polarisation is produced by interaction of light with surfaces and particles, whenever Sunlight interacts with the Earth's atmosphere or surface, it usually becomes (partly) linearly polarised. As such, we do find an abundance of polarised light by looking at the Earth's atmosphere or surface. Various of these polarising scattering mechanisms, like Rayleigh scattering and reflections at air-water interfaces, are well understood (Cronin & Marshall, 2011). Despite all this knowledge, the interpretation of remotely sensed linear polarisation data of the real world is challenging as it involves e.g. depolarisation effects, varying atmospheric aerosol concentrations and a diversity of (cloud)particle phases, shapes, and orientations.

Circularly polarised light is much more scarce in nature. It can be produced through multiple scattering processes. Single scattering processed usually generate linearly polarised light, after which a second scattering event with atmospheric aerosols can produce circularly polarised light. We refer to Gassó & Knobelspiesse (2022) for an elaborate summary of circular polarisation due to atmospheric aerosols. In addition to multiple scattering processes, circularly polarised light can be produced by the homochirality of biotic systems (Patty et al., 2019; Patty et al., 2021).

The development of theoretical scattering models including both linear and circular polarisation is essential to understand all information coming from remotely sensed spec-

tropolarimetric data. There exist various extensive spectropolarimetric models of Earth-like (exo)planets featuring realistic atmosphere profiles (Stam, 2008) realistic cloud parameters (Groot et al., 2020), wind-ruffled oceans with sea foam and shadows of the waves (Trees & Stam, 2022) and multiple surface reflection scattering matrices based on bidirectional reflectance functions and characteristic (wavelength-dependent) surface albedos (Stam, 2008). For the latter, surface albedos for many different natural and man-made materials are provided by libraries such as the ASTER (Baldridge et al., 2009) and the ECOSTRESS spectral library (Meerdink et al., 2019).

Surface albedos can be used for surface identification. For example, the spectral shapes of vegetation features can be easily distinguished from bare soils (Liang et al., 2002), see Fig. 3.1. Albedos might vary over the year due to the change of seasons, change in vegetation characteristics or their moistness. The vegetation albedo spectra share the following characteristics: (i) absorption bands of chlorophyll around 435 – 485 nm and around 645-685 nm, (ii) a high albedo at wavelengths longer than 700 nm, which is also referred to as the red edge and (iii) the absorption of light due to intracellular liquid water causing slight dips around 0.97, 1.15, 1.45, and 1.92 μm (Hegde et al., 2015). The definition of surface albedo is commonly used in the field of astronomy and climate research. For simplicity, we will refer to the surface albedo as the (surface) reflectance.

Even though there has been an extensive advancement of the models over the years, there is still room for improvement. The surface models derived from scattering matrices based on the surface reflectance serve their purpose very well when considering a planetary disk-integrated signal. Unfortunately, they do not include circular polarisation signals induced by vegetation features. In general, and especially in nature, circular polarisation signals are very faint compared to those of linear polarisation: the difference can easily be three orders of magnitude. However, being a powerful tool for the remote-sensing of biotic matter, we do want to investigate the possibility of adding circular polarisation to existing surface models.

Remote-sensing of (circularly) polarised biosignatures has received a lot of interest in recent years (Patty et al., 2019; Patty et al., 2021; Snik et al., 2019; Sparks et al., 2020). Data acquired through remote-sensing offers crucial information for preparation for the design and development of the next generation of space-based spectropolarimeters. We follow up upon the results of Patty et al. (2021). They used a helicopter to perform airborne measurements. In this work, we are using a stable and cheaper airborne platform: a hot-air balloon. One of the biggest advantages of a hot-air balloon is that our proximity to our instrument during the flight allows us make on the fly adjustments to the optical-setup. We measure the light that is reflected by the surface from the moving balloon basket. Hence, a single measurement is limited to a single illumination angle, viewing angle and elevation. Therefore, our main focus lies with measuring the circular polarisation spectra from landscapes and their use in surface identification. In addition to circular polarisation, we continuously record four individual linear polarisation states using an ordinary polarisation camera. We investigate the contribution and practicality of using a polarisation camera for future airborne field campaigns.

This chapter has the following structure. In Section 3.2, we describe the basics of polarimetry and the concept of the normalised difference vegetation index to distinguish between different surface types. In Section 3.3, we describe our instrumental set-up that was designed to measure the fractional circular polarised reflection of the Earth from a balloon.

In Section 3.4, we summarise the main results from the airborne measurements. At the end, we finalise this chapter with our conclusions and discussion in Section 3.5.

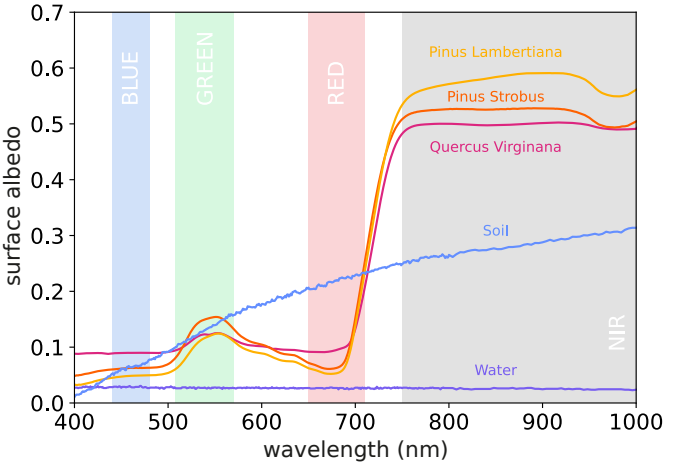


Figure 3.1: The wavelength dependent surface albedos of 3 different types of trees, (i) Quercus Virginana, (ii) Pinus Strobus, and (iii) Pinus Lambertiana, and soil and water. The data for the five albedos originate from the ECOSTRESS Spectral Library (Meerdink et al., 2019).

## 3.2 Methods

### 3.2.1 Polarisation

Polarisation is generally described with a Stokes vector $\mathbf{S} = (\mathtt{I}, \mathtt{Q}, \mathtt{U}, \mathtt{V})$, where $\mathtt{I}$ is the total intensity, $\mathtt{Q}$ and $\mathtt{U}$ are the linearly polarised intensities and $\mathtt{V}$ the circularly polarised intensity. The complete polarisation states are described in terms of the normalised Stokes parameters $\mathtt{Q/I}$, $\mathtt{U/I}$ and $\mathtt{V/I}$ (each ranging from -1 to 1), where $\mathtt{Q/I}$ denotes the difference between linearly polarised intensities normal and parallel to the plane of scattering, $\mathtt{U/I}$ denotes the difference between ±45° to the plane of scattering, and $\mathtt{V/I}$ denotes the difference between right-handed and left-handed circularly polarised light.

The linear Stokes parameters $\mathtt{Q}$ and $\mathtt{U}$ can be combined into the (dimensionless) degree of linear polarisation, $P_\mathrm{L}$. The $P_\mathrm{L}$ of a surface indicates the fraction of the reflected light that is linearly polarised. It can provide us with essential information about land surface characteristics. The angle of linear polarisation, $\chi_\mathrm{L}$, contains additional information related to surface or material properties. The degree and angle are expressed as:

$$P_\mathrm{L} = \frac{\sqrt{\mathtt{Q}^2 + \mathtt{U}^2}}{\mathtt{I}}; \quad \chi_\mathrm{L} = \frac{1}{2}\tan^{-1}\left(\frac{\mathtt{U}}{\mathtt{Q}}\right). \tag{3.1}$$

### 3.2.2 The normalised difference vegetation index

Using satellite imaging techniques, we can measure the reflected light spectra of different types of terrestrial surfaces. However, calculating an accurate widespread surface reflectance can be complex. Instead, we choose to calculate the normalised difference vegetation index (NDVI; Rouse et al., 1974) for individual measurements to distinguish between different surface types. We calculate the NDVI similar to Patty et al. (2021)

$$\mathrm{NDVI} = \frac{I_{\mathrm{NIR}} - I_{\mathrm{R}}}{I_{\mathrm{NIR}} + I_{\mathrm{R}}}, \tag{3.2}$$

where $I_{\mathrm{R}}$ is the mean of the reflectance from 650 – 710 nm and $I_{\mathrm{NIR}}$ from 750 – 780 nm.

By definition, the NDVI ranges from –1.0 to +1.0. Negative values generally correspond to water. Values approaching +1.0 typically indicate dense green vegetation: plants absorb most solar radiation between 400 and 700 nm for photosynthesis, while strongly reflecting light in the near-infrared (the 'red edge'). As a result, for healthy vegetation $I_{\mathrm{NIR}}$ is much larger than $I_{\mathrm{R}}$, giving NDVI values close to 1.0. Values around zero indicate little or no green vegetation, such as urban surfaces like roofs, roads, and/or concrete.



## 3.3 Instrumental set-up

The circular spectropolarimetric measurements presented in this work were performed using the FlyPol instrument (Patty et al., 2021). FlyPol is a spectropolarimeter based on the TreePol design (Patty et al., 2017, 2019). It uses fast temporal polarisation modulation to measure the fractionally induced circular polarisation (V/I) as a function of wavelength, from 400 to 900 nm. Its sensitivity ($< 10^{-4}$) and accuracy ($< 10^{-3}$) are sufficient to measure less than a tenth of a percent of the incident light that may become circularly polarised after reflection from biological samples, e.g. vegetation. To improve stability during fieldwork, FlyPol actively controls the temperature of its optics and electronics. Its angular field of view is approximately 1.2° (Patty et al., 2021).

All airborne measurements presented in this chapter were collected during a single flight in an Ultramagic hot-air balloon (8,500 $m^3$) equipped with a T-partition basket with a capacity of 11 passengers including the pilot. Four scientists were allowed to join the campaign, because of the relatively large basket ($3.05 \times 1.75 \times 1.20$ m) A single partition was sufficiently large enough ($\sim 2.00 \times 0.80$ m) to unfold ans secure the tripod on which FlyPol was mounted. All electronics were stored beneath the tripod, leaving enough space to manually point the instrument and perform potential small repairs.

FlyPol was oriented using a calibrated parallax-free telescope pointer (Patty et al., 2021). A GoPro HERO7 reference camera and a broadband Thorlabs polarisation-sensitive Kiralux® camera were aligned with the pointer and mounted on top of the instrument casing, see Fig. 3.2. The polarisation camera features a monochrome CMOS detector with a wire-grid polariser array consisting of a repeating pattern of four linear polarisers oriented at 0°, 45°, 90°, and 135°. One combination of these four pixels with these orientations is referred to as a super-pixel. A super-pixel calibration algorithm (Gimenez et al., 2019; Lane et al., 2022)

corrects the images for dark noise, flat-field variations, and optical imperfections in the polarisation filter array. This setup provides pointing information and additional context for the observed areas, which is useful during data analysis.

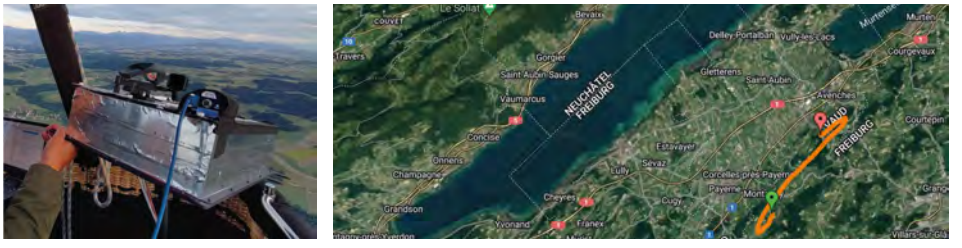


Figure 3.2: **Left panel:** Photo of the instrument set-up on top of a tripod pointing over the edge of the hot-air balloon basket, during the flight. **Right panel:** Map of the flight trajectory.

Two individual GPS trackers were used to record the flight trajectory, see Fig. 3.2. The balloon flew over the Broye district in the canton of Fribourg, Switzerland. This region lies on an elevated, relatively flat plain that is called the Swiss Plateau. The canton is predominantly rural, featuring farm sites, valleys and small forests. With an altitude of 2389 m, the Vanil Noir is the highest mountain in the canton. This is about 200 m lower than the highest altitude that we reached during our flight. Hereon we refer to the elevation of the balloon, which is the difference between measured GPS altitude in the air and the local ground-level altitude. The highest elevation was just below 2000 m. The wind determines both the flight speed and direction. At altitudes $< 1500$ m we were heading south with a ground speed of $\sim 10$ km/h, while the winds at altitudes $> 1500$ m droves us north with a ground speed of $\sim$27 km/h. The pilot could turn the orientation of the balloon, and thus the basket, in the time frame between the end of the take-off and the start of the landing.

In total, 31 measurements were obtained under clear sky conditions on May 30, 2022, from 19:45 to 20:45 CEST, just before sunset (21:20 CEST). We choose to fly during the evening hours, as hot-air balloons are only able to fly within the time-span of three hours before sunset until three hours after sunrise. In this work, we refer to a single, continuous measurement as a *scene*. During the flight, the solar zenith and azimuth angle were approximately $86° - 90°$ and $300° - 310°$, respectively. Throughout the flight, FlyPol's integration times were varied per *scene* to obtain the highest average photon count possible while preventing saturation, see Fig. 3.3. For the first and last measurements, the average photon count ($< 10000$ counts) is low compared to the later measurements. While approaching sunset, the integration time increased as the photon counts strongly decreased with time. At the same time, we adjusted the integration times of the polarisation camera, as the auto-exposure mode caused saturation of the first set of images. The polarisation camera was set to record one exposure every five seconds. Unfortunately, adjusting the integration times took at least a minute, leaving holes in the dataset. The reference camera took automatic shutter images every 30 seconds[1].

[1] 30 seconds is the minimum interval for automatic shutter imaging with the GoPro HERO7.

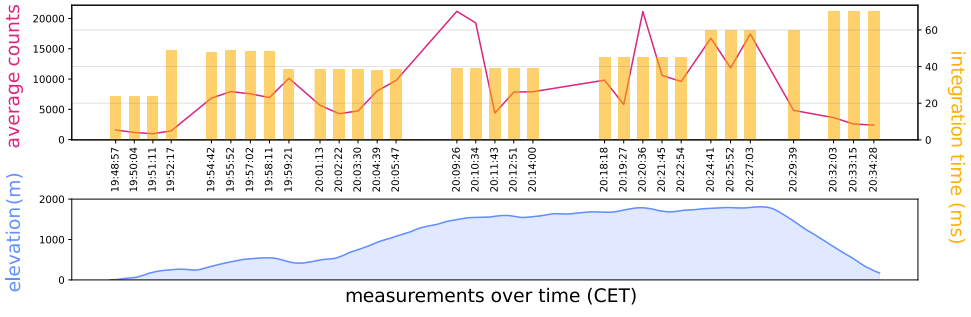


Figure 3.3: **Top panel:** The average spectrometer raw photon count over a given integration time for the individual *scenes*. **Bottom panel:** The elevation of the balloon during the flight (hence distance to the ground).



## 3.4 Results

In Fig. 3.4, we show the results of a *scene* observed during take-off, at an elevation of about 20 m. The reference photo on the left contains three transparent black/white dots that mark the central pointing of FlyPol for three sequential measurements with a 30 seconds time interval. The line connecting the dots indicates the likely intermediate pointing trajectory. The panels on the right show the qualitative reflectance and circular polarisation V/I for the trajectory per wavelength, over time. Both plots show a very clear separation between the reflected light signals of the soil and the grass after ~ 400 measurements. The soil shows a spectrally flat reflectance and a negligible circular polarisation. The grass shows a strong increase in the reflectance in the red edge, around 710 nm. The inset in the left image reveals the circular polarisation spectrum averaged over time for the soil and grass features on the right. The grass spectrum reveals a negative band with a minimum at 675 nm with a magnitude of $\mathrm{V/I}_{\mathrm{min}} = 2.0 \cdot 10^{-3}$.

In Fig. 3.5 we show the results for a *scene*, pointing at a rural area from an elevation of ~ 650 m. The yellow and pink lines in the white line trajectory match the location of the in yellow and pink highlighted qualitative reflectance data for the trajectory per wavelength, over time. We were able to identify the two different surface types using the reflectance and the NDVI. Just as for the reflectance in Fig. 3.4, there is an increase in the reflectance around 675 nm due to the red edge. The measured V/I is smaller than for the previous *scene*.

Using the NDVI values and the reference photos for the individual *scenes*, we were able to differentiate between five surface types; grass, soil, trees, urban, and water. The spectra presented in Fig. 3.6 are time averaged V/I spectra. The *scenes* that feature vegetation (grass, trees) are easily distinguishable from the others, due to their high (> 0.75) NDVI values. As explained earlier, this is due to the relative strong reflection of near-infrared light and absorption of red light by the chlorophyll molecules. The circular polarisation spectra of trees had a positive polarisation band of $\mathrm{V/I} = 1.0 \cdot 10^{-3}$ around 650 nm. The grass has a

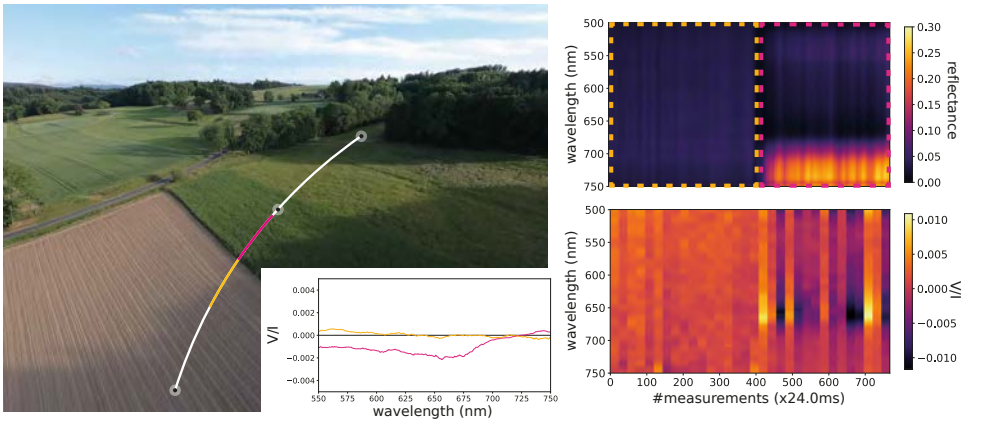


Figure 3.4: **Right panel:** Single measurement *scene* during take-off near Montagny, at 19:48:57 CEST at an elevation of ~ 20 m and with a ground speed of ~ 5 km/h. The transparent black/white dots mark the pointing of FlyPol for three sequential measurements with a 30 seconds time interval. The inset indicates the circular polarisation spectrum averaged over the individual soil and grass *scenes* in yellow and pink, respectively. **Top right panel:** Qualitative reflectance spectra for the full trajectory. **Bottom right panel:** `V/I` spectra for the full trajectory.

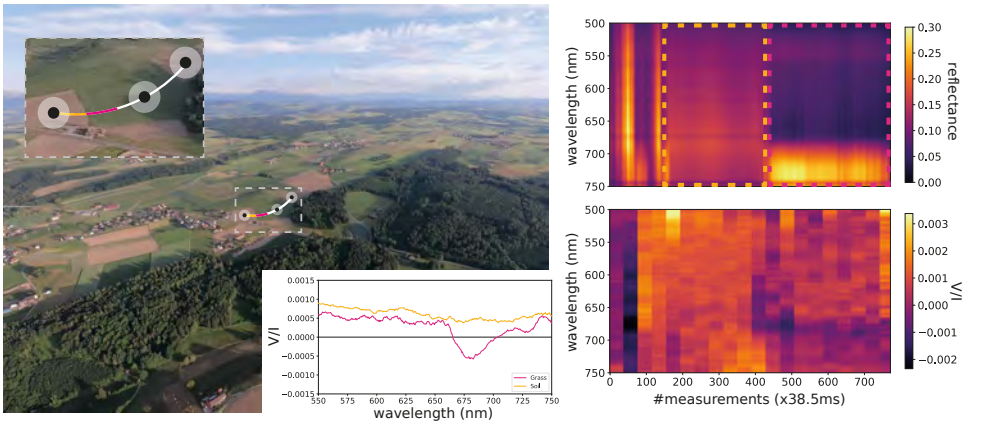


Figure 3.5: Similar to Fig. 3.4, except at 20:01:13 CEST, with an elevation of ~ 650 m and a ground speed of ~8.5 km/h.

negative band with a minimum of $\mathtt{V/I} = 2.0 \cdot 10^{-3}$ around 660 nm. Beyond ~ 675 nm, `V/I` decreases. As expected, *scenes* that feature the soil, urban and water do not show significant circular polarisation signals.

Patty et al. (2021) flew over the lake Lac des Taillères and measured a circular polarisation

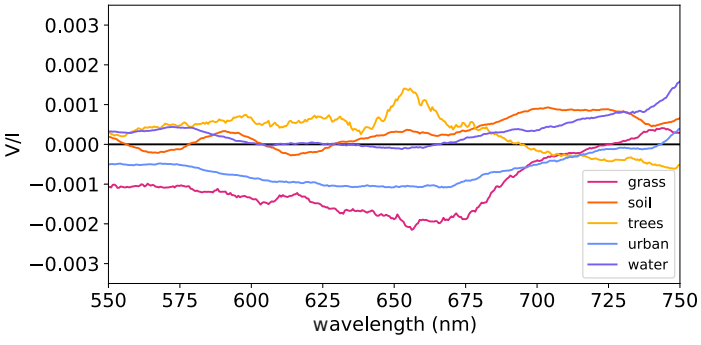


Figure 3.6: V/I spectra measured while pointing at various surfaces *scenes*: grass, soil, trees, urban, and (lake) water.



signal of $V/I = 1.1 \cdot 10^{-3}$, which indicates a possible presence of photosynthetic organisms like algae. Multiple measurements were taken while pointing towards the Murtzensee, resulting in the time-averaged V/I spectra of Fig. 3.7. From these spectra, we concluded that there was no detection of circular polarisation while pointing at the lake, which suggests an absence of biotic organisms.

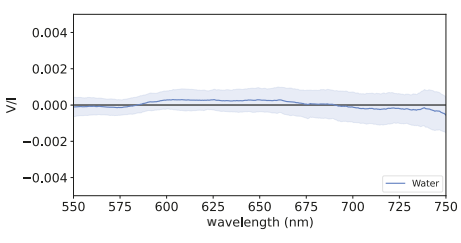


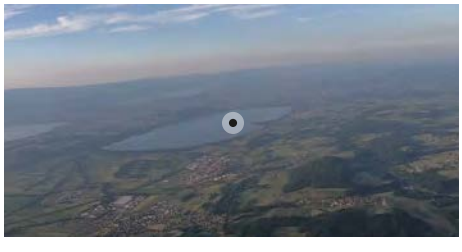

Figure 3.7: **Left panel:** Flat V/I spectra measured while pointing towards the Murtzensee. **Right panel:** Reference photo of the observed *scene* during take-off (20:12:51 CEST with ~1870 m elevation and ~25.0 km/h ground speed) flying in a NE direction.

Figures 3.8 and 3.9 illustrate the difficulty of identifying multiple distinct surface features within one *scene*. Figure 3.8 contains 15 subsequent three-second duration circular polarisation spectra originating from one observation *scene* while flying over farmland. The magnitude varies from $V/I_{min} = -9.0 \cdot 10^{-3}$ to $V/I_{max} = 2.5 \cdot 10^{-3}$ due to a large variety of observed grass and soil. This large variety makes it difficult to designate an accurate source to all the individual lines. We end up with a signal of $V/I = 2.0 \cdot 10^{-3}$, see pink line in Fig. 3.8, when averaging over all 15 spectra. The three spectra, large-, no- and small red edge, presented in Fig. 3.8 are also originating from one observation *scene*. The 'small red edge'-spectra shows one positive band of $V/I = 1.0 \cdot 10^{-3}$, where the 'large red edge'-spectra shows a similar positive band and a large negative band of $V/I = -4.2 \cdot 10^{-3}$. By looking at the trajectory, we identify the small and the large red edge as grass and trees respectively. The

circular polarisation spectrum averaged over the entire *scene* does not reveal a clear circular polarisation signature due to the relative large soil ('no red edge') coverage across the *scene*.

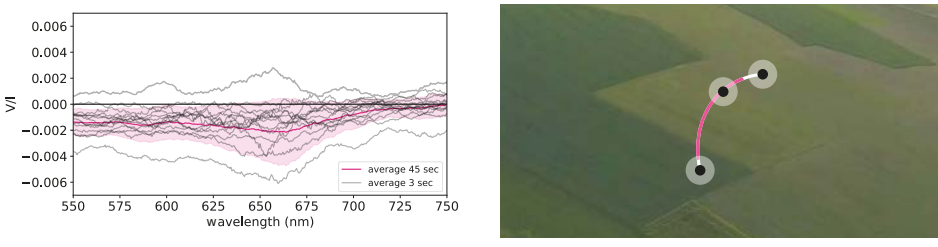


Figure 3.8: **Left panel:** 15 subsequent three-second-averaged and the total 45-second-averaged circular polarisation spectra. The *scene* captures farmland that features various types of grass and soil. **Right panel:** Reference photo of a *scene* during take-off (19:52:17 CEST at ~ 790 m elevation and ~ 7.8 km/h ground speed) flying towards Ruisseau de Pra Laurent, in the S direction while pointing at farmland. The colours on the white trajectory indicate the measurement locations of the `V/I` spectra displayed in the left figure.

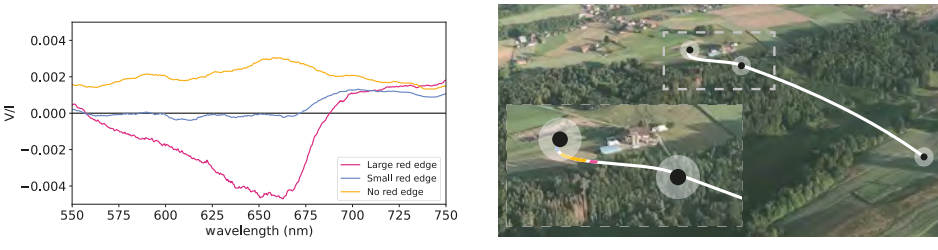


Figure 3.9: **Left panel:** Time-averaged `V/I` of a large, a small and no red edge effect, identified as trees, grass and soil respectively. **Right panel:** Reference photo of a measurement *scene* during take-off (19:54:42 p.m. CEST with ~540 m elevation and ~ 3.9 km/h ground speed) flying towards Mannens-Grandsivaz, flown in SW direction while pointing towards Marais Martin.

From top to bottom, Fig. 3.10 shows four polarisation camera images of the Murtensee and its coast, a distant mountain top, a central point of the Murtensee and an urban landscape. The images capturing the degree of linear polarisation reveal structural features of the landscapes. This allows us to e.g. distinguish a mountain top covered in ice from foggy clouds that are located just above the horizon. For the urban landscape (the middle bottom plot), we clearly distinguish the (white) buildings located in the lower half of the image from the grass fields located in the top half of the image. The angle of linear polarisation of the 'Murtzensee' and 'Glint Murtzensee' images reveal a patchy structure on the water surface that we identify as a glint phenomenon.

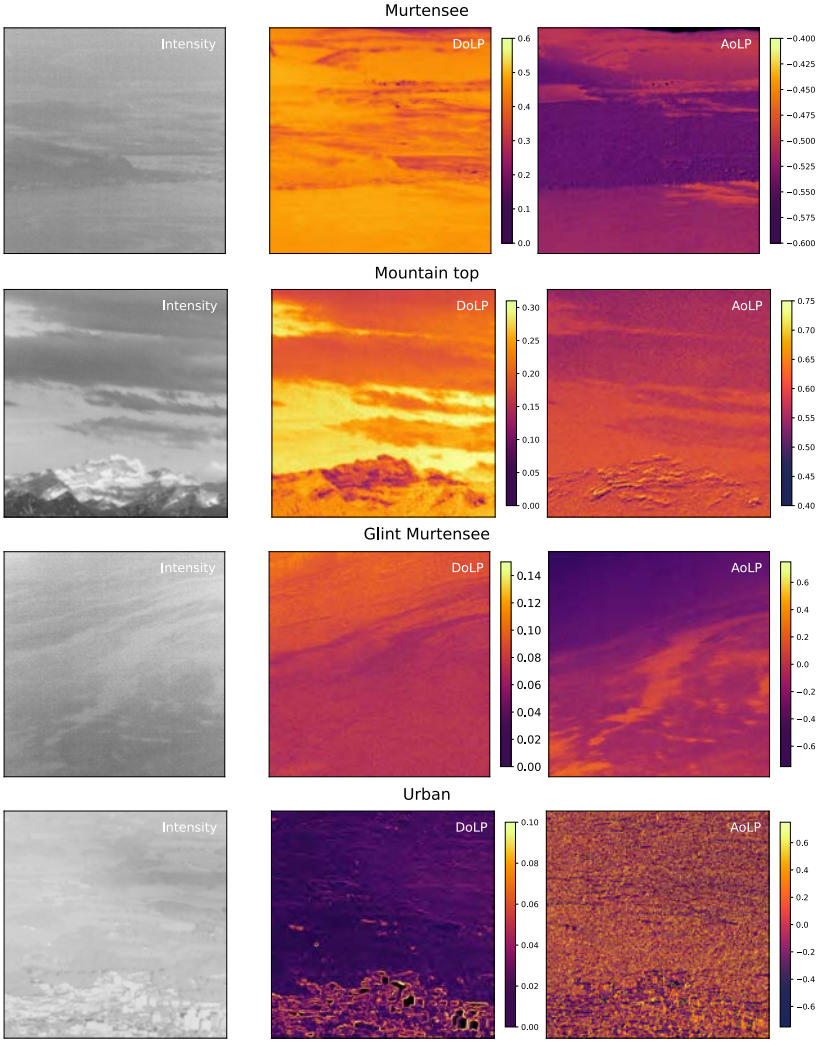


Figure 3.10: 600 × 600 pixel cut-out of polarisation camera images. **Panels top to bottom**: Murtensee and its coast, distant mountain top, the Murtensee featuring a glint and urban landscape. **Panels left to right**: Intensity, degree- and angle of linear polarisation maps, see Eq. 3.1. Note that the detector edges reveal polarisation artifacts with strong gradients, producing false signals within the super pixels on the polarisation camera.

## 3.5 Conclusion & discussion

We described an airborne optical-setup that we used to simultaneously measure circular polarisation spectra and broadband degree- and angle of linear polarisation from various *scenes* that include biotic and abiotic features. During the entire flight, reference photos were taken with a regular imaging camera. These encapsulated the area that we were pointing towards, allowing for concise identification of the sources inducing the observed the circular polarisation spectra. To our knowledge, this was the first time that a hot-air balloon was used as an observing platform for spectropolarimetric measurements of the Earth's surface. We established the maximum solar angle and integration time for which we can obtain circular polarisation spectra. This information is of great value for the next upcoming flights.

At elevations of ~ 20 m and ~ 650 m, we could distinguish between circular polarisation spectra of grass and soil. The spectral characteristics of the grass landscapes in this chapter are qualitatively similar to those presented by Patty et al. (2021). We measured a circular polarisation of grass of $\mathtt{V/I} = 2 \cdot 10^{-3}$ (~ 20 m elevation) and $\mathtt{V/I} = -5 \cdot 10^{-4}$ (~ 650 m elevation). Unlike Patty et al. (2021), we did not observe any presence of circular polarisation in sunlight reflected by lake water. A possible explanation is that there is a smaller biomass of photosynthetic organisms in the water, as this study was conducted in the early spring, while patty et al. measured during late summer. In addition, the lake was observed in the second half of the balloon flight, close to sunset. The lack of signal could thus also be due to the combination of a large viewing and solar angle.

We were able to capture how V/I varies for a subsequent observation of farmland featuring various types of grass and possibly dry, and wet soil types. The circular polarisation spectra for 15 subsequent three-second duration measurements of the farm land reveal the circular polarisation ranging between $\mathtt{V/I} = -9.0 \cdot 10^{-2}$ and $\mathtt{V/I} = 0.25 \cdot 10^{-2}$. We have two explanations for this variation: (i) the arrangement of e.g. crops in soil causes the variation as we interchange observing crops and soil, or (ii) the variation is a consequence of a diversity in health of the observed vegetation. The latter explanation is the more likely one, as we do not see clear crop(-like) fields on the reference photo. Although quantitative circular polarisation measurements on the health of the vegetation are lacking, we do know that leaves so show a reduced circular polarisation when decaying (Patty et al., 2017). Further quantitative and qualitative analysis is required to verify our hypothesis.

The circular polarisation spectra from grass feature solely a single band, often being negative. Unlike the grass spectra, those from tree canopies show vary both from shape and sign. The forest spectra, as presented in Patty et al. (2021), have both a positive and negative band that exhibit a larger variation in shape and magnitude than the grass spectra. The difference between the two is illustrated in Fig. 3.9. The spectra showing the large negative peak is identified as grass, whereas the single positive peak around 710 nm appears to be induced by tree canopies. During this field campaign, we noticed a high diversity in circular polarisation spectra for forests. It remains unclear what mechanisms could cause these variations. Measurements performed on individual (tree) leaves is a first step towards understanding the signals resulting from a canopy. As far as we know, Patty et al. (2022) is the only study that

investigated the full-Stokes spectropolarimetry of single leaves from different species and its dependency on the incidence angle of the light source. In their experiment, they varied between a phase angle of $10° - 75°$ where the phase angle is similar to the angle of the incident light. In general, all their fractional linear (`Q/I`) polarisation spectra show a peak around 680 nm due to absorption by chlorophyll and all their fractional circular (`V/I`) spectra feature a negative band around 670 nm and a positive band around 700 nm. The `Q/I` spectra reveal a strong dependence on phase angle, whereas the `V/I` spectra are relatively insensitive to changes in the phase angle. We are currently investigating the effect of changing the phase angle and viewing angle of multiple-, leaf-to-leaf reflections. With this knowledge, we will be a step closer to formulate a realistic circular polarisation surface model that can be used to accurately simulate various tree canopies and therefore also aid in the interpretation of airborne full-Stokes spectropolarimetric measurements. In addition, these realistic circular polarisation surface models would be valuable for realistic Earth-like (exo)planet models (Stam, 2008; Groot et al., 2020).



We used the obtained broadband degree- and angle of linear polarisation information for landscape identification purposes. It would be interesting to capture linear polarisation spectra together with our circular polarisation spectra of the surface *scenes*. This can be achieved by either adding a second spectropolarimeter or a spectropolarimeter that is capable of acquiring full-Stokes polarisation from a single data frame (Snik et al., 2019; Sparks et al., 2019; Keller et al., 2020; Mulder et al., 2021). Peltoniemi et al. (2015) points out that linear polarisation would predominantly provide scalar reflectance information. However, we might be able to obtain more information than surface reflectance, especially when covering multiple phase angles.

Due to the relatively fast ascend and descend, the effect of the balloon elevation on the circular polarised spectra from abiotic and biotic surfaces remains inconclusive. Further research (including numerical simulations) will help us to understand the influence of illumination, viewing angles on the circular polarisation spectra for various landscapes including high elevation biomes (e.g. tundra, moss, lichens), barren land, possible water bodies (in shallow water) ice, snow, and red algae on snow from different elevations. Hot-air balloons are only able to fly within the timespan of three hours before sunset until three hours after sunrise. We will plan our next balloon flight in the early morning. This allows us to prepare our instrument during take-off, e.g. taking flat fields, while setting up the polarisation and reference camera. Doing so, we are able to start the observations just after sunrise, which prevents long integration times and large scattering angles. In upcoming research, we would like to include measurements of grass and various tree canopies from one single observation point over the course of a full day. With this quantitative and qualitative data, we will be able to formulate a realistic circular polarisation vegetation model.

## 3.6 Acknowledgements

We thank the team of Balloons du Leman (the entire ground team, Julie, pilot Laura and Gael) personally for their enthusiasm, flexibility and help in the preparations for and during the balloon flight. We thank Remko Stuik for the airborne platform brainstorm session. This work has been carried out within the framework of the NCCR PlanetS supported by the Swiss National Science Foundation under grants 51NF40_182901 and 51NF40_205606. This work was supported by the second Planetary and Exoplanetary Science Programme (PEPSci-II) of the Netherlands Organisation for Scientific Research (NWO).

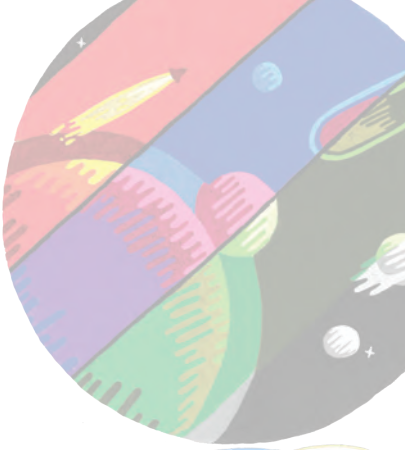

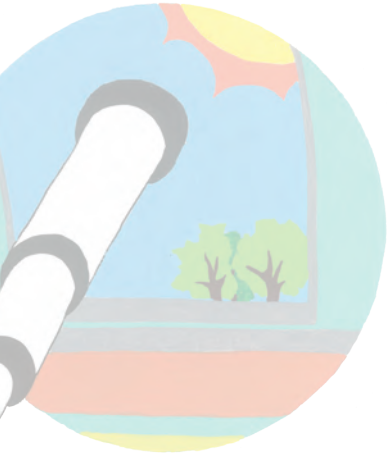

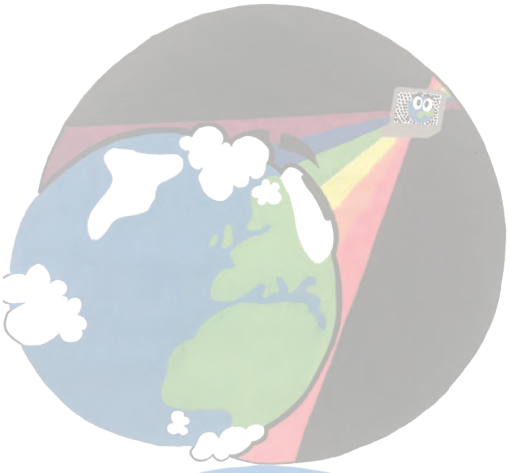

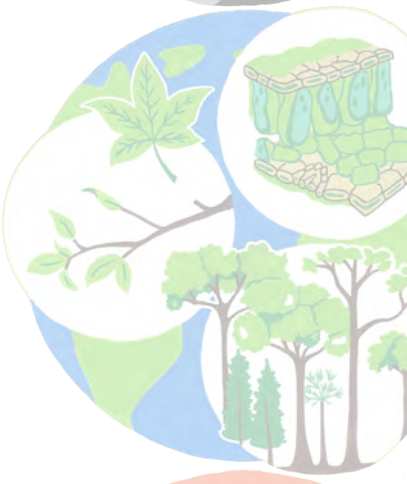


ANGRY PHOTONS


THE BEETLES

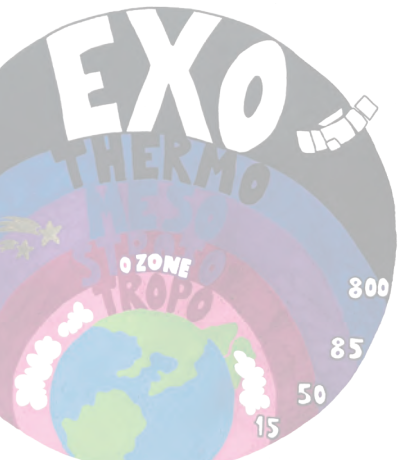
EXO
THERMO
OZONE
TROPO
800
85
50
15



# 4 Diffraction effects from spatial polarisation modulators

Adapted from

**Spatial polarisation modulators:**
**distinguishing diffraction effects from spatial polarisation modulation**

W. Mulder, D. S. Doelman, C. U. Keller, C. H. L. Patty, F. Snik

*Polarisation Science and Remote Sensing X,*
*Proceedings of the SPIE, 11833, 118330M (2021)*



Are we alone? In our quest to find life beyond Earth, we can make use of our own planet as a laboratory to develop and verify new methods and techniques to remotely detect life. Our Life Signature Detection polarimeter (LSDpol), a snapshot full-Stokes spectropolarimeter is designed to look for signals of life on Earth. This is done by sensing the linear and circular polarisation states of scattered and reflected sunlight, e.g. linear polarisation resulting from atmospheric oxygen-A band or vegetation on the Earths surface, e.g. the 'red edge' and the 'green bump', and circular polarisation resulting from the homochiral nature of biotic molecules. The optical design of LSDpol is optimised for sensing circular polarisation. To this end, LSDpol employs a spatial polarisation modulator in the entrance slit of the spectrograph, a liquid-crystal quarter-wave retarder with a fast axis orientation rotating along the slit direction. The original design combines a fixed quarter-wave plate and a polarisation grating, that together act as a dual-beam spectropolarimeter. Despite the clever design, the set-up introduces a significant linear-to-circular cross-talk, revealed by spurious polarisation modulation effects. In this work, we present numerical simulations to explain these spurious modulations with Fresnel diffraction effects. The simulations are verified with lab measurements using unpolarised and linear polarised light.

## 4.1 Introduction

Homochirality is an unambiguous bio-signature that can be detected through spectropolarimetry (Gil, 2014; Patty et al., 2017, 2019; Patty et al., 2021). Because life on Earth exhibits homochirality, its presence can be inferred from measurements of the circular polarisation of reflected sunlight. An orbiting polarimeter would therefore allow us to determine the disc-integrated circular polarisation signal of Earth, which is a relevant quantity for assessing whether similar signatures could be detected on unresolved exoplanets. The optical requirements of LSDPol are guided by the long-term goal of deploying a full-Stokes spectropolarimeter in space, which demands a compact, lightweight design that minimises or eliminates moving parts (Snik et al., 2019).

LSDPol measures the polarisation of scattered sunlight as a function of wavelength. The LSDpol prototype design prioritises accurate and sensitive polarimetry over spectroscopy and angular resolution. Therefore, the very first element is a patterned liquid crystal retarder (Snik et al., 2019; Keller et al., 2020) that modulates the polarisation of the incoming light. Sensitive polarimeters commonly measure two orthogonal polarisation states simultaneously to minimise artefacts, such as those due to variations in the spectrograph slit illumination. LSDpol combines polarimetry and spectroscopy with a fixed quarter-wave retarder and a polarisation grating to form a linear polarising beam splitter that allows for a measurement of two orthogonal polarisation states over the visible spectrum in a single snapshot (Snik et al., 2019; Keller et al., 2020).

The zeroth order of the polarisation grating re-images the illuminated slit, following the liquid crystal retarder. In the case of an incident, homogenous illumination, this image should, in theory, be homogeneous as well. However, Keller et al. (2020) found that the intensity in the zeroth order follows a sinusoidal pattern, even in the case of incoming unpolarised light. The modulation corresponds to a modulation frequency expected from incident light with a circular polarisation state, yet phase-shifted by 90°. In this chapter, we will refer to this effect as the spurious signal. A simple Mueller matrix model can investigate the consequences due to retardance or fast axis orientation deviations of the liquid crystal retarder. However, it can not reproduce possible diffraction effects. In this work, a realistic diffraction simulation is used to investigate how both Fresnel and Fraunhofer diffraction effects manifest themselves on the detector.

This chapter has the following structure. In Section 4.2 we explain the working principle and the prototype design of LSDPol and summarise the discrepancies between theory and lab measurements that were found during the initial data analysis. We investigate the source of the spurious signal using a full-diffraction simulation. The results of the simulations were verified with lab measurements. The results of the simulation and measurements will follow respectively in Section 4.3 and 4.4 after which we will discuss our main results and conclusions in Section 4.5.

## 4.2 Full-Stokes spectropolarimeter

Sparks et al. (2012) combined classical spectroscopy along one direction and polarisation as an intensity modulation in the orthogonal direction into a snapshot full-Stokes spectropolarimeter. Their approach is based on a spatially variable retarder. Sparks et al. (2019) used the concept of a quarter wave plate whose fast axis direction changes with location to demonstrate the concept of a full-stokes spectropolarimeter. This principle is described in Section 4.2.1 and Section 4.2.2.

The concept presented by Sparks et al. (2019) employs a linear polariser as the analyser, which does not allow for a snapshot measurement of the total intensity and therefore falls short of the requirements for a compact, full-Stokes, snapshot instrument. To overcome this limitation, the LSDpol incorporates a combination of an achromatic quarter-wave retarder and a polarisation grating. This combination theoretically acts as a linear polarisation beam splitter, enabling the simultaneous measurement of all Stokes parameters. As a result, the system supports true snapshot spectropolarimetry by capturing the full polarisation state, including I, in a single exposure (Snik et al., 2019). In Section 4.2.3, we discuss the main components of the LSDpol prototype in more detail.



### 4.2.1 Polarimetry

Light can be fully described by the Stokes vector $\mathbf{S} = [\mathtt{I}, \mathtt{Q}, \mathtt{U}, \mathtt{V}]^T$, consisting of the four Stokes parameters (I, Q, U, V). I is the total intensity and (Q, U, V) encode the linear and circular polarisation states of light. When referring to the Stokes parameters of the incident light entering the instrument, we explicitly denote them as ($I_0$, $Q_0$, $U_0$, $V_0$) to distinguish them from the measured or modelled quantities further downstream.

Throughout this work, we will refer to light that is either fully polarised or unpolarised. Incident unpolarised light is described by

$$\mathbf{S_0} = [I_0, Q_0, U_0, V_0] = [1, 0, 0, 0],$$

while fully polarised light can be expressed as horizontal linear (Q+), vertical linear (Q−); +45° linear (U+) and −45° linear (U−); or right- (V+) and left-handed (V−) circular polarisation. These states provide a convenient set of reference vectors for analysing the instrument response. In the special case of fully polarised input, Q+ corresponds to $\mathbf{S_0} = [1, 1, 0, 0]$, while V+ corresponds to $\mathbf{S_0} = [1, 0, 0, 1]$.

At least two intensity measurements are required to measure the polarisation state of light (Berry et al., 1977). Polarimeters can use both the principle of temporal or spatial modulation. An example of a temporal modulation is the combination of a physically rotating retarder in front of a linear polariser. The observed intensity, $I'$ is a function of the orientation of the fast axis orientation, $\theta$, and the retardance, $\delta$, of the retarder. The intensity modulation introduced by a perfect rotating retarder followed by an ideal linear polariser is given by

$$I'(\theta) = \frac{1}{2}\left(I_0 + \frac{Q_0}{2}((1+\cos\delta) + (1-\cos\delta)\cos 4\theta) + \frac{U_0}{2}(1-\cos\delta)\sin 4\theta - V_0 \sin\delta \sin 2\theta\right), \tag{4.1}$$

where $\theta$ is the retarder fast-axis orientation angle and $\delta$ its retardance.

The modulation behaviour for these basis states is shown in Fig. 4.1.

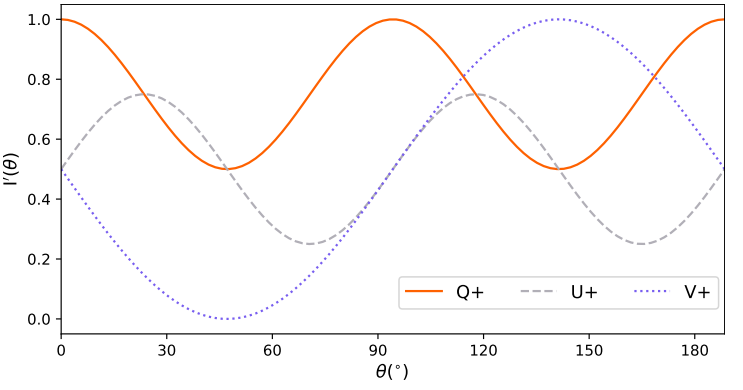


Figure 4.1: The observed modulated intensity ($I'$) as a function of the fast axis orientation $\theta$ of a retarder with retardance $\delta = \pi/2$ for fully linear (Q+, U+) or circular (V+) polarised incident light.

Equation 4.1 implies maximum circular polarisation sensitivity for an ideal quarter-wave retarder with $\delta = \pi/2$ when the fast-axis orientation angle covers $0 < \theta < \pi$. Figure 4.1 shows the resulting intensity modulation $I'(\theta)$. The orange, grey and purple lines represent the intensity modulations resulting from incident light with polarisation Q+, U+, and V+, respectively for an ideal quarter-wave retarder, $\delta = \pi/2$, when the fast-axis orientation angle covers $0° < \theta < 180°$. The set-up yields a maximum V polarisation modulation. For both Q and U the set-up can reach half the efficiency. Each each full rotation of the fast-axis orientation angle, $\theta$ corresponds to a $\theta$ modulation cycle for circular, and $2\theta$ for linear polarisation. The enhanced modulation efficiency for incident circular polarisation is desirable considering that (in the general) incident linear polarisation is much stronger than circular.

### 4.2.2 Spectroscopy

Light can be dispersed into a spectrum of wavelengths with an ordinary diffraction grating, whose resolving power is determined by the grating period - the spacing between adjacent grooves. A smaller grating period produces a larger angular separation of wavelengths. When such a grating is placed in front of an imaging detector, the dispersed wavelengths extend along the horizontal axis, forming the spectral dimension, while the vertical axis preserves the spatial structure of the incoming beam. This vertical axis will be used to record the intensity modulation that encodes the polarisation state, hence we refer to it as the polarimetric dimension.

LSDpol's optical design incorporates a polarisation grating (Oh & Escuti, 2008; Packham et al., 2010). It separates the incoming beam into a maximum of two diffraction orders ($m = -1, 0, 1$). In the case of a theoretically perfect polarisation grating, no light is directed into the zeroth order; instead, all incident light is efficiently split into the first positive and negative orders ($m = \pm 1$). These two orders correspond to opposite circular-polarisation states,

meaning that the grating simultaneously disperses the light and acts as a circular-polarisation beam splitter. The grating sends the two circular-polarised components along different paths on the detector plane, allowing their respective polarisation states to be measured independently. A linear-polarisation beam splitter can be realised by adding a quarter-wave retarder in front of the grating (Chen et al., 2019).

### 4.2.3 Spectropolarimeter principle and prototype design

To measure all Stokes parameters, LSDPol combines the principles of spectral dispersion and spatial polarisation modulation. The key element for encoding polarisation is a patterned quarter-wave retarder, which mimics a rotating quarter-wave plate by varying the fast-axis orientation angle, $\theta$, along the vertical spatial dimension. We refer to this element as the polarisation modulator or simply modulator.

When the modulator is placed upstream of the polarisation grating, it imposes a spatially dependent phase shift on the incoming light. The polarisation grating then disperses the light along the horizontal spectral dimension and separates the circular-polarisation components into the first positive and first negative diffraction orders. The detector therefore records a two-dimensional pattern in which the horizontal axis encodes wavelength, and the vertical axis encodes polarisation through the intensity modulation introduced by the modulator. The resulting intensity pattern depends on all Stokes parameters, as described in Eq. 4.1.

Figure 4.2 illustrates the simulated detector response of this system for fully linear (Q, U) and circular (V) polarised light. The false rainbow colours indicate the spectral dispersion created by the grating, while the alternating bright and dark regions originate from the patterned quarter-wave retarder, which encodes the polarisation state.

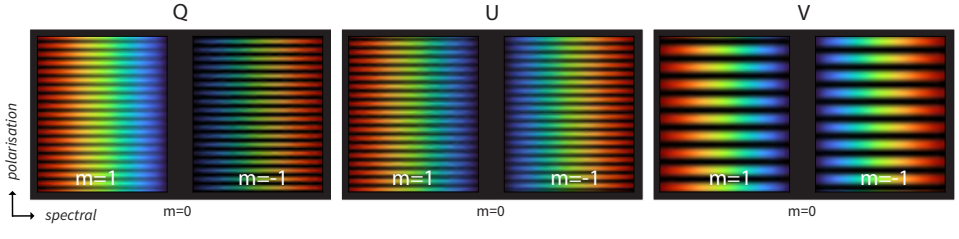


Figure 4.2: **Left to right:** Simulated intensity $I'$ (detector images) resulting from fully polarised incident light $\pm$Q, $\pm$U, $\pm$V. The vertical polarisation dimension reveals the sinusoidal observed intensity modulation. The fake colours indicate how the light spectrum would be distributed over the horizontal spectral axis of the detector and the brightness shows the intensity modulation. Note these images are created using trivial calculations of an observed intensity from Mueller matrix calculations.

The number of sinusoidal intensity variations along the vertical axis defines the *modulation frequency*. Specifically, each full rotation of the fast-axis orientation angle $\theta$ corresponds to one or two modulation cycles for the linear and circular polarisation base, respectively. During the design phase of LSDPol, the optimal modulation frequency was not known in advance. To address this, the polarisation modulator was patterned with multiple modulation

frequencies along the horizontal axis. As mentioned before, each each full rotation of the fast-axis orientation angle $\theta$ corresponds to one or two modulation cycles for the circular and linear polarisation base, respectively. A higher frequency, allows to capture more full modulation cycles on the detector, exchanging a decrease in resolution for better accuracy. During the design phase of LSDPol, the optimal modulation frequency was not known. Therefore, the polarisation modulator was patterned with multiple modulation frequencies along the horizontal axis. This design allowed different frequencies to be tested simultaneously and ensures that the most reliable polarisation signal can be extracted from the detector images.

We now break down the design concept of LSDPol to describe the role of each optic:

- The polarisation modulator is the first optical component in LSDpol. Hence, the incident polarisation state is modulated immediately upon entering the instrument. This design choice minimises the impact of downstream instrumental polarisation, as subsequent optics may introduce small amounts of cross-talk between linear and circular polarisation, or even generate spurious circular signals from unpolarised light.

- The polarisation modulator formally equivalent to a low-efficiency polarisation grating, hence acts as a weak circular beam splitter. By placing three baffles in front of the modulator, we are able to limit the field of view, which ensures that the internal field stop - used to determine the field of view - an identical field for the left- and right-handed circular beams.

- The modulator is mounted directly in front of a $0.1 \times 10$ mm entrance slit. The modulator can be shifted laterally (perpendicular to the slit), which allows the slit to select the desired modulation frequency (see Keller et al. (2020) for an elaborate description of the polarisation modulator).

- A collimating lens minimises the divergence of the beam incident on the polarisation grating in order to preserve spectral resolution.

- The modulation is analysed by a fixed quarter-wave retarder followed by a 10-degree polarisation grating. The grating alone diffracts the beam into two orders of opposite circular polarisation, but when preceded by a quarter-wave plate whose fast axis is fixed at 45° to the grating grooves, the combined system acts as a linear polarising beam splitter. In this configuration, the two diffracted orders correspond to two orthogonal linear polarisation states, each carrying the imprint of the upstream spatial modulation.

- This analyser design enables LSDPol to record two orthogonal polarisation states simultaneously in a single snapshot, ensuring that the spatial modulation introduced by the modulator can be retrieved without temporal scanning.

- Lastly, a camera lens ensures that the diffracted and modulated image of the slit is projected onto the CMOS detector.

### 4.2.4 Discrepancies between observations and theory

Combining a polarisation modulator with a polarising beam splitter is an elegant way to achieve snapshot full-Stokes spectropolarimetry. However, the current prototype suffers from several issues.

- The instrument introduces linear-to-circular crosstalk because any retardance error of the fixed quarter-wave retarder produces wavelength-dependent leakage between Stokes parameters. Deviations from the fast-axis angle only shift the absolute phase of the modulation, which is inconsequential for the demodulation, but departures from the nominal retardance directly alter the modulation efficiency and induce crosstalk. Although we attempted to characterise the true (spectrally varying) retardance of the retarder in front of the polarisation grating, these efforts have not yet converged to a reliable calibration.

- Linear-polariser calibration images made with LSDPol reveal a spurious signal in the zeroth diffraction order, and - even more problematic - what appears to be a 'fake circular polarisation' modulation in the first diffraction orders. This behaviour is consistent with the polarisation modulator acting as a weak diffractive optic, generating additional phase gradients that perturb the intended intensity modulation. Only a full vector diffraction simulation can quantify the extent to which the modulator's geometric-phase pattern unintentionally behaves as a low-efficiency grating.



The latter effect is the primary focus of this work. We investigate the impact of diffraction from the modulator using both simulations and laboratory measurements. Two configurations are analysed to decouple the influence of the quarter-wave retarder and the polarisation grating from that of the modulator.

The original LSDPol design uses a quarter-wave retarder placed immediately before a polarisation grating; this configuration is referred to as $\mathrm{LSDPol}_{\mathrm{QWR}}$. To isolate the effects of Fresnel propagation from those of imperfect retardance, a second configuration replaces the retarder with a wire-grid polariser, denoted $\mathrm{LSDPol}_{\mathrm{WGP}}$. The latter is simulated and tested, however due to the scope of this work, its results are not discussed in this chapter[1].

In both configurations the original 10-degree polarisation grating was replaced by a 5-degree polarisation grating. The smaller diffraction angle reduces the overall dispersion, trading spectral resolution for a noticeable reduction in barrel distortion, which is most prominent near the detector edges. This distortion introduced an apparent tilt in the spatial modulation, causing the retrieved modulation frequency to vary across pixel columns. This effect can be corrected once the full polarisation behaviour of the LSDPol prototype is understood.

## 4.3 Numerical simulation including Fresnel diffraction

The Mueller-matrix formalism accurately describes the polarisation modulation produced by a rotating quarter-wave retarder and analysed by a linear polariser (Sparks et al., 2019). It can also model a patterned retardance element whose fast-axis orientation varies along the vertical

[1] Chapter 5 will be an continuation.

spatial dimension (Snik et al., 2019; Keller et al., 2020). However, the incoherent Mueller model does not capture propagation-induced phase effects or diffraction, and therefore cannot reproduce changes in the amplitude, phase, or spatial frequency of the modulation that arise as the beam propagates as a function of distance - away from the polarisation modulator. Such effects could be misinterpreted as genuine polarisation signatures or as instrumental cross-talk.

Raw linear-polariser calibration images of LSDPol exhibit a spurious signal (Keller et al., 2020) in the zeroth diffraction order along the polarimetry dimension that is not predicted and could not be explained using the Mueller formalism. This behaviour suggests that the liquid-crystal spatial polarisation modulator acts as a weak diffractive element: even its low-efficiency grating behaviour can imprint additional phase gradients. Diffraction originating in the very first optical element may therefore explain both the unexpected zeroth-order structure and the 'fake circular polarisation' modulation observed in the dispersed spectra. Identifying the origin of these features requires a fully coherent simulation that includes both vector polarisation effects and Fresnel propagation.

With our diffraction simulation, we aim to model the instrument's response to polarised light and compare it directly to the predictions from the Mueller model. Our working hypothesis is near-field (Fresnel) diffraction from the modulator is responsible for the spurious structure observed in the calibration images. The results of the full-polarisation simulation are presented in Section 4.3.2.

The next step is to investigate how these artefacts evolve as a function of the separation between the modulator and the entrance slit, hereafter referred to as the propagation distance. Section 4.3.2 examines the behaviour of the zeroth-order signal as this distance is varied. Section 4.3.2 analyses how the responses in the $m = \pm 1$ diffraction orders change under the same conditions. Finally, Section 4.3.3 presents the simulated response to unpolarised light, which offers a plausible explanation for the shifted 'fake circular polarisation' signal.

Taken together, these simulations provide a clearer understanding of the additional distortions introduced by Fresnel diffraction in the LSDPol prototype, and allow us to assess whether such effects can account for both the spurious zeroth-order signal and the shifted 'fake circular polarisation' signal.

### 4.3.1 Fresnel propagation of a monochromatic wavefront

Our full diffraction simulation is based on `HCIPy` (Por et al., 2018), a Python package designed for end-to-end optical propagation and high-contrast imaging simulations.

Our model includes the full optical train element by element. The simulation traces how either (i) fully polarised or unpolarised monochromatic light propagates through (ii) the polarisation modulator, (iii) the entrance slit, (iv) the collimating lens, (v) the field stop, (vi) the fixed quarter-wave retarder, and (vii) the polarisation grating, before being re-imaged onto the detector. A schematic overview of the simulated optical layout is shown in Fig. 4.3.

HCIPy allows the initialisation of monochromatic wavefronts and allows for diffraction calculations using so-called Fresnel and Fraunhofer propagators. All the simulations in this proceeding are carried out for a wavelength range from 450 nm to 750 nm, with a 1 nm resolution. The simulation is described below:

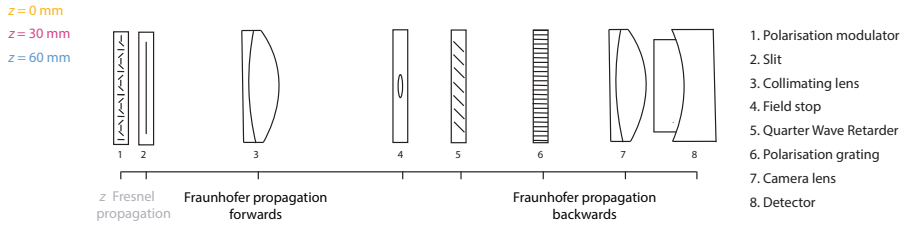


Figure 4.3: A schematic overview of the optical components included in the simulation. The numbered elements correspond to the steps described in the text on the right. The diffraction regimes used at each propagation step are indicated below the horizontal line: the Fresnel propagation describes near-field propagation across the propagation distance, while the Fraunhofer propagation (forwards) and Fraunhofer propagation (backwards) are used to model the collimating and camera lenses, respectively.



(i) **Incident input wavefront** A monochromatic, planar wavefront is generated with an amplitude profile that slightly exceeds the height of the entrance slit. The polarisation of the wavefront is defined using Stokes parameters, and may therefore either be fully polarised or unpolarised.

(ii) **Polarisation modulator** The wavefront passes through the liquid crystal polarisation modulator. The modulator is modelled as a linear retarder with a retardance of $\delta = \pi/2$. Its fast-axis variation is implemented via a phase ramp along the vertical axis, reproducing the spatially rotating fast-axis pattern.

(iii) **Fresnel propagation to the slit** After the modulator, near-field diffraction must be taken into account. We therefore apply Fresnel propagation over a distance of 3 mm (referred to as the 0 mm models in this work). The entrance slit is represented by a rectangular aperture with a 10 mm height and 0.1 mm width.

(iv) **Collimating lens** The collimating lens is simulated using a forward Fraunhofer propagator, mapping the complex electric field in the slit plane to the focal plane where the field stop resides.

(v) **Field stop** The field stop is modelled as a 4 mm-diameter circular aperture located in the focal plane, possibly truncating the spatial extent of the transmitted field.

(vi) **Quarter-wave retarder and backward propagation** A quarter-wave retarder is placed in the same focal plane. After applying the Mueller-Jones transformation, the field is propagated back to a pupil plane using a backward Fraunhofer propagator.

(vii) **Polarisation grating and detector plane** The polarisation grating is identical in structure to the initial modulator but uses a retardance of $\delta = 0.93\pi$ to reproduce leakage into the $m = 0$ order. Propagation to the detector plane yields the intensity distribution containing the $m = 0$ and $m \pm 1$ diffraction orders.

### 4.3.2 Response to a fully polarised light source

The performance of coherent simulation can be compared directly to the intensity modulation as described by Eq. 4.1, plotted in Fig. 4.2. The Mueller model represents the idealised, incoherent response obtained from sequential Mueller matrix multiplications. All simulations presented here are computed over the wavelength range 450–750 nm, sampled at 1 nm. The broadband detector intensity is obtained by incoherently summing the individual monochromatic intensities in the detector plane.

Fig. 4.4 shows the simulated detector response for three different incident wavefronts with various polarisation states. From left to right, the panels reveal the result for horizontal linear (Q+), vertical linear (U+), and right-hand circular (V+) polarisation.

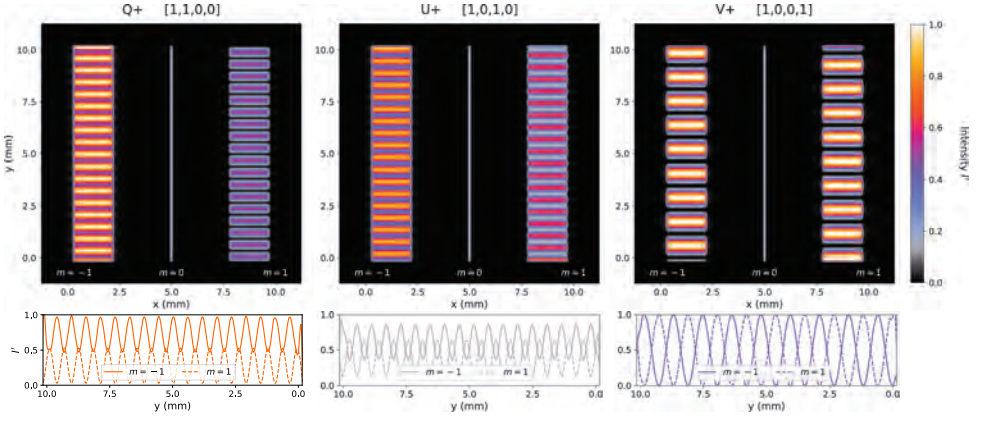


Figure 4.4: Simulated detector images obtained by propagating fully linear horizontal, linear vertical and circular polarised light through the LSDpol optical system. The propagation distance between the modulator and the entrance slit is set to 0 mm. The simulated modulation patterns reproduce the expected behaviour from the Mueller model, including the characteristic intensity imbalance for Q.

The resulting patterns reproduce the expected Mueller-theory behaviour, including the characteristic intensity imbalance between $m \pm 1$ for Q, arising from the $\frac{Q_0}{2}(1 + \cos\delta)$ term in Eq. 4.1. This agreement confirms that the coherent simulation produces the correct modulation for a fully polarised light source when the propagation distance between the polarisation modulator and slit is 0 mm.

We then increase the propagation distance between the polarisation modulator and the slit (optical elements 1 and 2 in Fig. 4.3. The results for 0 mm, 30 mm, and 60 mm for horizontal linear (Q+) are discussed below.

#### Intensity variations in ($m = 0$) due to Fresnel propagation

The intensity modulation in ($m = 0$) is selected from the simulated wavefront in the central detector column. To isolate small-scale variations, we subtract the mean along the vertical

axis, leaving only the residual intensity structure relative to a uniformly illuminated slit image. The resulting deviations for propagation distances of 0 mm, 30 mm and 60 mm are plotted in Fig. 4.6 using the corresponding colour coding.

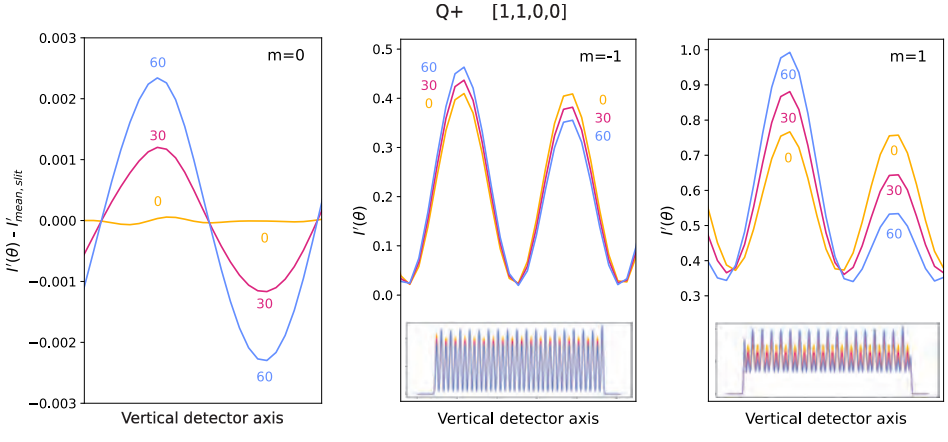


Figure 4.5: Simulated intensity modulations resulting from an incident wavefront carrying a Q+ polarisation state. **Left panel:** The yellow, pink and blue lines reveal the deviation from the mean slit intensity, hence in the $m = 0$ diffraction order. **Center and right panel:** Single $I'(\theta)$ modulation period of the $m = \pm 1$ diffraction orders. The smaller panels reveal $I'(\theta)$ along full range of the vertical detector axis for the respective orders.

For a propagation distance of 0 mm, the response closely matches the spatial modulation predicted by Eq. 4.1. The small fluctuations of order of $\pm 10^{-4}$ likely arise from diffraction at the field stop. Both the amplitude and visibility of the variation increase with propagation distance.

For the 30 mm and 60 mm case, an additional slower oscillation appears with a period approximately one quarter of the modulation period. This secondary structure is a characteristic Fresnel beating pattern that cannot be reproduced by an incoherent Mueller model. Based on these results, we conclude that the observed spurious zeroth-order signal is most likely caused by near-field diffraction from the spatially patterned polarisation modulator.

### Intensity variations in $(m \pm 1)$ due to Fresnel propagation

The polarisation grating is set to diffract the incident beam into the first orders, $m \pm 1$, with up to 96% diffraction efficiency. Figure 4.4 indicates the spatial location of diffraction orders ($m = \pm 1$). Figure 4.5 shows the corresponding slit intensities for a horizontal linear polarised Q+ input.

The left–right asymmetry visible in the two orders arises from the additional $\frac{Q_0}{2}(1 + \cos\delta)$ term in Eq. 4.1. This makes the Q± states immediately distinguishable. However, a key discrepancy emerges: at 0 mm propagation distance the intensity modulation reaches only 35%,

rather then the 50% expected from Eq. 4.1, see Fig. 4.1. With increasing propagation distance, the modulation amplitude rises, but an additional, unwanted modulation component at half the nominal frequency appears. This secondary modulation is systematically stronger in the $m = -1$ order than in $m = 1$. Both the modulation amplitude and the strength of this parasitic half-frequency term depend on: the propagation distance, the Stokes parameters of the incident light, and the orientation of the fixed quarter-wave retarder.

Since the LSDPol calibration pipeline assumes that the intensities in both orders provide a clean estimate of the incident `I`, understanding and correcting these Fresnel-induced dissimilarities is essential for accurate calibration.

### 4.3.3 Response to an unpolarised light source

To further isolate and diagnose diffraction effects, we simulated the response of LSDPol to an unpolarised source. Figure 4.6 shows the detector images for propagation distances of 30 mm and 60 mm. The 0 mm case is nearly flat and therefore omitted.

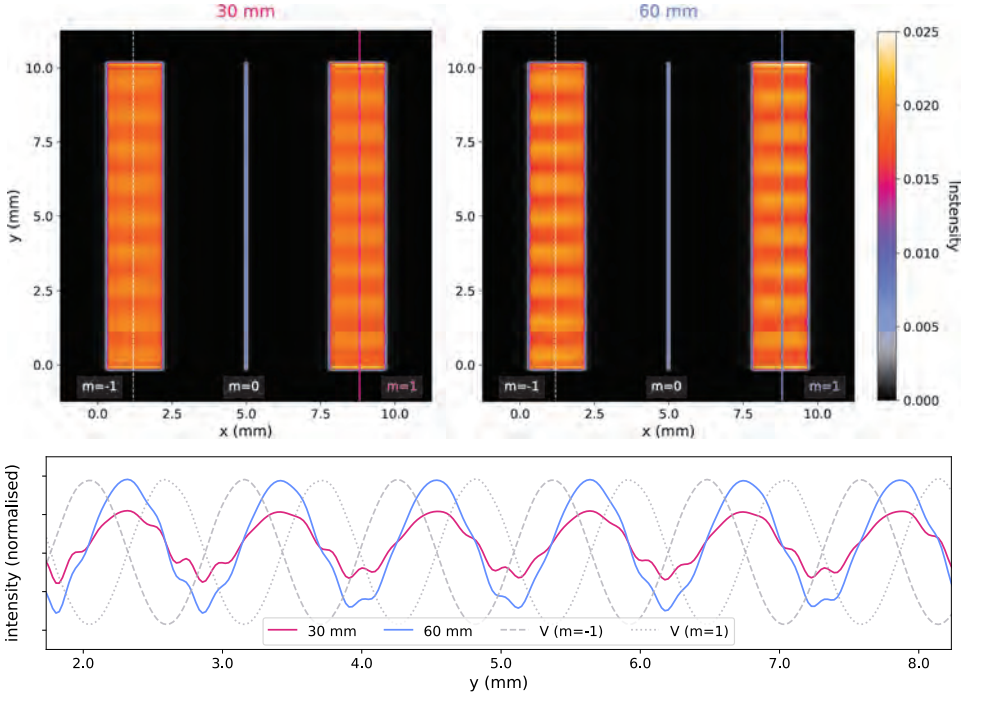


Figure 4.6: **Top panels:** Simulated detector images resulting from an uniform incident unpolarised wavefront, for a polarisation modulator-slit distance of 30 mm (**left**) and 60 mm (**right**). **Bottom panel:** Isolated $I'(\theta)$ modulation from the $m = 1$ diffraction orders. The dotted curves show the isolated $I'(\theta)$ modulation from the $m = 1$ diffraction orders, from an incident wavefront carrying a `V+` polarisation state. The unpolarised light reveals a similar modulation (frequency) to `V`, however with a phase difference of 90°.

The bottom panel compares the normalised intensity in the $m = -1$ diffraction order for both distances. For reference, the dotted curves show the expected modulation for a right-handed circular polarised V+ input in both $m = -1$ and $m = 1$. One interesting emerging feature is that the unpolarised signal displays the same modulation frequency as the intensity modulation induced by the V+ input. In addition, the modulation is shifted by 90°in phase, compared to the V+, and this phase relation occurs only once the detector is placed at a defocused (non-zero) propagation distance.

The amplitudes of the displayed curves are scaled for visual comparison; only the frequency and phase are physically meaningful here. The fact that unpolarised light mimics a shifted V+ signal demonstrates that Fresnel diffraction alone can introduce apparent circular polarisation signatures in the first diffraction orders.

## 4.4 Measurements using LSDPol prototype set-up



Our numerical simulations indicate that the discrepancies with the Mueller model are, at least in part, caused by Fresnel diffraction. To validate this interpretation, we present laboratory measurements of a linear polarised, Q+, light source and the resulting $m = 0$ and $m = \pm 1$ diffraction orders as recorded by the detector.

As for our simulations, we vary the distance between the polarisation modulator and the entrance slit. Measurements were obtained for modulator–slit separations between 0 mm to 60 mm in 5-mm±1.5 mm steps. The uncertainty is estimated by the minimum possible distance between the polarisation modulator and entrance slit and the manual adjustments on the optical bench.

A dark-field subtraction and flat-field correction is applied to each measurement to remove detector artefacts. The flat field is obtained by illuminating the detector with a diffuse, unpolarised halogen lightbulb. Having an uniform and pure unpolarised source for our flat field is essential for reliable calibration.

In the following section, we present the dark-corrected detector images for an incident Q+, with modulator–slit distances of 0 mm, 30 mm, and 60 mm. Thereafter, a more detailed description explains the behaviour of the $m = 0$ and $m = \pm 1$ diffraction orders.

### 4.4.1 Change of intensity modulation due to modulator-slit distance

Both the simulations and physical intuition predict that the intensity modulation produced by the spatial polarisation modulator should vary with propagation distance. Figure 4.7 reveals the detector response for Q+ and unpolarised incident light, for modulator–slit distances of 0 mm, 30 mm, and 60 mm.

A direct visual comparison shows that the alternating modulation predicted by the simulations is also present in the laboratory data. The effect strengthens with increasing propagation distance, and it is clearly visible in the flat fields as well. This secondary modulation has half the Q frequency and a characteristic phase shift, making it appear as a spurious V-like signal when demodulating full-Stokes measurements.

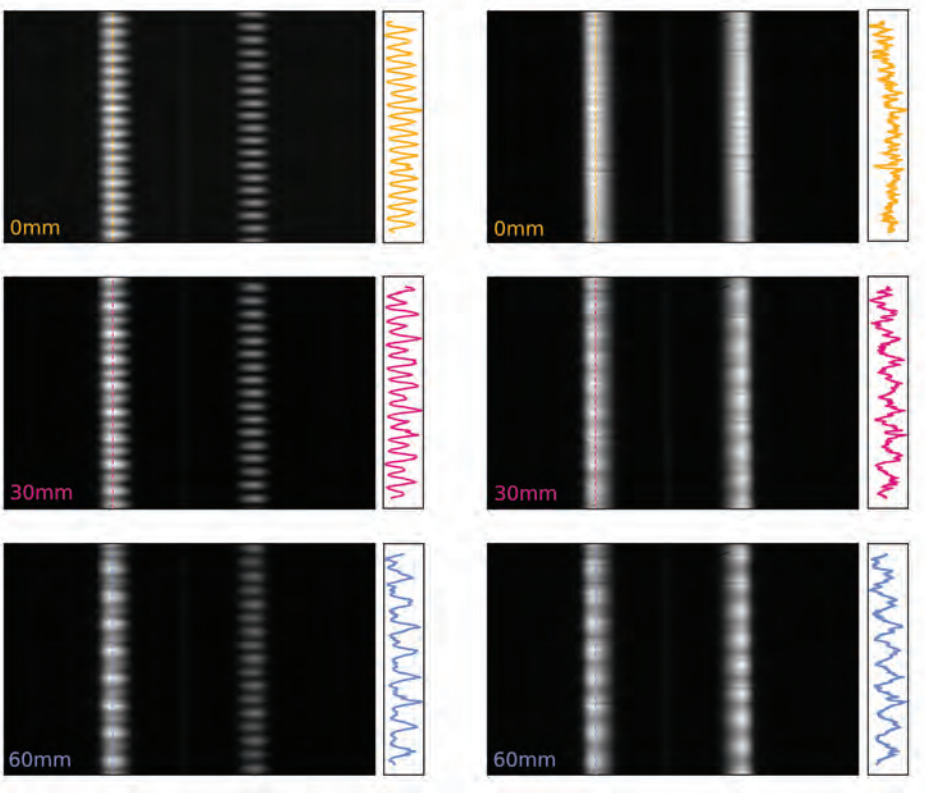


Figure 4.7: Detector images obtained with LSDPol using an light source that is linear polarised (Q, **left panels**) and unpolarised (**right panels**). The polarisation modulator-slit distance was set to 1.5 ± 2.0 mm (referred to as 0 mm), 31.5 ± 2.0 mm (referred to as 30 mm) and 61.5 ± 2.0 mm (referred to as 60 mm) (**top to bottom**). The coloured vertical lines mark the detector columns used to extract the intensity modulation shown beside each image.

### 4.4.2 Influence of increasing distance on the $m = 0$ diffraction order

The zeroth diffraction order is analysed by extracting the central 40 detector columns (see Fig. 4.7). The resulting median profiles for Q, the flat field, and the flat-calibrated Q signal are shown in Fig. 4.8.

The flat-calibrated Q signals exhibit the same modulation frequency as the dark-subtracted Q signals, reflecting the nearly uniform nature of the flat field. The modulation frequency decreases measurably with increasing distance, and at 60 mm a clear phase-shifted, V-like signature appears.

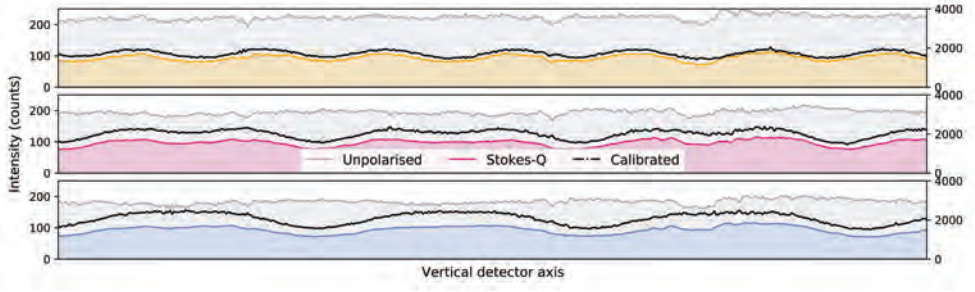


Figure 4.8: Intensity modulation in the $m = 0$ diffraction order for Q+ (coloured curves), flat/unpolarised signal (grey) and the flat-calibrated Q+ response (black dotted). The panels correspond to polarisation modulator-slit propagation distances of 0 mm, 30 mm and 60 mm.

### 4.4.3 Influence of increasing distance on the $m = \pm 1$ orders

The first diffraction orders are analysed by selecting two symmetric single-pixel detector columns on opposite sides of the image, rather than averaging over the intensity measured by multiple columns.



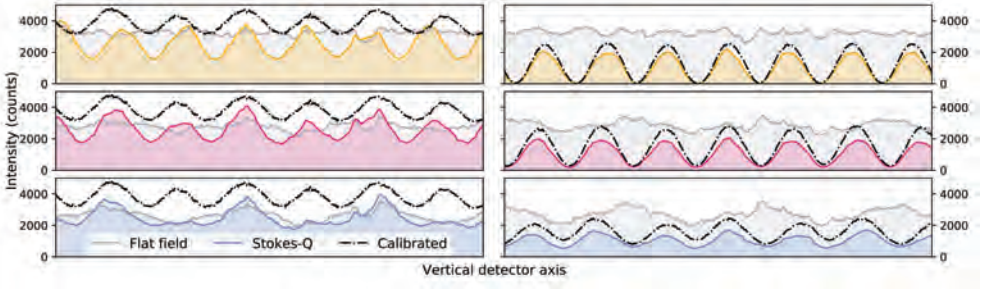


Figure 4.9: The **left** and **right panel** ($m = -1$) and right plot ($m = 1$) reveal the intensity modulation present in the first diffraction orders. The calibrated data (black dotted line, identical calibration steps as for the previous Figure) is plotted to compare the raw and calibrated Q+. The right axis indicates the intensity in counts of the calibrated signal.

As with the zeroth order, the first-order intensity modulation depends strongly on propagation distance. The $m = 1$ order is more strongly affected than the $m = -1$, showing enhanced secondary modulation. The flat field again contains a weak V-like signature with a 90°phase shift, and applying the flat correction partially removes this component, especially in the $m = -1$ order. Accurate flat-fielding therefore remains essential if the flat is to be used to correct diffraction-induced systematics.

## 4.5 Conclusions

Keller et al. (2020) found an additional spurious ghost signal and a phase-shifted spurious modulation with a frequency equal to the V modulation while performing data analysis for the LSDPol prototype. Possible explanations that were provided were circular-to-linear cross talk and diffraction effects of the spatial polarisation modulator.

Our simulations revealed that the two signals can be explained by Fresnel diffraction. The results of these simulations were validated with LSDPol measurements in the lab.

- Fresnel diffraction downstream of the polarisation modulator introduces unwanted modulation on top of the ideal polarisation signal. The magnitude of this effect depends on both the diffraction order and input Stokes vector.
- By varying the polarisation modulator-slit distance, we identify several spurious signatures:
    1. The $m = 0$ diffraction order that in theory was expected to be homogeneous acquires an additional oscillation with a $2\theta$ frequency.
    2. The $m = \pm 1$ diffraction orders show a secondary modulation component whose strength increases with distance.
    3. Unpolarised light produces a weak, V-like modulation with a 90° phase shift. This modulation is amplified when increasing polarisation modulator-slit distance.
- Laboratory measurements confirm the strong dependence of these spurious signals on the polarisation modulator-slit distance.
- Flat-field accuracy is critical: the flat field itself varies with the type of diffuser and with the diffuser's distance to the instrument. These variations affect the correction of the V-like artefact.
- A full analytical Fresnel-diffraction model will be required to explain the wavelength-dependent amplitude changes and their dependence on diffraction order and polarisation state of the incident light.

## 4.6 Acknowledgements

We want to thank Emiel Por personally for his help regarding setting up the simulations. This research made use of HCIPy (Por et al., 2018), an open-source object-oriented framework written in Python for performing end-to-end simulations of high-contrast imaging instruments.

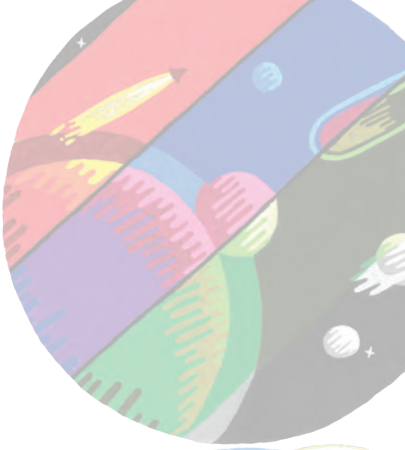

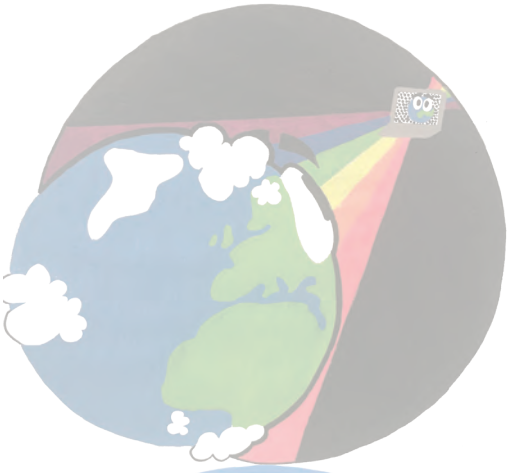

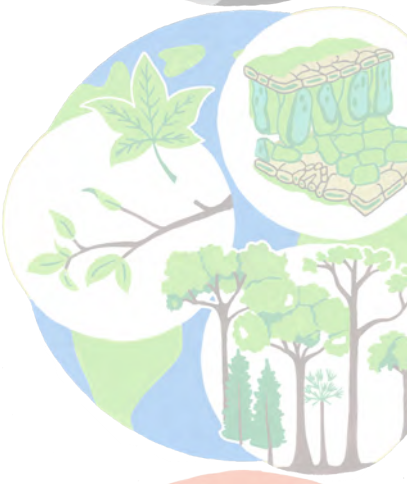


ANGRY
PHOTONS


THE
BEETLES

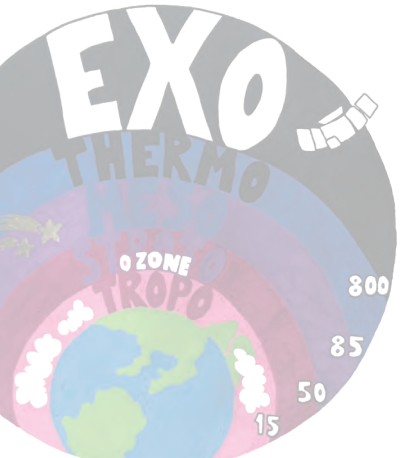
EXO
THERMO
OZONE
TROPO
800
85
50
15



# 5 | Polarisation-dependent Talbot diffraction in spatial polarisation modulators

Adapted from

**Spatial polarisation modulators:**
**exploring the polarisation-dependent Talbot effect induced by liquid crystal diffractive patterns**

W. Mulder, D. S. Doelman, and C. U. Keller

*ready for submission*

Spatial Polarisation Modulators (SPMs) offer a promising solution for full-Stokes spectropolarimetry by enabling snapshot polarisation measurements without moving parts. However, their structured phase patterns introduce diffraction effects, notably the polarisation-dependent Talbot effect, which can lead to unintended intensity modulations in laboratory measurements.

In this study, we investigate the origins of an unexpected modulation pattern observed during the calibration of an SPM-based spectropolarimeter. Through a combination of Fresnel diffraction simulations and laboratory experiments, we confirm that this additional modulation can be explained by the Talbot effect, introduced by slight defocusing of the detector. Our analysis reveals that the residual modulation exhibits an intensity pattern at half the expected modulation frequency, mimicking a false polarisation signal. Importantly, this effect is dynamic and varies with the incident polarisation state.

These findings highlight the need for precise optical alignment and calibration procedures to mitigate diffraction-induced artefacts in polarimetric instruments. Future work should focus on refining experimental setups and exploring advanced calibration techniques to improve the accuracy of SPM-based polarimetry.

## 5.1 Introduction

The next generation of ground and space-based observatories will be able to deepen our knowledge of (exo)planets. As they will be equipped with advanced instrumentation, they have the angular resolution and sensitivity to directly image Earth-size rocky exoplanets around the closest stars. The extraordinary spatial resolution that will be offered by the Extremely Large Telescopes that are currently under construction and the Habitable Worlds Observatory (Harada et al., 2024) will allow us to separate direct starlight and light reflected by smaller (rocky) exoplanets located in the habitable zone (close to the host star). By doing so, we are able to directly detect more exoplanets, and potentially characterize life-bearing exoplanets. The combination of spectroscopy and polarimetry, observed at multiple phase angles[1], forms a powerful tool to search for and detect signatures of habitability through the identification of liquid water (e.g. through the presence of rain- or icebows (e.g. Karalidi et al., 2012), and the glint of starlight reflected by an ocean (e.g. Trees & Stam, 2022; Vaughan et al., 2023)), large amounts of molecular oxygen, vegetation (e.g. through detecting the green bump and red edge) and possibly homochiral molecules that form a universal and unambiguous biomarker required for life on Earth. Observations of these terrestrial biomarkers would serve as the ultimate challenge to test new instruments and/or technologies, such as spectropolarimeters designed for the exploration of habitability on other planets.

Detecting biosignatures with spectropolarimetry will soon be within our technological capabilities. For Earth, linearly polarised signatures of atmospheric molecular oxygen, the vegetation red edge and green bump, and oceans have been detected in Earthshine[2] data (Sterzik et al., 2012; Bazzon et al., 2013; Takahashi et al., 2013; Miles-Páez et al., 2014; Sterzik et al., 2019; Takahashi, J. et al., 2021), as observed by large ground-based observatories. Despite the measurement of fractional circular polarisation in Earthshine observations (Sterzik & Bagnulo, 2009), there has not been any detection of circular polarisation induced by reflections on homochiral molecules yet. These signatures are expected to be orders of magnitude lower than any linear polarised reflections. The combination of the weak signals and the added polarisation cross-talk induced by the telescope (Bagnulo et al., 2011) hinders these potential detections. In addition, in the case of Earthshine observations, the range of phase angles we can cover while observing from the Earth is limited. Hence, placing spectropolarimeters on a spacecraft will broaden the observable range of phase angles. Various space-based spectropolarimeters have been or are being designed. The Lunar Observatory for Unresolved Polarimetry of Earth (LOUPE; Klindžić et al., 2020, 2021) mission is an example of an instrument that will provide highly time-resolved linear spectropolarimetry for all phase angles as seen from the Moon. The next step involves investigating the possibility to add the detection of homochiral molecules. To do so, we need to explore the possibility of full-Stokes spectropolarimetry from space.

Full-Stokes spectropolarimetry is a critical technique for capturing the complete polarisation state of light, described by all four Stokes parameters. Achieving this in a snapshot requires spatial modulation of the incoming polarisation. While temporal modulation using rotating elements is an alternative, it is less desirable due to the increased instrument com-

[1] The angle between the vectors from the planet towards the star and the observer.
[2] The sunlight reflected by the earth that illuminates the dark part of the moon

plexity, i.e. using moving parts in space. Moreover, the Earth's rotation and atmospheric variability introduce temporal artefacts. Capturing all Stokes parameters in one snapshot ensures accurate and efficient data acquisition, particularly in dynamic observing conditions. Various static snapshot full-Stokes spectropolarimeters concepts have been proposed (Sparks et al., 2012; Hsu et al., 2014; Pertenais et al., 2015; Youngs & Kudenov, 2017; Snik et al., 2019; Sparks et al., 2019; Bai et al., 2021; Swanson et al., 2024), all including a polarisation modulator in the form of a spatially variable retarder to eliminate the need for traditional rotating polarising optics and their associated mechanical components.

While liquid crystal (variable) retarders (LCVRs) have been widely utilised as electronically controlled polarisation modulators in space-based instrumentation (e.g. Lopez et al., 2007; Alvarez-Herrero et al., 2011; Parejo & Alvarez-Herrero, 2019), there is limited documentation of their use as fixed retarders in such applications. Most implementations focus on the dynamic control capabilities of LCVRs to modulate polarisation states. For example, the Imaging Magnetograph eXperiment (IMaX, Martínez Pillet et al., 2011) employed LCVRs for polarisation modulation in the SUNRISE balloon-borne solar observatory. Additionally, the Solar Orbiter mission's PHI and Metis instruments incorporated LCVR-based polarisation modulators to measure the Stokes vector of incoming light (Solanki et al., 2020; Liberatore et al., 2023).

Specific instances of fixed LCVRs serving as passive polarisation elements in space-based instruments are not well-documented in the available literature. However, theoretically they emerge as promising polarisation modulators for space-based instrumentation. These devices rely on liquid crystal polymers, composed of liquid crystalline molecules that can be aligned and subsequently fixed in place through polymerization. Photoalignment enables precise control over the optical axis orientation across the surface, leading to a spatially varying phase response. This phase shift, commonly known as the Pancharatnam-Berry phase (Pancharatnam, 1956; Berry, 1984), allows for the creation of spatially varying retarder plates, which we refer to as spatial phase modulators (SPMs).

SPMs belong to a broader class of geometric phase elements, which also include polarisation gratings (Nikolova & Todorov, 1984; Lajunen et al., 2005; Oh & Escuti, 2007) and geometric-phase plates. These elements are finding applications in astronomical instrumentation and polarimetry due to their unique ability to manipulate the phase and polarisation of light with high precision. Their flexibility enables the design of complex phase profiles, making them particularly valuable in applications such as beam shaping, optical vortex generation, and coronagraphy. Notable examples include Vortex Phase Plates (VVP; e.g. Marrucci et al., 2006; McEldowney et al., 2008), Holographic Aperture Masks (Doelman et al., 2018, 2021) used in high-contrast imaging instruments, both of which are integral to high-contrast imaging systems. Additionally, SPMs have proven useful in polarisation-sensitive imaging systems and spectral polarisation modulation applications (Snik et al., 2009; Rubin et al., 2021).

Thus, SPMs are versatile optical components that enable controlled wavefront manipulation through spatially varying phase patterns. Depending on their configuration, they can serve different functions, such as polarising beam splitters or spatial polarisation modulators. Despite their versatility, SPMs exhibit diffraction effects that may impact performance and

introduce crosstalk. One diffraction effect is known as the Talbot effect, an interference phenomenon. The Talbot effect results in self-imaging of periodic structures at well-defined distances behind the object when illuminated by coherent monochromatic light (Talbot, 1836). This effect has been extensively studied and finds applications in diverse optical systems (Lohmann & Thomas, 1990; Nowak et al., 1997; Yashiro et al., 2010; Wen et al., 2013). Previous studies highlight the significant role of polarisation in Talbot self-imaging (Bomzon et al., 2002; Lu et al., 2006). Bomzon et al. (2002) demonstrated how a periodic, space-variant polarised field, generated by a computer-designed subwavelength dielectric grating, undergoes Talbot self-imaging. Their theoretical framework describes the polarisation-dependent Talbot effect, which they validated through simulations of linearly polarised light inducing polarised intensity patterns in four Talbot planes by means of diffraction effects. Understanding these effects is crucial when employing SPMs for polarimetric applications, as Talbot effects could unintentionally affect incident polarisation states. Addressing these challenges requires a detailed analysis of the interplay between polarisation modulation and diffraction effects to ensure accurate polarisation modulation and/or measurements in practical applications.

In this work, we focus on the use of SPMs as spatial polarisation modulators, where structured phase patterns not only modulate the incident light's polarisation state but also introduce periodic diffraction effects. This diffraction behaviour is a direct consequence of the structured phase modulation, through which a self-replicating intensity and polarisation structure emerges at specific propagation distances. Understanding the interplay between phase modulation and diffraction is therefore crucial for accurately describing the performance of these devices. We explore the impact of the polarisation dependent Talbot effect produced by SPMs. The diffraction simulations presented in this paper provide a comprehensive visualisation of the theory underlying Pancharatnam-Berry phase. We build further upon the work of Bomzon et al. (2002) by investigating the polarisation of diffracted light for incident light carrying various polarisation states, while varying the overall retardance of the SPMs. To do so, we add a linear polarisation filter behind the SPMs to analyse the emergent polarised intensity patterns.

Section 5.2 formulates the polarisation dependent diffraction effects of a uniform (polarised) electric field transmitted through an SPM. The polarisation in the plane directly behind an ideal SPM can be calculated using both Mueller Matrix and Jones calculi. In Section 5.3 we use the Mueller formalism to provide an initial characterization of the optical setup, under the assumption that it does not suffer from diffraction effects. This result was used to verify the numerical Fresnel diffraction simulation that models the polarisation of the emerging field directly behind the SPM and propagated over various distances, as described in Section 5.4. The agreement between the fields resulting from Mueller and Jones calculus at $z = 0$ provides a validation step for the simulation, but also highlights how relying solely on Mueller calculus in the focus can lead to misinterpretation of the modulation pattern. Section 5.5 elaborates on our main lessons learned when implementing (long period) SPMs in a full-Stokes polarimeter. Lastly, we will conclude our discussion in Section 5.6.

## 5.2 Theory behind spatial phase modulators

SPMs are structured optical elements that introduce a controlled phase modulation across an incident wavefront. They can be employed in different configurations thanks to their spatially varying birefringence, such as polarising beam splitters or as modulators of the incident light's polarisation state. In this work, we focus on their use as spatial polarisation modulators where the periodically structured phase patterns are designed to modify the polarisation state of incident wavefronts along the spatial axis, $x$. Because of their periodic nature, these modulators act as a diffractive grating. As a direct result, they will give rise to polarisation-dependent Talbot self-imaging effects that become evident when a linear polarisation filter is introduced. This means that no matter the grating period, the system must account for diffraction effects whenever an SPM is used in combination with linearly polarised light or a linear polarisation filter.

The SPMs considered in this work are spatially periodic wave plates that impose a linear retardance, $\phi$, with a spatially rotating fast axis, $\Theta = \theta(x)$. When a uniform, polarised beam passes through such an SPM, the transmitted field acquires a periodic modulation in both polarisation and phase as it propagates. For short-period gratings $d \sim 10^{-5} - 10^{-6}$ m with perfect half-wave retardance, SPMs act as polarisation gratings, imposing a geometric phase that enables high diffraction efficiency with minimal losses. In this special case, the modulator induces an angular separation of the incident beam's right- and left-handed circular polarisation components into distinct diffraction orders. The applied geometric phase causes a handedness flip, as right-handed circular polarisation is converted to left-handed, and vice versa. Figure 5.1 depicts this behaviour. These gratings demonstrate exceptional diffraction efficiency (e.g. Nikolova & Todorov, 1984; Lajunen et al., 2005; Oh & Escuti, 2007; Weng et al., 2016), highlighting their potential for photonic and polarimetric applications. SPMs with long-period gratings $d \sim$ mm will primarily be used for polarisation modulation, rather than its diffractive capability. Nonetheless, implementing these long-period SPMs require careful consideration of diffraction effects such as Talbot modulation, as the grating still weakly diffracts the transmitted beam.



An SPM with its space-variant structure can be represented by a space-variant Jones matrix. We start with from a spatially uniform linear retarder represented by

$$\mathbf{J}_{\text{ret}}(\phi) = \begin{bmatrix} e^{-i\phi/2} & 0 \\ 0 & e^{i\phi/2}, \end{bmatrix}, \tag{5.1}$$

where $\phi$ is the linear retardance. A space-variant linear retarder is created by multiplication by the rotation matrix, $\mathbf{J}_{\text{rot}}(\Theta)$, where $\Theta = \theta(x)$ is the spatially varying fast-axis orientation of the retarder

$$\mathbf{J}_{\text{lin ret}}(\phi, \Theta) = \mathbf{J}_{\text{rot}}(\Theta)\mathbf{J}_{\text{ret}}(\phi)\mathbf{J}_{\text{rot}}^{-1}(\Theta), \text{ where, } \mathbf{J}_{\text{rot}}(\Theta) = \begin{bmatrix} \cos\Theta & -\sin\Theta \\ \sin\Theta & \cos\Theta \end{bmatrix} \tag{5.2}$$

For simplicity, it is convenient to convert the Jones matrices from a linear base (↑↓) to a helical base (↻↺), also referred to as circular polarisation base (Doelman et al., 2020).

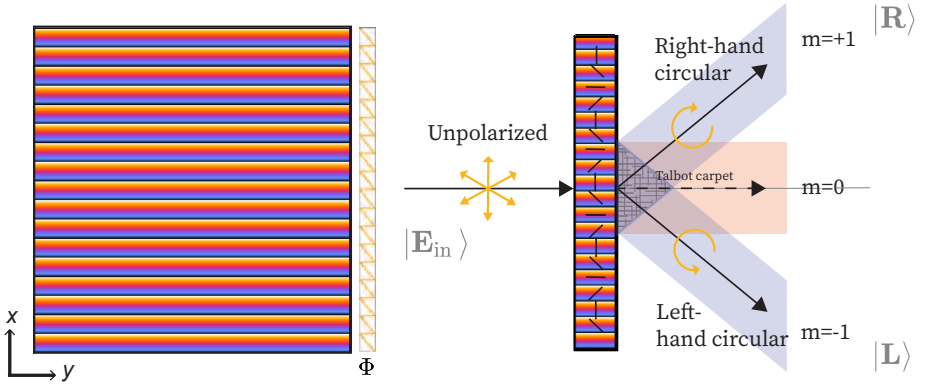


Figure 5.1: **Left panel**: Geometry of the fast-axis orientation, $\Theta = \theta(x)$. The sawtooth pattern results from the modulo $\pi$. **Right panel**: Diffraction geometry of unpolarised light incident on the SPM. An incident unpolarised plane wave (electric field) is diffracted into three orders: the primary $m = +1$, conjugate $m = -1$ and leakage $m = 0$.

Instead of describing the horizontally/vertically linear polarised components, the Jones unit vectors now describe the right/left circularly polarised components.

The vectorial field of the Jones matrix is then transformed from the linear to the helical base using $\mathbf{J}_{\cup\cup}(\Theta) = \mathbf{U}\mathbf{J}_{\uparrow\downarrow}(\Theta)\mathbf{U}^{-1}$, where $\mathbf{U}$ is the helical-base transformation matrix (Bomzon et al., 2002; Mawet et al., 2005, 2009)

$$\mathbf{U} = \frac{1}{\sqrt{2}}\begin{bmatrix} 1 & i \\ 1 & -i \end{bmatrix} \tag{5.3}$$

The result is the expression of a space-variant Jones matrix of a retarder in the helical base (Bomzon et al., 2002; Mawet et al., 2009; Steen, 2000; Doelman et al., 2020):

$$\mathbf{J}_{\cup\cup}(x,y) = \cos\left(\frac{\phi}{2}\right)\begin{bmatrix} 1 & 0 \\ 0 & 1 \end{bmatrix} - i\sin\left(\frac{\phi}{2}\right)\begin{bmatrix} 0 & \exp(-2i\Theta) \\ \exp(2i\Theta) & 0 \end{bmatrix}, \tag{5.4}$$

The local fast-axis orientation of the SPM, $\Theta$, varies spatially along $x$ while remaining constant over the spatial dimension, $y$, and is expressed as:

$$\Theta = \theta(x) = \frac{\pi x}{d} = g\pi x, \tag{5.5}$$

where $d$ is the period of the diffraction grating, and $g$ is the number of grooves per unit length, which we refer to as the *modulation frequency*.

Following the formulation of Bomzon et al. (2002); Hasman et al. (2002); Kim et al. (2015), and Escuti et al. (2016), when a uniform wavefront passes through the grating struc-

ture, the emerging field $|\mathbf{E}_{\text{out}}\rangle$ directly behind the grating (at a distance $z = 0$) can be represented as

$$|\mathbf{E}_{\text{out}}(x, z = 0)\rangle = \cos\frac{\phi}{2}\,|\mathbf{E}_{\text{in}}\rangle - i\sin\frac{\phi}{2}\left(\eta_+\,|\mathbf{R}\rangle\,e^{i2g\pi x} + \eta_-\,|\mathbf{L}\rangle\,e^{-i2g\pi x}\right), \tag{5.6}$$

$$\text{where, } |\mathbf{R}\rangle = \begin{bmatrix} 1 \\ 0 \end{bmatrix} \qquad \text{and} \qquad |\mathbf{L}\rangle = \begin{bmatrix} 0 \\ 1 \end{bmatrix}. \tag{5.7}$$

The exponential terms encapsulate both the transverse and longitudinal phase evolution of the diffracted components.
From equation (5.6) becomes clear that the emerging field $|\mathbf{E}_{\text{out}}\rangle$ is a superposition of the following three components:

i. The **leakage**, $|\mathbf{E}_{\text{in}}\rangle$, carries a polarisation state identical to the incident wavefront and does not acquire any geometric phase, propagating in a direction identical to the incident wavefront.

ii. The **primary diffraction order**, $|\mathbf{R}\rangle$, carries right-handed circular polarisation and acquires a geometric phase with a periodicity equal to twice the grating period $d = 1/g$.

iii. The **conjugate diffraction order**, $|\mathbf{L}\rangle$, carries left-handed circular polarisation. It also acquires a geometric phase with a periodicity $d$ similar to $|\mathbf{L}\rangle$, only since the phase has opposite sign, the propagation direction will be in the opposite direction to $|\mathbf{L}\rangle$, as illustrated in Figure 5.1.



The coefficients $\eta_+$ and $\eta_-$ represent the diffraction efficiency into the primary and conjugate diffraction orders, respectively, and depend on the input polarisation state. The leakage term $\eta_0$ corresponds to the fraction of the electric field that does not undergo geometric phase modulation. These are given by

$$\eta_+ = \langle\mathbf{E}_{\text{in}}|\mathbf{L}\rangle\,, \quad \eta_- = \langle\mathbf{E}_{\text{in}}|\mathbf{R}\rangle \tag{5.8}$$

The total diffraction efficiency, defined as $1/2 * (\eta_+ + \eta_-)$, is independent of the input polarisation state and depends solely on how closely the retardance matches a perfect half-wave retardance[3].

### 5.2.1 Diffraction effects beyond the SPM ($z > 0$)

When a spatially homogeneous wavefront passes through the SPM, it is split into distinct polarisation components; primarily the right- and left-circularly polarised states, $|\mathbf{R}\rangle$ and $|\mathbf{L}\rangle$. Each of these components acquires a geometric phase that varies periodically along the transverse $x$-direction, sharing a common grating period $d$. As the field propagates beyond the SPM, these periodic phase modulations give rise to Fresnel diffraction, ultimately producing a spatial recurrence of the field known as Talbot self-imaging.

[3]The diffraction efficiency of GPHs or polarisation gratings reaches up to $\eta_\pm \sim 99\%$ (Doelman et al., 2020)

The Talbot effect refers to the phenomenon where a periodic field reproduces itself at regular intervals along the propagation axis $z$. These recurrence planes, called Talbot planes, occur at integer multiples of the Talbot length, $z_T$, given by:

$$z_T = \frac{2}{g^2\lambda} = \frac{2d^2}{\lambda}. \tag{5.9}$$

This classical result is well known in diffraction theory (e.g., Goodman, 1996; Bomzon et al., 2002; Lu et al., 2006), and its extension to vectorial light fields, including polarisation effects, was demonstrated analytically by Bomzon et al. (2002).

In their treatment, Bomzon et al. (2002). showed that the emerging wavefront $|\mathbf{E}_{\text{out}}\rangle$ undergoes self-imaging due to coherent interference of its diffracted orders. Assuming three significant diffraction orders (the leakage, and the $\pm 1$ diffracted orders), and using the Fresnel approximation, the field at a propagation distance $z$ becomes:

$$\begin{aligned} |\mathbf{E}_{\text{out}}(x,z)\rangle = \Big\{ \cos\frac{\phi}{2}\,|\mathbf{E}_{\text{in}}\rangle - i\sin\frac{\phi}{2}\big[\,\sqrt{\eta_+}\,|\mathbf{L}\rangle \exp\left(-i2g\pi x - ig^2\pi\lambda z\right) \\ + \sqrt{\eta_-}\,|\mathbf{R}\rangle \exp\left(-i2g\pi x - ig^2\pi\lambda z\right)\big]\Big\} \\ \times \exp\left(\frac{i2\pi z}{\lambda}\right) \end{aligned} \tag{5.10}$$

From equations (5.6) and (5.10), it follows that the emerging wavefront at $z = z_T$ is identical (up to a global phase) to that at $z = 0$. For each integer multiple, $k$, of $z_T$, a self-image of $|\mathbf{E}_{\text{out}}\rangle$ at $z = 0$ occurs, provided the SPM is infinitely extended and the illumination remains coherent (Bomzon et al., 2002).

$$|\mathbf{E}_{\text{out}}(x, z = 0)\rangle = |\mathbf{E}_{\text{out}}(x, z = kz_T)\rangle\,, \quad \forall k \in \mathbb{N}. \tag{5.11}$$

This recurrence defines the Talbot effect in the context of vectorial fields with spatially varying polarisation. While full Talbot planes appear at integer multiples of the Talbot length, partial self-imaging can also occur at intermediate propagation distances, known as fractional Talbot images. For scalar periodic gratings, the field at $z = z_T/2$ is known to reappear with a lateral shift of $d/2$, due to phase differences between even and odd diffraction orders. In vectorial cases such as the polarisation-dependent Talbot effect, this behaviour can be more complex: the interference of diffracted polarisation components (e.g., $|R\rangle, |L\rangle$) may lead to shifted or modulated patterns at $z_T/2$, but the presence of polarisation mixing and geometric phase means that the fractional images are not simply shifted replicas. Their structure depends on the input polarisation state and the SPM design.

**Polarisation-dependent diffraction**

For spectropolarimetry applications, linear polarisation filters are used to analyse the light incident of the instrument. This motivates the need to understand diffraction effects when filtering for linear polarisation, or using incident linear polarisation, e.g. during calibration measurements. One critical component required for self-imaging is the coherency between the leakage beam and the diffracted beams. This coherency is achieved by using linearly polarised incident light, which ensures a fixed relative phase between the leakage and diffracted

components, and/or by applying a linear polarisation filter after diffraction, which aligns the polarisation states, effectively enforcing coherence between the beams when they are overlapping.

Thus, the Talbot self-imaging phenomenon is not an intrinsic property of the phase modulator alone but a function of the coherence of the polarised beams. This highlights the role of initial polarisation conditions and post-diffraction filtering in governing the self-imaging process.

In a general optical system, the degree of coherence between interfering beams affects their ability to form stable self-images. The coherency matrix, which describes the statistical properties of polarised light, shows that only beams with well-defined phase relationships will interfere constructively at periodic distances $z_T$. This property is directly related to polarisation purity in spectropolarimetric measurements, where depolarisation effects can reduce image contrast. Even when the incident light is depolarised, the placement of a linear polariser after the diffraction process enables the recovery of the self-imaging pattern by selecting parallel coherent linearly polarised waves and therefore maintain coherent phase relationships necessary for constructive interference. This insight is critical for designing optical devices that exploit polarisation-dependent diffraction effects in imaging and spectropolarimetry applications.

### 5.2.2 Definition of our spatial phase modulators



As briefly discussed earlier, SPMs featuring short-period gratings ($d \sim 10^{-5} - 10^{-6}$ m) with ideal half-wave retardance, function as polarisation gratings that impose a geometric phase that facilitates high diffraction efficiency with minimal losses. However, when the SPM retardance deviates from the half-wave condition and linear polarisation filtering is introduced, the transmitted beam undergoes diffraction. To further analyse the diffraction effects, we will simulate two different SPMs that we denote as $\text{SPM}_{\text{(i)}}$ and $\text{SPM}_{\text{(ii)}}$.

$\text{SPM}_{\text{(i)}}$ is an **ideal half-wave retarder**: This SPM has exact half-wave retardance $\phi = \pi$ and optimal diffraction efficiencies $\eta_+ = 1$, $\eta_- = 1$. According to equation (5.10), $\cos \pi/2 = 0$, resulting in no leakage term. Furthermore, the whole incident wavefront acquires a geometric phase. Therefore, it resembles an ideal polarisation grating. An incident wavefront that is right circularly polarised $|R\rangle_{\text{in}}$, will be diffracted into the $|L\rangle$ component, transforming the polarisation from right- into left-handed circular, and vice versa:

$$|\mathbf{R}_{\text{out}}\rangle = \mathbf{J}(x, y)\,|\mathbf{R}_{\text{in}}\rangle = \exp(-i2g\pi x)\,|\mathbf{L}\rangle \tag{5.12}$$

$$|\mathbf{L}_{\text{out}}\rangle = \mathbf{J}(x, y)\,|\mathbf{L}_{\text{in}}\rangle = \exp(i2g\pi x)\,|\mathbf{R}\rangle \tag{5.13}$$

Incident linearly polarised wavefronts will be equally divided between the two diffracted components, $|\mathbf{R}\rangle$ and $|\mathbf{L}\rangle$, resulting in orthogonal linearly polarised waves that will not interfere.

$SPM_{(ii)}$ is an **ideal quarter-wave retarder**: This SPM has exact quarter-wave retardance $\phi = \pi/2$ and we assume optimal diffraction efficiencies. More than half of the incident wavefront does not acquire a geometric phase and is transmitted into the leakage beam ($\cos \pi/4 = 1/\sqrt{2}$). When the incident light is polarised and maintains a well-defined phase relationship, either inherently or through post-selection via a linear polariser, the transmitted field exhibits mutual coherence between the components of the same output circularly polarised light (diffracted + leakage) that once belonged to orthogonal circularly polarisation states for the source of natural light. This coherence causes the formation of a Talbot carpet through constructive interference.

Note that we solely simulate the retardance and diffraction efficiency for the above-mentioned SPMs. In reality, both SPMs are subject to additional optical effects. For example, since a liquid crystal substrate consists of multiple layers, internal reflections may induce unwanted polarisation changes. The variation of Fresnel reflection coefficients with the local orientation of the fast and slow axes, that is due to their differing refractive indices. This results in small amplitude and phase differences between polarisation components, typically on the order of a few percent. In this context, a 100% difference would correspond to complete suppression of one component, significantly distorting the polarisation state. However, since the actual effect is minor, it is neglected here to avoid unnecessary complexity in the analysis.

## 5.3 Polarisation transformation and intensity maps via Mueller Matrix formalism

The Mueller Matrix formalism does not describe electric fields themselves: it describes an intensity and polarisation state of light using the Stokes parameters, but does not contain phase information. Consequently, it cannot capture free-space propagation, interference or coherence effects, which require knowledge of the complex field amplitudes. However, at the plane immediately following the SPMs ($z = 0$), the polarisation state of the output light is of particular interest—especially in configurations involving a linear polariser, which converts polarisation-dependent structure into observable intensity variations. In this context, the Mueller matrix formalism provides a practical and physically meaningful way to predict how various input polarisation states are transformed by the optical elements.

The Mueller matrices displayed in Figure 5.2 represent an optical system where incident light, described by a Stokes vector ($I_0, Q_0, U_0$, and $V_0$), passes through a linear retarder with a fast axis orientation $\theta_s$ and a retardance $\delta_s$, and a linear polariser with a polarisation axis orientation of 0°(hereafter referred to as analyser). The linear retarder modifies the intensity and polarisation of the incident light after which the analyser projects these components onto a common polarisation axis. Because of this, the emerging intensity (e.g. measured by a detector) is sensitive to both the local polarisation state and the underlying interference between modes.

The spatially resolved intensity maps shown in Figure 5.3 simulate the response of a detector positioned immediately behind the analyser at $z = 0$. These maps are constructed by evaluating the optical response at each position of a two-dimensional incident field $(x', y')$,

$$\begin{bmatrix} I_s \\ Q_s \\ U_s \\ V_s \end{bmatrix} = \begin{bmatrix} \frac{1}{2} & \frac{1}{2} & 0 & 0 \\ \frac{1}{2} & \frac{1}{2} & 0 & 0 \\ 0 & 0 & 0 & 0 \\ 0 & 0 & 0 & 0 \end{bmatrix} \begin{bmatrix} 1 & 0 & 0 & 0 \\ 0 & \left(\frac{1}{2} - \frac{\mathbf{c}\delta_s}{2}\right)\mathbf{c}4\theta_s + \frac{\mathbf{c}\delta_s}{2} + \frac{1}{2} & \left(\frac{1}{2} - \frac{\mathbf{c}\delta_s}{2}\right)\mathbf{s}4\theta_s & \mathbf{s}\delta_s\mathbf{s}2\theta_s \\ 0 & \left(\frac{1}{2} - \frac{\mathbf{c}\delta_s}{2}\right)\mathbf{s}4\theta_s & -\left(\frac{1}{2} - \frac{\mathbf{c}\delta_s}{2}\right)\mathbf{c}4\theta_s + \frac{\mathbf{c}\delta_s}{2} + \frac{1}{2} & -\mathbf{s}\delta_s\mathbf{c}2\theta_s \\ 0 & -\mathbf{s}\delta_s\mathbf{s}2\theta_s & \mathbf{s}\delta_s\mathbf{c}2\theta_s & \mathbf{c}\delta_s \end{bmatrix} \begin{bmatrix} I_0 \\ Q_0 \\ U_0 \\ V_0 \end{bmatrix}$$

detector — polarization analyzer (0°) — $\mathrm{SPM}_{(i)}(\delta_s, \theta_s)$ or $\mathrm{SPM}_{(ii)}(\delta_s, \theta_s)$ — lightsource

Figure 5.2: Mueller Matrices of the set-up to analyse how incident light, described by ($I_0, Q_0, U_0,$ and $V_0$), is transformed into the outgoing Stokes vector ($[I_s, Q_s, U_s, V_s]$). The letters $c$ and $s$ represent cos and sin, and the angles $\theta_s$ and $\delta_s$ represent the fast axis orientation and the retardance of the SPMs spatially varying linear retarder. $\mathrm{SPM}_{(i)}$ has a retardance of $\delta_s = \pi$ and $\mathrm{SPM}_{(ii)}$ or $\delta_s = \pi/2$. The range of $\theta_s$ depends on $g$, where $|\theta_s| < g\pi$.

which is mapped onto a detector grid $(x, y)$ of equal resolution. At every pixel position, the local polarisation state is described by an input Stokes vector $\mathbf{S}(x', y')$, which is transformed by a spatially dependent Mueller matrix $M_{\mathrm{sys}}(x', y')$ that characterises the full optical system, including the SPM and the fixed linear analyser. For each pixel, a resulting output Stokes vector $\mathbf{S}_{\mathrm{out}}(x, y) = M_{\mathrm{sys}}(x', y')\,\mathbf{S}(x', y')$ contains the full set of polarisation components, of which only the intensity component $I_s(x, y)$ is used to generate the final detector image. We refer to this detector image as an intensity map.

To simulate the spatial modulation introduced by the SPM, the Mueller matrix of the linear retarder has a fixed retardance $\delta_s$ (constant across the field) and a fast-axis orientation $\theta_s$ that varies along the horizontal direction $x$, see Figure 5.3. This models the grating-like phase modulation pattern. For each SPM type, with either half-wave $\delta_s = \pi$ or quarter-wave retardance $\delta_s = \pi/2$, we compute the system response to a set of fully polarised input states, each normalised to a total intensity of $I_0 = 1$. The resulting maps reflect how different polarisation inputs interact with the spatial modulation of the SPM and how this interaction is modified by the analyser.

The intensity maps presented in Figure 5.3 reveal distinct behaviours depending on the polarisation state of the incident wavefront and the (expected[4]) characteristics of the SPM:"

- When circularly polarised light is transmitted through $\mathrm{SPM}_{(i)}$ the handedness of the polarisation state is inverted, and a geometric phase is imparted. However, this transformation is independent of the local fast-axis orientation $\theta_s$. The intensity map does not reveal any linear polarisation modulation.

- In contrast, when the incident light is linearly polarised, the same half-wave SPM rotates the polarisation vector by an angle $2\theta_s$. Due to the continuous variation of $\theta_s$ along the horizontal axis, the resulting polarisation undergoes a full $4\pi$ rotation across

[4]When the detector is positioned immediately behind the analyser at $z = 0$, hence without any defocus, only the polarization modulation predicted by the Mueller calculus in Figure 5.2 is seen.

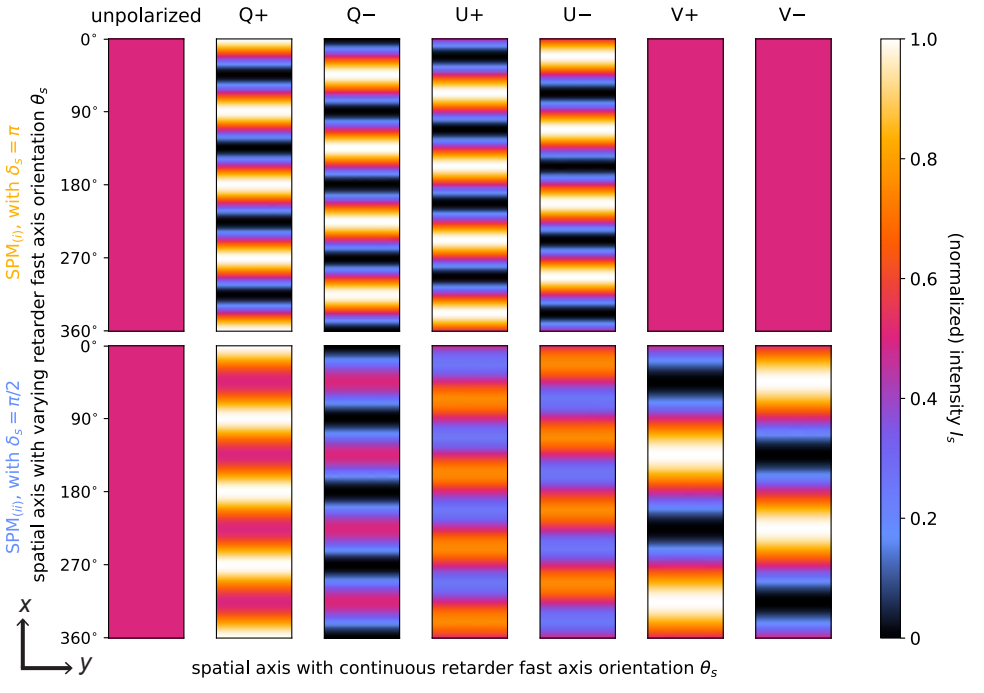


Figure 5.3: Intensity maps $I_s(x, y)$ of the simulated horizontally polarised wavefront at $z = 0$. The simulated SPMs (**top panels**: $\text{SPM}_{\text{(i)}}$, **bottom panels**: $\text{SPM}_{\text{(ii)}}$) have a modulation frequency of $g = 2$. The images from left to right reveal the response to incident unpolarised and horizontal, vertical, 45°, -45° linear and, right and left-handed circular polarised light, e.g. $\mathtt{Q}^+$ refers to $Q_0 = 1$ and $\mathtt{Q}^-$ to $Q_0 = -1$, etc. For all wavefronts, the incident intensity is set to unity $I_0 = 1$.

the field. This results in four distinct maxima and minima in the transmitted intensity. This effect is particularly visible in the intensity maps corresponding to the input Stokes states $\mathtt{Q}^+$, $\mathtt{Q}^-$, $\mathtt{U}^+$, and $\mathtt{U}^-$.

- The behaviour becomes more intricate for $\text{SPM}_{\text{(ii)}}$, which is configured as a quarter-wave plate. At specific orientations, notably $\theta_s = 45°$ and 225°, the quarter-wave plate converts circularly polarised light into linearly polarised states. The transmitted intensity then depends critically on the alignment between the resulting linear polarisation and the fixed orientation of the output analyser. For instance, right-handed circularly polarised light ($\mathtt{V}^-$) is transformed into a polarisation orthogonal to the analyser when $\theta_s = 45°$, resulting in minimal transmitted intensity. Conversely, left-handed circularly polarised light ($\mathtt{V}^+$) is converted into a polarisation state that is well aligned with the analyser, yielding high transmission.

- Finally for $\mathrm{SPM}_{(ii)}$, incident light with linearly polarised components, such as those associated with $\mathtt{Q}^{\pm}$ and $\mathtt{U}^{\pm}$, will be transformed into elliptically or circularly polarised components, depending on the local value of $\theta_s$. Together with the linear analyser, this induces spatially varying intensity patterns that reflect the polarisation sensitivity of the optical system and the analyser configuration.

When the same simulation is repeated using unpolarised light, the output becomes spatially uniform. In this case, all input polarisation components are equally affected by the optical system, and the linear polariser transmits exactly half of the total intensity. This yields a flat field with $I_s(x, y) = I_0(x', y')/2 = 1/2$. This behaviour can be understood by recognising that the Mueller calculus averages over all polarisation orientations in the unpolarised case, leading to a loss of spatial variation in the output intensity. Consequently, the spatial patterns visible for polarised inputs disappear. This confirms that the observed modulation arises purely from polarisation-dependent effects introduced by the SPM.

These results illustrate the polarisation-dependent intensity modulations introduced by the spatially varying retardance of the SPMs and offer a visual representation of how incident polarisation states are transformed. It is important to note that the simulated intensity maps at $z = 0$ do not represent intensity planes in the usual sense; rather, each pixel corresponds to the result of a Mueller matrix transformation applied to a specific input Stokes vector at a given position $(x, y)$. The resulting maps therefore mimic how a detector, positioned immediately behind the analyser, would record the spatially resolved intensity across the beam profile.

Up to this point, diffraction, and propagation effects have been neglected, as the analysis has been confined to the plane of the SPMs. Having established how the SPMs modify the local polarisation state by means of Mueller calculus, we now shift to description that allows us to explore the effects of free-space propagation. In the following section, we investigate the emergence of self-imaging patterns governed by the Talbot effect. To this end, we reconstruct spatially modulated optical wavefronts that are consistent with the local polarisation transformations induced by the SPMs. These wavefronts are then numerically propagated over a distance $z$ using the Fresnel diffraction approximation. This approach enables us to capture how interference between differently polarised components gives rise to the characteristic Talbot patterns observed in the far field.



## 5.4 Numerical Fresnel diffraction simulation

Exploring the polarisation dependent diffraction effects behind the SPMs requires a numerical Fresnel diffraction simulation. The simulation calculates how an incident flat wavefront with a given polarisation state, propagates through the SPM and a linear analyser. The intensity of the emerging wavefronts at $z = 0$ will be cross-validated with the intensity maps generated using the Mueller Matrix formalism, presented in the previous section. Thereafter, the code is used to analyse the field as it freely propagates over a distance $z > 0$ between the SPM and the analyser.

### 5.4.1 Simulation set-up

The Fresnel diffraction simulations are based on the Python `HCIPy` (Por et al., 2018) package. `HCIPy` is used to perform end-to-end simulations of astronomical high-contrast imaging instruments, including diffraction effects and coronagraphic phase plates (e.g. Por, 2020; Doelman et al., 2020; Laginja et al., 2021; Milani et al., 2024). The code examines the diffraction and free propagation of a monochromatic wavefront using the Fresnel approximation. A chromatic solution can be simulated by averaging over multiple individually propagated wavefronts, however, in this work we focus solely on monochromatic light.

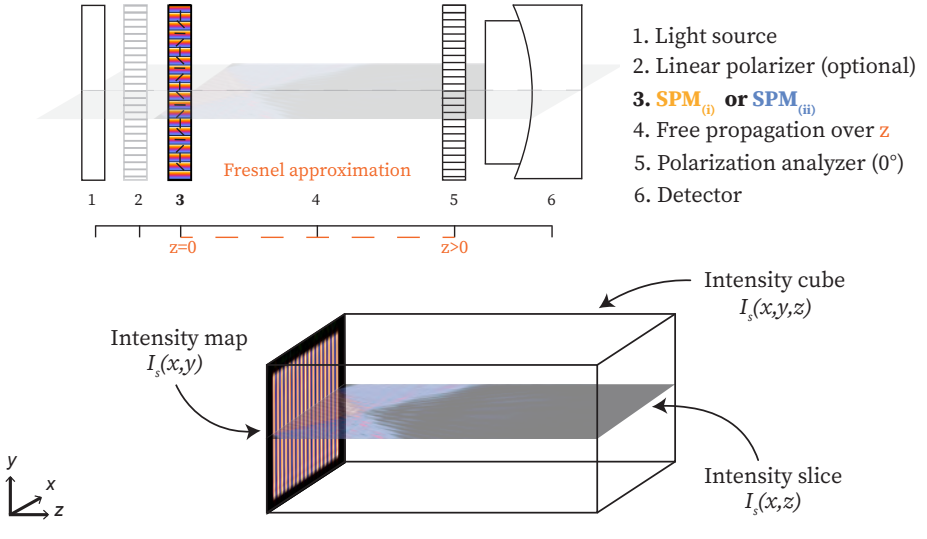


Figure 5.4: **Top panel**: A schematic overview of the simulated set-up. **Bottom panel**: Each simulation run returns an two-dimensional electric field $x_i, y_i$ of a monochromatic propagated wavefront. An intensity cube $I_s(x, y, z)$ is a stack of intensity maps $I_s(x, y)$, from which intensity slices, $I_s(x, z)$, can be retrieved.

The top panel of Figure 5.4 presents a schematic representation of the simulated set-up:

(1) **Light source** The initial wavefront is defined over a square grid in the $(x, y)$-plane, representing a spatially resolved, uniform optical field. At each grid point $(x_i, y_i)$, the local state of light is characterised by a normalised Stokes vector with an initial intensity $I_0 = 1$, zero phase, and a wavelength of 550 nm.[5] By default, the remaining Stokes parameters are set to zero, i.e, $Q_0 = U_0 = V_0 = 0$, corresponding to a spatially uniform, unpolarised source. This defines a homogeneous and coherent wavefront across the

[5]The choice of 550 nm reflects the author's experience with typical operating wavelengths in structured polarisation optics. Since the simulation is monochromatic, the precise value of the wavelength does not influence the qualitative results.

grid, suitable for analysing polarisation-dependent transformations in the subsequent optical system.[6]

(2) **Linear polariser (optional)** A rotatable linear polariser can be placed in between the light source and the SPM. By doing so, the electric field at each field point $(x_i, y_i)$ will become polarised in the direction of the polarisation axis $\theta_p$. The polariser reduces the total intensity $I_s$ by half whenever the incident light if unpolarised.

(3) **SPM$_{(i)}$ or SPM$_{(ii)}$** The SPM is a linear retarder with a retardance, $\delta_s$, and a spatially varying fast-axis orientation, $\theta_s$, along the spatial axis $x$. The type of SPM is selected by changing the retardance of the linear retarder to $\delta_s = \pi$ or $\delta_s = \pi/2$, respectively. At each position $(x_i, y_i)$, the electric field undergoes a phase shift equal to twice the local orientation angle, see equation (5.10). The modulation frequency, $g$, determines the total range of $\theta_s$. An opaque square aperture located behind the linear retarder will induce diffraction effects on the edges to mimic an optical element with a finite dimension.

(4) **Free propagation over** $z$ The wavefront propagates over the distance $z$ using the Fresnel approximation (Goodman, 1996). The number of simulations, $n_z$, is defined by the maximum propagation distance, $z_{\max}$, and a specified resolution $\Delta z$.

(5) **Polarisation analyser** At a distance $z$, each electric field point $(x_i, y_i)$ passes through a linear polariser with its polarisation axis at $\theta_a = 0°$.

(6) **Detector** The emerging field is transformed into and stored as an intensity map $I_s(x, y)$ capturing the intensity for all electric field points $x_i, y_i$ for a given propagation distance $z$. The simulations are repeated for various distances, stacked and stored as an intensity cube $I_s(x, y, z)$, from which both intensity slices, $I_s(x, z)$, and the original maps, $I_s(x, y)$ are retrieved (see Figure 5.4).



### 5.4.2 Wavefront at the focus (z=0)

To validate the propagation model, Fresnel diffraction simulations were performed at a propagation distance of $z = 0$, enabling direct comparison with the intensity maps previously obtained using the Mueller Matrix formalism. In this configuration, the resulting intensity maps should be identical to those presented in Section 5.3 since the intensity maps $I_s(x, y)$ are computed without any free-space propagation, as only a single transverse intensity plane is required. To maintain consistency with the results, the grating periods of SPM$_{(i)}$ and SPM$_{(ii)}$ are selected to correspond to a modulation frequency of $g = 1/d = 2$.

Figure 5.5 presents four intensity maps resulting from incident horizontal polarised light ($Q_+$)). The narrow panels correspond to the intensity maps calculated using the Mueller matrix formalism (see Figure 5.3), and the square intensity maps display the outcomes of the Fresnel diffraction simulations. The two methods yield identical results.

[6] In the results presented in Figure 5.5, the local polarisation state of the incident wavefront is prescribed by directly assigning the desired Stokes vector at each grid point.

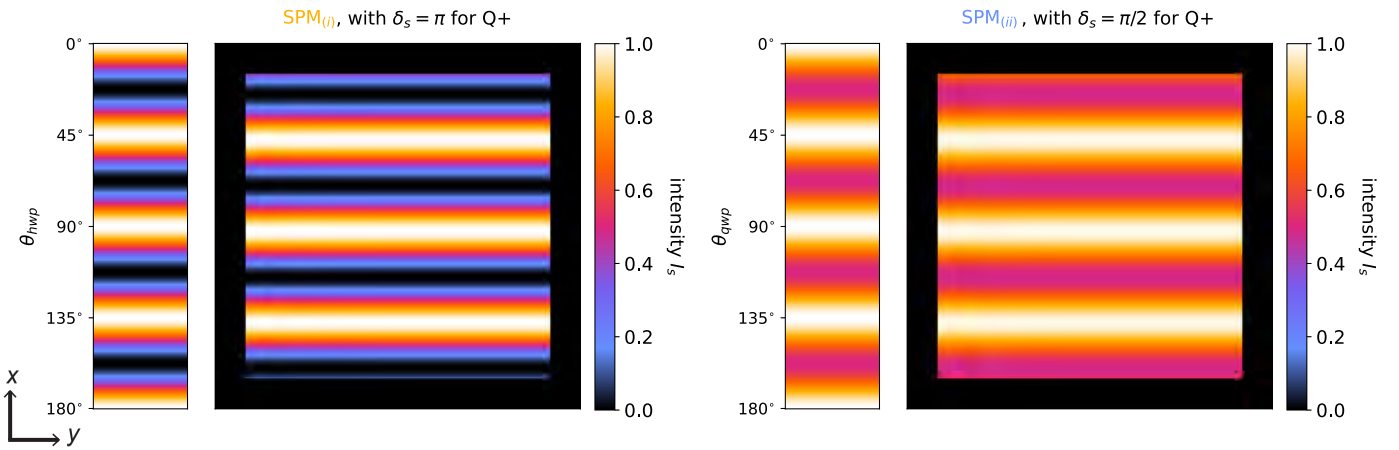


Figure 5.5: Intensity maps $I_s(x, y)$ at $z = 0$ of fields emerging from $SPM_{(i)}$ (**left panel**) or $SPM_{(ii)}$ (**right panel**) with $g = 2$. The square maps are simulated using the Fresnel diffraction code, whereas the narrow maps are generated using Mueller calculus (see Figure 5.3). The maps are identical with the exception of the black frame in the diffraction-based simulations. This frame originates from an opaque square aperture, which is included to model the hard edges of the SPM.

### 5.4.3 Wavefront propagation beyond the focus (z>0)

The propagation and diffraction effects occurring after the SPMs can be analysed by simulating the wavefronts and the associated intensity maps beyond the focal plane $z > 0$. As the wavefront propagates along the $z$ direction, each electric field point $(x_i, y_i)$ evolves independently according to Fresnel diffraction. In this regime, characteristic diffraction effects—such as Talbot self-imaging—may emerge. To be able to resolve the Talbot self-imaging, the maximum propagation distance $z_{\max}$ should be longer than one Talbot length ($z_T$) and the resolution $\Delta z$ should be at least $\Delta z = z_T/4$, to recognise the partial Talbot self-imaging.

For a grating period of $d = 0.3\,\text{mm}$ and a wavelength of $\lambda = 550\,\text{nm}$, the Talbot length is approximately $z_T \approx 0.6\,\text{m}$. This implies that by setting the $z_{\max}$ to 0.9 m, the resulting three-dimensional intensity cube $I_s(x, y, z)$ will cover 1.5 Talbot lengths. There will be one intensity cube for each unique combination of an incident polarisation state and SPM. Thus, seven distinct input polarisation states and two SPMs yield a total of 14 intensity cubes.

Figure 5.6 presents intensity slices $I_s(x, z)$ extracted from each of the 14 simulated intensity cubes $I_s(x, y, z)$. These slices correspond to a vertical cross-section through the centre of the $I_s(x, y, z)$, visualising the evolution of the diffraction patterns over a propagation distance of $1.5z_T$. The results illustrate how polarisation-dependent Fresnel diffraction develops beyond the SPMs and reveal differences in the resulting field distributions depending on the type of modulator and the incident polarisation state. Recall from Equation (5.10) that, the phase applied by the SPM has an opposite sign for opposite handedness of the incoming circular polarisation state and the SPM flips the circular polarisation state. For an SPM with a retardance value of $\phi = \delta_s = \pi$, the emerging wavefront is composed of two polarisation components, $|\mathbf{R}\rangle$ and $|\mathbf{L}\rangle$, that are diffracted in opposite directions. Any retardance that deviates from half-wave, $\phi = \delta_s \neq \pi$, will decrease the diffraction efficiency and introduces a transverse (non-diffractive) leakage component, $|\mathbf{E}_{\text{in}}\rangle$. As a direct consequence, the wavefront emerging from $\text{SPM}_{\text{(ii)}}$ will reveal more complex propagation behaviour and interference patterns than the one from $\text{SPM}_{\text{(i)}}$. The key features revealed in Figure 5.6 summarised as follows:

- For $\phi = \pi$, an incident uniform and full right or left circular polarised field undergoes a phase modification and is diffracted as a uniform wavefront into a single order with opposite handedness (see top `V+` and `V−` panels). Incident linear polarised light is equally split between the two diffracted polarisation components, $|\mathbf{R}\rangle$, $|\mathbf{L}\rangle$. The spatial varying fast axis orientation and polarisation analyser produce a polarisation dependent intensity pattern. Since $|\mathbf{R}\rangle$, $|\mathbf{L}\rangle$ carry the same geometric phase but with opposite sign, their intensity maxima and minima add up along the propagation axis $z$ producing a sinusoidal intensity pattern at $z \geq 0$, as shown for `Q+`, `Q−`, `U+`, `U−`. Unpolarised light has no preferred state of polarisation and contains on average equal amounts of left and right circular polarisation. As a result, it will be equally divided between the two diffracted components (see top unpolarised panel).

- For $\phi \neq \pi$, the retardance deviates from half-wave and a leakage component, $|\mathbf{E}_{\text{in}}\rangle$, emerges, carrying the same polarisation as the incident wave. For $\phi = \pi/2$, this leakage accounts for half the incident intensity. In the case of incident circularly polarised

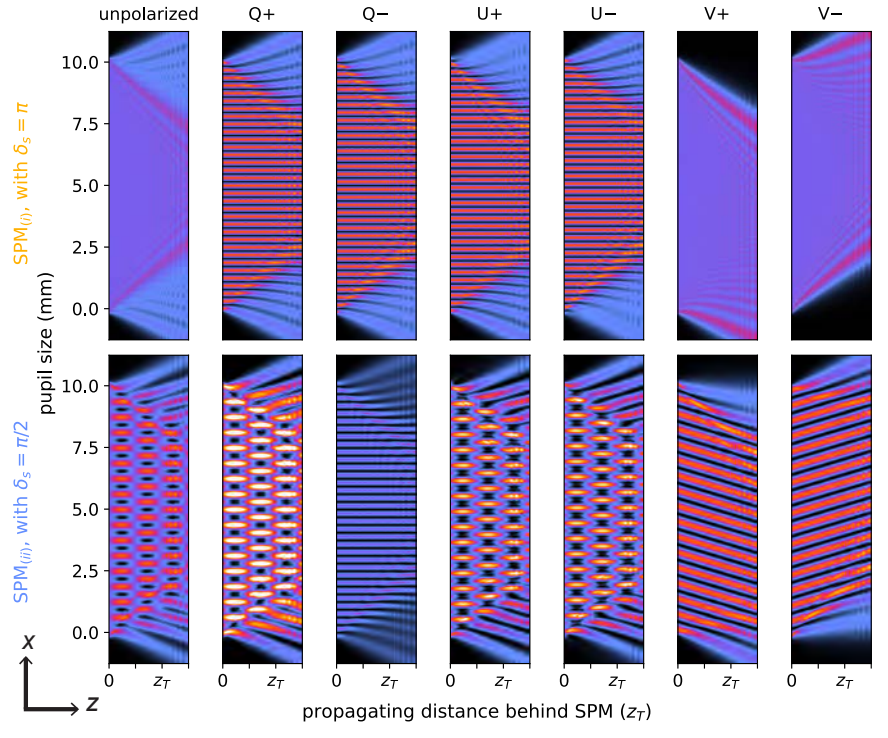


Figure 5.6: Central intensity slices $I_s(x, z)$ (a vertical centred slice of the intensity cubes $I_s(x, y, z)$) for a propagation distance up to $z_{\max} \approx 0.9\,\mathrm{m} \sim 1.5 z_T$, sampled in steps of $\Delta z = 0.007\,\mathrm{m}$, showing the diffracted fields emerging from $\mathrm{SPM}_{(\mathrm{i})}$ (**top panel**) or $\mathrm{SPM}_{(\mathrm{ii})}$ (**bottom panel**). For both SPMs the grating period is $d = 0.3\,\mathrm{mm}$ and for all incident light the wavelength is $\lambda = 550\mathrm{nm}$. Each panel corresponds to one of seven distinct incident polarisation states—defined by their initial Stokes parameters: unpolarised, horizontal (`Q+`), vertical (`Q−`), ±45° linear (`U+`, `U−`), and right/left circular polarised (`V+`, `V−`).

light, the resulting field comprises two coherent components: the non-diffracted leakage beam and a diffracted component with opposite handedness. While the leakage is spatially uniform, the diffracted component accumulates a geometric phase gradient. When passed through a linear polarisation analyser, these components interfere, and produce the resulting interference effects on the (simulated) detector oriented along the same direction as the diffracted order (see lower `V+` and `V−` panels). For linearly polarised or unpolarised input fields, the interference between leakage and diffracted beams gives rise to more complex patterns, including Talbot-like self-imaging. These effects are strongest when the diffraction angle is sufficiently steep, which occurs for high spatial frequency gratings (small period $g$). The resulting Talbot distance scales

inversely with the grating period, $z_T \propto 1/g$, as described by Equation (5.11). Notably, for certain input polarisation states such as Q−, the leakage and diffracted components have orthogonal polarisation states at the point of analysis, preventing interference and thereby suppressing the Talbot carpet. In this case, only a grating-like intensity pattern is visible (see lower Q− panel).

Additional examples of Talbot carpets for varying polarisation states and grating periods are presented in Appendix 5.7.

**Influence of SPM retardance on Fresnel-diffraction effects**

We have considered SPMs with either half- or quarter-wave retardance demonstrating how the resulting diffracted fields evolve for different incident polarisation states. To investigate how the strength of the Talbot effect depends on the modulator's retardance, we introduce a third configuration, $\text{SPM}_{\text{(iii)}}$. This SPM has a variable retardance that is parametrised by a polarisation leakage factor $\eta_{\text{pl}}$, defined such that the local retardance is given by $\delta_s = \phi = \eta_{\text{pl}} \cdot \pi$, ranging from half- to quarter-wave ($\eta_{\text{pl}} = 1.0 - 0.5$).

Figure 5.7 presents the resulting intensity slices $I_s(x, z)$ obtained by propagating uniform, unpolarised light through $\text{SPM}_{\text{(iii)}}$, analysed with the polarisation analyser. As the retardance decreases from $\pi$ to $\pi/2$, a growing fraction of the input field is transmitted as a leakage component that does not acquire a geometric phase shift. This leakage overlaps and interferes with the diffracted orders, giving rise to characteristic Talbot carpets. The interference pattern becomes increasingly visible for lower $\eta_{\text{pl}}$, with the strongest effect observed at $\eta_{\text{pl}} = 0.5$, where the leakage and diffracted components have comparable amplitude. Conversely, for $\eta_{\text{pl}} = 1.0$, no leakage is present and hence no Talbot-like pattern emerges only a uniform diffraction into two well-separated orders. These results confirm that the emergence of polarisation-dependent Talbot carpets under unpolarised illumination requires partial retardance and is enabled by the interference between diffracted and leakage components.

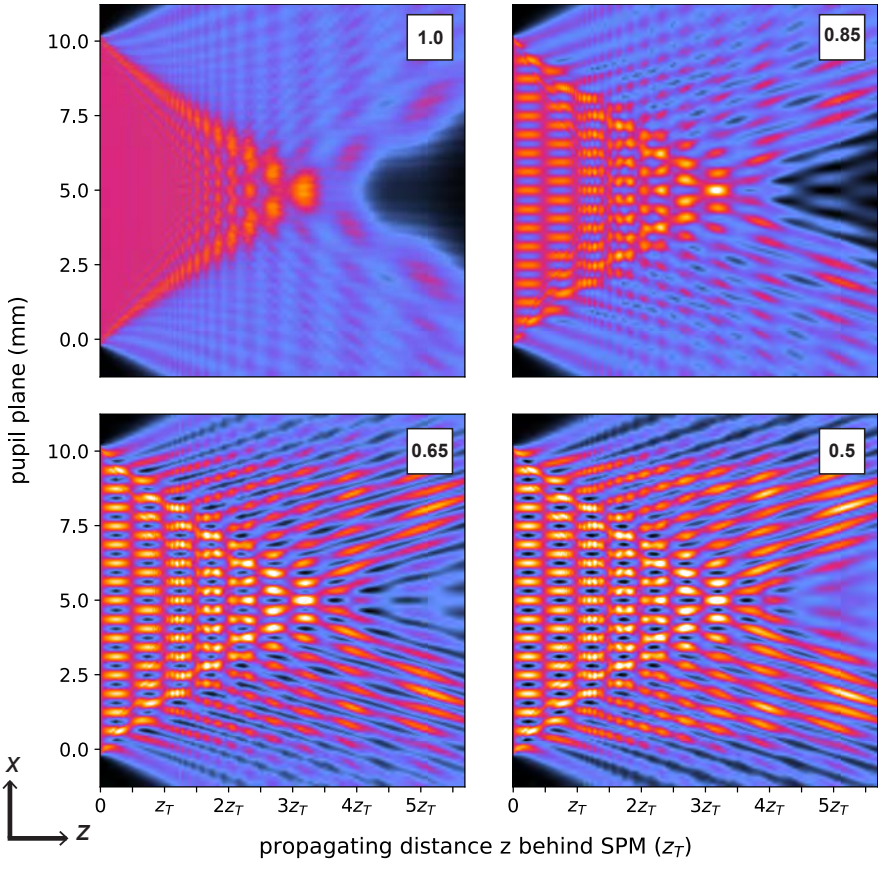


Figure 5.7: Intensity slices $I_s(x, z)$ for $z_{\max} \approx 3.5\text{m} \sim 5.8z_T$, $z_{\max} = 3.5\,\text{m}$ and $\Delta z = 0.007\,\text{m}$, depicting how incident unpolarised light ($\lambda = 550$ nm) emerges from SPM$_{\text{(iii)}}$, with a grating period of $d = 0.3\,\text{mm}$, and a linear polariser behind the SPM. From top left to bottom right, the retardance varies from half-wave ($\eta_{\text{pl}} = 1.0$) to quarter-wave ($\eta_{\text{pl}} = 0.5$).

## 5.5 Application in full-Stokes spectropolarimetry

In this study, we have explored the polarisation-dependent Talbot effect resulting from Fresnel diffraction behind SPMs. These modulators offer an appealing alternative to traditional rotating optical elements, enabling robust polarimetric modulation without moving parts. A liquid-crystal-based SPM, consisting of a patterned quarter-wave retarder with a continuously varying fast-axis orientation across one spatial dimension, can emulate a rotating wave plate. This approach preserves modulation frequencies even in the presence of retardance errors, and its wavelength dependence (scaling inversely with wavelength) can be mitigated through

multi-layer designs.

We implemented such a liquid-crystal SPM in the design of a full-Stokes spectropolarimeter, LSDPol[7] (Snik et al., 2019; Keller et al., 2020), developed to detect biosignatures, such as the homochirality of chlorophyll, from space (e.g. Patty et al., 2017, 2018b,a, 2019). These signals are expected at levels of $10^{-3}$–$10^{-4}$, while linear polarisation may reach tens of percent. To achieve meaningful detection, any possible instrumental cross-talk ($\mathtt{Q}, \mathtt{U} \rightarrow \mathtt{V}$) must remain below $10^{-3}$. This motivates the use of modulation techniques in which Stokes V is modulated at half the spatial frequency of Stokes Q and U, enabling unambiguous separation of circular and linear polarisation components (e.g. Sparks et al., 2012, 2019; Keller et al., 2020).

The optical design of LSDPol employs a patterned quarter-wave SPM with 10 different modulation frequencies that increase by a factor of two from one to the next patter. The modulator is placed at the instrument entrance, immediately in front of a $0.1 \times 10$ mm slit that is used to select one specific modulation frequency. A set of external baffles ensures spatial co-registration of left- and right-handed circular polarisation. A collimating lens placed one focal length behind the slit produces a telecentric beam, which is further defined by an internal field stop. A fixed quarter-wave retarder, oriented at 45°, converts polarisation states for analysis by a 5°-polarisation grating that simultaneously acts as a spectral disperser and circular polarising beam splitter. A final camera lens re-images the slit onto the detector, capturing two orthogonal polarisation states in a single exposure.

During initial laboratory tests of LSDPol, spurious modulation patterns were observed superimposed on the expected signal from the SPM (Keller et al., 2020). To isolate the origin of this effect, the fixed quarter-wave retarder was temporarily replaced with a wire-grid polariser, simplifying the setup and replicating the conditions with the set-up of our Fresnel diffraction simulation. This allows us to directly compare the observed spurious modulation with predictions from diffraction theory, specifically the emergence of a polarisation-dependent Talbot pattern when an SPM is analysed at a distance beyond the focus $z > 0$.



### Measurements in the optical laboratory

To investigate polarisation cross-talk introduced by diffraction effects behind the spatial polarisation modulator (SPM), a series of linear polarisation measurements was performed in the optical laboratory. The set-up utilised fully linearly polarised, monochromatic light at $\lambda = 650 \pm 5$ nm, produced by a halogen light source, a narrowband colour filter, and a rotating wire-grid polariser.

The measurement procedure consisted of the following steps:

1. **Data acquisition**: A total of 72 detector images were acquired, corresponding to successive 5° increments of the rotating polariser, thereby covering one full 360° rotation. A dark frame was captured and subtracted from each image to correct for detector background noise.

2. **Modulation extraction**: For each polariser angle, the intensity modulation along the spatially varying fast axis direction of the SPM ($\theta_{\mathrm{qwp}}$) was isolated. This was achieved

[7] A full description of LSDPol is provided in Chapter 4.

by selecting and averaging the signal across the region of interest, effectively condensing the detector image into a representative one-dimensional intensity profile. Each profile was stored as a single detector column.

3. **Construction of the intensity map**: The resulting columns were assembled to form the two-dimensional intensity map, as shown in the left panel of Figure 5.8. In this map, the horizontal axis represents the spatial variation in $\theta_{\text{qwp}}$, corresponding to a modulation frequency of $g = 4.8$. The vertical axis traces the response to different incident polarisation angles, as the polariser rotates through one full cycle.

4. **Theoretical modelling**: The observed modulation was compared to the theoretical model $I_{\text{th}}(\theta, \delta)$, of a rotating retarder followed by a linear polariser, given by:

$$I_{\text{th}}(\theta,\delta) = \frac{1}{2}\Bigg(\mathrm{I}_0 + \frac{Q_0}{2}\left[(1+\cos\delta) + (1-\cos\delta)\cos(4\theta)\right] + \frac{U_0}{2}(1-\cos\delta)\sin(4\theta) - V_0\sin\delta\sin(2\theta)\Bigg), \tag{5.14}$$

   where $\theta$ is the fast-axis orientation of the SPM, $\delta$ is its retardance, and $I_0$, $Q_0$, $U_0$, and $V_0$ are the Stokes parameters of the input light.

5. **Residual analysis**: A least-squares fit of the theoretical model $I_{\text{th}}(\theta, \delta)$ was performed on the measured intensity map. The model was then subtracted from the data to yield a residual map (top middle panel, Figure 5.8).

6. **Distortion correction**: The residuals showed systematic variations near the edges of the detector, attributed to geometric distortion. A fourth-order polynomial was fitted to these residuals to model the distortion, taking care to preserve any underlying low-amplitude modulation patterns.

7. **Cross-Talk identification**: The polynomial distortion model was subtracted from the original intensity map, followed by a renewed fit of the theoretical model. The updated residuals revealed a persistent modulation component at half the spatial frequency of the original signal (top right panel, Figure 5.8). This component is indicative of polarisation cross-talk, specifically a leakage from linear to circular polarisation.

The final residual demonstrates that the cross-talk varies as a function of the incident polarisation angle, confirming it is not a static artefact. This variation is consistent with the expected polarisation-dependent diffraction effects produced by the patterned liquid-crystal SPM.

### Validation of Fresnel Diffraction Effects through Simulation

To determine whether the residual modulation observed in the calibration data originates from polarisation-dependent diffraction effects, additional Fresnel diffraction simulations were conducted under laboratory-replicating conditions. Two simulations were performed

using $\text{SPM}_{(ii)}$ with a grating period of $d = 0.3\,\text{mm}$ and a wavelength of $\lambda = 650\,\text{nm}$, corresponding to the conditions used in the measurements performed with LSDPol. The incident light was fully linearly polarised, with its orientation identical to the laboratory procedure.

The first simulation assumed a perfectly focused configuration, with the detector plane coinciding with the SPM at $z = 0\,\text{m}$. The second simulation introduced a small defocus, with $z \approx 0.005\,\text{m}$, allowing for slight Fresnel diffraction. For both cases, intensity maps were generated by isolating the modulation signal across the simulated detector. The in-focus simulation at $z = 0\,\text{m}$ closely matched the theoretical intensity modulation $I_{\text{th}}(\theta, \delta)$, as expected. When the $z = 0\,\text{m}$ result was subtracted from the slightly defocused case, the resulting residuals (lower right panel, Figure 5.8) reproduced the same half-frequency modulation pattern observed in the experimental residuals (upper right panel, Figure 5.8).

This direct match confirms that the spurious modulation observed in the calibration measurements originates from polarisation-dependent Fresnel diffraction—specifically, a Talbot-like self-imaging effect introduced by the periodicity of the patterned SPM and the finite detector distance. These findings imply that even the slightest deviation from perfect focus is sufficient to induce measurable cross-talk between linear and circular polarisation components. While this phenomenon can be mitigated through perfect alignment of the SPM, we want to emphasise the implications a small deviation can have on the demodulation, especially since the diffraction effects are wavelength dependent. In the end, both an accurate and precise measurement of polarisation and wavelength are essential for LSDPol's intended application in space-based full-Stokes spectropolarimetry.



## 5.6 Conclusions and discussion

The results presented in this paper demonstrate the versatility and promise of spatial polarisation modulators for applications in snapshot spectropolarimetry. Diffraction simulations and laboratory measurements have provided valuable insights into geometric phase effects, diffraction-induced artifacts, and cross-talk mechanisms. However, several key challenges remain for the practical implementation of such systems in operational instruments like LSDpol.

A crucial next step is to translate these findings into an optical design. For instance, what constitutes a realistic combination of modulation period and distance between the spatial modulator and the slit or detector plane? What is the minimum allowable propagation distance that still ensures sufficient fringe contrast, and what physical or optical constraints (e.g., beam divergence, optical aberrations, or the Talbot length) set that lower bound? The simulations reveal, as expected, that the Talbot effect is non-existent when the detector is focussed on the modulator. Further outlook should investigate how field curvature or other optical imperfections impact the effective focus across the slit and potentially introduce spatially variable defocus and thus polarization-dependent artifacts.

These considerations are closely linked to the calibration strategy. An effective approach begins with a monochromatic light source and strictly linearly polarized input light, allowing a detailed mapping of the instrument's linear polarization response under well-controlled conditions. In parallel, a truly unpolarised light source is essential for reliable flat-fielding and to establish the system's baseline response. Once the linear response is characterized, the

next step is to introduce fully circularly polarized input light to probe the system's ability to distinguish circular from linear and unpolarised states. This process will also reveal how the smallest optical defocus affects the modulation pattern and any resulting cross-talk between Stokes parameters. Through this stepwise calibration scheme, we aim to evaluate whether the system can robustly recover full-Stokes information across a range of practical conditions.

Ultimately, if the system response proves to be stable over time, a comprehensive calibration and modelling approach could allow for predictive reconstruction of Stokes parameters from complex spatial and spectral modulation patterns. This will be essential to ensure the reliability of future full-Stokes snapshot spectropolarimeters in both laboratory and remote-sensing environments.

## Acknowledgements

This research made use of `HCIPy` (Por et al., 2018), an open-source object-oriented framework written in Python for performing end-to-end simulations of high-contrast imaging instruments. The author wants to thank Dr. Dane Kleiner for his help during the experiments, both with taking measurements as well as providing late-night dinners.

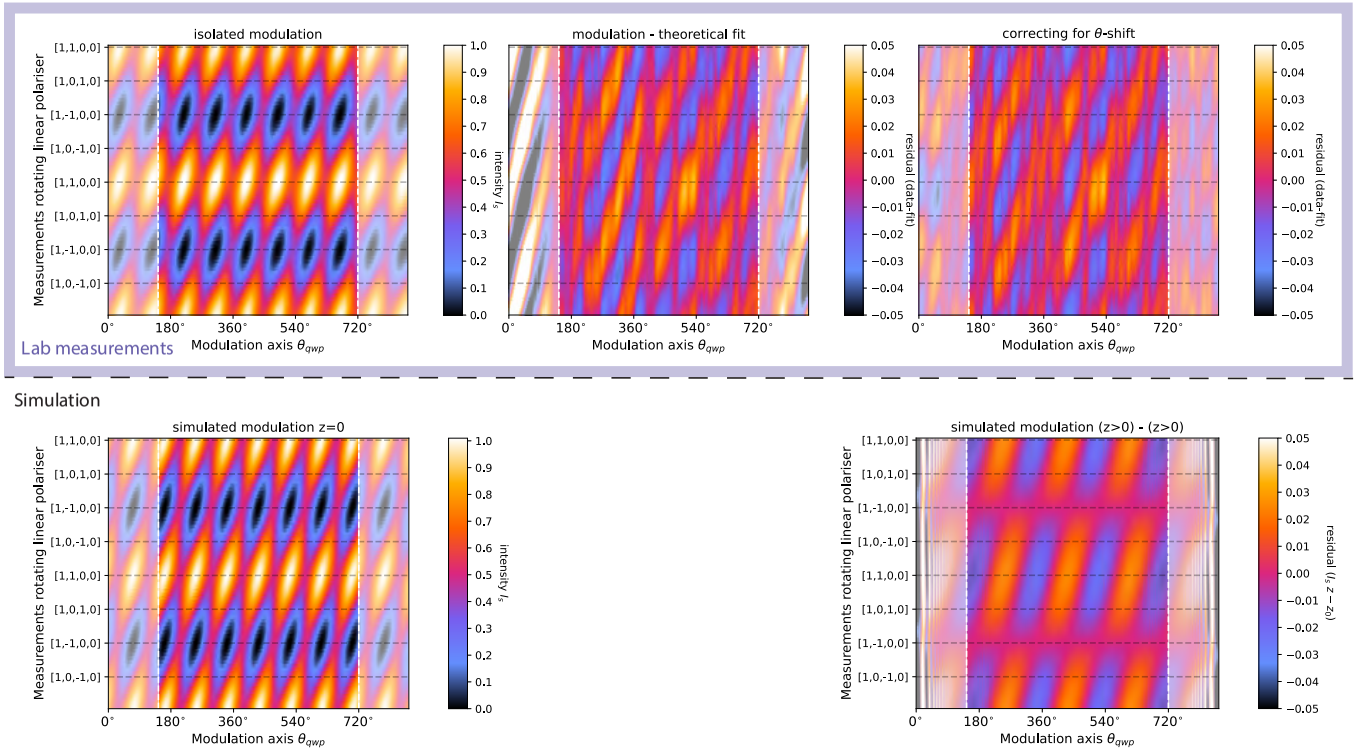


Figure 5.8: The top panels show data collected with the LSDPol instrument, while the bottom panels present simulated responses of the instrument. **Top left panel**: Summary of all 72 calibration measurements, with the vertical axis representing the variation in intensity $I_s$ due to changes in the orientation of the fully linearly polarised incident light, and the horizontal axis showing the 4.8 modulation cycles resulting from the changing fast-axis orientation of the patterned SPM $\theta_{qwp}$. **Top centre panel**: The expected intensity modulation, derived from theoretical predictions, is fitted and subtracted from the isolated data, leaving a residual modulation. **Top right panel**: The residual modulation after polynomial subtraction reveals an additional offset with half the modulation frequency, indicating potential linear to circular cross-talk. This cross-talk is dynamic, varying with the incident polarisation, as evidenced by the fluctuating intensity pattern. **Bottom left panel**: Simulated detector response for the isolated intensity pattern when perfectly in focus at $z = 0$. **Bottom right panel**: The residual modulation obtained when the simulation is slightly out of focus $z > 0$ and the solution for $z = 0$ is subtracted. This highlights additional effects caused by defocusing, illustrating how the modulation pattern changes with slight offsets in the focus plane.

# Appendix

## 5.7 Talbot carpet for different incident polarisation states

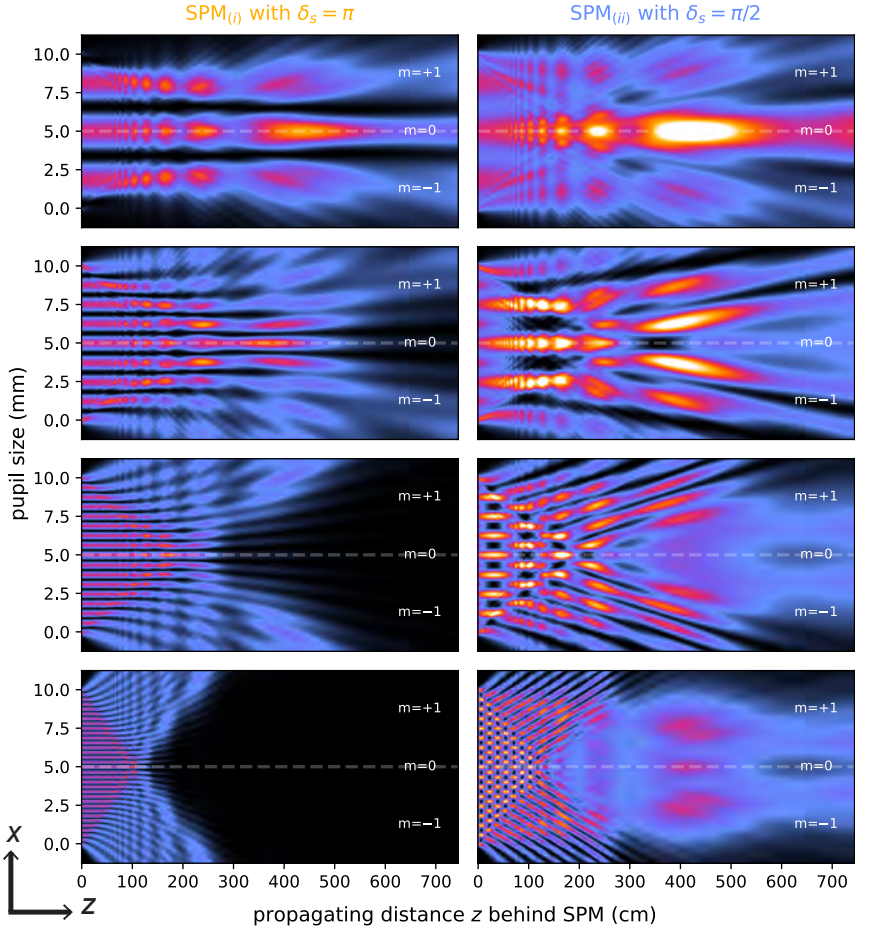


Figure 5.9: Intensity slices $I_s(x, z)$ for $z_{\max} \approx 7.5$ m, depicting how incident unpolarised light with a wavelength of $\lambda = 650$ nm emerges from SPM$_{(i)}$ and SPM$_{(ii)}$ with a varying grating period $d$ of 1.2, 0.6, 0.3, and 0.15 mm (from top to bottom).

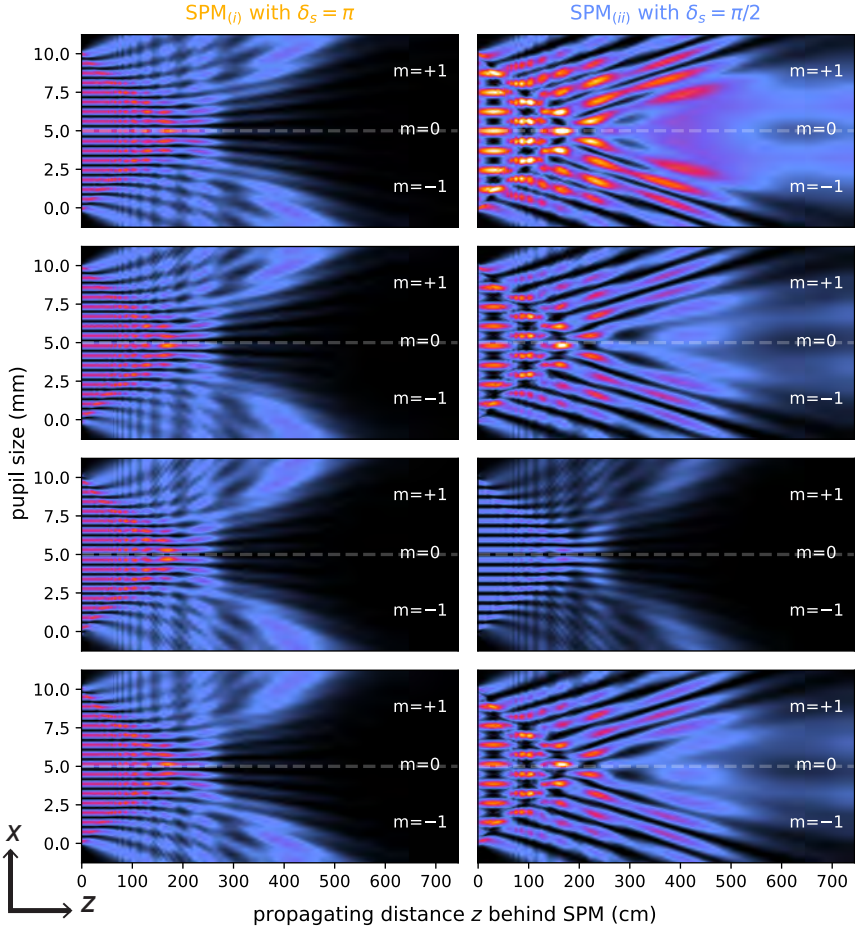


Figure 5.10: Intensity slices $I_s(x, z)$ for $z_{\max} \approx 7.5$ m, depicting how incident linear polarised light emerges from SPM$_{(i)}$ SPM$_{(ii)}$ with a grating period of $d = 0.3$ mm and a wavelength of $\lambda = 650$ nm.

# Bibliography


Adam, J. A. 2002, Phys. Rep., 356, 229, doi: 10.1016/S0370-1573(01)00076-X
Ahrer, E., Alderson, L., Batalha, N. M., et al. 2022, Nature, 614, 649–652, doi: 10.1038/s41586-022-05269-w
Aikawa, Y., & Herbst, E. 1999, in Cologne-Zermatt Symp. Proc. Vol. 3, 403
Allard, N. F., Spiegelman, F., Leininger, T., & Molliere, P. 2019, A&A, 628, A120, doi: 10.1051/0004-6361/201935593
Allers, K. N., & Liu, M. C. 2013, ApJ, 772, 79, doi: 10.1088/0004-637X/772/2/79
Allers, K. N., Jaffe, D. T., Luhman, K. L., et al. 2007, ApJ, 657, 511, doi: 10.1086/510845
Alvarez-Herrero, A., Uribe-Patarroyo, N., García Parejo, P., et al. 2011, in SPIE Conf. Ser. Proc., Vol. 8160, doi: 10.1117/12.892732
Amdursky, N., & Stevens, M. M. 2015, ChemPhysChem, 16, 2768–2774, doi: 10.1002/cphc.201500260
Andrei, A. H., Smart, R. L., Penna, J. L., et al. 2011, AJ, 141, 54, doi: 10.1088/0004-6256/141/2/54
Andreou, A., & Kalayjian, Z. 2002, IEEE Sens. J., 2, 566, doi: 10.1109/JSEN.2003.807946
Anglada-Escudé, G., Amado, P. J., Barnes, J., et al. 2016, Nature, 536, 437, doi: 10.1038/nature19106
Asplund, M., Amarsi, A. M., & Grevesse, N. 2021, A&A, 653, A141, doi: 10.1051/0004-6361/202140445
Asplund, M., Grevesse, N., Sauval, A. J., & Scott, P. 2009, ARA&A, 47, 481, doi: 10.1146/annurev.astro.46.060407.145222
Astropy Collaboration, Price-Whelan, A. M., Lim, P. L., et al. 2022, ApJ, 935, 167, doi: 10.3847/1538-4357/ac7c74
Baglin, A., Auvergne, M., Barge, P., et al. 2009, in IAU Symp., Vol. 253, 71–81, doi: 10.1017/S1743921308026252
Bagnulo, S., Landolfi, M., Landstreet, J. D., et al. 2009, PASP, 121, 993, doi: 10.1086/605654
Bagnulo, S., Sterzik, M., & Fossati, L. 2011, in ASPCS, Vol. 449, 76
Bai, C., Li, J., Zhang, W., Xu, Y., & Feng, Y. 2021, Opt. Express, 29, 38623, doi: 10.1364/OE.443350
Bailey, J. 2007, Astrobiology, 7, 320, doi: 10.1089/ast.2006.0039
Baldridge, A., Hook, S., Grove, C., & Rivera, G. 2009, RSE, 113, 711, doi: 10.1016/j.rse.2008.11.007
Baliunas, S. L., Henry, G. W., Donahue, R. A., Fekel, F. C., & Soon, W. H. 1997, ApJ Lett., 474, L119, doi: 10.1086/310442
Baraffe, I., Chabrier, G., Allard, F., & Hauschildt, P. H. 2002, A&A, 382, 563, doi: 10.1051/0004-6361:20011638
Barman, T. S., Macintosh, B., Konopacky, Q. M., & Marois, C. 2011, ApJ, 733, 65, doi: 10.1088/0004-637X/733/1/65
Bate, M. R., Bonnell, I. A., & Bromm, V. 2002, MNRAS, 332, L65–L68, doi: 10.1046/j.1365-8711.2002.05539.x
Bazzon, A., Schmid, H. M., & Gisler, D. 2013, A&A, 556, A117, doi: 10.1051/0004-6361/201321855
Bell, T. J., Welbanks, L., Schlawin, E., et al. 2023, Nature, 623, 709, doi: 10.1038/s41586-023-06687-0
Benneke, B., & Seager, . 2013, ApJ, 778, 153, doi: 10.1088/0004-637X/778/2/153
Bergin, E. A., Bosman, A., Teague, R., et al. 2024, ApJ, 965, 147, doi: 10.3847/1538-4357/ad3443
Berry, H., Gabrielse, G., & Livingston, A. E. 1977, Appl. Opt., 16 12, 3200, doi: 10.1364/AO.16.003200
Berry, M. V. 1984, Proc. R. Soc. Lond. A, 392, 45, doi: 10.1098/rspa.1984.0023
Best, W. M. J., Dupuy, T. J., Liu, M., et al. 2024, The UltracoolSheet (2.0.1) [Data set], doi: 10.5281/zenodo.13993077
Blake, C. H., Charbonneau, D., & White, R. J. 2010, ApJ, 723, 684–706, doi: 10.1088/0004-637x/723/1/684
Bomzon, Z., Niv, A., Biener, G, & Kleiner, V., H. 2002, Appl. Opt., 41, 5218, doi: 10.1364/AO.41.005218
Bonnefoy, M., Chauvin, G., Lagrange, A. M., et al. 2014, A&A, 562, A127, doi: 10.1051/0004-6361/201118270
Borysow, J., Frommhold, L., & Birnbaum, G. 1988, ApJ, 326, 509, doi: 10.1086/166112
Boss, A. P. 1997, Science, 276, 1836, doi: 10.1126/science.276.5320.1836
Brandl, B., Bettonvil, F., Van Boekel, R., et al. 2021, The Messenger, 182, 22, doi: 10.18727/0722-6691/5218
Brewster, D. 1815, Philos. Trans. R. Soc. Lond., 105, 125. http://www.jstor.org/stable/107362
Brogi, M., de Kok, R. J., Albrecht, S., et al. 2016, ApJ, 817, 106, doi: 10.3847/0004-637X/817/2/106
Brogi, M., & Line, M. R. 2019, AJ, 157, 114, doi: 10.3847/1538-3881/aaffd3
Brogi, M., Snellen, I. A. G., de Kok, R. J., et al. 2012, Nature, 486, 502, doi: 10.1038/nature11161
Bryson, S., Kunimoto, M., Kopparapu, R. K., et al. 2021, AJ, 161, 36, doi: 10.3847/1538-3881/abc418
Buchner, J., Georgakakis, A., Nandra, K., et al. 2014, A&A, 564, A125, doi: 10.1051/0004-6361/201322971
Bulheller, B. M., Rodger, A., & Hirst, J. D. 2007, Phys. Chem. Chem. Phys., 9, 2020, doi: 10.1039/B615870F
Burgasser, A. J., Cruz, K. L., Cushing, M., et al. 2010, ApJ, 710, 1142, doi: 10.1088/0004-637X/710/2/1142
Burningham, B., Marley, M. S., Line, M. R., et al. 2017, MNRAS, 470, 1177–1197, doi: 10.1093/mnras/stx1246
Burrows, A., Hubeny, I., Budaj, J., Knutson, H. A., & Charbonneau, D. 2007, ApJ Lett., 668, L171, doi: 10.1086/522834
Caglioti, L., Micskei, K., & Pályi, G. 2010, Chirality, 23, 65–68, doi: 10.1002/chir.20796
Caramazza, M., Stelzer, B., Magaudda, E., et al. 2023, A&A, 676, A14, doi: 10.1051/0004-6361/202346470
Carroll, J. 2009, Chirality, 21, 354, doi: 10.1002/chir.20590
Cassan, A., Kubas, D., Beaulieu, J.-P., et al. 2012, Nature, 481, 167–169, doi: 10.1038/nature10684
Castelli, F., & Kurucz, R. L. 2003, IAU Symp., 210, poster A20. https://arxiv.org/abs/astro-ph/0405087
Ceccarelli, C., Caselli, P., Bockelée-Morvan, D., et al. 2014, in Protostars and Planets VI (University of Arizona Press), 859–882, doi: 10.2458/azu_uapress_9780816531240-ch037
Chan, Y. M., & Dalgarno, A. 1965, Proc. Phys. Soc., 85, 227, doi: 10.1088/0370-1328/85/2/304
Chandrasekhar, S. 1946, ApJ, 104, 110, doi: 10.1086/144837
—. 1950, Q. J. R. Meteorol. Soc., 76, 498, doi: 10.1002/qj.49707633016
Charbonneau, D., Brown, T. M., Latham, D. W., & Mayor, M. 1999, ApJ, 529, L45, doi: 10.1086/312457
Charbonneau, D., Brown, T. M., Noyes, R. W., & Gilliland, R. L. 2002, ApJ, 568, 377, doi: 10.1086/338770
Charbonneau, D., Allen, L. E., Megeath, S. T., et al. 2005, ApJ, 626, 523, doi: 10.1086/429991
Chauvin, G., Lagrange, A. M., Dumas, C., et al. 2004, A&A, 425, L29, doi: 10.1051/0004-6361:200400056
Chen, W., Zhao, Z., Wang, C., et al. 2019, Opt. Express, 27 23, 33378, doi: 10.1364/OE.27.033378

Clarke, D., & Barocas, V. 1965, MNRAS, 130, 75, doi: 10.1093/mnras/130.1.75
Clayton, D. D., & Nittler, L. R. 2004, ARA&A, 42, 39, doi: 10.1146/annurev.astro.42.053102.134022
Collett, E. 2005, Field Guide to Polarized Light (SPIE Conf. Ser. Proc.), doi: 10.1117/3.626141
Coxon, J. A., & Hajigeorgiou, P. G. 2015, J. Quant. Spec. Radiat. Transf., 151, 133, doi: 10.1016/j.jqsrt.2014.08.028
Cridland, A. J., Pudritz, R. E., & Alessi, M. 2016, MNRAS, 461, 3274, doi: 10.1093/mnras/stw1511
Cronin, T. W., & Marshall, J. N. 2011, Philos. Trans. R. Soc. B, Biol. Sc, 366, 619
Crossfield, I. J. M., Lothringer, J. D., Flores, B., et al. 2019, ApJ Lett., 871, L3, doi: 10.3847/2041-8213/aaf9b6
Cruz, K. L., Kirkpatrick, J. D., & Burgasser, A. J. 2009, AJ, 137, 3345–3357, doi: 10.1088/0004-6256/137/2/3345
Cruz, K. L., Reid, I. N., Liebert, J., Kirkpatrick, J. D., & Lowrance, P. J. 2003, AJ, 126, 2421, doi: 10.1086/378607
Cubillos, P. E., Rojo, P., & Fortney, J. J. 2011, A&A, 529, A88, doi: 10.1051/0004-6361/201015802
Currie, T., Burrows, A., Itoh, Y., et al. 2011, ApJ, 729, 128, doi: 10.1088/0004-637X/729/2/128
Cutri, R. M., Skrutskie, M. F., van Dyk, S., et al. 2003, VizieR On-line Data Catalog
Czesla, S., Schröter, S., Schneider, C. P., et al. 2019, PyA: Python astronomy-related packages. http://ascl.net/1906.010
Dalgarno, A., & Williams, D. A. 1962, ApJ, 136, 690, doi: 10.1086/147428
de Boer, J., Langlois, M., van Holstein, R. G., et al. 2020, A&A, 633, A63, doi: 10.1051/0004-6361/201834989
de Regt, S., Gandhi, S., Snellen, I. A. G. F., et al. 2024, A&A, 688, A116, doi: 10.1051/0004-6361/202348508
de Regt, S., Snellen, I. A. G., Allard, N. F., et al. 2025, A&A, 696, A225, doi: 10.1051/0004-6361/202453190
Delorme, J.-R., Jovanovic, N., Echeverri, D., et al. 2021, JATIS, 7, 035006, doi: 10.1117/1.JATIS.7.3.035006
Deming, D., Wilkins, A., McCullough, P., et al. 2013, ApJ, 774, 95, doi: 10.1088/0004-637X/774/2/95
Deschamps, P.-Y., Breon, F.-M., Leroy, M., et al. 1994, IEEE Trans. Geosci. Remote Sens., 32, 598, doi: 10.1109/36.297978
Doelman, D., Por, E., Ruane, G., Escuti, M. J., & Snik, F. 2020, Publ. Astron. Soc. Pac., 132, doi: 10.1088/1538-3873/ab755f
Doelman, D., Wardenier, J. P., Tuthill, P., et al. 2021, A&A, 649, A168, doi: 10.1051/0004-6361/202039027
Doelman, D., Belaouchi, H., Riggs, A., et al. 2023, in SPIE Conf. Ser. Proc., Vol. 12680, doi: 10.1117/12.2677450
Doelman, D. S., Tuthill, P., Norris, B., et al. 2018, in SPIE Conf. Ser. Proc., Vol. 10701, doi: 10.1117/12.2313547
Dohlen, K., Langlois, M., Saisse, M., et al. 2008, in SPIE Conf. Ser. Proc., Vol. 7014, doi: 10.1117/12.789786
Dorn, R. J., Anglada-Escude, G., Baade, D., et al. 2014, The Messenger, 156, 7
Dorn, R. J., Bristow, P., Smoker, J. V., et al. 2023, A&A, 671, A24, doi: 10.1051/0004-6361/202245217
Dubber, S. C., Mortier, A., Rice, K., et al. 2019, MNRAS, 490, 5103, doi: 10.1093/mnras/stz2856
Eistrup, C., & Henning, T. 2022, A&A, 667, A160, doi: 10.1051/0004-6361/202243982
Elias, J. H., Joyce, R. R., Liang, M., et al. 2006, in SPIE Conf. Ser. Proc., Vol. 6269, 62694C, doi: 10.1117/12.671817
Escuti, M., Jihwan Kim, J., & Kudenov, M. 2016, Opt. Photon. News, 27, 22, doi: 10.1364/OPN.27.2.000022
Evans, T. M., Sing, D. K., Wakeford, H. R., et al. 2016, ApJ Lett., 822, L4, doi: 10.3847/2041-8205/822/1/L4
Faherty, J. K., Riedel, A. R., Cruz, K. L., et al. 2016, ApJS, 225, 10, doi: 10.3847/0067-0049/225/1/10
Faria, J. P., Suárez Mascareño, A., Figueira, P., et al. 2022, A&A, 658, A115, doi: 10.1051/0004-6361/202142337
Fauchez, T. J., Rossi, L., & Stam, D. M. 2017, ApJ, 842, 41, doi: 10.3847/1538-4357/aa6e53
Feroz, F., Hobson, M. P., Cameron, E., & Pettitt, A. N. 2019, OJAP, 2, doi: 10.21105/astro.1306.2144
Ferrari, A., Soummer, R., & Aime, C. 2007, C. R. Phys., 8, 277, doi: 10.1016/j.crhy.2007.05.008
Filippazzo, J. C., Rice, E. L., Faherty, J., et al. 2015, ApJ, 810, 158, doi: 10.1088/0004-637X/810/2/158
Foreman-Mackey, D. 2016, JOSS, 1, 24, doi: 10.21105/joss.00024
Fresnel, A. 1819, Mémoire sur la diffraction de la lumière (De l'Imprimerie de Feugueray), doi: 10.4000/bibnum.749
Freytag, B., Allard, F., Ludwig, H.-G., Homeier, D., & Steffen, M. 2010, A&A, 513, A19, doi: 10.1051/0004-6361/200913354
Fu, G., Welbanks, L., Deming, D., et al. 2024, Nature, 632, doi: 10.1038/s41586-024-07760-y
Fuß, W. 2008, Chirality, 21, 299–304, doi: 10.1002/chir.20576
Gagné, J., Faherty, J. K., Cruz, K. L., et al. 2015, ApJS, 219, 33, doi: 10.1088/0067-0049/219/2/33
Gaia Collaboration. 2020, doi: 10.26093/cds/vizier.1350
Gandhi, S., de Regt, S., Snellen, I., et al. 2023, ApJ Lett., 957, L36, doi: 10.3847/2041-8213/ad07e2
Gandhi, S., de Regt, S., Snellen, I., et al. 2025, MNRAS, 537, 134, doi: 10.1093/mnras/staf004
Gassó, S., & Knobelspiesse, K. D. 2022, Atmos. Chem. Phys., 2022, 1, doi: 10.5194/acp-2022-55
Gil, J. J. 2014, J. Appl. Remote Sens., 8, 1 , doi: 10.1117/1.JRS.8.081599
Gimenez, Y., Lapray, P.-J., Foulonneau, A., & Biguea, L. 2019, in SPIE Conf. Ser. Proc., Vol. 11172, 79, doi: 10.1117/12.2521752
Ginski, G., Tazaki, R., Dominik, C., & Stolker, T. 2023, ApJ, 953, 92, doi: 10.3847/1538-4357/acdc97
Glavin, D. P., Burton, A. S., Elsila, J. E., Aponte, J. C., & Dworkin, J. P. 2019, Chem. Rev., 120, 4660–4689, doi: 10.1021/acs.chemrev.9b00474
Gledhill, T. M. 1991, MNRAS, 252, 138, doi: 10.1093/mnras/252.1.138
Gledhill, T. M., Chrysostomou, A., Hough, J. H., & Yates, J. A. 2001, MNRAS, 322, 321, doi: 10.1046/j.1365-8711.2001.04112.x
Gleiser, M. 2022, Orig. Life Evol. Biosph., 52, 93–104, doi: 10.1007/s11084-022-09623-w
Goldstein, D. H. 2011, Polarized light (CRC Press), doi: 10.1201/b10436
González Picos, D., Snellen, I. F., de Regt, S., et al. 2024, A&A, 689, A212, doi: 10.1051/0004-6361/202450028
Goodman, J. W. 1996, Introduction to Fourier optics, Vol. 1 (New York: McGraw-Hill), doi: 10.1063/1.3035549
Gordon, K., Karalidi, T., Bott, K., et al. 2023, ApJ, 945, 166, doi: 10.3847/1538-4357/aca7fe
Gorlova, N. I., Meyer, M. R., Rieke, G. H., & Liebert, J. 2003, ApJ, 593, 1074, doi: 10.1086/376730
Grasser, N., Snellen, I. A. G., Landman, R., González Picos, D., & Gandhi, S. 2024, A&A, 688, A191, doi: 10.1051/0004-6361/202449932
Gray, D. F. 2008, Observation and Analysis of Stellar Photospheres (Cambridge Uni. Press), doi: 10.1017/9781009082136
Groot, A., Rossi, L., Trees, V. J. H., Cheung, J. C. Y., & Stam, D. M. 2020, A&A, 640, A121, doi: 10.1051/0004-6361/202037569

Guijarro, A., & Yus, M. 2008, The Origin of Chirality in the Molecules of Life (RSC), doi: 10.1039/9781847558756
Haffert, S., Males, J., Close, L. M., et al. 2021, JATIS, 7, doi: 10.1117/1.JATIS.7.2.029001
Haffert, S., Males, J. R., Ahn, K., et al. 2023, A&A, 673, A28, doi: 10.1051/0004-6361/202244960
Hansen, J. E. 1971, J. Atmos. Sci., 28, 1400, doi: 10.1175/1520-0469
Hansen, J. E., & Travis, L. D. 1974, Space Sci. Rev., 16, 527, doi: 10.1007/BF00168069
Harada, C. K., Dressing, C. D., Kane, S. R., & Ardestani, B. A. 2024, ApJS, 272, 30, doi: 10.3847/1538-4365/ad3e81
Hardegree-Ullman, K. K., Apai, D., Bergsten, G. J., Pascucci, I., & López-Morales, M. 2023, ApJ, 165, 267, doi: 10.3847/1538-3881/acd1ec
Harris, C. R., Millman, K. J., van der Walt, S. J., et al. 2020, Nature, 585, 357, doi: 10.1038/s41586-020-2649-2
Harsono, D., Bjerkeli, P., van der Wiel, M. H. D., et al. 2018, Nature Astronomy, 2, 646–651, doi: 10.1038/s41550-018-0497-x
Hasman, E., Bomzon, Z., Niv, A., Biener, G., & Kleiner, V. 2002, Opt. Commun., 209, 45, doi: 10.1016/S0030-4018(02)01598-5
Hecht, E. 2017, Optics (Pearson), doi: 10.4236/gep.2022.1010005
Hegde, S., Paulino-Lima, I. G., Kent, R., Kaltenegger, L., & Rothschild, L. 2015, PNAS, 112, 3886, doi: 10.1073/pnas.1421237112
Helled, R., Bodenheimer, P., Podolak, M., et al. 2014, Giant Planet Formation, Evolution, and Internal Structure (University of Arizona Press), doi: 10.2458/azu_uapress_9780816531240-ch028
Henry, G. W., Baliunas, S. L., Donahue, R. A., Soon, W. H., & Saar, S. H. 1997, ApJ, 474, 503, doi: 10.1086/303451
Henry, G. W., Marcy, G. W., Butler, R. P., & Vogt, S. S. 2000, ApJ Lett., 529, L41, doi: 10.1086/312458
Hoeijmakers, H. J., Seidel, J. V., Pino, L., et al. 2020, A&A, 641, A123, doi: 10.1051/0004-6361/202038365
Horne, K. 1986, PASP, 98, 609, doi: 10.1086/131801
Hough, J. H., Lucas, P. W., Bailey, J. A., et al. 2006, PASP, 118, 1302, doi: 10.1086/507955
Hovenier, J. W. 1971, A&A, 13, 7, doi: 10.1175/1520-0469(1971)028<0120:MSOPLI>2.0.CO;2
Hovenier, J. W., & van der Mee, C. V. M. 1983, A&A, 128, 1
—. 1988, A&A, 196, 287
Howell, S. B., Sobeck, C., Haas, M., et al. 2014, PASP, 126, 398, doi: 10.1086/676406
Hsu, D. C., Ford, E. B., Ragozzine, D., & Ashby, K. 2019, AJ, 158, doi: 10.3847/1538-3881/ab31ab
Hsu, W., Graham, M., Balakrishnan, K., et al. 2014, Opt. Express, 22, 3063, doi: 10.1364/OE.22.003063
Hulst, H. 1981, Light Scattering by Small Particles (Dover Publications)
Hunter, J. D. 2007, CiSE, 9, 90, doi: 10.1109/MCSE.2007.55
Iben, I., J., & Renzini, A. 1983, ARA&A, 21, 271, doi: 10.1146/annurev.aa.21.090183.001415
Ichimoto, K., Lites, B. W., Suematsu, Y., et al. 2008, Sol. Phys., 249, 233, doi: 10.1007/s11207-008-9169-9
Jacobs, E. E., Holt, A. S., Kromhout, R., & Rabinowitch, E. 1957, Arch Biochem. Biophys., 72, 495, doi: 10.1016/0003-9861(57)90225-4
Janson, M., Bergfors, C., Goto, M., Brandner, W., & Lafrenière, D. 2010, ApJ Lett., 710, L35, doi: 10.1088/2041-8205/710/1/L35
Johnson, W. C. 1987, Advs. in Carbohydr. Chem. and Biochem.: The Circ. Dichroism of Carbohydr., Vol. 45 (Academic Press), 73–124, doi: 10.1016/S0065-2318(08)60137-7
Kaeufl, H. U., Ballester, P., Biereichel, P., et al. 2004, in SPIE Conf. Ser. Proc., Vol. 5492, doi: 10.1117/12.551480
Karalidi, T., Stam, D. M., & Guirado, D. 2013, A&A, 555, doi: 10.1051/0004-6361/201321492
Karalidi, T., Stam, D. M., & Hovenier, J. W. 2012, A&A, 548, A90, doi: 10.1051/0004-6361/201220245
Kasdin, N. J., Bailey, V., Mennesson, B., et al. 2020, in SPIE Conf. Ser. Proc., doi: 10.1117/12.2562997
Kawahara, H., Kawashima, Y., Masuda, K., et al. 2022, ApJS, 258, 31, doi: 10.3847/1538-4365/ac3b4d
Keller, C. U., Snik, F., Patty, C. H. L., et al. 2020, in SPIE Conf. Ser. Proc., Vol. 11443, 114433R, doi: 10.1117/12.2562656
Kemp, J. C., Henson, G. D., Steiner, C. T., & Powell, E. R. 1987, Nature, 326, 270, doi: 10.1038/326270a0
Keppler, M., Benisty, M., Müller, A., et al. 2018, A&A, 617, A44, doi: 10.1051/0004-6361/201832957
Kienle, A., Forster, F. K., & Hibst, R. 2001, Opt. Lett., 26, 1571, doi: 10.1364/OL.26.001571
Kim, J., Li, Y., Miskiewicz, M. N., et al. 2015, Optica, 2, 958, doi: 10.1364/OPTICA.2.000958
Kirkpatrick, J. D., Cruz, K. L., Barman, T. S., et al. 2008, ApJ, 689, 1295, doi: 10.1086/592768
Kitzmann, D., Stock, J. W., & Patzer, A. B. C. 2024, MNRAS, 527, 7263, doi: 10.1093/mnras/stad3515
Klindžić, D., Stam, D. M., Snik, F., et al. 2020, Philos. Trans. R. Soc. A, 379, doi: 10.1098/rsta.2019.0577
Klindžić, D., Snik, F., Stam, D. M., et al. 2021, in SPIE Conf. Ser. Proc., Vol. 11833, doi: 10.1117/12.2595402
Knutson, H. A., Charbonneau, D., Allen, L. E., Burrows, A., & Megeath, S. T. 2008, ApJ, 673, 526, doi: 10.1086/523894
Koen, C., Matsunaga, N., & Menzies, J. 2004, MNRAS, 354, 466, doi: 10.1111/j.1365-2966.2004.08208.x
Kuhn, J. R., Potter, D., & Parise, B. 2001, ApJ Lett., 553, L189, doi: 10.1086/320686
Laginja, I., Soummer, R., Mugnier, L. M., et al. 2021, JATIS, 7, 015004, doi: 10.1117/1.JATIS.7.1.015004
Lajunen, H., Turunen, J., & Tervo, J. 2005, Optical Express, 13, 3055, doi: 10.1364/OPEX.13.003055
Landman, R., Haffert, S. Y., Radhakrishnan, V. M., & Keller, C. U. 2021, JATIS, 7, 039002, doi: 10.1117/1.JATIS.7.3.039002
Landman, R., Stolker, T., Snellen, I. A. G., et al. 2024, A&A, 682, A48, doi: 10.1051/0004-6361/202347846
Lane, C., Rode, D., & Rösgen, T. 2022, Appl. Opt., 61, C37, doi: 10.1364/AO.437391
Langer, W. D., & Penzias, A. A. 1993, ApJ, 408, 539, doi: 10.1086/172611
Langlois, M., Gratton, R., Lagrange, A.-M., et al. 2021, A&A, 651, A71, doi: 10.1051/0004-6361/202039753
Li, G., Gordon, I. E., Le Roy, R. J., et al. 2013, J. Quant. Spec. Radiat. Transf., 121, 78, doi: 10.1016/j.jqsrt.2013.02.005
Li, G., Gordon, I. E., Rothman, L. S., et al. 2015, ApJS, 216, 15, doi: 10.1088/0067-0049/216/1/15
Liang, S., Fang, H., Chen, M., et al. 2002, RSE, 83, 149, doi: 10.1016/S0034-4257(02)00092-5
Liberatore, A., Fineschi, S., Casti, M., et al. 2023, A&A, 672, A14, doi: 10.1051/0004-6361/202244069
Line, M. R., Brogi, M., Bean, J. L., et al. 2021, 598, 580, doi: 10.1038/s41586-021-03912-6

Liou, K.-N., & Takano, Y. 2002, Geophys. Res. Lett., 29, 27, doi: 10.1029/2001GL014613
Liu, M. C., Dupuy, T. J., & Allers, K. N. 2016, ApJ, 833, 96, doi: 10.3847/1538-4357/833/1/96
Lohmann, A. W., & Thomas, J. A. 1990, Appl. Opt., 29, 4337, doi: 10.1364/AO.29.004337
Lopez, R., Uribe-Patarroyo, N., Belenguer, T., et al. 2007, Appl. Opt., 46, 689, doi: 10.1364/AO.46.000689
Lothringer, J. D., Rustamkulov, Z., Sing, D. K., et al. 2021, ApJ, 914, 12, doi: 10.3847/1538-4357/abf8a9
Lu, Y., Zhou, C., Wang, S., & Wang, B. 2006, J. Opt. Soc. Am. A, 23, 2154, doi: 10.1364/JOSAA.23.002154
Ludwig, H. G., Allard, F., & Hauschildt, P. H. 2006, A&A, 459, 599, doi: 10.1051/0004-6361:20054010
Lyapustin, A., Gatebe, C., Kahn, R., et al. 2010, ACP, 10, 4359, doi: 10.5194/acp-10-4359-2010
Lynch, D. K., Dearborn, D. S. P., & Lock, J. A. 2011, Appl. Opt., 50, F39, doi: 10.1364/AO.50.000F39
Lyons, J., Gharib-Nezhad, E., & Ayres, T. 2018, Nature Communications, 9, doi: 10.1038/s41467-018-03093-3
Lyot, B. 1939, MNRAS, 99, 580, doi: 10.1093/mnras/99.8.580
Madhusudhan, N. 2012, ApJ, 758, 36, doi: 10.1088/0004-637X/758/1/36
Madhusudhan, N. 2019, ARA&A, 57, 617, doi: 10.1146/annurev-astro-081817-051846
Madhusudhan, N., Amin, M. A., & Kennedy, G. M. 2014, ApJ Lett., 794, L12, doi: 10.1088/2041-8205/794/1/L12
Madhusudhan, N., Sarkar, S., Constantinou, S., et al. 2023, ApJ Lett., 956, L13, doi: 10.3847/2041-8213/acf577
Madhusudhan, N., Harrington, J., Stevenson, K. B., et al. 2010, Nature, 469, 64–67, doi: 10.1038/nature09602
Maignan, F., Bréon, F.-M., Fédèle, E., & Bouvier, M. 2009, Remote Sens. Environ., 113, 2642, doi: 10.1016/j.rse.2009.07.022
Males, J. R., & Guyon, O. 2018, JATIS, 4, 019001, doi: 10.1117/1.JATIS.4.1.019001
Manjavacas, E., Lodieu, N., Béjar, V. J. S., et al. 2020, MNRAS, 491, 5925, doi: 10.1093/mnras/stz3441
Marley, M. S., & Robinson, T. D. 2015, ARA&A, 53, 279, doi: 10.1146/annurev-astro-082214-122522
Marois, C., Lafrenière, D., Doyon, R., Macintosh, B., & Nadeau, D. 2006, ApJ, 641, 556, doi: 10.1086/500401
Marrucci, L., Manzo, C., & Paparo, D. 2006, Appl. Phys. Lett., 88, 221102, doi: 10.1063/1.2207993
Martin, E. C., Mace, G. N., McLean, I. S., et al. 2017, ApJ, 838, 73, doi: 10.3847/1538-4357/aa6338
Martínez Pillet, V., del Toro Iniesta, J. C., Álvarez-Herrero, A., et al. 2011, Sol. Phys., 268, 57, doi: 10.1007/s11207-010-9644-y
Martí-Vidal, I., Vlemmings, W. H. T., & Muller, S. 2016, A&A, 593, A61, doi: 10.1051/0004-6361/201628225
Mawet, D., Riaud, P., Absil, O., & Surdej, J. 2005, ApJ, 633, 1191, doi: 10.1086/462409
Mawet, D., Serabyn, E., Liewer, K., et al. 2009, Opt. Express, 17, 1902, doi: 10.1364/OE.17.001902
Mayor, M., & Queloz, D. 1995, Nature, 378, 355, doi: 10.1038/378355a0
McCullough, P. R. 2006, arXiv e-prints, astro, doi: 10.48550/arXiv.astro-ph/0610518
McEldowney, S. C., Shemo, D. M., Chipman, R. A., & Smith, P. K. 2008, Opt. Lett., 33, 134, doi: 10.1364/OL.33.000134
Meerdink, S. K., Hook, S. J., Roberts, D. A., & Abbott, E. A. 2019, RSE, 230, 111196, doi: 10.1016/j.rse.2019.05.015
Meija, J., Coplen, T. B., Berglund, M., et al. 2016, Pure Appl. Chem., 88, 265, doi: doi:10.1515/pac-2015-0305
Milam, S. N., Savage, C., Brewster, M. A., Ziurys, L. M., & Wyckoff, S. 2005, ApJ, 634, 1126, doi: 10.1086/497123
Milani, K., Douglas, E. S., Haffert, S. Y., & Van Gorkom, K. 2024, JATIS, 10, 029001, doi: 10.1117/1.JATIS.10.2.029001
Miles, B. E., Biller, B. A., Patapis, P., et al. 2023, ApJ Lett., 946, L6, doi: 10.3847/2041-8213/acb04a
Miles-Páez, P. A., Pallé, E., & Zapatero Osorio, M. R. 2014, A&A, 562, L5, doi: 10.1051/0004-6361/201323009
Mizuno, H. 1980, Prog. Theor. Phys., 64, 544, doi: 10.1143/PTP.64.544
Mollière, P., Stolker, T., Lacour, S., et al. 2020, A&A, 640, A131, doi: 10.1051/0004-6361/202038325
Mollière, P., & Snellen, I. A. G. 2019, A&A, 622, A139, doi: 10.1051/0004-6361/201834169
Mollière, P., Wardenier, J. P., van Boekel, R., et al. 2019, A&A, 627, A67, doi: 10.1051/0004-6361/201935470
Mollière, P., Molyarova, T., Bitsch, B., et al. 2022, ApJ, 934, 74, doi: 10.3847/1538-4357/ac6a56
Mukherjee, S., Batalha, N. E., Fortney, J. J., & Marley, M. S. 2023, ApJ, 942, 71, doi: 10.3847/1538-4357/ac9f48
Mukherjee, S., Fortney, J., Morley, C., et al. 2024, ApJ, 963, 73, doi: 10.3847/1538-4357/ad18c2
Mulder, W., Doelman, D., Keller, C., Patty, C., & Snik, F. 2021, in SPIE Conf. Ser. Proc., Vol. 11833, doi: 10.1117/12.2595152
Mulder, W., Patty, C. H. L., Spadaccia, S., et al. 2022, in SPIE Conf. Ser. Proc., Vol. 12214, doi: 10.1117/12.2633271
Mulder, W., de Regt, S., Landman, R., et al. 2025, A&A, 694, A164, doi: 10.1051/0004-6361/202452859
Myneni, R., Maggion, S., Iaquinta, J., et al. 1995, Remote Sens. Environ., 51, 169, doi: 10.1016/0034-4257(94)00073-V
Nadal, F., & Breon, F.-M. 1999, IEEE Trans. Geosci. Remote Sens., 37, 1709, doi: 10.1109/36.763292
Nicodemus, F. E. 1965, Appl. Opt., 4, 767, doi: 10.1364/AO.4.000767
Nielsen, E. L., Rosa, R. J. D., Macintosh, B., et al. 2019, AJ, 158, 13, doi: 10.3847/1538-3881/ab16e9
Nikolova, L., & Todorov, T. 1984, Opt. Acta., 31, 579, doi: 10.1080/713821547
Nowak, S., Kurtsiefer, C., Pfau, T., & David, C. 1997, Opt. Lett., 22, 1430, doi: 10.1364/OL.22.001430
O'Dell, C. W., Connor, B., Bösch, H., et al. 2012, Atmos. Meas. Tech., 5, 99, doi: 10.5194/amt-5-99-2012
Oh, C., & Escuti, M. J. 2007, Phys. Rev. A, 76, 043815, doi: 10.1103/PhysRevA.76.043815
—. 2008, Opt. Lett., 33, 2287, doi: 10.1364/OL.33.002287
Oppenheimer, B. R., Baranec, C., Beichman, C., et al. 2013, ApJ, 768, 24, doi: 10.1088/0004-637X/768/1/24
Packham, C., Escuti, M., Ginn, J., et al. 2010, PASP, 122, 1471, doi: 10.1086/657904
Pancharatnam, S. 1956, Proc. Indian Acad. Sci., 44, 247, doi: 10.1007/BF03046050
Parejo, P., & Alvarez-Herrero, A. 2019, Opt. Mater. Express, 9, 2681, doi: 10.13f64/OME.9.002681
Patruno, A., & Kama, M. 2017, A&A, 608, A147, doi: 10.1051/0004-6361/201731102
Patty, C. H. L., Pommerol, A., Kühn, J. G., Demory, B.-O., & Thomas, N. 2022, Astrobiology, doi: 10.1089/ast.2021.0156
Patty, C. H. L., Kühn, J. G., Lambrev, P. H., et al. 2021, A&A, 651, A68, doi: 10.1051/0004-6361/202140845
Patty, C. L., ten Kate, I. L., Buma, W. J., et al. 2019, Astrobiology, 19, 1221–1229, doi: 10.1089/ast.2019.2050
Patty, C. L., ten Kate, I. L., Sparks, W. B., & Snik, F. 2018a, in Chiral Analysis (Second Edition) (Elsevier), 29–69, doi: 10.1016/B978-0-444-64027-7.00002-1
Patty, C. L., Visser, L. J., Ariese, F., et al. 2017, J. Quant. Spectrosc. Radiat. Transf., 189, 303–311, doi: 10.1016/j.jqsrt.2016.

12.023
Patty, C. L., Luo, D. A., Snik, F., et al. 2018b, BBA, 1862, 1350–1363, doi: 10.1016/j.bbagen.2018.03.005
Paufique, J., Biereichel, P., Donaldson, R., et al. 2004, in SPIE Conf. Ser. Proc., doi: 10.1117/12.551675
Pedrotti, F. L., Pedrotti, L. M., & Pedrotti, L. S. 2019, Introduction to Optics (Cambridge Uni. Press), doi: 10.1017/9781108552493
Peltoniemi, J. I., Gritsevich, M., Hakala, T., et al. 2015, TC, 9, 2323, doi: 10.5194/tc-9-2323-2015
Pertenais, M., Neiner, C., Bernardi, P., Reess, J.-M., & Petit, P. 2015, Appl. Opt., 54, 7377, doi: 10.1364/AO.54.007377
Piso, A.-M. A., Öberg, K. I., Birnstiel, T., & Murray-Clay, R. A. 2015, ApJ, 815, 109, doi: 10.1088/0004-637x/815/2/109
Pollack, J. B., Hubickyj, O., Bodenheimer, P., et al. 1996, Icarus, 124, 62, doi: 10.1006/icar.1996.0190
Polyansky, O. L., Kyuberis, A. A., Lodi, L., et al. 2017, VizieR Online Data Catalog: ExoMol line list for $H_2{}^{18}O$ and $H_2$, Originally: 2017MNRAS.466.1363P
Polyansky, O. L., Kyuberis, A. A., Zobov, N. F., et al. 2018, MNRAS, 480, 2597, doi: 10.1093/mnras/sty1877
Por, E. 2020, ApJ, 888, 127, doi: 10.3847/1538-4357/ab3857
Por, E. H., Haffert, S. Y., Radhakrishnan, V. M., et al. 2018, in SPIE Conf. Ser. Proc., Vol. 10703, doi: 10.1117/12.2314407
Povel, H. P., Keller, C. U., & Yadigaroglu, I.-A. 1994, Appl. Opt., 33, 4254, doi: 10.1364/AO.33.004254
Qin, W., Herman, J., & Ahmad, Z. 2001, J. Geophys. Res., 106, 22671, doi: 10.1029/2001JD900215
Racine, R., Walker, G. A. H., Nadeau, D., Doyon, R., & Marois, C. 1999, PASP, 111, 587, doi: 10.1086/316367
Reid, I. N., Cruz, K. L., Kirkpatrick, J. D., et al. 2008, AJ, 136, 1290, doi: 10.1088/0004-6256/136/3/1290
Richardson, L. J., Deming, D., Wiedemann, G., et al. 2003, ApJ, 584, 1053, doi: 10.1086/345813
Ricker, G. R., Winn, J. N., Vanderspek, R., et al. 2015, JATIS, 1, 014003, doi: 10.1117/1.JATIS.1.1.014003
Rogers, J. D., Radosevich, A. J., Yi, J., & Backman, V. 2014, IEEE J. Sel. Top. Quantum Electron., 20, 173–186, doi: 10.1109/jstqe.2013.2280999
Rothman, L. S., Gordon, I. E., Barber, R. J., et al. 2010, J. Quant. Spec. Radiat. Transf., 111, 2139, doi: 10.1016/j.jqsrt.2010.05.001
Rouse, J. W., J., Haas, R. H., Schell, J. A., & Deering, D. W. 1974, in NASA Special Publication, Vol. 351, 309
Rubin, N., Shi, Z., & Capasso, F. 2021, Adv. Opt. Photon., 13, 836, doi: 10.1364/AOP.439986
Ruffio, J.-B., Macintosh, B., Konopacky, Q. M., et al. 2019, AJ, 158, 200, doi: 10.3847/1538-3881/ab4594
Rustamkulov, Z., Sing, D. K., Mukherjee, S., et al. 2023, Nature, 614, 659–663, doi: 10.1038/s41586-022-05677-y
Sanghi, A., Liu, M. C., Best, W. M. J., et al. 2023, ApJ, 959, 63, doi: 10.3847/1538-4357/acff66
Schlawin, E., Burgasser, A. J., Karalidi, T., Gizis, J. E., & Teske, J. 2017, ApJ, 849, 163, doi: 10.3847/1538-4357/aa90b8
Schlieder, J. E., Lépine, S., Rice, E., et al. 2012, AJ, 143, 114, doi: 10.1088/0004-6256/143/5/114
Schneider, A., & Bitsch, B. 2021, A&A, 654, A71, doi: 10.1051/0004-6361/202039640
Schwarz, H., Ginski, G., de Kok, R. J., et al. 2016, A&A, 593, A74, doi: 10.1051/0004-6361/201628908
Seager, S., Kuchner, M., Hier-Majumder, C. A., & Militzer, B. 2007, ApJ, 669, 1279, doi: 10.1086/521346
Seager, S., & Sasselov, D. D. 2000, ApJ, 537, 916, doi: 10.1086/309088
Seager, S., Turner, E. L., Schafer, J., & Ford, E. B. 2005, Astrobiology, 5, 372
Serindag, D. B., & Snellen, I. A. G. 2019, ApJ Lett., 871, L7, doi: 10.3847/2041-8213/aafa1f
Shaw, J., & Vollmer, M. 2017, Appl. Opt., 56, G36, doi: 10.1364/AO.56.000G36
Skemer, A. J., Hinz, P. M., Esposito, S., et al. 2012, ApJ, 753, 14, doi: 10.1088/0004-637X/753/1/14
Smette, A., Sana, H., Noll, S., et al. 2015, A&A, 576, A77, doi: 10.1051/0004-6361/201423932
Snellen, I., de Kok, R., Birkby, J. L., et al. 2015, A&A, 576, A59, doi: 10.1051/0004-6361/201425018
Snellen, I. A. G., Brandl, B. R., de Kok, R. J., et al. 2014, Nature, 509, 63, doi: 10.1038/nature13253
Snellen, I. A. G., de Kok, R. J., de Mooij, E. J. W., & Albrecht, S. 2010, Nature, 465, 1049, doi: 10.1038/nature09111
Snik, F., Karalidi, T., & Keller, C. U. 2009, Appl. Opt., 48, 1337, doi: 10.1364/AO.48.001337
Snik, F., & Keller, C. 2013, Astronomical Polarimetry: Polarized Views of Stars and Planets, Vol. 2 (Springer), 175–221, doi: 10.1007/978-94-007-5618-2_4
Snik, F., Keller, C. U., Doelman, D. S., et al. 2019, in SPIE Conf. Ser. Proc., Vol. 11132, doi: 10.1117/12.2529548
Sobolev, V. V. 1963, A Treatise On Radiative Transfer (Astronomical Notes), doi: https://doi.org/10.1002/asna.19632870511
Solanki, S. K., del Toro Iniesta, J. C., Woch, J., et al. 2020, A&A, 642, A11, doi: 10.1051/0004-6361/201935325
Somogyi, W., Yurchenko, S. N., & Yachmenev, A. 2021, J. Chem. Phys., 155, 214303, doi: 10.1063/5.0063256
Sparks, W., Parenteau, M., Blankenship, R., et al. 2020, Astrobiology, 21, doi: 10.1089/ast.2020.2272
Sparks, W. B., & Ford, H. C. 2002, ApJ, 578, 543, doi: 10.1086/342401
Sparks, W. B., Germer, T. A., MacKenty, J. W., & Snik, F. 2012, Appl. Opt., 51, 5495, doi: 10.1364/AO.51.005495
Sparks, W. B., Germer, T. A., & Sparks, R. M. 2019, PASP, 131, 075002, doi: 10.1088/1538-3873/ab1933
Sparks, W. B., Hough, J. H., & Bergeron, L. E. 2005, Astrobiology, 5, 737, doi: 10.1089/ast.2005.5.737
Stam, D., Dehaan, J., Hovenier, J., & Stammes, P. 1999, J. Geophys. Res., 104, 16843, doi: 10.1029/1999JD900159
Stam, D. M. 2008, A&A, 482, 989, doi: 10.1051/0004-6361:20078358
Steele, I. A., & Jameson, R. F. 1995, MNRAS, 272, 630, doi: 10.1093/mnras/272.3.630
Steen, W. M. 2000, Principles of Optics M. Born and E. Wolf (Cambridge Uni. Press), 952, doi: 10.1017/CBO9781139644181
Sterzik, M. F., & Bagnulo, S. 2009, in ASP Conf. Ser., Vol. 420, 371
Sterzik, M. F., Bagnulo, S., & Palle, E. 2012, Nature Astronomy, 483, 64, doi: 10.1038/nature10778
Sterzik, M. F., Bagnulo, S., Stam, D. M., Emde, C., & Manev, M. 2019, A&A, 622, A41, doi: 10.1051/0004-6361/201834213
Stock, J. W., Kitzmann, D., & Patzer, A. B. C. 2022, MNRAS, 517, 4070–4080, doi: 10.1093/mnras/stac2623
Stock, J. W., Kitzmann, D., Patzer, A. B. C., & Sedlmayr, E. 2018, MNRAS, 479, 865, doi: 10.1093/mnras/sty1531
Stokes, G. G. 1852, Annalen der Physik, 163, 480, doi: 10.1002/andp.18521631109
Swanson, P., Telesco, C., Sparks, W., et al. 2024, BAAS, 56

Szentgyorgyi, A., Baldwin, D., Barnes, S., et al. 2016, in SPIE Conf. Ser. Proc., Vol. 9908, doi: 10.1117/12.2233506
Takahashi, J., Itoh, Y., Akitaya, H., et al. 2013, PASJ, 65, 38, doi: 10.1093/pasj/65.2.38
Takahashi, J., Itoh, Y., Matsuo, T., et al. 2021, A&A, 653, A99, doi: 10.1051/0004-6361/202039331
Talbot, H. F. 1836, Philosophical Magazine, Series 3, 401, doi: 10.1080/14786443608649032
Tanré, D., Breon, F.-M., Deuzé, J., et al. 2011, Atmos. Meas. Tech., 4, 1383, doi: 10.5194/amt-4-1383-2011
Thiabaud, A., Marboeuf, U., Alibert, Y., et al. 2014, A&A, 562, A27, doi: 10.1051/0004-6361/201322208
Tinbergen, J. 1996, Astronomical Polarimetry (Cambridge Uni. Press), doi: 10.1017/CBO9780511525100
Trees, V. J. H., & Stam, D. M. 2019, A&A, 626, A129, doi: 10.1051/0004-6361/201935399
—. 2022, A&A, 664, A172, doi: 10.1051/0004-6361/202243591
Tsai, S.-M., Lee, E. K. H., Powell, D., et al. 2023, Nature, 617, 483–487, doi: 10.1038/s41586-023-05902-2
Tsuji, T., Ohnaka, K., Aoki, W., & Nakajima, T. 1996, A&A, 308, L29
Turrini, D., Schisano, E., Fonte, S., et al. 2021, ApJ, 909, 40, doi: 10.3847/1538-4357/abd6e5
van Holstein, R., Stolker, T., Jensen-Clem, R., et al. 2021, A&A, 647, A21, doi: 10.1051/0004-6361/202039290
Vanderbilt, V., Grant, L., & Daughtry, C. 1985, Proc. IEEE Int., 73, 1012 , doi: 10.1109/PROC.1985.13232
Vanderbilt, V. C., Grant, L., & Ustin, S. L. 1991, Polarization of Light by Vegetation (Springer), 191–228, doi: 10.1007/978-3-642-75389-3_7
Vaughan, S. R., Gebhard, T. D., Bott, K., et al. 2023, MNRAS, 524, 5477, doi: 10.1093/mnras/stad2127
Verhoef, W. 1998, Theory of radiative transfer models applied in optical remote sensing of vegetation canopies
Visscher, C., Lodders, K., & Fegley, Bruce, J. 2010, ApJ, 716, 1060, doi: 10.1088/0004-637X/716/2/1060
Vos, J. M., Biller, B. A., Allers, K. N., et al. 2020, AJ, 160, 38, doi: 10.3847/1538-3881/ab9642
Wang, J. J., Ruffio, J.-B., Morris, E., et al. 2021, AJ, 162, 148, doi: 10.3847/1538-3881/ac1349
Welbanks, L., Madhusudhan, N., Allard, N. F., et al. 2019, ApJ Lett., 887, L20, doi: 10.3847/2041-8213/ab5a89
Weller, M. G. 2024, Life, 14, 341, doi: 10.3390/life14030341
Wen, J., Zhang, Y., & Xiao, M. 2013, Adv. Opt. Photon., 5, 83, doi: 10.1364/AOP.5.000083
Weng, Y., Xu, D., Zhang, Y., Li, X., & Wu, S.-T. 2016, Opt. Express, 24, 17746, doi: 10.1364/OE.24.017746
Whitworth, A., Bate, M. R., Nordlund, Å., Reipurth, B., & Zinnecker, H. 2007, in Protostars and Planets V, ed. B. Reipurth, D. Jewitt, & K. Keil, 459
Wilson, P. A., Rajan, A., & Patience, J. 2014, A&A, 566, A111, doi: 10.1051/0004-6361/201322995
Wilson, T. L. 1999, Rep. Prog. Phys, 62, 143, doi: 10.1088/0034-4885/62/2/002
Wilzewski, J. S., Gordon, I. E., Kochanov, R. V., Hill, C., & Rothman, L. S. 2016, J. Quant. Spec. Radiat. Transf., 168, 193, doi: 10.1016/j.jqsrt.2015.09.003
Wolstencroft, R., & Breon, F.-M. 2005, ASP Conf. Ser., 343, 211
Wolstencroft, R., Breon, F.-M., & Tranter, G. 2005, AAS Meeting Abstracts, 210, 210
Wolstencroft, R. D., Tranter, G. E., & Le Pevelen, D. D. 2004, in IAU Symp., Vol. 213, 149–153, doi: 10.1017/S0074180900193167
Wolszczan, A., & Frail, D. A. 1992, Nature, 355, 145, doi: 10.1038/355145a0
Woods, P. M., & Willacy, K. 2009, ApJ, 693, 1360, doi: 10.1088/0004-637X/693/2/1360
Xuan, J. W., Wang, J., Ruffio, J. B., et al. 2022, ApJ, 937, 54, doi: 10.3847/1538-4357/ac8673
Xuan, J. W., Hsu, C.-C., Finnerty, L., et al. 2024, ApJ, 970, 71, doi: 10.3847/1538-4357/ad4796
Yan, F., Reiners, A., Pallé, E., et al. 2022, A&A, 659, A7, doi: 10.1051/0004-6361/202142395
Yashiro, W., Terui, Y., Kawabata, K., & Momose, A. 2010, Opt. Express, 18, 16890, doi: 10.1364/OE.18.016890
Youngs, E. J., & Kudenov, M. W. 2017, in SPIE Conf. Ser. Proc., Vol. 10407, doi: 10.1117/12.2273866
Zahnle, K. J., & Marley, M. S. 2014, ApJ, 797, 41, doi: 10.1088/0004-637X/797/1/41
Zapatero Osorio, M. R., Béjar, V. J. S., Miles-Páez, P. A., et al. 2014, A&A, 568, A6, doi: 10.1051/0004-6361/201321340
Zhang, Y., Snellen, I. A. G., Brogi, M., & Birkby, J. L. 2022, RNAAS, 6, 194, doi: 10.3847/2515-5172/ac9309
Zhang, Y., Snellen, I. A. G., & Mollière, P. 2021, A&A, 656, A76, doi: 10.1051/0004-6361/202141502
Zhang, Y., Snellen, I. A. G., Bohn, A. J., et al. 2021, Nature, 595, 370–372, doi: 10.1038/s41586-021-03616-x
Zhang, Y., González Picos, D., de Regt, S., et al. 2024, arXiv e-prints, arXiv:2409.16660, doi: 10.48550/arXiv.2409.16660
Zhang, Z., Mollière, P., Hawkins, K., et al. 2023, ApJ, 166, 198, doi: 10.3847/1538-3881/acf768
Öberg, K. I., Murray-Clay, R., & Bergin, E. A. 2011, ApJ Lett., 743, L16, doi: 10.1088/2041-8205/743/1/L16


ON TAP

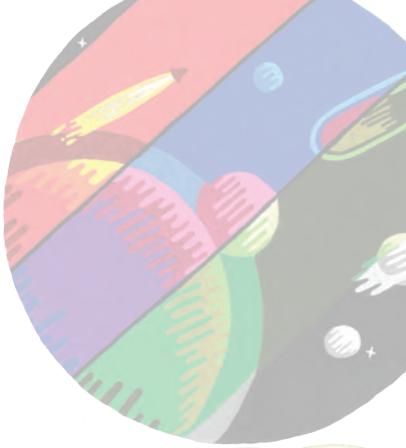

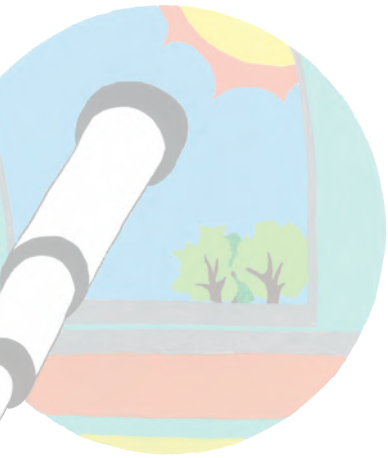

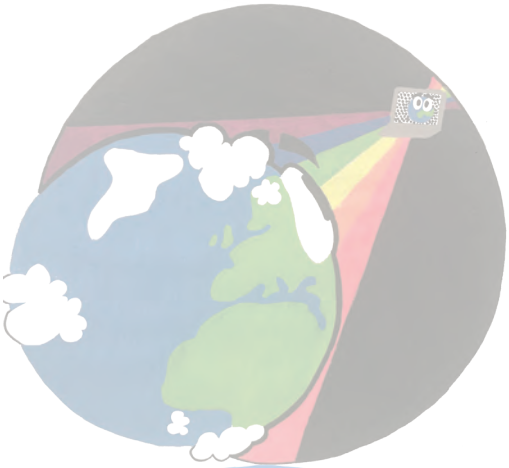

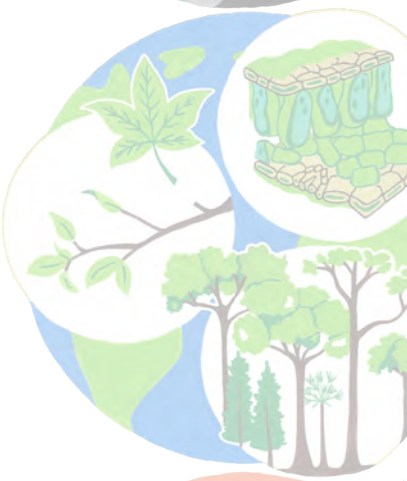


ANGRY PHOTONS


THE
BEETLES

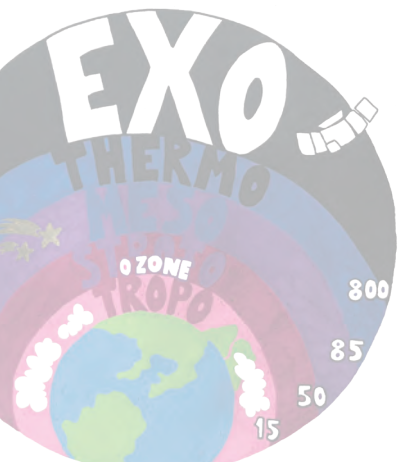
EXO
THERMO
OZONE
TROPO
800
85
50
15



# English summary

*How did we come into existence? Are we alone in this Universe?* For centuries, these questions navigate and drive the limitless curiosity of humanity. Today, November 2026, the discovery of more than six thousand exoplanets offers a glimpse into the incredible diversity of worlds beyond our Solar System. In our desire to truly understand these distant worlds, discovery is merely the first step. We need to know their fundamental properties in order to assess their potential to host life, starting with the planet's size and mass. By calculating their densities we can classify the exoplanets as either rocky (e.g. Earth-like), or gaseous planets (e.g. Neptune-like, Jupiter-like, or even a colossal super-Jupiter). In addition, if we know the mass of the and the distance to their host star, we can find out whether a planet orbits within the so-called habitable zone. In this zone, temperatures allow liquid water to exist: one of the crucial ingredients of life as we know.

## Observing distant worlds: direct imaging & spectroscopy

*How can we study the invisible worlds that orbit distant stars?* Firstly, what do I mean by invisible worlds? Stars, whether our Sun or far-off suns in the Milky way, emit light across the electromagnetic spectrum: infrared radiation that we can feel as warmth, visible light that we can see, and ultraviolet light that can even cause sunburn. Planets, on the other hand, are very different. They do not produce their own visible light. Instead, they shine only by reflecting the light of their host star and by emitting a faint amount of infrared radiation as they warm up under that starlight. In our own night sky, we can spot planets like Mars, Venus or Jupiter. With the naked eye, they appear as bright points of light, not so different from nearby stars. During the day, however, these planets completely disappear from our view. Not because they stop reflecting sunlight, but because the Sun is overwhelmingly bright and drowns out their faint reflected light.

The same principle applies to exoplanets, but on a far more extreme scale. These planets orbit stars that are not just brighter than the planets themselves, but also much farther away. From our vantage point, an exoplanet sits right next to its dazzling host star, and the contrast between them becomes enormous: the light from the star can be ten thousand to tens of billions of times brighter than the light reflected by the planet. This illustrates the difficulty of imaging exoplanets. To image an exoplanet, astronomers need to apply a technique called **high-contrast imaging**. High-contrast imaging allows telescopes to suppress the light from the host star, which would otherwise overwhelm the dim reflected light of the planets. This method is better known as **direct imaging**.

The possibility of directly imaging planets is inherently limited to the contrast of the planetary system. Fortunately, there are methods to examine distant words, like using **spectroscopy** which measures the wavelength (or 'colour') and the intensity of light. All exoplanets move in an orbit around their host star. When a planet passes directly between its star and a telescope, part of the starlight filters through its atmosphere. By analysing this light, we can reveal the planet's chemical composition. Spectroscopy allows us to detect the

unique 'fingerprints' of atoms and molecules, and to determine the atmospheric composition, temperature, and the presence of clouds or hazes. Especially **high-resolution spectroscopy** is a powerful tool - sensitive enough to detect even trace gases and to measure atmospheric motions such as winds or planetary rotation.

In Chapter 2, we use high-resolution spectroscopy to study the atmospheres of three **brown dwarfs**. These are celestial objects that bridge the gap between planets and stars: they are more massive than giant planets, yet too light to sustain hydrogen fusion and therefore do not shine with stable starlight of their own. The observations are part of the *SupJup Survey*, which uses the CRIRES+ instrument on the Very Large Telescope in Chile to collect detailed spectra of a sample of brown dwarfs and super-Jupiters. The three spectra reveal an enhanced carbon-to-oxygen ratio and a higher metallicity compared to our Sun, suggesting that part of the oxygen may have been locked into solid materials during formation. We also measured the ratio between two isotopes of carbon, $^{12}$C and $^{13}$C, which provides clues about the chemical evolution of the region where the object was born. Our results show slightly less $^{13}$C than typically found in the diffuse interstellar gas and dust within our Galaxy. Ongoing work within the SupJup Survey will analyse the remaining spectra to build a more complete picture of how planets and related substellar objects form and evolve.

## The search for life as we know it: homochirality

While the study of distant exoplanets reveals the astonishing diversity of worlds in our Universe, one simple truth remains: the only planet we know that harbours life is our own Earth. If we aim to search for similar forms of life beyond the Solar System, we must first understand how to recognise unmistakable signs of life as seen from our own planet. One of the most compelling of these signs is a phenomenon known as **homochirality**. On Earth, the essential building blocks of life, such as chlorophyll, amino acids, proteins, DNA, and sugars, all exhibit a single molecular 'handedness'. This consistent preference for one mirror-image form over another does not occur naturally without biological influence, making it a unique and unambiguous fingerprint of life.

To prepare for future space missions that will search for extraterrestrial life, it is crucial to test whether we can detect this signature remotely, under realistic conditions outside the laboratory. One of the most powerful techniques for this purpose is **spectropolarimetry**. Unlike standard spectroscopy where we measure the intensity of specific wavelengths of incoming light, spectropolarimetry reveals how the light waves are oriented: a property known as **polarisation**. Light can become linearly polarised when it scattered by atmospheric particles or reflected from planetary surfaces such as oceans or deserts, an effect that is already well understood. A more elusive form, however, is **circular polarisation**, where the light waves twist into a spiral shape. Intriguingly, this type of polarisation can be produced when light interacts with biological molecules due to their homochiral nature. This makes circular polarisation a highly promising, and perhaps the most unambiguous, remote indicator of life.

Although existing models of how planetary surfaces and atmospheres reflect light already take various scattering effects into account, they often neglect circular polarisation contributions from vegetation and other biological materials. This omission is largely due to the extreme difficulty of measuring circularly polarised light: the signals are typically only a few

tens to hundredths of a percent of the reflected light. In addition to that, there is no such thing as a perfect static circular analyser that can measure such weak circular polarisation reliably across the visible-light spectrum.

Having established that circular polarisation can serve as a unique indicator of biological activity, in Chapter 3 we aim to refine those models by incorporating the effects of circular polarisation produced by the **homochiral** nature of biological materials. In this study, we use a **hot-air balloon** as an observing platform, a choice that offers several advantages: it provides a remarkably stable flight, is considerably less costly than using a helicopter or aeroplane, and allows for real-time instrument adjustments during observations. We measure circular polarisation signals from diverse landscapes. such as forests, fields, and bodies of water, to better understand how living surfaces can be identified remotely. Furthermore, we evaluate the performance of a polarisation camera, assessing their potential for future airborne missions dedicated to the search for life.

## Designing a snapshot Full-Stokes spectropolarimeter

While spectropolarimetry shows great promise for detecting life from a distance, one major challenge remains: we need extremely sensitive instruments to reliably measure these delicate signals. Building on our balloon-based observations, the next step is to design an instrument capable of measuring polarisation signals, including both circular and the promising linear component, from a vantage point where the Earth can be observed as if it were an exoplanet. Such a perspective can be achieved from space, for example from the International Space Station or even the Moon, allowing us to capture the full-disk polarisation signal of our planet. Instruments intended for these platforms must therefore be capable of detecting all components of polarisation in a single snapshot and without relying on moving or active (optical) parts. Developing such a full-Stokes spectropolarimeter is no easy task, and the final two chapters of this thesis focus on the opportunities and challenges involved in designing and realising such an instrument.

In Chapter 4, we introduce **LSDPol** (the Life Signature Detection Polarimeter), a prototype instrument designed to detect signs of homochirality using visible-light polarimetry. Building on the motivation to measure polarisation from a space-based perspective, the main goal of LSDPol is to detect extremely small polarisation signals - in particular the tiny fractions of circularly polarised light generated by biological matter. Crucially, the instrument must be able to distinguish these minute circular components from the far larger linearly polarised signals, which can reach tens of percent of the reflected light. One of the main challenges in the prototype is the appearance of unwanted, false-positive polarisation signals, primarily caused by the way light diffracts and spreads after passing through the polarisation modulator.

To understand where these signals come from, we run detailed computer simulations, followed by laboratory experiments. The results show that light bending (known as Fresnel diffraction) creates unexpected patterns in the measurements: small wavy features appear in parts of the data where none should exist, and shifts are observed even when measuring unpolarised light. We also find that the distance between the modulator and the subsequent optical components plays a significant role. Achieving the most accurate results therefore

requires cautious calibration. To further improve LSDPol's performance and prepare for future space-based deployment, we recommend developing a comprehensive mathematical model that accounts for wavelength-dependent light behaviour.

Finally, in **Chapter 5**, the use of **spatial polarisation modulators** is investigated. These advanced optical elements, based on liquid-crystal technology, enable the measurement of all polarisation components of incoming light in a single snapshot. A major challenge with these modulators is the appearance of unwanted self-images. This occurs because the modulator and a linear polariser together function as a kind of virtual grating, giving rise to the Talbot effect. The pattern of this virtual grating repeats at specific distances, known as Talbot distances. Between these Talbot distances, the patterns change: the original pattern can appear doubled or shifted relative to the original grating pattern. These subtle intensity modulations can interfere with the measurement of the true polarisation state. Therefore, it is essential to carefully understand and correct for these effects to ensure reliable spectropolarimetric measurements.

***Thanks to these technological advances, we are moving closer to building instruments capable of detecting clear and unmistakable signs of life on planets orbiting distant stars.***

# Nederlandse samenvatting

*Hoe zijn we ontstaan? Zijn we alleen in dit universum?* Al eeuwenlang prikkelen deze vragen de grenzeloze nieuwsgierigheid van de mensheid. Vandaag de dag, november 2026, biedt de ontdekking van meer dan zesduizend exoplaneten een kijkje in de ongelooflijke diversiteit van de werelden die zich buiten ons zonnestelsel bevinden. In het verlangen om deze verre werelden écht te kunnen begrijpen, is ontdekking nog maar een eerste stap. Als we willen beoordelen of er leven kan bestaan op deze planeten, is het noodzakelijk om hun basiseigenschappen te kennen, bijvoorbeeld de grootte en massa van de planeet. Door de dichtheid van de planeten te berekenen, kunnen we ze classificeren als rotsachtige (bijvoorbeeld Aardeachtige) of gasachtige planeten (zoals Neptunus, Jupiter of zelfs een kolossale super-Jupiter). Als we de grootte van moederster en de afstand tussen de planeet ster weten, kunnen we uitzoeken of deze planeet in de zogeheten leefbare zone valt. In deze zone is de temperatuur geschikt voor het bestaan van vloeibaar water: een van de cruciale ingrediënten voor leven zoals wij dat kennen.

## Verre werelden observeren: directe waarneming & spectroscopie

*Hoe kunnen we de onzichtbare werelden rond verre sterren bestuderen?* Sterren, of het nu onze Zon is of verre sterren in de Melkweg, zenden licht uit over het hele elektromagnetische spectrum: infraroodstraling die we kunnen voelen als warmte, zichtbaar licht dat we kunnen zien, en ultraviolette straling die zelfs zonnebrand kan veroorzaken. Planeten daarentegen zijn heel anders. Ze produceren geen zichtbaar licht van zichzelf. In plaats daarvan worden ze alleen zichtbaar doordat ze het licht van hun moederster weerkaatsen en een klein beetje infrarood uitstralen wanneer ze opwarmen door dat sterlicht. In onze eigen nachtelijke hemel kunnen we planeten zoals Mars, Venus en Jupiter zien. Met het blote oog lijken ze heldere lichtpuntjes, niet zo verschillend van nabije sterren. Overdag verdwijnen deze planeten echter volledig uit zicht. Dit komt niet omdat ze ophouden met het weerkaatsen van zonlicht, maar omdat de Zon zó fel is dat haar licht al het zwakke gereflecteerde licht van de planeten volledig overstemt.

Ditzelfde principe geldt ook voor exoplaneten, maar dan op een veel extremere schaal. Deze planeten draaien om sterren die niet alleen veel helderder zijn dan de planeet zelf, maar ook enorm ver van ons vandaan staan. Vanuit ons perspectief staat een exoplaneet pal naast zijn verblindend heldere ster, waardoor het contrast tussen beiden gigantisch wordt: het licht van de ster kan wel tienduizend tot tientallen miljarden keer sterker zijn dan het gereflecteerde licht van de planeet. Dit illustreert hoe moeilijk het is om een exoplaneet daadwerkelijk te fotograferen. Toch zijn er inmiddels planeten direct waargenomen. Om dit te doen gebruiken astronomen een techniek die **high-contrast imaging** heet. Hierbij onderdrukken telescopen het felle licht van de moederster, zodat het zwakke gereflecteerde licht van de planeet zichtbaar kan worden. Deze methode staat ook wel bekend als **directe waarneming**.

Echter, zelfs met deze directe waarneming techniek is het niet altijd mogelijk om exop-

laneten waar te nemen. Gelukkig kunnen we ook andere methodes gebruiken, zoals spectroscopie, om exoplaneten te bestuderen. Spectroscopie meet de golflengte (of 'kleur') en de intensiteit van licht. Alle exoplaneten draaien met een constante snelheid rondom hun moederster. Als de planeet in zijn ronde precies tussen zijn ster en een telescoop staat, passeert een deel van het sterlicht door de atmosfeer van de planeet. Door dit licht te analyseren, kunnen we de chemische samenstelling van de planeet achterhalen. Spectroscopie maakt het mogelijk om de unieke 'vingerafdrukken' van atomen en moleculen te detecteren, en zo de samenstelling van de atmosfeer, de temperatuur en de aanwezigheid van wolken of nevels te bepalen. **Hoge-resolutie spectroscopie** kan zelfs sporen van gassen detecteren en atmosferische bewegingen zoals wind of de rotatie van de planeet meten.

In Hoofdstuk 2 gebruiken we hoge-resolutie spectroscopie om de atmosferen van drie **bruine dwergen** te bestuderen. Dit zijn objecten die noch planeten noch sterren zijn: ze zijn zwaarder dan reuzenplaneten, maar te licht om waterstoffusie in stand te houden en stralen daardoor geen stabiel eigen licht uit. De waarnemingen maken deel uit van de *SupJup Survey*, waarvoor het CRIRES+-instrument op de Very Large Telescope in Chili is gebruikt. Dit instrument is in staat om gedetailleerde spectra van astronomische objecten waar te nemen.

De drie spectra van de bruine dwergen die wij bestuderen laten een verhoogde koolstof-zuurstofverhouding en een hogere metalliciteit zien in vergelijking met onze zon. Dit suggereert dat een deel van de zuurstof tijdens de vorming van deze objecten mogelijk in vaste materialen is opgeslagen. We hebben ook de verhouding tussen twee isotopen van koolstof gemeten, $^{12}$C en $^{13}$C. Deze verhouding geeft aanwijzingen over de chemische evolutie van het gebied waar de objecten zijn ontstaan. Onze resultaten laten een iets lager gehalte aan $^{13}$C zien dan doorgaans wordt aangetroffen in het diffuse interstellaire gas en stof in de Melkweg. Binnen het SupJup Survey-project worden momenteel de resterende spectra geanalyseerd om een vollediger beeld te krijgen van hoe planeten en aanverwante substellaire objecten ontstaan en zich ontwikkelen.

## De zoektocht naar leven zoals wij dat kennen: homochiraliteit & spectropolarimetrie

Hoewel de studie van verre exoplaneten de enorme diversiteit aan werelden in ons universum laat zien, blijft één simpele waarheid bestaan: de enige planeet waarvan we weten dat er leven op is, is de Aarde. Om naar vergelijkbare levensvormen buiten ons zonnestelsel te zoeken, moeten we eerst begrijpen hoe we de essentiële tekenen van leven op Aarde kunnen herkennen. Een van de duidelijkste signalen is het fenomeen **homochiraliteit**. De bouwstenen van leven zoals wij dat kennen - chlorofyl, aminozuren, eiwitten, DNA en suikers - hebben allemaal een specifieke moleculaire 'links- of rechtshandigheid'. Deze consistente voorkeur voor één spiegelbeeldvorm wordt biologisch bepaald en vormt daardoor een unieke en ondubbelzinnige vingerafdruk van leven.

Om ons voor te bereiden op toekomstige ruimtemissies die gericht zijn op het opsporen van buitenaards leven, is het essentieel om te testen of we dit signaal op afstand kunnen detecteren, onder realistische omstandigheden buiten het laboratorium. Een van de krachtigste technieken hiervoor is **spectropolarimetrie**. In tegenstelling tot spectroscopie, waarbij we alleen de intensiteit van specifieke golflengten van binnenkomend licht meten, laat spectro-

polarimetrie zien hoe de lichtgolven zijn georiënteerd - een eigenschap die bekend staat als **polarisatie**. Licht kan lineair gepolariseerd raken wanneer het wordt verstrooid door de atmosfeer of gereflecteerd door planetaire oppervlakken zoals oceanen of zandgronden, een effect dat goed wordt begrepen. Een minder voor de hand liggende, maar intrigerende vorm is **circulaire polarisatie**, waarbij de lichtgolven in een spiraalvorm bewegen. Interessant is dat dit type polarisatie kan ontstaan wanneer licht in wisselwerking staat met biologische moleculen vanwege hun homochirale aard. Hierdoor wordt circulaire polarisatie gezien als een veelbelovende en wellicht de meest eenduidige indicator van leven op afstand.

Hoewel bestaande modellen van hoe planetaire oppervlakken en atmosferen licht reflecteren al rekening houden met verschillende verstrooiingseffecten, negeren ze vaak de bijdrage van circulaire polarisatie afkomstig van vegetatie en andere biologische materialen. Dit komt vooral door de uiterst moeilijke meetbaarheid van circulair gepolariseerd licht: de signalen bedragen meestal slechts enkele tienden tot honderdsten van een procent van het gereflecteerde licht. Daarnaast, bestaat geen perfect circulair polarisatie-analyse-instrument dat deze zwakke signalen betrouwbaar over het volledige zichtbare spectrum kan meten.

Nu we weten dat circulaire polarisatie een unieke signatuur van biologische activiteit kan zijn, richten we ons in **Hoofdstuk 3** op het verfijnen van deze modellen door de effecten van biologische materialen mee te nemen. Voor deze studie gebruiken we een **heteluchtballon** als observatieplatform. Dit biedt een aantal voordelen: een stabiele vlucht, aanzienlijk lagere kosten dan een helikopter of vliegtuig, en de mogelijkheid om tijdens observaties instrumenten in realtime aan te passen. We meten circulaire polarisatiesignalen van verschillende landschappen, zoals bossen, velden en watermassa's, om beter te begrijpen hoe levende oppervlakken op afstand kunnen worden herkend. Daarnaast evalueren we de prestaties van een polarisatiecamera en onderzoeken we het potentieel ervan voor toekomstige meetcampagnes die gericht zijn op het opsporen van leven.

## Ontwerp van een snapshot Full-Stokes spectropolarimeter

Hoewel spectropolarimetrie veelbelovend is voor het detecteren van leven op afstand, blijft er één grote uitdaging: we hebben uiterst gevoelige instrumenten nodig om deze subtiele signalen precies en betrouwbaar te meten. Voortbouwend op onze observaties vanuit de luchtballon, is de volgende stap het ontwerpen van een instrument dat polarisatiesignalen kan meten, zowel circulaire als de veelbelovende lineaire component, vanuit een uitkijkpunt waar de aarde kan worden waargenomen alsof het een exoplaneet is. Een dergelijk perspectief kan alleen vanuit de ruimte worden bereikt, bijvoorbeeld vanaf het internationale ruimtestation ISS of vanaf de maan. Vanaf deze kijkpunten kunnen we het volledige polarisatiesignaal van onze planeet vastleggen. Voor instrumenten in de ruimte is het wenselijk om alle componenten van polarisatie in één enkele momentopname te detecteren, zonder bewegende onderdelen of actieve optische elementen te gebruiken. Het ontwikkelen van een dergelijke volledige Stokes-spectropolarimeter is geen eenvoudige taak, en de laatste twee hoofdstukken van dit proefschrift richten zich op de mogelijkheden en uitdagingen die gepaard gaan met het ontwerpen en realiseren van zo'n instrument.

In **Hoofdstuk 4** introduceren we **LSDPol** (Life Signature Detection Polarimeter), een prototype-instrument dat is ontworpen om tekenen van homochiraliteit te detecteren met be-

hulp van polarimetrie in zichtbaar licht. Het belangrijkste doel van LSDPol is het meten van uiterst kleine polarisatiesignalen - met name de minuscule fracties circulair gepolariseerd licht die door biologische materialen worden gegenereerd. Daarbij moet het instrument deze kleine circulaire signalen kunnen onderscheiden van de veel grotere lineaire polarisatiesignalen, die tot tientallen procenten van het gereflecteerde licht kunnen bedragen, zelfs als dat ten koste gaat van spectrale of spatiële resolutie. Een van de grootste uitdagingen is het optreden van ongewenste, vals-positieve polarisatiesignalen, die veroorzaakt worden door de manier waarop licht buigt en zich verspreidt nadat het door een polarisatiemodulator beweeegt.

Om te begrijpen waar deze signalen vandaan komen, voeren we gedetailleerde computersimulaties uit, gevolgd door laboratoriumexperimenten. De resultaten tonen aan dat lichtbuiging (ook wel Fresnel-diffractie genoemd) onverwachte patronen in de metingen veroorzaakt: kleine golvende kenmerken verschijnen in delen van de gegevens waar die niet zouden moeten voorkomen, en er worden verschuivingen waargenomen, zelfs bij het meten van ongepolariseerd licht. We hebben ook ontdekt dat de afstand tussen de modulator en de daaropvolgende optische componenten een cruciale rol speelt. Voor de meest nauwkeurige resultaten is daarom een uiterst zorgvuldige kalibratie vereist. Om de prestaties van LSDPol verder te verbeteren en voor te bereiden op toekomstige ruimtevaarttoepassingen, raden we aan een uitgebreid wiskundig model te ontwikkelen dat rekening houdt met golflengte-afhankelijk lichtgedrag.

Ten slotte wordt in **Hoofdstuk 5** het gebruik van **spatiële polarisatiemodulatoren** onderzocht. Deze geavanceerde optische elementen, gebaseerd op vloeibare-kristaltechnologie, maken het mogelijk om alle polarisatiecomponenten van het invallende licht in één enkele momentopname te meten. Een belangrijke uitdaging bij deze modulatoren is het ontstaan van ongewenste zelfbeelden. Dit gebeurt doordat de modulator en een lineair polarisatiefilter samen functioneren ze als een soort virtueel tralie, waardoor het Talbot-effect optreedt. Het patroon van dit tralie herhaalt zich op specifieke afstanden, de zogenaamde Talbot-afstanden. Tussen deze Talbot-afstanden veranderen de patronen: het oorspronkelijke patroon kan verdubbeld verschijnen of verschoven worden ten opzichte van het originele traliepatroon. Deze subtiele intensiteitsmodulaties kunnen interfereren met de meting van de echte polarisatietoestand. Daarom is het essentieel om deze effecten zorgvuldig te begrijpen en te corrigeren om betrouwbare spectropolarimetrische metingen te garanderen.

***Dankzij deze technologische vooruitgang komen we steeds dichter bij het bouwen van instrumenten die nauwkeurig de onmiskenbare tekenen van leven kunnen detecteren op planeten die rondom verre sterren, buiten ons zonnestelsel, draaien.***

# Curriculum vitae

I was born in Hengelo on the 12th of July 1993, just one minute before my sister, Liesbeth. As a child, my inquisitive nature became apparent, from spending hours in the science museum's laboratory, to asking many questions. It is no wonder that my favourite television series was Willem Wever, a show that claimed to know all the answers to every question a child could think of. Around the age of eight, I sent them a letter, because I had a question as well: "Why does the Universe never stop?". Within a month, the studio called me back and apologised that they did not know the answer and asked me if I had another question about the Universe. I was so disappointed that I instantly hung up the phone, and realised that I just had to become a scientist, and answer the question myself.

At the senior general secondary education (HAVO), I was the only female student to choose all science subjects in her major. After graduating cum laude, and working hard to finish my pre-university (VWO) degree, I was super excited to started my Bachelor Sterrenkunde (Astronomy) in Groningen.

My bachelor project was to build a radio telescope from scratch, together with three peers. My responsibility was to determine the design requirements and accurately calibrate the instrument.

During my Master's degree, I explored a broad range of topics - from theoretical astrophysics to instrumentation and even business aspects of science. As part of my Master's research, I contributed to the development of an evolving astrometric reference system in collaboration with the Euclid consortium, and completed an internship at ASTRON (the Netherlands Institute for Radio Astronomy). There, I was challenged to apply machine learning techniques to improve the health monitoring of the LOFAR radio telescope system. With no predefined approach, I independently explored, selected, and implemented suitable methods.

Beyond my studies, I enjoyed sharing my enthusiasm for astronomy: promoting the astronomy degree in Groningen to pre-university students, engaging with the general public during outreach events, and tutoring physics at high schools. In the later years of my Master's, I coordinated the Blaauw Observatory, where I managed the mobile planetarium and organized open nights and public events.

After the opportunity arose to join a conference covering the topic of astronomical outreach in Japan, I realised I could continue my astronomy career with a PhD. It was that same year that I met my future-supervisor, Frans Snik, at the Dutch Conference for Astronomy, during a presentation about artists that use Astronomy as inspiration. I sent a letter to the University of Leiden, specifically directed to Frans, to apply for one of the instrumentation projects he was offering. My application was successful, and I begun my PhD research in collaboration with the instrumentation group at the Leiden Observatory and the planetary group from the Technical University of Delft.

The project took an interdisciplinary approach to develop a full-Stokes spectropolarimetric model of Earth, implementing data that we would collect ourselves using in-house developed spectropolarimeters.

During my PhD, I collaborated with a fantastic team of astronomers and physicists from Leiden University, the University of Bern, the University of Maryland, and the University of Central Florida. With this team I was able to calibrate spectropolarimeters, use them during various field campaigns, and simulated Earth-like exoplanets using radiative transfer models. In the final year of my PhD, I joined Leiden's exoplanet group, where I explored the fascinating atmospheres of brown dwarfs.

In February 2025, I started working as a senior data specialist at Valcon in Utrecht. Here I am combining my ability to quickly switch between different projects, communicate with data scientists, engineers, customers and other stakeholders. From May 2025, I have been lucky to become part of ProRail's computer vision team, where we analyse images from measurement trains and ensure rail safety. As a consultant, I learn new skills every day.

# List of publications

## Refereed publications

1. *The ESO SupJup Survey VI:*
   *$^{12}C/^{13}C$ isotope ratio comparison of three L-type brown dwarfs*
   **Mulder, W.**, de Regt, S., Landman, R., González Picos, D., Snellen, I. A. G., Zhang, Y., Gandhi, S., Ginski, C., Kesseli, A. Y., Mollière, P., Nasedkin, E., Sánchez-López, A., Stolker, T.
   Astronomy and Astrophysics, 694, A164 (2025)
   DOI: 10.1051/0004-6361/202452859

## Non-refereed publications

1. *Spectropolarimetry of life:*
   *airborne measurements from a hot air balloon*
   **Mulder, W.**, Doelman, Patty, L.C.U., Spadaccia, S., et al.
   Light in Nature (SPIE) Conf. Series, 12214, 1221404 (2022),
   DOI: 10.1117/12.2633271

2. *Spatial polarization modulators:*
   *distinguishing diffraction effects from spatial polarization modulation*
   **Mulder, W.**, Doelman, D.S., Keller, C.U., Patty, L.C.U., Snik, F.
   Polarization Science & Remote Sensing (SPIE) Conf. Series, 11833, 118330M (2021),
   DOI: 10.1117/12.2595152

## Co-author publications

1. *Conceptual design and prototyping of a three-color polarimetric*
   *imaging instrument for auroral observations*
   Stockmans, T.A., Strelow, K., Scheinowitz, N., Fagginger Auer, F., **Mulder, W.**, Stuik, R., Cessateur, G., Bosse, L., Lamy, H., and Snik, F.
   Journal of Space Weather and Space Climate (*submitted* 2025),
   DOI: xx.xxxx/xxxx

2. *ESO SupJup Survey VIII: Chemical fingerprints of young L dwarf twins*
Grasser, N., Snellen, I. A. G., de Regt, S., González Picos, D., Zhang, Y., Mollière, P., Stolker, T., Gandhi, S., Nasedki, E., Landman, R., Allard, N. F., Ginski, C., Kesseli, A. Y., **Mulder, W.**, and Sánchez-López, A.,
Astronomy & Astrophysics, 698, A252 (2025),
DOI: 10.1051/0004-6361/202554195

3. *ESO SupJup Survey V: Exploring Atmospheric Variability and Orbit of the Super-Jupiter AB Pictoris b with CRIRES+*
Gandhi, S., de Regt, S., Snellen, I. A. G., Palma-Bifani, P., Abdoulwahab, I., Chauvin, G., González Picos, D., Zhang, Y., Landman, R., Stolker, T., Kesseli, A. Y., **Mulder, W.**, Chomez, A., Lagrange and A., Zurlo, A.
Monthly Notices of the Royal Astronomical Society, (2024),
DOI: 10.1093/mnras/staf004

4. *Polarized Signatures of a Habitable World:*
*Comparing Models of an Exoplanet Earth with Visible and Near-infrared Earthshine Spectra*
Gordon, E.K., Karalidi, T., Bott, K.M., Miles-Páez, P.A., **Mulder, W.**, Stam, D.M.
the Astrophysical Journal 945 166 (2023),
DOI: 10.3847/1538-4357/aca7fe

5. *Biosignatures of the Earth:*
*I. Airborne spectropolarimetric detection of photosynthetic life*
Patty, C.H.L., Kühn, J.G., Lambrev, P.H., Spadaccia, S., Hoeijmakers, J.H., Keller, C.U., **Mulder, W.**, Pallichadath, V., Poch, O., Snik, F., Stam, D.M., Pommerol, A., Demory, B.O.
Astronomy & Astrophysics, 651, A68 (2021),
DOI: 10.1051/0004-6361/202140845

6. *Comparing Models of an Exoplanet-Earth to Earthshine Observations*
Gordon, K.E., Karalidi, T., Miles-Páez, P.A., Stam, D.M., Bott, K.M., **Mulder, W.**
Bulletin of the AAS, AAS, 53(1). (2021),
URL: baas.aas.org/pub/2021n1i505p03

# Acknowledgments

Much like planetary orbits, my progress in this thesis had its fair share of eccentricities, perturbations, and unexpected retrograde motions. But thanks to an incredible support system, of subsequently named people, I've managed to stay in a trajectory toward completion. In my search for life beyond Earth, I have at least confirmed one thing - intelligent life remains elusive. Fortunately, my advisors, colleagues, friends, and coffee supply have provided enough habitability conditions to sustain this academic mission.

**Christoph**, thank you for the time and effort you put into guiding me and my research, even after moving to the US. I am especially grateful for the incredible hospitality you and Rennie showed me during my stay in Flagstaff, Arizona. **Ignas**, thank you for your unwavering support in the final year of my PhD. You welcomed me into the exoplanet group with open arms, making sure I felt part of the team. Your guidance and help during the last year made all the difference. **Frans**, your enthusiasm for science (and science communication) is truly endless and contagious. I am grateful we had the opportunity to work together and that I was able to visit you and Sabina multiple times in Utrecht for inspiring conversations and invaluable support. **Daphne**, the planetary science community has lost not only an incredibly strong woman but above all, an extraordinary scientist. You were the one who introduced me to this field, and for that, I will always be grateful.

Beyond my supervisors, I want to dedicate a special thank you to three scientists, each of whom deserves at least a full page of appreciation: Lucas, David, and Sam. Without you, this dissertation would not have been published. **Lucas**, you have been there for me in the lab from the very beginning of my PhD. During the height of COVID-19, you remotely guided me through the incomplete TreePol and LSDpol setups. We were an incredible team. I enjoyed working together, my visits to Switzerland, the early morning balloon flights where we almost forgot our optical fibres despite the to-do-list and the after-work climbing sessions. **David** - or should I say, Buurman? You were the first colleague I met in person during the pandemic: a doctor always ready to talk science, but just as ready to be there as a dear friend. That one Halloween - I'll never forget it. The two of us dressed up as Buurman & Buurman: you with your impressive drill and Nathalie's yellow jumper, me with my fingers glued together by instant glue. With our knitted hats perched on our heads and out oversized do-it-yourself shoes on our feet. You were always there to help me out, e.g. chauffeuring me to the *Heel Holland Bakt* auditions on a hot summer day in a car without air conditioning. Despite the melting cake, you still trusted me to make your wedding cake. **Sam**, thank you for your time and all the help with the SupJup paper. Not only are you an exceptional scientist, but also a patient and dedicated mentor who never hesitates to explain any theory or code. Because of (and together with) you, we managed to publish a paper in no time - despite me having no prior knowledge of the field. I could not have done this without you.

Then I want to thank the members of the instrumentation group, **Bernhard**, **Dirk**, **Dora**, **Emiel**, **Emily**, **Floor**, **Matt**, **Michiel**, **Mireille**, **Kira**, **Naor**, **Olivier**, **Richelle**, **Steven**, and Leiden Observatory, including **Alina**, **Andrea**, **Jeroen**, **Joey**, **Josh**, **Jurjen**, **Koen**, **Morgan**, **Nancy**, **Sanjana**, **Turgay**. **Elina** & **Tara**, I will never forget our endless fits of laughter, **Luna**, you will always be my most favourite office mate. **Piyush**, your ability to connect

people is awe-inspiring. **Remko**, without your humour and technical support, there would not be an instrumentation group. **Rico**, with your energy and positive attitude, you would brighten every day. **Thijs**, we shared some outstanding USA adventures together, those I will never forget. **Thomas**, you are Leiden's best barista and philosopher.

In addition, I want to thank some friends, all scattered over the Netherlands. **Janneke**, **Jolien**, **Kristel**, **Nikki**, and **Serte**, thank you for your everlasting support, ever since the start of the 'Eetclub'. **Jasper**, our deep conversations on the phone while running or walking Tjibbe. Friends from my jaarclub; **Bernadette**, **Loes** and **Nanouk**, from my bachelors; **Frits**, **Maik** and **Jonas**, from my masters; **Marrick** and **Amit** and from my years in Groningen; **Katya** and **Enrico**. **Laurent**, you were physically and emotionally there for me, especially when I broke both my arm and ankle during the pandemic, for which I am forever grateful. All friends of the "Browurst", especially **Thijn**, my experienced life advisor and above all dance partner. **Stijn**, thank you for listening: we will always remain commission Multivitamin and **Remco**, if there was anyone who believed in me all those years, it was you!

Friends I made through the USC sport centre: **Christin** and **Melissa**, I enjoyed our morning cappuccinos at the USC and sports lessons together, so much. **Lisa**, **Sanne** and **Vera**, our tummies hurt from both the exercises and the laughter, and you always put a smile on my face after a long workday. **Natascha** and **Heleen**, my positive and favourite circuit training buddies. But also **Alxiomar**, **Antonio**, **Jara**, and many others, thank you!

Mr. Dr. Dane Kleiner, or **Apples**. I am incredibly grateful to have had you by my side during the last years of my PhD. Thank you for your unwavering support - whether it was offering your home in Groningen as a quiet workspace while I wrote my last chapter or assisting me in the optical lab with my final measurements. You would make tea and spoil me with Tim Tam slams during late-night or weekend work sessions, bravely taste all my (stress-relieving) lamington or caramel slice baking experiments, and help me unwind with spontaneous (very early morning) adventures. I am extremely thankful that you are part of the next chapter in my life.

Lastly, I want to express my gratitude to my family, for which I will continue in Dutch. **Mam** en **pap**, wat een avontuur is het toch: twee dochters die besluiten om een PhD te gaan doen aan de universiteit. Ik mag me ongelooflijk gelukkig prijzen met ouders zoals jullie - onvoorwaardelijk steunend, meedenkend, altijd dicht bij, zelfs als de kilometers tussen ons lagen. Of ik nu in Groningen, Leiden of Hengelo woonde, jullie stonden en staan altijd klaar met een luisterend oor. Zelfs wanneer mijn verhalen zich in wetenschappelijke wolkenlagen begaven waar jullie niet per se thuis waren, bleef jullie interesse onveranderd. Jullie betrokkenheid betekent meer dan ik kan zeggen - dankjewel. **Liesbeth**. Tweeling-zijn is een band die zich nauwelijks laat uitleggen: we bewegen vaak in verschillende richtingen, maar toch blijft er die vanzelfsprekende samenhang. Misschien daardoor dat ik - traditioneel inmiddels - weer achter je aan ben gelopen: eerst het vwo, toen de universiteit, en uiteindelijk zelfs een PhD. Ik kon altijd bij jou terecht met vragen, twijfels of gedachten die nergens anders wilden landen. **Gerdie**, jij bent degene die een sterrenkundige weer zachtjes terug op aarde zet wanneer ze te ver omhoog begint te zweven. Met jouw filosofische, bijna socratische manier van vragen stellen en je vermogen om (e.g. met het kralenspel) alle opties helder te krijgen, help je me telkens de juiste weg te vinden. Je luistert met aandacht, met warmte, en met een open blik die ik enorm bewonder. Jouw steun in de afgelopen jaren was van onschatbare waarde.